STATISTICAL AND WAVELET ANALYSIS OF DENSITY AND MAGNETIC SUSCEPTIBILITY DATA FROM THE BUSHVELD COMPLEX, SOUTH AFRICA

Obone Sepato

A dissertation submitted to the Faculty of Science, University of the Witwatersrand, in fulfilment of the requirements for the degree of Master of Science

Johannesburg, 2015

DECLARATION

I declare that this thesis is my own, unaided work. It is being submitted for the Degree of Master of Science at the University of the Witwatersrand, Johannesburg. It has not been submitted before for any degree or examination at any other University.

_____

Obone Sepato

_____ day of _____2015 in _____.

ABSTRACT

The Bushveld Complex (BC) is the largest known layered intrusion. This suite of rock crop out in northern South Africa to form the Western, Eastern and Northern Limbs. Most research carried out focuses on the mineralized horizons in the Rustenburg Layered Suite (RLS) of the BC. This study presents a large database of wireline geophysical logs across a substantive part of the stratigraphy of the RLS. These consist of density and magnetic susceptibility datasets sampled at 1 cm. The major lithologies of the RLS intersected in the boreholes presented are gabbro, gabbronorite, norite and anorthosite whose density histograms reveal that they are predominantly normally distributed, with density averages of 2.86-2.91 g/cm^3. The lithologies consist of mainly two minerals, pyroxene and plagioclase. In general, the average density increases with an increase in pyroxene. The distribution of the magnetic susceptibility for these lithologies has a large variation from 6.67×10^{-7} SI to 13.2 SI, which is typical of layered intrusions. Susceptibility distributions are also multi-modal, asymmetric and not normally distributed, which makes the average magnetic susceptibilities less representative of the lithologies.

Cross-correlation plots between density and magnetic susceptibility for several boreholes show that the above-mentioned lithologies form clusters (circular to elliptical), which typically overlap. This has been further investigated using *k*-means classification, to automatically detect these clusters in the cross-correlation plots and to compare these with those created by lithologies. The comparison shows some degree of correlation, implying that physical properties can be used to identify lithologies. This is particularly true for the Eastern Limb. However the classification has not been effective in all of the boreholes and often becomes complicated and an inaccurate representation of lithology log. This occurs in boreholes in which there is an overlap in the physical properties of the abovementioned lithologies.

Analysis on the density and magnetic susceptibility data has also been carried out using wavelet analysis at individual locations across the BC. This has revealed multi-scale cyclicity in all of the boreholes studied, which is attributed to subtle layering created by variations in modal proportions between plagioclase and pyroxene. In addition to this, since layering is generally ubiquitous across layered intrusions, this cyclicity can be assumed to be present across the entire BC. This technique may become increasingly important should the cyclicity in physical property data correlate with reversals in fractionation trends since this may suggest zones of magma addition, whose thickness or

volumes can be quantified using wavelet analysis. This could be an important contribution since the current perspective on magma addition in the RLS is that four major additions have formed this 8 km thick suite of rocks, as opposed to smaller periodic influxes of magma.

Wavelet-based semblance analysis has been used to compare the wavelengths at which the cyclicity occurs across boreholes. A comparison of wavelengths of this cyclicity shows that boreholes in the northern Western Limb show positive correlation in the density data at wavelengths >160 m and 20-60 m, while those further south show correlations at wavelengths of 120-200 m and 60-80 m. Boreholes of the Eastern Limb show positive correlation in the density and magnetic susceptibility data at wavelengths of 10-20 m, 20-30 m and 5m. These positive correlations across boreholes in density and magnetic susceptibility respectively, may imply that cyclicity may be produced by a chamber-wide process for several kilometres of the BC.

ACKNOWLEDGEMENTS

The author wishes to thank:

- Anglo American for funding the project
- My supervisors Prof. Gordon Cooper and Dr Susan Webb for all their assistance throughout this research
- Anglo Platinum Ltd and Royal Bafokeng Platinum for allowing me access to the wireline and geological logs used in this thesis
- Bathandwa Mabedla, Agnes Jikelo and Mr Wayne Pettit from Anglo American for assisting with obtaining the data and their invaluable support throughout the project
- Mrs Mary Evans, Prof. Lew Ashwal, and Dr Grant Bybee are thanked for their constructive criticism
- Lerato Moagi, Keith Saunders, John Jeffrey and Blake Smith from Weatherford Wireless Services for exposing me to various wireline logging tools and data processing procedures
- Marcia van Aswegen, Judy Schlegel, Rajes Reddy and Itumeleng Jean Dyasi from SABLE for providing an academic license of SABLE Data Warehouse
- Marcus Chatfield from the Wireline Workshop for his insight on logging practices in the mining industry
- The following postgraduate students, who have made my time spent at Wits University enriching: William Rankin, Dr Musa Manzi, Siyanda Mngadi and Stephanie Enslin
- Mr Isaac Sepato, Mrs Yvonne Sepato and Ms Nthabiseng Mutloane for all of their love and support during my research

LIST OF FIGURES

LIST OF TABLES

TABLE OF CONTENT

CHAPTER 1: INTRODUCTION

Layered intrusions are large bodies of igneous rocks that intrude into the crust to form laterally continuous layers. Layer thicknesses vary on the scale of several hundreds of metres to a few centimetres, with varying modal proportions, mineral compositions, grain-sizes and textures. The various processes that have been attributed to the origin of layering are summarized by Naslund and McBirney (1996). They have compiled a list of over twenty proposed mechanisms, which operate from the infilling of a magma chamber to the late stages of crystallization. The consensus is that various magmatic processes could have occurred simultaneously, resulting in mineral segregation to form layers. Although there is genuine scientific intrigue surrounding the formation of these bodies, there is also an economic interest as they host worldwide supplies of platinum and palladium (Schouwstra and Kinloch, 2000). Some of the best studied and most well-known large igneous intrusions include Stillwater (U.S.A), Great Dyke (Zimbabwe), Munni-Munni (Western Australia), Skaergaard (East Greenland), Muskox (Canada) and the Bushveld Igneous Complex (South Africa) (Wager and Brown, 1968; Eales and Cawthorn, 1996).

The largest known igneous intrusion is the Bushveld Complex (BC), which is the focus of this study (Lee, 1996; Wilson, 2012). Conventional studies of layered intrusions feature a myriad of techniques, including but not limited to; mapping, petrography, electron microprobe analysis, whole rock geochemistry and isotope analysis. These tend to mainly focus on the mineralized layers of economic interest (Ashwal et al., 2005). The aim of this research is to study the layering of the BC using rock physical properties such as density and magnetic susceptibility, which are currently poorly studied and underutilised when collected. The focus on rock physical properties have the advantage of allowing for detailed studies of the rocks as they are closely sampled and multiple properties can be studied at the same time.

1.1 Background

The BC (Figure 1.1) formed at 2.06 Ga and covers an estimated 65 000 km^2 in northern South Africa, with a maximum thickness of ~8 km (Cawthorn et al., 2006). This suite of rocks is suggested to have formed from several pulses of magma and outcrops to form the Northern, Eastern, Western and the Far Western Limbs. The Southeastern or Bethal Limb is known only from geophysics and drilling and has no surface exposure (Cawthorn et al.,

2006). The Western and Eastern Limbs of the Bushveld are slightly arcuate in shape, and extend for approximately 200 km.

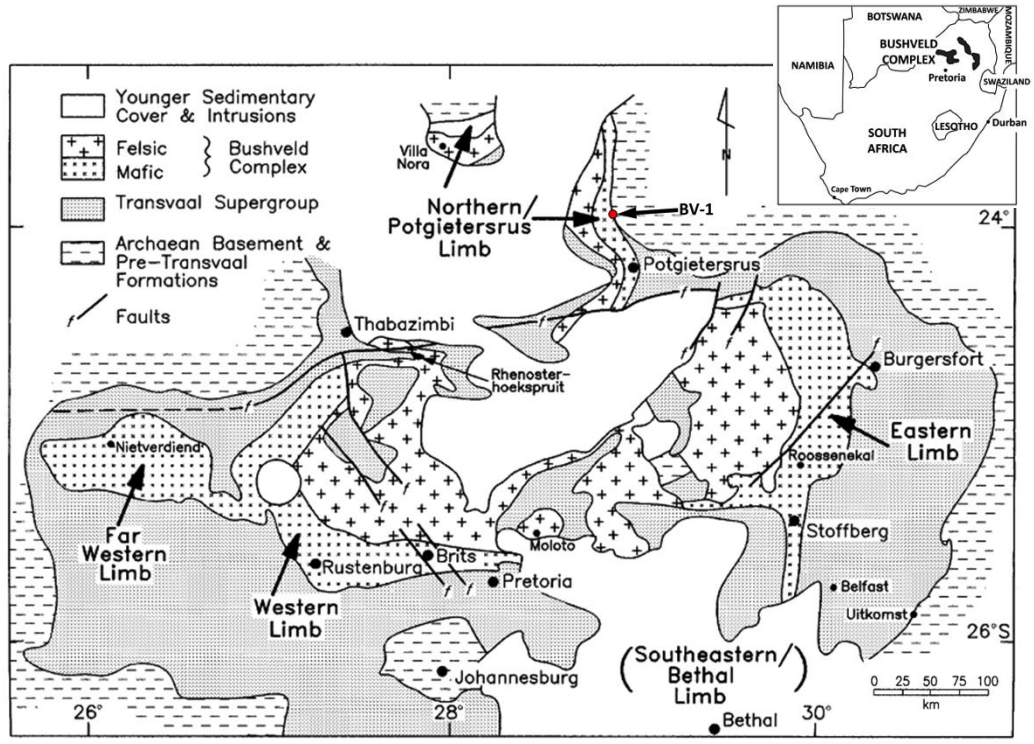

Figure 1.1 Geological map of the Bushveld Complex, with older Transvaal Supergroup rocks and younger sedimentary cover (modified after Barnes et al., 2004 and Cawthorn and Walraven, 1998). Location of the Bellevue BV-1 borehole is shown as a red dot (see text for details).

The rocks of the BC have been largely subdivided into four suites of rocks with the extrusive volcanic rocks of the Rooiberg Group forming the base of the Complex. This is followed by the Rustenburg Layered Suite, the Rashoop Granophyre Suite and finally the Lebowa Granite Suite (Schweitzer et al., 1997). Of all these suites the most studied is the Rustenburg Layered Suite (RLS) (Cawthorn et al., 2006), which hosts some of the world's largest reserves of platinum-group elements and is the focus of this study. The stratigraphy of the RLS is subdivided into the Upper Zone (UZ), Main Zone (MZ), Critical Zone (CZ), Lower Zone (LZ) and Marginal Zone (MaZ).

Ashwal et al. (2005) collected geophysical measurements from the 3 km Bellevue BV-1 borehole in the Northern Limb (Figure 1.1) that allowed for the detailed study of geophysical measurements of the entire UZ and approximately half of the MZ of the BC. Their study revealed surprising reversals or cyclicity in the density data in the MZ on

several scales, in which density increases upwards in individual homogeneous layers. These data are shown in Figure 1.2a and b.

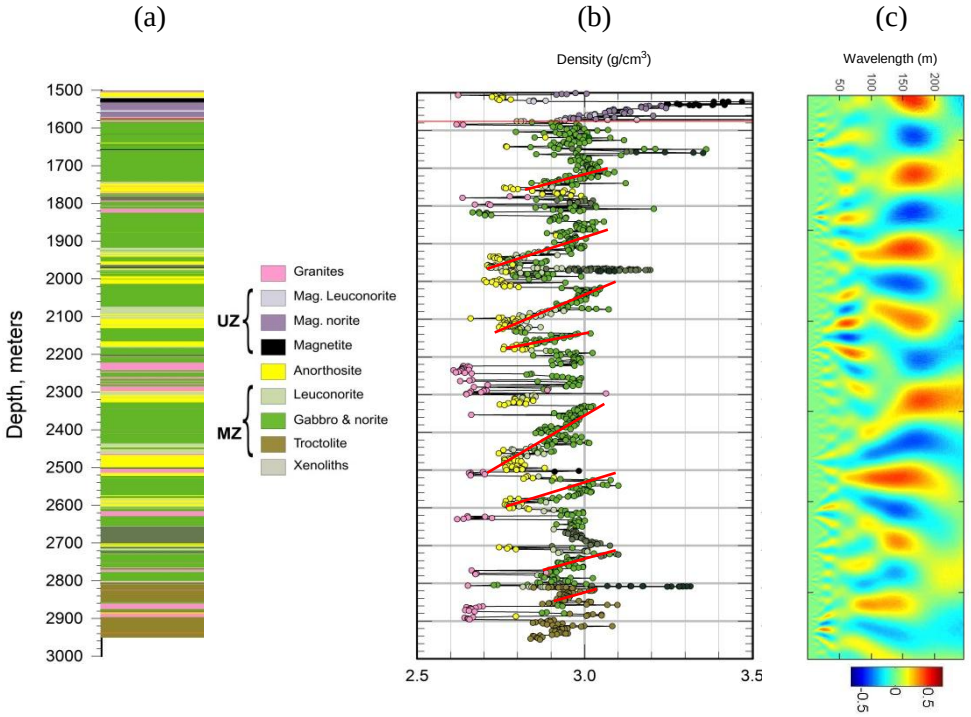

Figure 1.2 (a) Lithology log for borehole BV-1. (b) Density data (g/cm^3) vs. depth (m), with prominent reversals in density with stratigraphic height indicated. (c) Wavelet transform (using the Morlet wavelet) of the measured data, with the maxima and minima in red and blue respectively at wavelengths of between 50 m and 200 m (modified after Webb et al., 2008).

These correlated (in some instances), with upward reversals in mineral compositions. This study concluded that the density reversals may indicate magma additions or pulses. Webb et al. (2008) applied several mathematical tools (power spectra, windowed histogram plots and wavelet analysis) to the density data to study layering. The wavelet analysis was used to quantify the abovementioned cyclicity in density and magnetic susceptibility measurements. From this data analysis, they were able to detect layering between and within units of the MZ and UZ of the Northern Limb of the BC. They discovered different scales of layering changing from 50 m to 150 m in the section of the borehole in which they worked, shown in Figure 1.2c. While this layering was seen in the Northern Limb by Ashwal et al. (2005) and Webb et al. (2008), no similar studies have been done in the Western and Eastern Limbs of the BC. It is therefore unknown whether or not layering at this scale can be detected using rock physical properties and the geological implications.

To investigate whether rock physical properties can detect layering an extensive catalogue of borehole density and magnetic susceptibility wireline logs across the BC have been provided by Anglo Platinum Ltd. These data are from platinum mining operations in the Western and Eastern Limbs of the Bushveld, which will allow for a comparative study of these physical properties to be done across the entire BC.

1.2 Project Aim

Studies by Webb et al. (2008) have already shown that wavelet analysis applied to density and magnetic susceptibility measurements of the Bellevue BV-1 core has revealed cyclicity, which has been attributed to layering. These different scales in layering have been quantified for the Bellevue BV-1 borehole in the Northern Limb of the BC. The aim of this study will be to study cyclicity of physical properties in several boreholes across the Eastern and Western of the BC using wavelet analysis and the implication on the emplacement processes which formed this layered intrusion. The cyclicity will then be compared across the BC, to study if the same scales are observed at similar stratigraphic heights, using wavelet-based semblance analysis. The deepest and most evenly spread boreholes have been sought for this project, as these will allow for a large part of the stratigraphy to be studied at individual locations as well as correlated. Since such a vast amount of data is available, it also lends itself to statistical analysis. Cross-correlation plots and classification techniques have been carried out on physical property data to ascertain the extent to these data can be used to characterise various lithologies of the BC. MATLAB code have been written by the author and are supplied in APPENDIX A and B.

1.3 Thesis Structure

The Data Collection and Quality Control (Chapter 2) which follows summarizes wireline logging principles and the various quality measures used to select the data to use for further analysis. The Datasets (Chapter 3) section presents the geological logs in the context of the stratigraphy of the BC, and the physical properties are discussed using frequency histograms and using cross-correlation plots. Cluster Analysis (Chapter 4) evaluates the extent to which physical property data can be used to classify lithologies. The degree to which this method can be used as a semi-automatic interpretation tool for lithology logs is discussed. Chapters on wavelet analysis have been separated into two as they constitute the largest volume of the thesis. These are the Background - Wavelet

Analysis (Chapter 5) and Results - Wavelet Analysis (Chapter 6) chapters. The Discussion (Chapter 7) expands on the findings of this thesis and Conclusion and Further Work (Chapter 8) consolidates all of the findings.

CHAPTER 2: DATA COLLECTION AND QUALITY CONTROL

This chapter summarizes principles of various logging techniques used to collect rock physical properties. The caliper, density and magnetic susceptibility logs are discussed individually together with the factors which influence their quality during collection. In addition to this, a brief discussion is given on the quality control measures carried out on the data. This section also highlights some peculiarities which have been noticed in some of these data, and gives grounds for why some of the data were neglected in further data analysis.

2.1 Introduction to Borehole Logging

Logging is the general term used to describe the process of making a record. The two main types of logging are geological logging, which is the recording of lithology information from drill core, and the logging of rock physical properties. The latter is commonly referred to as geophysical or wireline logging (Hallenburg 1984; Chandrasekhar and Rao, 2012). The first wireline log was conducted in 1928 in an oil well, and it was the oil industry which headed the development of wireline logging tools for decades following this. This chapter aims to give an introduction to wireline logging in the minerals industry. A term commonly used as a synonym for wireline logging in the minerals industry is slimline logging. This is the logging of coal and non-hydrocarbon minerals in small diameter holes, a term first coined by BPB Wireline (Firth, 1999).

Slimline logging became popular following the realization that coal seams could be delineated using density, neutron and gamma ray (γ-ray) logs. Its rapid development and sophistication over the years allowed it to be used for base and precious metal exploration, as well as geotechnical and environmental applications (Firth, 1999). The main components required in wireline logging are the following (Killeen, 1997):

- Downhole logging probe or sonde
- Wireline or logging cable connected to the logging probe
- Winch drum to wind wireline
- Depth counter or wheel to measure the depth
- Pulleys to deliver the sonde to the borehole
- Equipment at surface for data capturing and power supply.

Figure 2.1 shows a typical mineral logging set-up. The wireline cable connected to the sonde allows for data transmission from the sonde to the surface equipment before being

passed to a computer for further processing. However some systems allow for the data to be stored in the sensor and retrieved later (Hallenburg, 1984). The information is received and stored in an internationally recognised ".las" or ".lis" format (Firth, 1999). The former, which is the format in which the datasets for this project were delivered, stands for Log ASCII Standard. One of the most important items of surface equipment is the slimline computer interface or SCI (Figure 2.2). This is the interface which shows the current and voltage being supplied to the sonde, its depth, the logging speed, the physical property being measured (channel) and the measurements (counts) being done.

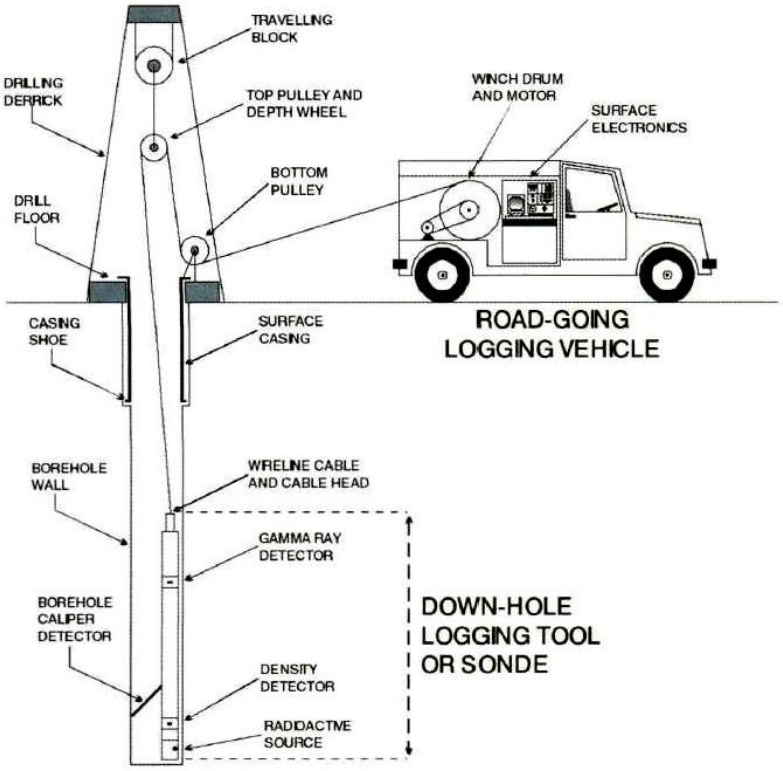

Figure 2.1 The wireline logging set-up showing the main components required to make measurements (not to scale). The logging cable is released from a winch drum and passes through several pulleys including a depth wheel, before being delivered to the borehole. The sonde is attached (in this case a density sonde) to the end of a wireline cable and is then able take physical property measurements. The measurements are processed and stored at the surface in the logging vehicle with the help of surface electronics and a computer (not shown in the diagram). This logging set-up is not unique, but encompasses the main components required to make measurements (Firth, 1999).

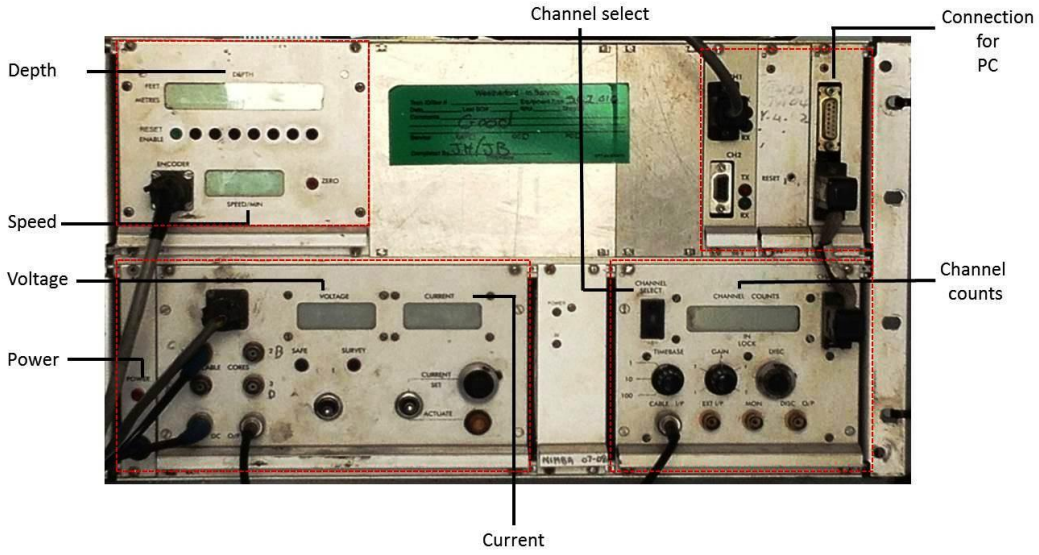

Figure 2.2 Photo of a modern digital recording panel. Top left: Shows where the depth measurements and speed of the sonde are reflected during logging. Top right: Shows connection outlets for a PC. Bottom left: Shows the input current and voltage being supplied to the logging probe. Bottom right: This panel displays the counts that are being made for each respective physical property or channel.

2.2 The Borehole Environment

Several factors in the borehole environment play an important role in the data quality during collection. These are:

- *Borehole fluid*: Boreholes can be logged in air or a fluid, depending on the physical properties being logged. Fluid in boreholes is used for the logging equipment to have contact with the surrounding formation (Serra, 1984). However since it has measurable physical properties (e.g. density), it lends itself to measurement during logging. The types of borehole fluid used include mud mixtures, oils, oil-water emulsions or foam. Heavy mud-mixtures such as bentonite (clay) are used to help support the borehole from collapsing or caving, but are also beneficial to the quality of density logs (Chatfield, 2008). However muds should be compensated in measurements

- *Borehole diameter*: The borehole diameter affects the volume of mud in the borehole. Thus the larger the diameter, the higher the response of the surrounding muds over the formation. In South Africa, the most common borehole diameters are 60 mm, 74 mm and 90 mm (Chatfield, 2008). The datasets for this project were logged in boreholes with diameters of either 60 mm or 76 mm.

- *Borehole direction*: Boreholes are often drilled in a various directions. For this project only vertical (also referred to as "D0" or zero-deflection holes) are used. However truly vertical holes are hardly encountered and the deviation is said to be between 0 and 5° (Ellis and Singer, 2007).

- *Casing*: Steel borehole casings affect measured readings. The effect of steel casing on density and magnetic susceptibility logs is to increase both of these properties. Since this does not represent actual rock properties, data points associated with borehole casings are removed.

2.3 Physical Property Measurements

Rock physical property measurements are grouped into two, namely active and passive. Active or induced measurements require energy to "excite" the formation using an emitter and a response is measured using a detector. Passive measurements simply employ a suitable detector to acquire the desired rock property (Serra, 1984; Ellis and Singer, 2007). Typical passive phenomena which can be measured employing a detector system are the natural gamma, spontaneous potential (SP), temperature and deviation logs. Examples of properties measured using an emitter-detector system are electrical measurements (resistivity), nuclear measurements (gamma-gamma density, photoelectric density) and the magnetic susceptibility log (Serra, 1984). The caliper log is sometimes separated from the "passive group" and put in a third category called mechanical logs.

Because of the many types of physical property measurements, there are many associated tools. According to Ellis and Singer (2007) there are over fifty types of logging instruments. The measurements used in this project are the density, magnetic susceptibility and caliper logs. Each of these logs is described briefly below.

2.3.1 Mechanical Methods- The Caliper Log

Borehole caliper logs are a continuous measurement of borehole diameter with depth. These are used to:

- Correct physical property logs (e.g. density logs).
- Determine conditions in the borehole including caving
- Determine the volume of the borehole. This helps determine the amount of cement required to close the borehole (Firth, 1999; Hallenburg, 1984).

- Crudely approximate lithology changes.

There are several types of caliper instruments including single, three-armed and multiple/gang-armed. The most common is the three-armed caliper, whose arms are separated by an angle of 120° when opened. This tool is preferred over single-arm tools since it is more stable in the borehole and has good contact with the borehole walls. Figure 2.3 shows an example of the type of caliper tool used to collect data for this project. The tool is lowered into the borehole with the arms in the closed position and they are released while it is pulled up.

Figure 2.3 Weatherford Wireline Services' Borehole Geometry Tool- BGT. The tool consists of an X and Y caliper arm to measure the borehole diameter in both directions. This tool is also able to record the natural gamma (Firth and Elkington, 2000).

Calibration of Caliper Tools

Calibration is important in analogue equipment whose power supply drifts with changes in temperature down the hole. The caliper also wears with continued use, and should be calibrated when any components are changed or repaired (Chatfield, 2008). Calibrating

devices are usually casings, pipes or any other type of rigid circular material whose diameter is known. Several diameters should be measured in order to determine if there is any nonlinearity in the system (Hallenburg, 1984).

2.3.2 Nuclear Methods

Nuclear logs were introduced in the 1940s, but became indispensable in geophysical logging in the 1960s. This was after probe sensitivity, calibration and stability had significantly improved (Snyder and Fleming, 1985). The basic nuclear physics principles behind density logging are discussed below. Radioactive decay of unstable nuclei produces γ-rays which interact with matter in several complex ways. There are three primary ways in which γ-rays lose their energy when interacting with matter:

- When an incident γ-ray has low energy (typically less than 200 keV) and interacts with material with a high atomic number (Z), it may eject an electron (or photoelectron) of the absorbing material. The γ-ray loses all of its energy in overcoming the energy associated with the bound electron. This is known as the photoelectric (PE) effect and is influenced greatly by Z and the photon energy of the ejected electron (Hallenburg, 1984; Telford et al., 1990). In general, the higher the Z of an atom, the easier it is to eject an orbital electron (Hallenburg, 1984). Figure 2.4a illustrates how the PE occurs.

- The second type of interaction does not involve absorption, but scattering of the incident γ-ray by atomic electrons resulting in deflection and loss of energy. Scattering may eject electrons, but the incident photons retain sufficient energy to not allow for absorption to take place. This is called Compton scattering, and is influenced by the number of electrons in the material. The energies that are conducive to this phenomenon are intermediate energies of between 100 keV and 2 MeV (Hallenburg, 1984). Figure 2.4b illustrates how Compton scattering occurs.

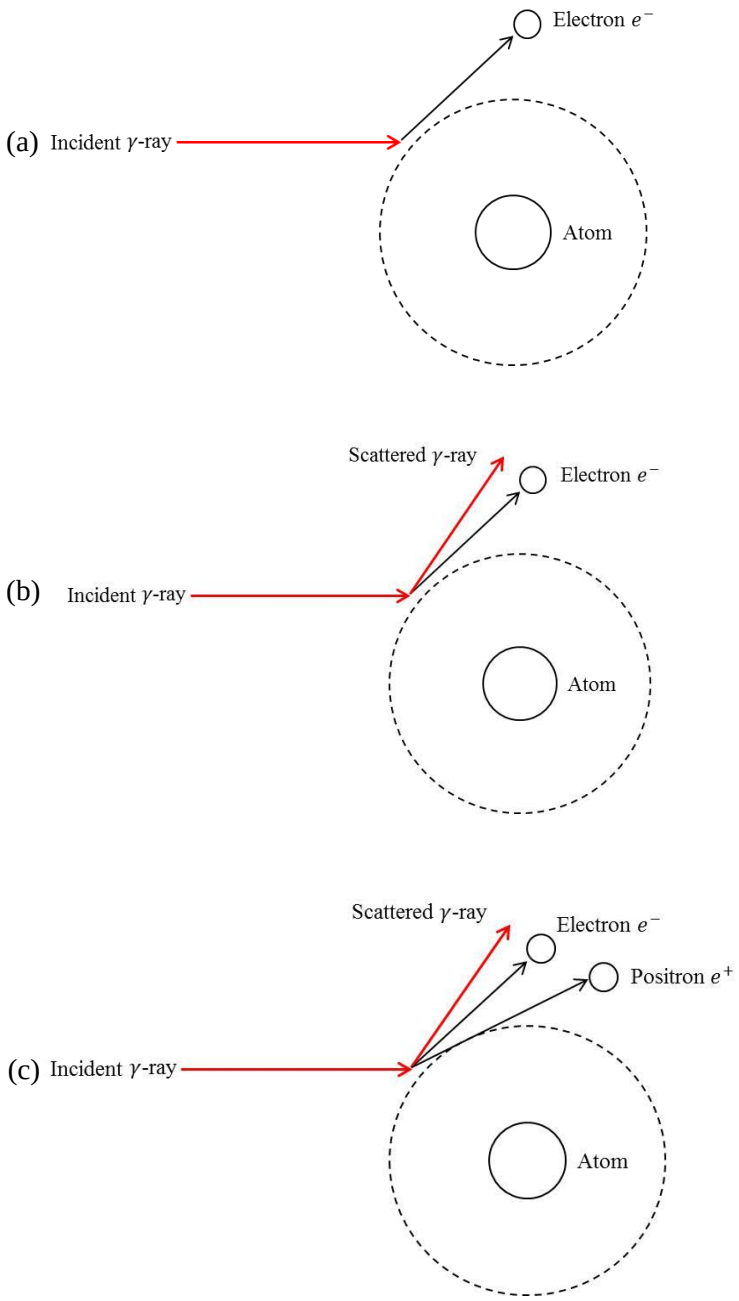

Figure 2.4 (a) The PE effect: The incident photon (γ-ray) ejects an electron in orbit and is absorbed if it loses sufficient energy. (b) Compton scattering: The incident photon ejects an electron in orbit but has sufficient energy that it is not absorbed. (c) Pair conduction: The incident photon interacts with the material to form an electron-positron pair (adapted from Hallenburg, 1984).

- The third way is by a high energy phenomenon called pair production. This is similar to Compton scattering except that the scattered γ-ray has enough energy to give rise to an electron-positron pair. These may later become annihilated during collision resulting in electromagnetic radiation. The amount of energy required for this phenomenon should exceed the sum of that of the electron-

positron rest energy of 1.02 MeV. This phenomenon does not take place for energies smaller than this (Tittman and Wahl, 1965; Telford et al., 1990). Figure 2.4c illustrates how pair conduction occurs.

Density logging uses the PE effect and Compton scattering to make measurements (Segesman, 1980; Serra 1984; Timur, 1985). Compton scattering is the most important phenomenon for which density measurements were made this for the project, and measures what is commonly referred to as "gamma-gamma density".

Sources and Detectors

Density measurements are made by irradiating a small volume of rock commonly achieved using an excitable Cs^{137} source. Measurements depend on source characteristics (energy, activity and half-life) and the mass attenuation coefficient (μ), defined as the ease with which rocks are able to absorb or scatter photons. For a Cs^{137} the μ for common rocks is 0.078 cm^2/g (Samworth, 1992; Zhou and Esterle, 2008). The interaction of γ-rays with a rock formation in the boreholes is shown in Figure 2.5.

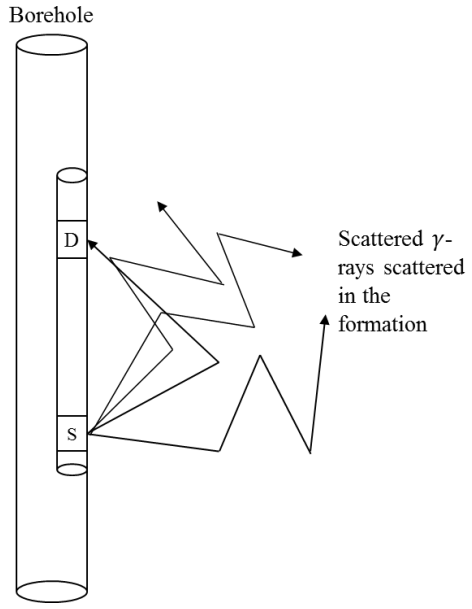

Figure 2.5 Source and detector system, showing scattered γ-rays in the adjacent formation. D and S symbols stand for detector and source respectively (adapted from Tittman and Wahl (1965)).

Cs^{137} is the natural choice for gamma emission since it has an energy of 0.662 MeV, which is ideally positioned in the centre of the γ-ray energies to allow for Compton scattering to take place (Figure 2.6).

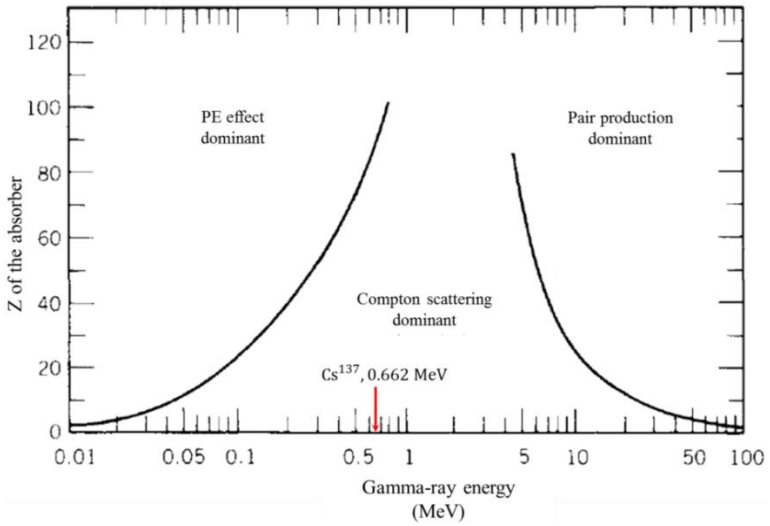

Figure 2.6 The diagram above shows various fields of γ-ray energies which allow the PE effect, Compton scattering and pair production to take place. Cs^{137} is one of the best choices for Compton scattering as it has an energy of 0.662 MeV, which is conducive to Compton scattering (modified after Krane, 1988).

There are several types of γ-ray detectors. These are ionization, Geiger-Muller, semi-conductor and scintillation detectors. Only scintillation detectors are described here as this the kind of detector used in gamma-gamma density logging. Early scintillation detectors were developed in the early 1900s and used a zinc sulphide screen which became illuminated when it came into contact with radiation. The most popular type of detector used in scintillation devices for logging purposes is a sodium iodide (NaI) crystal doped with thallium at its centre (Hallenburg, 1984).The molecules of the NaI crystal are loosely bound and excited by the passage of charged particles. When a γ-ray comes into contact with a NaI crystal, the energy associated the excitation is transferred to the "impurity" centre which de-excites by emitting a photon. This process takes place in 230 nanoseconds. The emission of the photon is in the visible spectrum, and is amplified by a photo-sensitive device known as a photo-multiplier tube (Hallenburg, 1984). This tube consists of several dynodes arranged with increasing potential difference towards an anode. The dynodes release electrons when they come into contact with photons which make them secondary sources of electrons. The increasing potential difference across the dynodes allows for the acceleration of the photoelectrons to each successive dynode surface. This process is shown in Figure 2.7. Dynode surfaces are coated with Cs_3Sb, which has a sufficiently low work-function that electrons are released easily. The typical photo-multiplier tube in logging devices has 9-11 dynodes, and achieves multiplication of electrons in the order of 10^5-10^7.

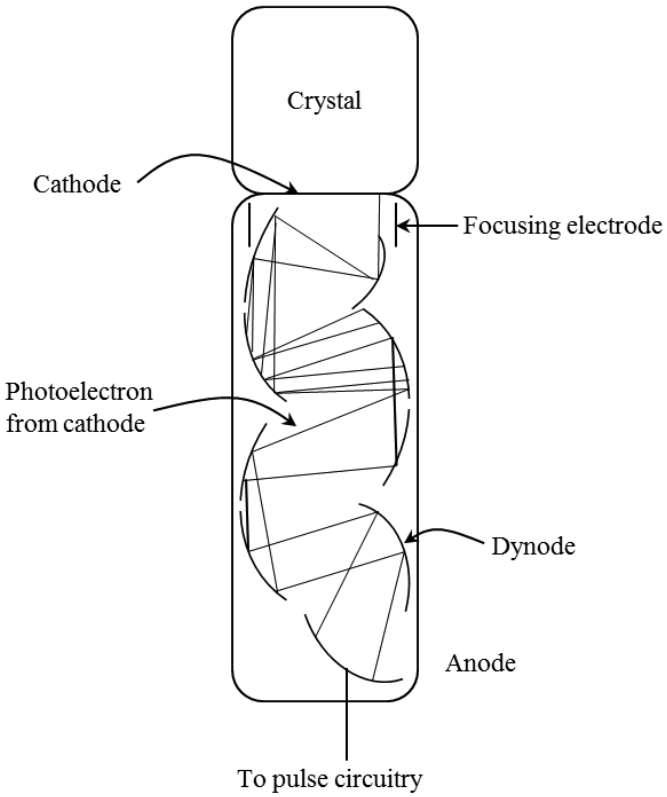

Figure 2.7 Photomultiplier tube, showing the path of electrons released from surfaces of dynodes, multiplying progressively towards the anode at the bottom. This produces a pulse with energy proportional to that of the incident γ-ray (modified from Hallenburg, 1984).

The last anode shown in Figure 2.7 produces a pulse when the electrons strike its surface, whose energy is proportional to that of the incident γ-ray (Serra, 1984).

The Density Log

There are two types of density tools: single spaced and compensated, or dual spaced detector tools. The type of tool used to collect density data in this project is the dual spaced detector system. Dual spaced detectors are made up short and long spaced detectors based on their proximity to the source. The short spaced detector is usually at an intermediate distance between the source below it, and the long spaced detector above it (Snyder and Fleming, 1985). This tool also has a caliper arm, which allows the source and detector windows to be pushed against the formation during measurements. This system is more popular than the single spaced detector system (single detector), since it allows for corrections related to mud cake build-up to be made (discussed later in the text). Figure 2.8 shows an example of the type of tool used to collect density data for this project.

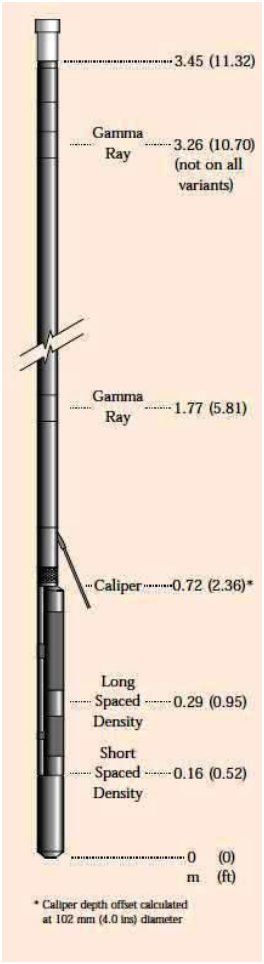

Figure 2.8 The dual spaced density sonde from the Weatherford Wireline Services' DD Series. The tool consists of a caliper armand two detectors to measure the short and long spaced densities. This tool is also able to record the natural gamma radiation towards the top of the tool (Firth and Elkington, 2000).The source is labelled "Gamma Ray" at a distance of 1.77 m from the bottom of the tool.

Density tools are not able to measure the bulk density of the formation directly. The tool shown in Figure 2.8 measures the count rate at each of the detectors i.e. the number of γ-rays reaching the detector windows. The count rate at a single detector is related to the density of the formation by (Firth, 1999);

$$I = A\,\rho e^{-\mu\rho d}, \qquad 2.1$$

where I is the count rate, ρ is the formation apparent density, d is the source-detector spacing and A is a constant. This equation assumes isotropic media and has a shape shown in Figure 2.9.

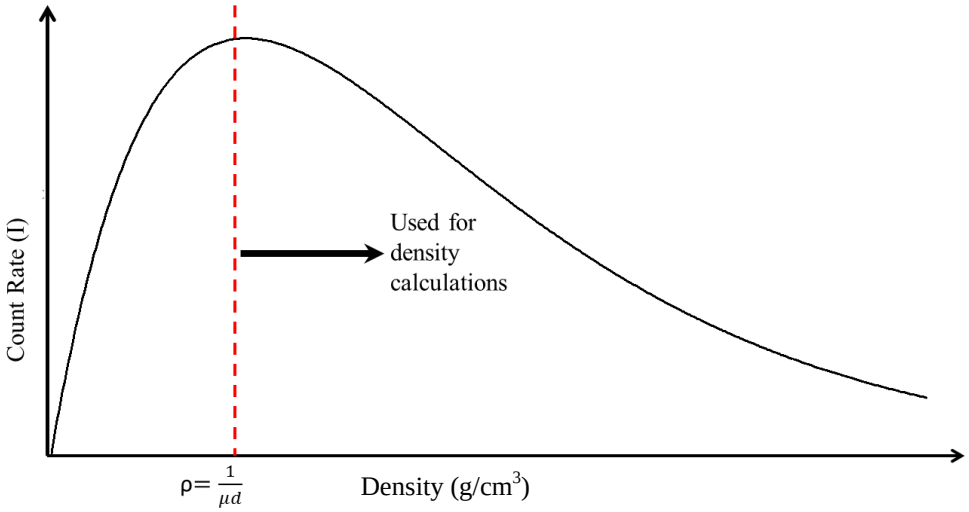

Figure 2.9 Shows the form of the curve between I and ρ with the maximum of the curve indicated as a red line. Only values to the right-hand of the line are used for density calculations.

The curve shows that there two densities associated with a single count rate and the maximum count rate is reached when $\rho = \frac{1}{\mu d}$ (Samworth, 1992). This ambiguity is resolved by only using densities larger than $\frac{1}{\mu d}$ i.e. to the right of the peak. Since is μ a constant, the detector spacing determines the position of the peak and hence the smallest value that the tool will measure. The peak is usually positioned at a density close to water. Single spaced density tools systems usually have a source to detector spacing of ~15 cm (Samworth, 1992). Figure 2.9 above shows that the source-detector spacing's are 16 cm and 29 cm for the short and long spaced density respectively. Another important observation from Figure 2.8 is that the count rate is also not linear with density. At low densities, γ-rays are scattered from the formation without losing much energy and therefore have sufficient energy to "escape" the detector. At higher densities, the γ-rays lose energy at a faster rate and therefore have a higher chance of being detected**.** Therefore, in general, the higher the density of rocks, the more γ-rays are absorbed, and the less γ-rays counted. However, the higher the count rate, the better the accuracy, which implies that light materials are measured more accurately than denser ones (Zhou and Esterle, 2008). Taking into account the detector spacing, borehole size and fluid, background radiation and sonde diameter, Samworth (1992) is able to show that the measured density value is given by:

$$I = E\,\rho e^{-K\rho} + F(c-t)(\rho_m e^{-K\rho_m} - \rho e^{-K\rho}) + H, \qquad 2.2$$

where, ρ_m is the borehole fluid density, c is the borehole diameter and t is the tool diameter. The constants E, K, F and H collectively account for the borehole fluid, natural background radiation and detector spacing. This equation contains only four unknowns, which can be evaluated by taking repeated measurements (Samworth, 1992) in a borehole whose properties are known.

Compensated or Dual Spaced Density Measurements

Geophysical logs do not take point readings, but measure the effect of a finite volume of the formation. The contribution of the measured signal through this volume is affected by the radial penetration of the γ-ray and the source-detector spacing. In general, the depth of investigation into a formation increases with sensor spacing, but compromises resolution. The short and long spaced densities therefore have different depths of penetrations. Figure 2.10 below from Samworth (1992) shows that the penetration of γ-rays is approximately 20 cm, with most of the signal coming from the first 16 cm.

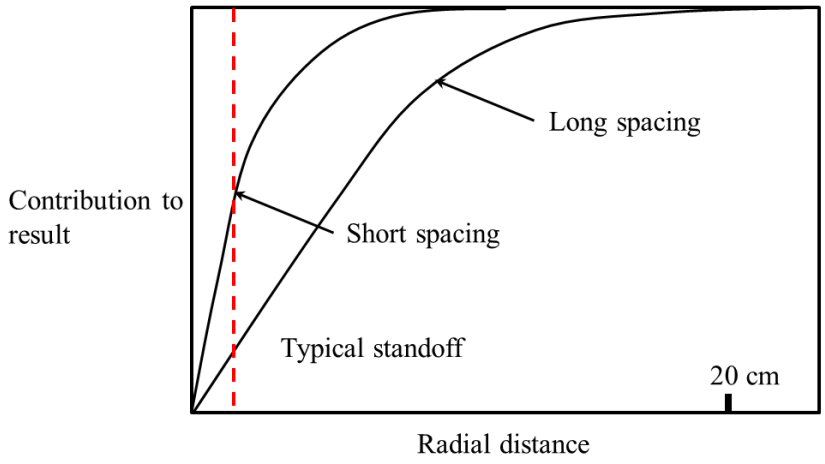

Figure 2.10 This shows the contribution to the result given by the short and long spaced densities based on their penetration depths into the medium (redrawn from Samworth, 1992).

The long spacing has deeper depth of investigating than the short spacing, and measures a much bigger volume. Dual density systems allow for compensation due to the mud cake build up to be made. The short spaced density is affected more by mud build up in the borehole wall than the long spaced density (Telford et al., 1990; Serra, 1984, Snyder and Fleming, 1985). The correction (Δ) can be found empirically or approximated using (Samworth, 1992):

$$\Delta = \frac{\rho_L - \rho_S}{3}, \qquad 2.3$$

where ρ_L and ρ_S are the long and short spaced densities respectively.

The response of the short-spaced density is almost entirely linear over a measured density range. It has better vertical higher resolution (as it is closer to the source) and gives better measurements at high densities than long-spaced density measurements.

The measurements described above measure an apparent density, which is the electron density of the material (Zhou and Esterle, 2008). The electron density is related to the bulk formation by the following relationship (Zhou and Esterle, 2008):

$$\rho_e = 2\frac{Z}{A}\rho_b, \qquad 2.4$$

where ρ_e is the electron density of the formation, Z is the atomic number, A is the atomic mass and ρ_b is the bulk density. In most cases the ratio of the atomic number to the atomic mass $\left(\frac{Z}{A}\right)$ is 0.5, which implies that the measured electron density is simply the bulk density (Firth, 1992). Density sondes are usually calibrated assuming a ratio of 0.5 as it holds for most rocks (Samworth, 1992). Important exceptions are water (Samworth, 1992) and heavy elements (Firth, 1999). Borehole fluid has a $\frac{Z}{A}$ ratio of 0.555, and therefore an apparent density of 1.11 g/cm^3, which is not the true density of water. A compensation for borehole fluid therefore needs to be made. The other departure is for iron ore and for other base and precious metals. Table 2.1 summarizes the $\left(\frac{Z}{A}\right)$ ratios for igneous rocks similar to those found the BC. A full catalogue of $\left(\frac{Z}{A}\right)$ for rocks can be found in Hallenburg (1984).

Table 2.1 Z/A for BC-type lithologies. The magnetite value is from Firth (1999).

Lithology	$\left(\frac{Z}{A}\right)$
Norite (11 samples)	0.4970
Diabase/Dolerite (6 samples)	0.4954
Gabbro (27 samples)	0.4938
Chromite	0.4753
Magnetite	0.475

The table shows that although Bushveld rocks generally show a $\frac{Z}{A}$ ratio of 0.5, heavy minerals magnetite and chromite show some departure.

Calibration of Density Tools

The density tool is calibrated in order to ensure accurate results. It is also to ensure that tools of the same type give the same result when used under the same conditions (repeatability) (Samworth, 1992). Calibration is done to ensure that density measurements are independent of:

- Background radiation
- Borehole diameter
- Borehole fluid
- Source characteristics. The Cs^{137} radioactive source has a half-life of 30 years and weakens with time. Changes in source characteristics therefore influence measurements.

Calibration is also important since the tool wears with continued use. It should therefore be calibrated over time and recalibrated should any components be repaired or replaced, especially if it is the source. Weatherford Wireline Services calibrates the short and long spaced densities independently. These are then combined in an algorithm which minimizes the effect of mud cake and mud density in their density logs (Firth and Elkington, 2000). The calibration takes place in a barrel of water and a block of aluminium of known density. The image below shows a typical setup during calibration (Figure 2.11).

Figure 2.11 Calibration using a water-filled jig (left) and a block of aluminium (right) (modified from Chatfield, 2008).

Factors that Influence Density Measurements

Density measurements are affected by several factors, which are combinations of the borehole environment as well as the sonde being used for physical property measurements. These are:

- *The activity of the radioactive source*: Although the energy of the source is constant (0.662 MeV), the activity may vary. The activity determines the number of gamma-rays emitted per second, which affects the number of gamma-rays interacting with the formation at any given time. So the activity of the source affects the resolution of the tool, and the higher it is, the higher the resolution of the tool. The activity does not influence the penetration depth of the gamma-rays nor does it influence the interaction of the particles in the wall rock. It does however; influence the counting statistics which then affects the density. Weatherford Wireline Services collect dual density data with a source activity of 100 mCi. According to Samworth (1992) the biggest discrepancy from sonde to sonde is that they have different source activities.

- *Presence or absence of fluid in the borehole* (Fullagar et al., 1999): Density of drilling-muds range from 1.1-2 g/cm^3. The effect of drilling muds is to absorb incident gamma-rays which leads to a higher measured density than the actual density (Hallenburg, 1984).

- *Borehole diameter*: There is a larger contribution of borehole fluid in larger holes than in slimmer ones. Thus if a tool is not well-calibrated for depending on the borehole diameter it will result in erroneous measurements. The influence of borehole diameter is negligible for small holes but can be up to ~0.03 g/cm^3 for larger holes (Telford et al., 1990).

- *Development of mud-cake*: Drilling mud is circulated down the drill pipe and up through the annulus (which is a region between the drill pipe and the formation rock) to the surface. Solids are added to the mud such that the drilling fluid pressure is equal to the pore fluid pressure of the formation. In practice this is not always true, and the fluid pressure may be slightly lower than the pore fluid pressure, which results in the solids being plastered against the borehole wall. The effect of the mud cake decreases the count rate which increases the measured

density. Flushing the borehole after drilling and before the logging can reduce this effect (Segesman, 1980).

- *Smoothness of the borehole wall*: Incident gamma-rays are absorbed by the formation close to the probe (first 15-20 cm), which makes the surface of the borehole important. The most severe case is where there is caving in the borehole. This region will have more borehole fluid than surrounding regions, which leads to a higher count rate at the detector resulting in an anomalously low density for the formation (Firth, 1999). This effect can be recognised and corrected for in compensated density systems using the caliper log (Segesman, 1980; Hallenburg, 1984).

- *Natural background gamma radiation*: Density tools are designed to minimize the effects of natural gamma radiation of the formation in the following ways:
    - Shielding the sonde
    - Using a minimum source activity of 100 mCi
    - Measuring a gamma log and using it to correct for this effect

- *Steel casing*: The steel casing used to support the borehole collar has a higher density than the surrounding formation. If logging is done through it, a lower count rate is measured and a higher density than that of the actual formation is recorded. Data points related to the collar are easily recognisable and removable.

- *Detector dead time*: The dead time of a detector system is a short period following a measurement when the instrument cannot make any counts. Serra (1984) refers to this period as a "recovery period" for the NaI crystal and the electronics. For a scintillator using a NaI crystal, a dead time of 1 microsecond can be achieved (Samworth, 1992). Dead time can be made as small as possible electronically or using a mathematical correction based on the count rate.

- *Instrument drift:* Drift in any tool results in the measured density being either lower or higher than the actual density of the formation. Instrument drift can occur due to poor temperature compensation, infrequent tool use or physical damage.

Most of these factors are addressed and minimized during calibration.

2.3.3 Rock Magnetism

A good starting point before discussing the magnetic susceptibility log is to describe the origin of rock magnetism. Magnetic susceptibility measures the degree or ease with which a material can become magnetized (Telford et al., 1990; Lowrie, 2007). It is the ratio of the magnetization of a material to an applied magnetic field. The magnetic susceptibility is a dimensionless proportionality constant given by (Maes et al., 2008),

$$k = \frac{M}{H}, \tag{2.5}$$

where M is the magnetization that a material takes on and H is the applied magnetic field. The measured magnetic susceptibility is the sum of diamagnetic, paramagnetic, ferrimagnetic, ferromagnetic and antimagnetic minerals. These are briefly described below.

Diamagnetism

Diamagnetic minerals are those in which the net magnetic dipole or magnetization is in the opposite direction to that of an applied field. All substances have this property but it is often overprinted by ferro- or ferrimagnetism (discussed below) (Maes et al., 2008). This property gives rocks a weak magnetic susceptibility value. Minerals with diamagnetic properties are plagioclase, quartz, graphite, calcite and salt, whose susceptibilities are typically around 10^{-5} in SI units (Ferré, et al., 2009).

Paramagnetism

Paramagnetic occurs in minerals whose magnetization is in the same direction as that of the applied field and proportional to its strength. The magnetic susceptibility in these materials is small and positive. Most rock-forming minerals are paramagnetic, and include pyroxene, garnet, biotite and olivine. They commonly have magnetic susceptibilities in the range of 10^{-5} to 10^{-3} in SI units (Maes et al., 2008; Ferré et al., 2009).

Ferro- and Ferrimagnetism

Ferromagnetic minerals have small domains with magnetic dipole moments aligned. The result of this is a material with high susceptibility values, up to ~10^{6} higher than then dia-

or paramagnetic materials (Telford et al., 1990). Examples of these kinds of materials are iron, cobalt and nickel. When there are more subdomains orientated in a preferential direction or stronger than other subdomains, the material has a non-zero magnetic susceptibility. These are called ferrimagnetic materials, and common examples include iron oxides such as magnetite and titanomagnetite. Most magnetic anomalies are caused by ferro- and ferrimagnetic minerals, with magnetite being the most frequent cause (Telford et al., 1990; Sherriff, 2002).

Antimagnetism

Antimagnetic materials have subdomains whose magnetic dipoles are in opposing directions, which results in an approximately zero net magnetic dipole. This then gives the material a weak and positive magnetic susceptibility. These materials would otherwise be ferromagnetic, and the most common mineral with this characteristic is ilmenite (Lowrie, 2007).

2.3.4 The Magnetic Susceptibility Log

Magnetic susceptibility logs are measured using an emitter and receiver coil housed in a sonde. An oscillating magnetic field is created in a coil which induces an alternating current. The alternating current induces a secondary magnetic field which permeates the surrounding rocks and is detected by a receiver coil in the sonde. The data can be collected in both water and air-filled boreholes, and is calibrated using nylon and pyrolucite, an acrylic material doped with iron (Saunders, pers. comm). Measurements are influenced by instrument drift and drilling artefacts such as iron fillings.

2.4 Sonde Depth Measurements

Depth measurements are made using an odometer or depth wheel (motorized drum), whose revolutions are counted as the wireline is pulled (Rider, 1996) (Figure 2.12). Counting of revolutions is achieved through a series of electronic pulses that are created when the wheel rotates, as it disrupts a light beam or a magnetic field (Firth, 1999). The reading from the odometer is then compared with the known drill depth and corrections are applied.

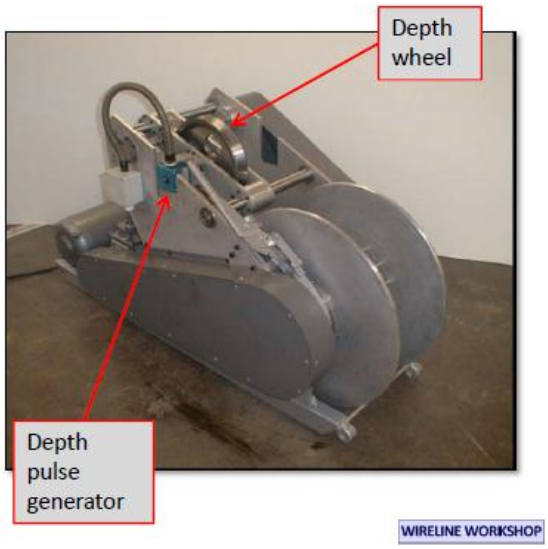

Figure 2.12 An example of a depth wheel with electronic pulse generator (Chatfield, 2008).

The sonde depth is usually measured with respect to a reference height. Several sensors are often run at the same time (Ellis and Singer, 2007), and a correction for depth is made for this since they are positioned at different heights on the wireline. Under good practice, the depth is usually checked by repeating measurements on certain sections of the borehole (Telford et al., 1990).

2.4.1 Errors in Depth Measurements

There are almost always errors in depth measurements. These are (Chatfield, 2008):

- Operational errors, where the wireline cable may "slip" on the depth wheel as well as temporarily "stick" during logging.
- Systematic errors, where wheel rotations are counted incorrectly

There are also inaccuracies associated with comparing depth across two different holes, especially if they are deep. These are known as log-to-log errors, and arise from differences in cable stretch due to different sonde weights. The density sonde for example is ten times heavier than the magnetic susceptibility sonde, which can create a depth error of up to 10 cm. The industry standard of depth errors is said to be a maximum error of 1 m every 1000 m (Chatfield, pers. comm).

2.5 Data Collected For This Project

The data collected for this project contains lithology, caliper, density and magnetic susceptibility logs for each borehole. Table 2.2 summarizes the data available for each of

the boreholes in the current database and the contractors used. Logs which were recorded are shown as “yes” and those which were not as “no”. The spread of the boreholes amassed for this study are shown in Figure 2.13. Quality control measures enforced on the physical properties are described below. There are comments on the quality of the lithology logs in later parts of the thesis (Chapter 3 and 4) as revealed by detailed studies of the physical properties deemed to be of high enough quality for this project. Geological logging is highly subjective and most the logs have been completed by various contractors over many years.

Table 2.2 Summary of boreholes in the BC, the logs completed and their locations in latitude and longitude. WL and EL beneath the name of the mine indicates the location of the mine in the BC, i.e. Western or Eastern Limb. W (Weatherford Wireline Services), QL (Quick Log) and CSIR are the contractors used by Anglo Platinum Ltd for data collection.

Mine	Borehole ID	Depth (m)	Lithology Log	Magnetic Susceptibility Log	Density Log	Caliper Log	Coordinates (Degrees, Minutes, Seconds)	Date	Contractor
Amandelbult WL	EL56	1080	Yes	Yes	Yes	Yes	24 51 08.26 S 27 16 52.22 E	Sep. 2002	W
	EL57	1070	Yes	Yes	Yes	Yes	24 50 44.19 S 27 17 54.56 E	Sep. 2002	W
	AB39	300	Yes	Yes	Yes	Yes	24 47 23.89 S 27 20 47.56 E	Unknown	QL
	AB42	600	Yes	Yes	Yes	Yes	24 47 24.74 S 27 20 45.36 E	Unknown	QL
Union WL	G11	1155	No	Yes	No	Yes	24 55 18.50 S 27 10 59.19 E	Unknown	Unknown
	SK59A	1860	Yes	Yes	Yes	Yes	24 58 07.99 S 27 11 38.70 E	Mar. 2008	QL
Styldrift WL	VO2	740	Yes	Yes	Yes	Yes	25 23 54.09 S 27 06 27.73 E	Nov. 2008	W, QL and CSIR
	SO2	770	Yes	Yes	Yes	Yes	25 23 56.32 S 27 06 28.54 E	Unknown	W, QL and CSIR
	SILO1	750	Yes	Yes	Yes	Yes	25 23 55.07 S 27 06 32.83 E	Nov. 2008	W, QL and CSIR

RPM WL	KLG19	1800	Yes	Yes	Yes	Yes	25 36 47.92 S 27 22 7.13 E	Mar. 2007	QL
	KLG52	1900	Yes	Yes	Yes	Yes	25 37 11.15 S 27 21 38.90 E	Jan. 2007	W and QL
	KLG8	1500	Yes	Yes	Yes	Yes	25 36 56.31 S 27 20 17.38 E	Jan. 2002	W
	DB136	400	Yes	Yes	Yes	Yes	25 05 12.51 S 30 06 13.27 E	May 2006	W
Der Brochen EL	DB135	580	Yes	Yes	Yes	Yes	25 03 53.73 S 30 06 06.96 E	Unknown	W
	RM123	155	Yes	Yes	Yes	Yes	24 59 23.12 S 30 05 50.17 E	May 2006	W
Booysendaal EL	BY60	300	Yes	Yes	Yes	Yes	25 05 49.00 S 30 06 41.38 E	Unknown	W
	BY62	700	Yes	Yes	Yes	Yes	25 05 58.71 S 30 06 11.34 E	Unknown	W
	BY63	580	Yes	Yes	Yes	Yes	25 05 58.71 S 30 06 11.34 E	Unknown	W
Lebowa EL	CH7	1200	No	Yes	Yes	Yes	Unknown	Dec. 2004	Unknown

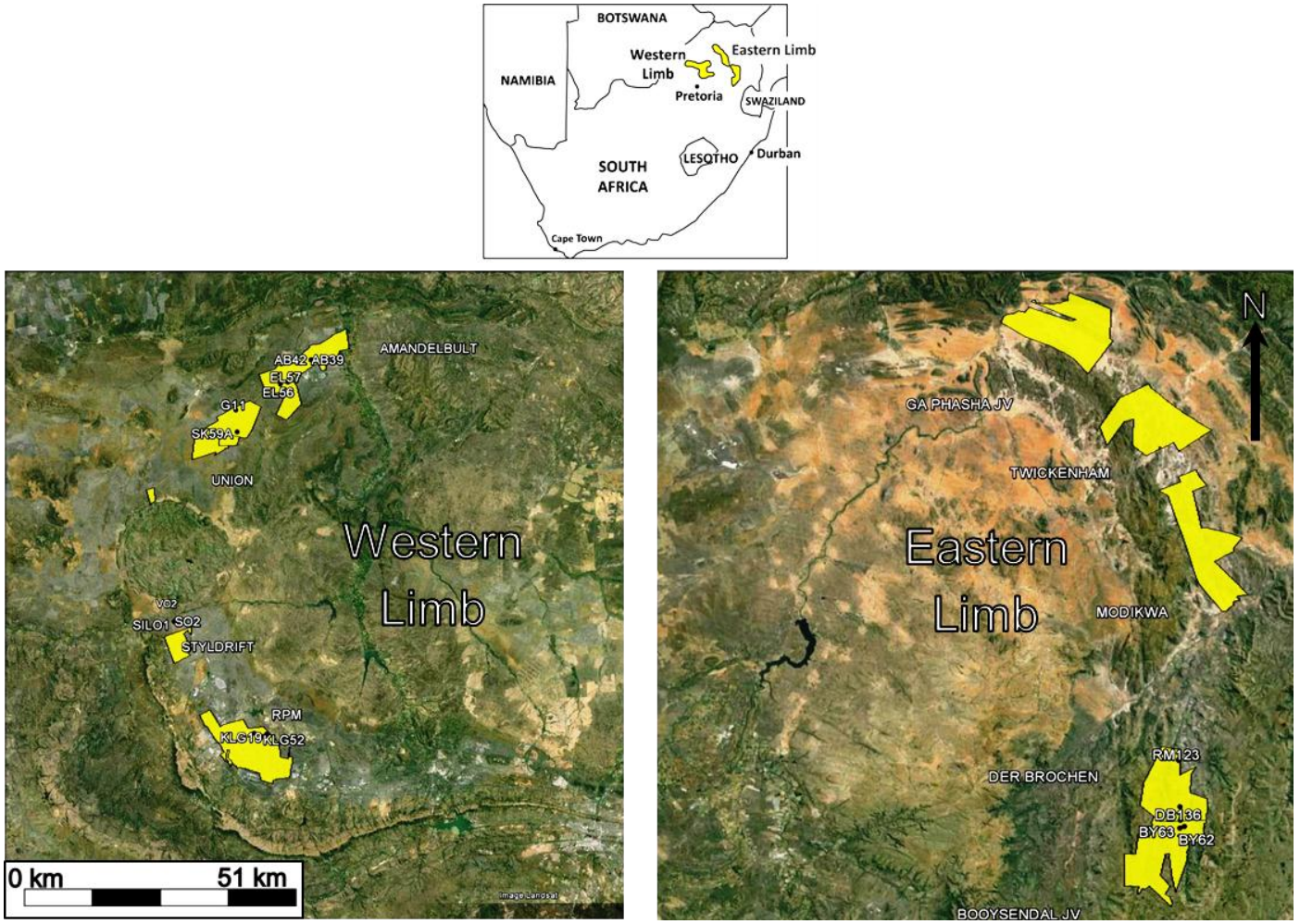

Figure 2.13 Google Earth image showing outlines of mining operations and locations of the boreholes.

.

2.6 Quality Control

Factors which influence the data quality for each of the respective logs with which this project is concerned have been covered. However there are some general factors which apply to all of them. These are listed below (Chatfield, 2008):

- Poor equipment. This may lead to component failures, power supply problems or intermittent electric failures in sensors. Equipment wears with time and should be calibrated routinely. Poor equipment gives poor results.
- Equipment may be wrongly calibrated.
- Poor sonde orientation.
- Fast sonde speeds can compromise data quality. Each of the tools have different response times between measurements, and should be logged according to these to ensure optimal data quality. Logging fast compromises data quality and may lead to unusable data. Table 2.3 summarizes the logging speeds that Anglo Platinum Ltd use.

Table 2.3 Summary of the depth sampling and logging speeds used by Anglo Platinum Ltd (Mabedla, pers. comm)

Physical property	**Depth sampling (cm)**	**Logging speed (m/min)**
Three-arm caliper log	1	10
Density log	1	9
Magnetic susceptibility log	1	9

- Logging environment. The logger may be faced with hostile logging conditions like caving borehole walls, mud-cakes down the hole and instruments becoming stuck.

All of these factors influence the data quality and hence the integrity of the data. These factors are generally mitigated through data processing. This section focuses on the quality control measures enforced before any further analysis was carried out on the data. Some peculiarities in some of the datasets are also highlighted and recommendations for quality control measures are given.

2.6.1 Borehole Casing

Data points associated with the borehole casing are easy to remove due to its large physical property contrast with the lithologies. The caliper log also often shows the end of casing. Figure 2.14 shows this influence and its removal using borehole SO2. This was also carried out in almost all of the boreholes.

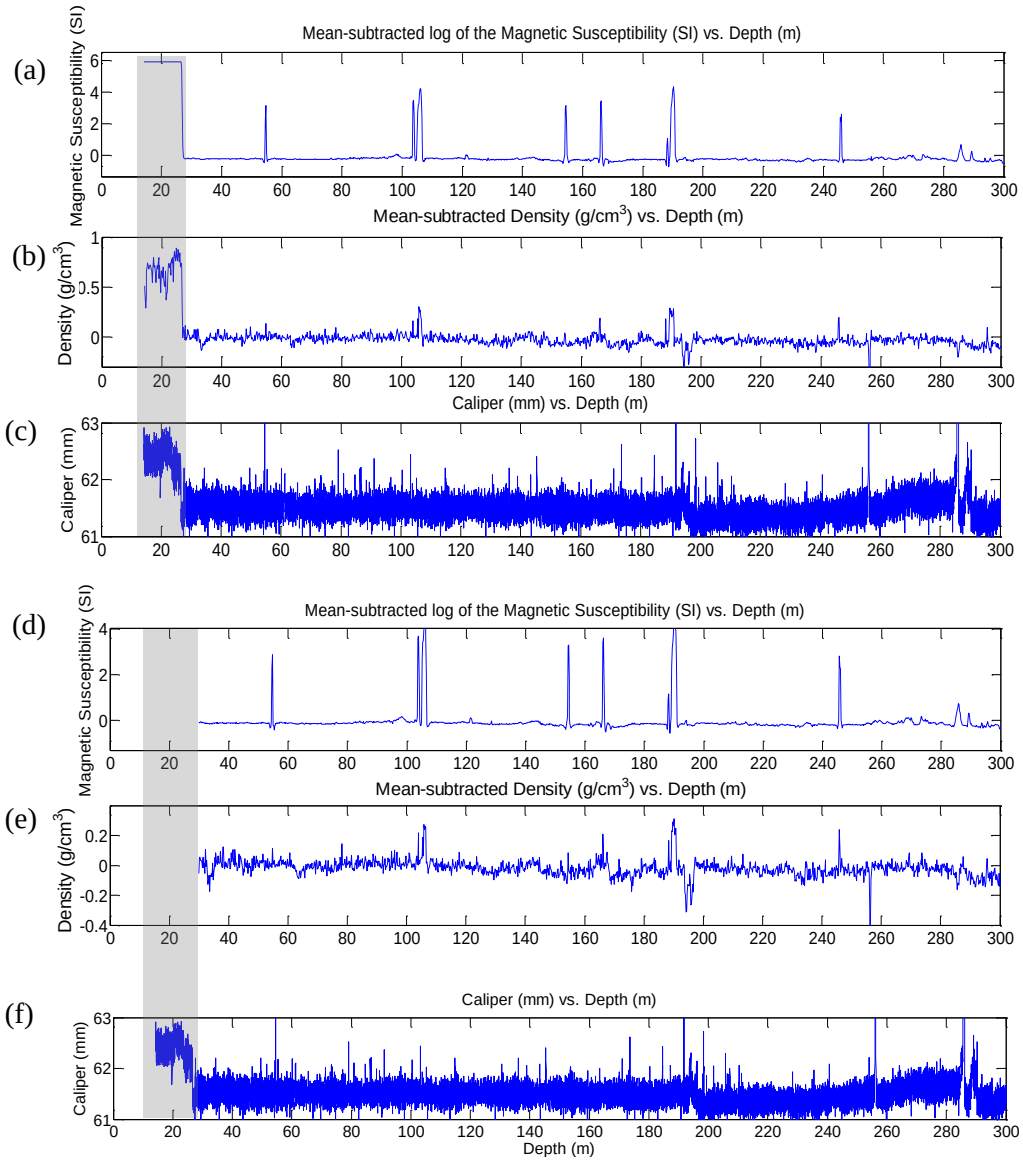

Figure 2.14 (a) Mean-subtracted log of the magnetic susceptibility (SI) vs. depth (m) for borehole SO2. (b) Mean-subtracted density data (g/cm^3) vs. depth (m). (c) Caliper log (mm) vs. depth (m). This set of images show the effect of the borehole steel casing, to a depth of approximately 25 m. This region is indicated by the grey block. The rest of the images (d), (e) and (f) are the same logs respectively, with the effect of the casing removed.

2.6.2 Borehole Fractures

An increase in borehole size leads to a low density recording. Sharp, localized changes in borehole diameter are easily recognizable in the caliper log, and a correction has been applied in the density log by removing this effect. The borehole SO2 is used once again in order to illustrate how this correction was carried out. This effect can also be observed at a depth of approximately 256 m in the caliper and density logs shown in Figure 2.15a and b. Figure 2.15a shows that the borehole diameter changes by approximately 4 mm, and the corresponding density log shows a decrease by 0.4 g/cm^3. These data points were then removed, and a simple linear interpolation was performed as shown in Figure 2.15b.

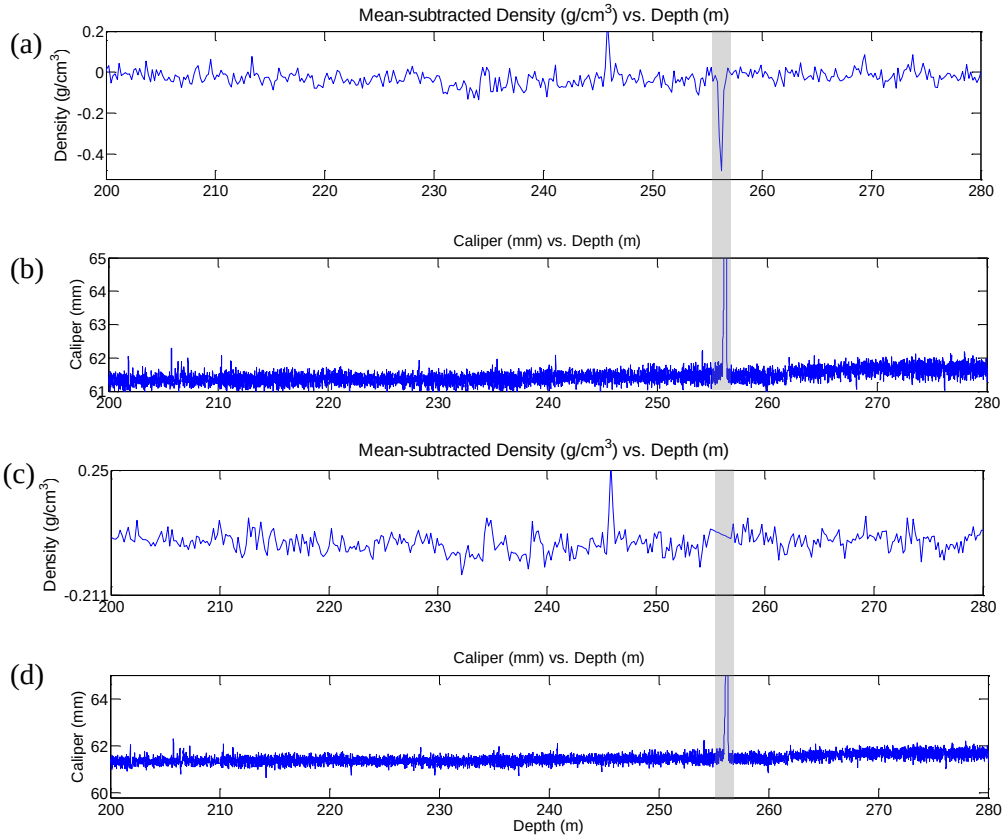

Figure 2.15 (a) Mean-subtracted density (g/cm^3) vs. depth (m) for borehole SO2. (b) Caliper log (mm) vs. depth (m). The caliper log shows an increase of 4 mm in the caliper log at a depth of 256 m, which corresponds to the sharp decrease of 0.4 g/cm^3 in the density log at the same depth. The rest of the images (c) and (d) are the same logs respectively, with the effect of the fracture removed. The density data in (c) have been removed and linearly interpolated.

2.6.3 Instrument Drift

Instrument drift has been identified in some of the magnetic susceptibility logs. Figure 2.16a shows the raw magnetic susceptibility log for borehole DB135, which shows an almost linear trend of decreasing magnetic susceptibility with increasing depth. A linear regression was calculated, and a linear-detrend was performed as shown in Figure 2.16b.

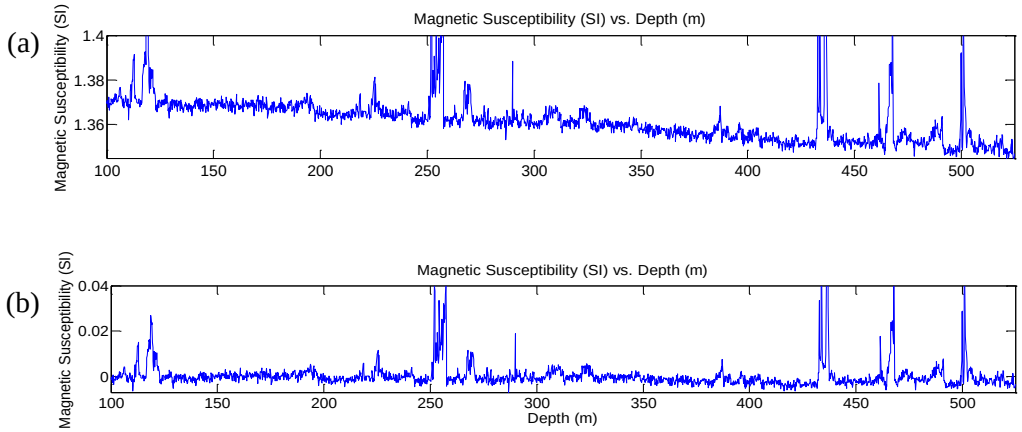

Figure 2.16 (a) Raw magnetic susceptibility data (SI) vs. depth (m) for borehole DB135. This data shows a linear trend due to instrument drift. (b) The magnetic susceptibility data with the linear trend removed.

2.6.4 Data Resolution

The density and magnetic susceptibility instruments have detection limits of 0.001 g/cm^3 and 0.0001 SI respectively. Several boreholes have been identified in which this limit has increased often by two or three orders of magnitude. This effect has been observed in both density and magnetic susceptibility data across several boreholes. Selected boreholes have been chosen below for discussion.

Magnetic Susceptibility

This feature is discussed in magnetic susceptibility data first, since it is more prevalent in these data. Borehole EL56 is used to illustrate how this can be identified in data. Figure 2.17 shows several logs, with the axes limits changed for emphasis. Figure 2.17a shows the raw magnetic susceptibility log for borehole EL56. This data shows distinct regions with high magnetic susceptibility and regions with susceptibilities close to zero. Figure 2.17b shows a section of the borehole at depths of 325-350 m, with amplitudes up to approximately 0.03 SI.

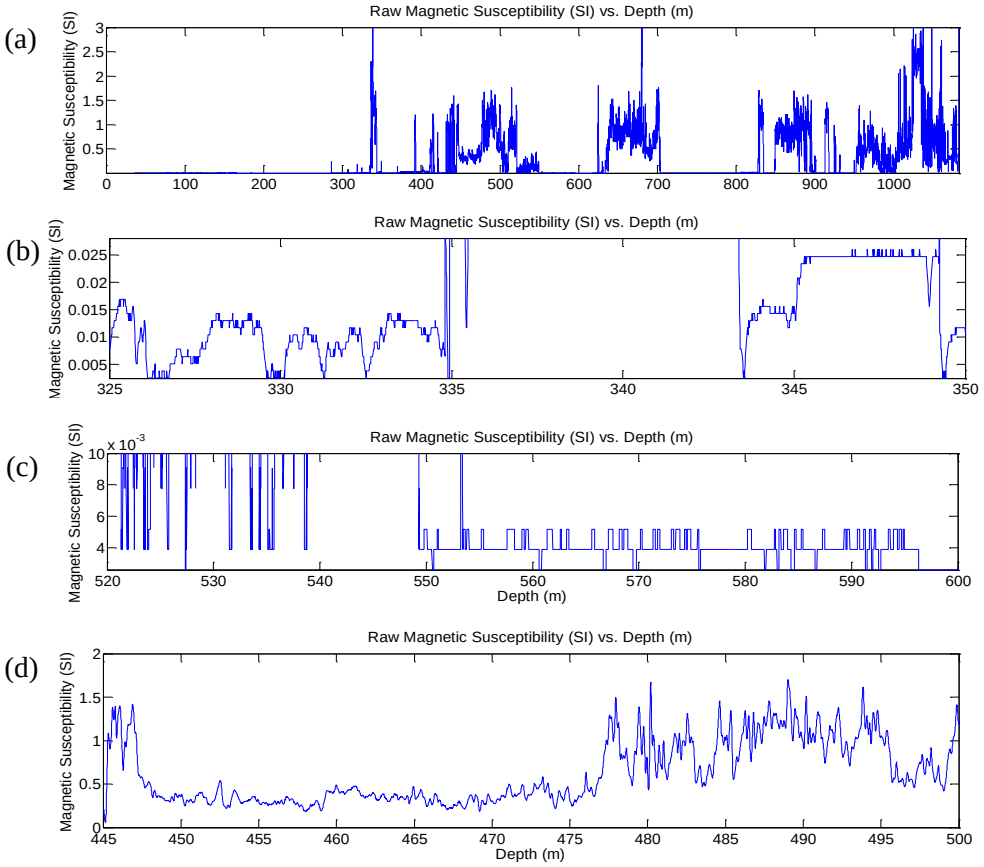

Figure 2.17 Raw magnetic susceptibility data (SI) vs. depth (m) for borehole EL56 shown for amplitudes of (a) 0-3 SI at depths of 0-1000 m, (b) 0-0.005 SI at depths of 325-350 m, (c) 0.003-0.01 SI at depths of 520-600 m and (d) 0-2 SI at depths of 445-500 m. These depths and amplitude ranges highlight various features described in the text.

The coarse structure seen shows the natural variation of the magnetic susceptibility, but at the small scale, the amplitudes appear "blocky" at the top. This effect is more pronounced in Figure 2.17c, showing the log at depths of depths of 520-600 m. At this scale, one can see how "blocky" the data becomes, and the natural variation in the data is no longer seen. It also shows that these "blocks" occur at certain values in the log, in this case $4x10^{-3}$ (SI) and $5x10^{-3}$ (SI), and in this occurs for 80 m in the section shows. Figure 2.17d has been included for completeness, to show sections of the borehole where the data appears to be normal at depths of 445-500 m, which are usually associated with higher amplitudes. There are therefore parts of the boreholes where the data show variation, and parts where the data resolution decreases dramatically. In this borehole, sections which appear to have normal data correspond mostly to layers of iron-rich ultramafic pegmatites (IRUPs), while the bad data occurs in the less magnetic gabbros and gabbronorites. Although only certain sections of the borehole are shown here, this is feature is pervasive

throughout the borehole. But this "blocky" data actually comprises of over 50% of the borehole. Another way to visualize this is to plot the magnetic susceptibility against the density data (i.e. cross-correlation or scatter plot). Figure 2.18a shows a semi-log cross-plot of these physical properties.

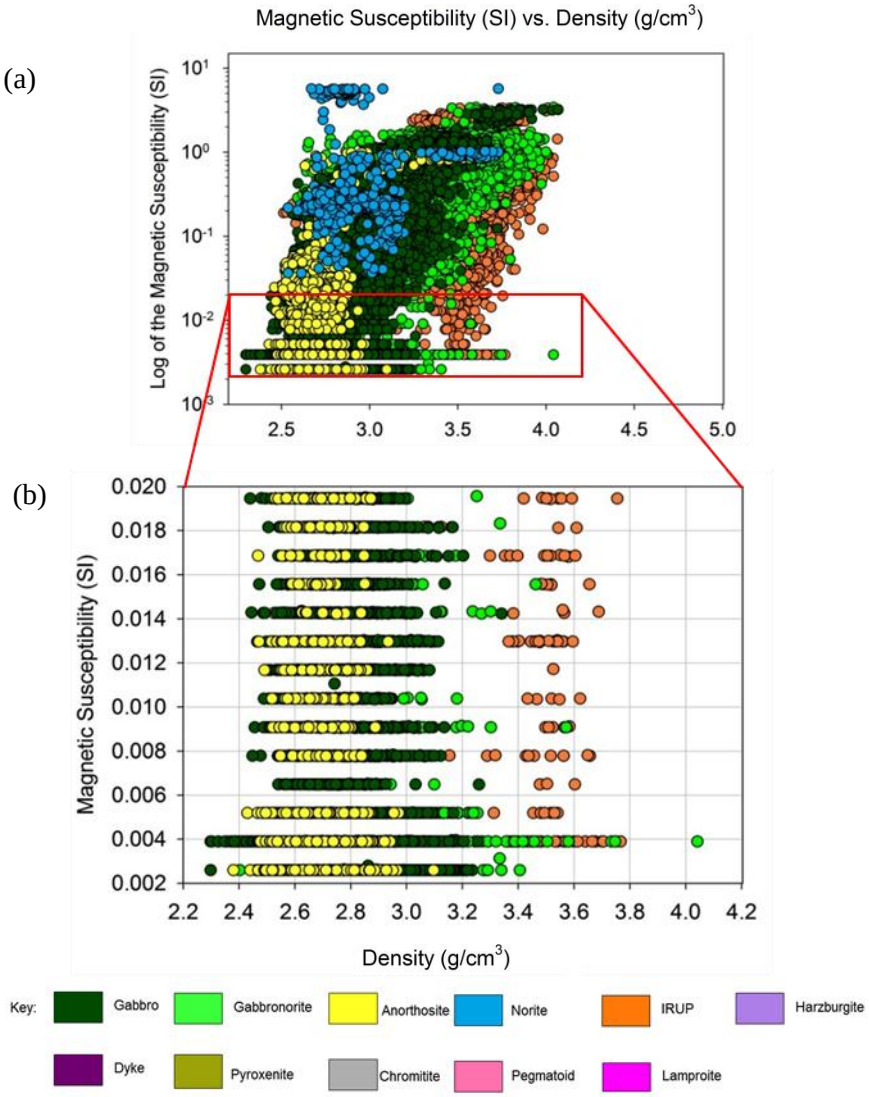

Figure 2.18 Plot of magnetic susceptibility (SI) vs density (g/cm^3) for borehole EL56 on a (a) semi-log scale and (b) a linear scale showing values from 0.002-0.02 SI on the y-axis, and 2.2-4.2 g/cm^3 on the x-axis.

The data points have been coloured to represent the different lithologies corresponding to the various lithologies. Figure 2.18b, shows the same image, but showing data points between 0.002 SI and 0.02 SI. This cross plots shows that data are only recorded at increments of approximately 0.001 SI, and that there are generally no data points between this. These increments also occur across almost all of the lithologies in the borehole, but

to a lesser extent in the IRUPs. This cannot possibly represent the resolution limit of the tool, since it is able to measure at a finer scale. To compare, a scatter plot for borehole KLG52 is shown, in Figure 2.19a and b with similar data ranges. The data shows scattering, as opposed to the discrete measurements shown in borehole EL56. These boreholes are from the same contractor, assumedly using the same tools.

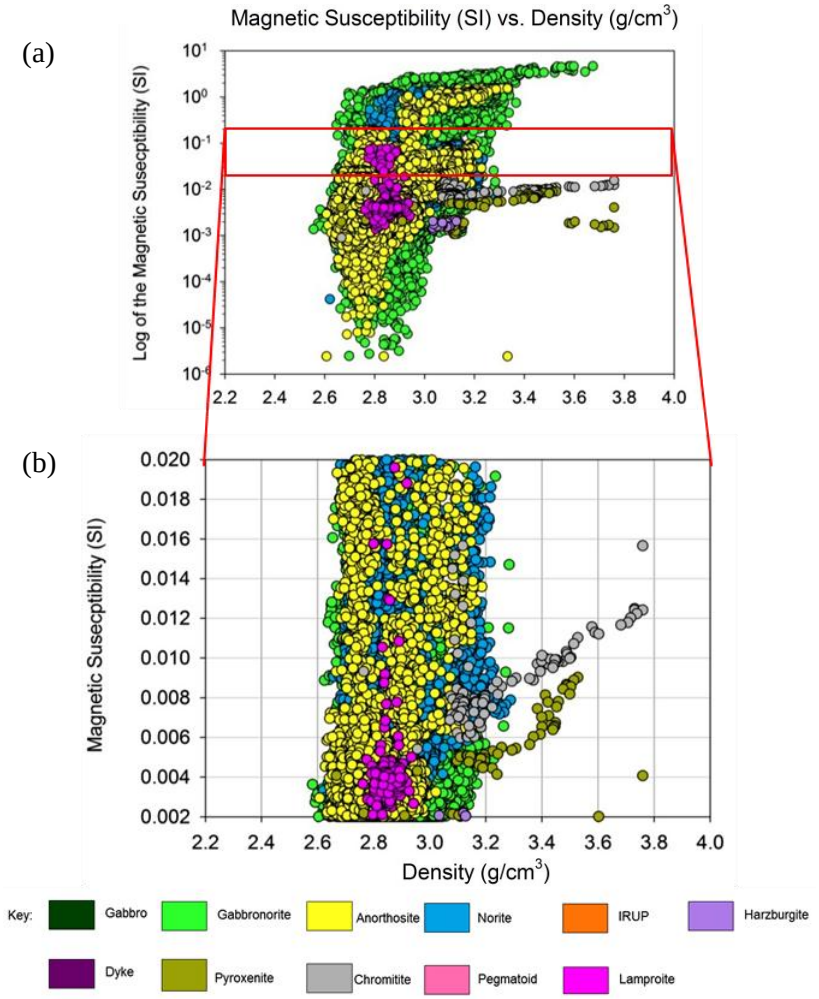

Figure 2.19 Plots of magnetic susceptibility (SI) vs density (g/cm^3) for borehole KLG52 on a (a) semi-log scale and (b) a linear scale showing values from 0.002-0.02 SI on the y-axis, and 2.2-4.2 g/cm^3 on the x-axis.

Density

The density data in borehole SILO1 are measured to five decimal places, although there are sections in which the resolution falls to one or two decimal places. This then produces the effect seen previously in the magnetic susceptibility data. Figure 2.20a shows the

density log for borehole SILO1, Figure 2.20b shows a section of the borehole up to 100 m, with data in the range of 1.60-2.85 g/cm^3.

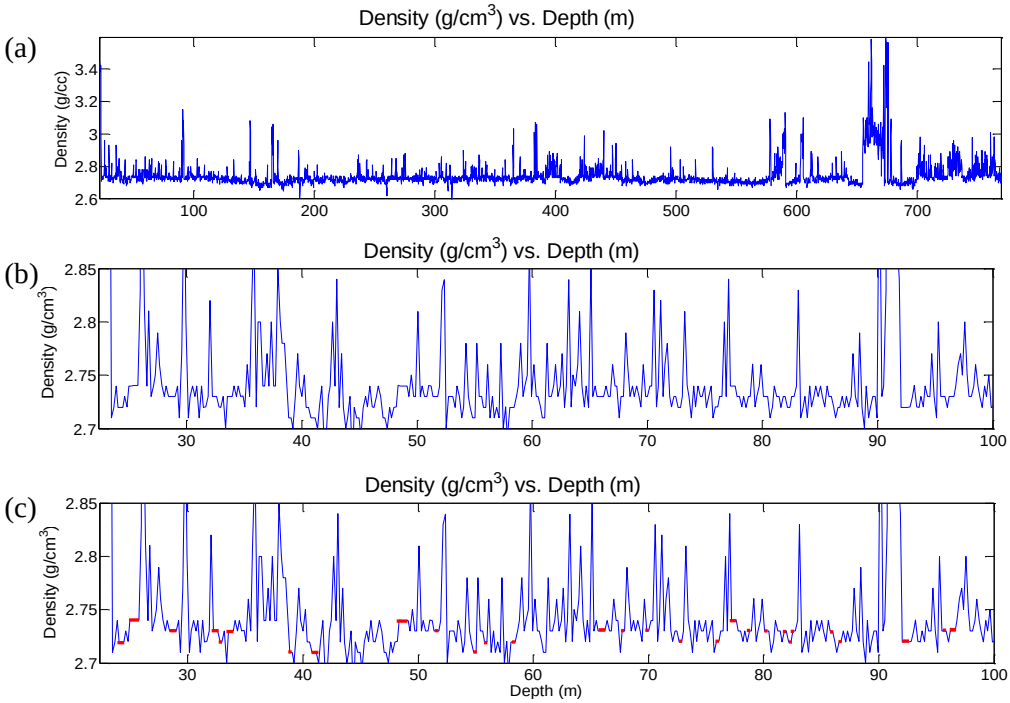

Figure 2.20 Density (g/cm^3) vs. depth (m) for borehole SILO1 shown for amplitudes of (a) 2.6-3.0 g/cm^3 at depths of 25-750 m, (b) 2.7-2.75 g/cm^3 at depths of 25-100 m and (c) 2.7-2.75 g/cm^3 at depths of 25-100 m with red data points where the resolution is courser.

Figure 2.20c is the same as b, with superimposed red data points where the tool resolution deteriorates. This occurs at the shoulders of most of the large peaks. This effect is not obvious as in Figure 2.17c but is easily revealed in the scatter plot shown in Figure 2.21a. This image shows vertical "striping". Figure 2.21b, c and d are scatter plots with density values from 2.6-2.9 g/cm^3, 2.71-2.75 g/cm^3 and 2.71-2.72 g/cm^3 respectively. Figure 2.21b shows the striping effect seen in Figure 2.21a, but much clearer. When the range of data shown is decreased in Figure 2.21c the striping becomes even more apparent. Secondly, some scatter is seen from 2.71-2.73 g/cm^3. An additional feature in this borehole is a "spray", shown in the red block. A close up of this feature is shown in Figure 2.21d. It summarizes all of the features seen in all of the other images: It shows the data with the fallen resolution at 2.71 g/cm^3 and 2.72 g/cm^3 (truncated decimal places), while showing scattering in between.

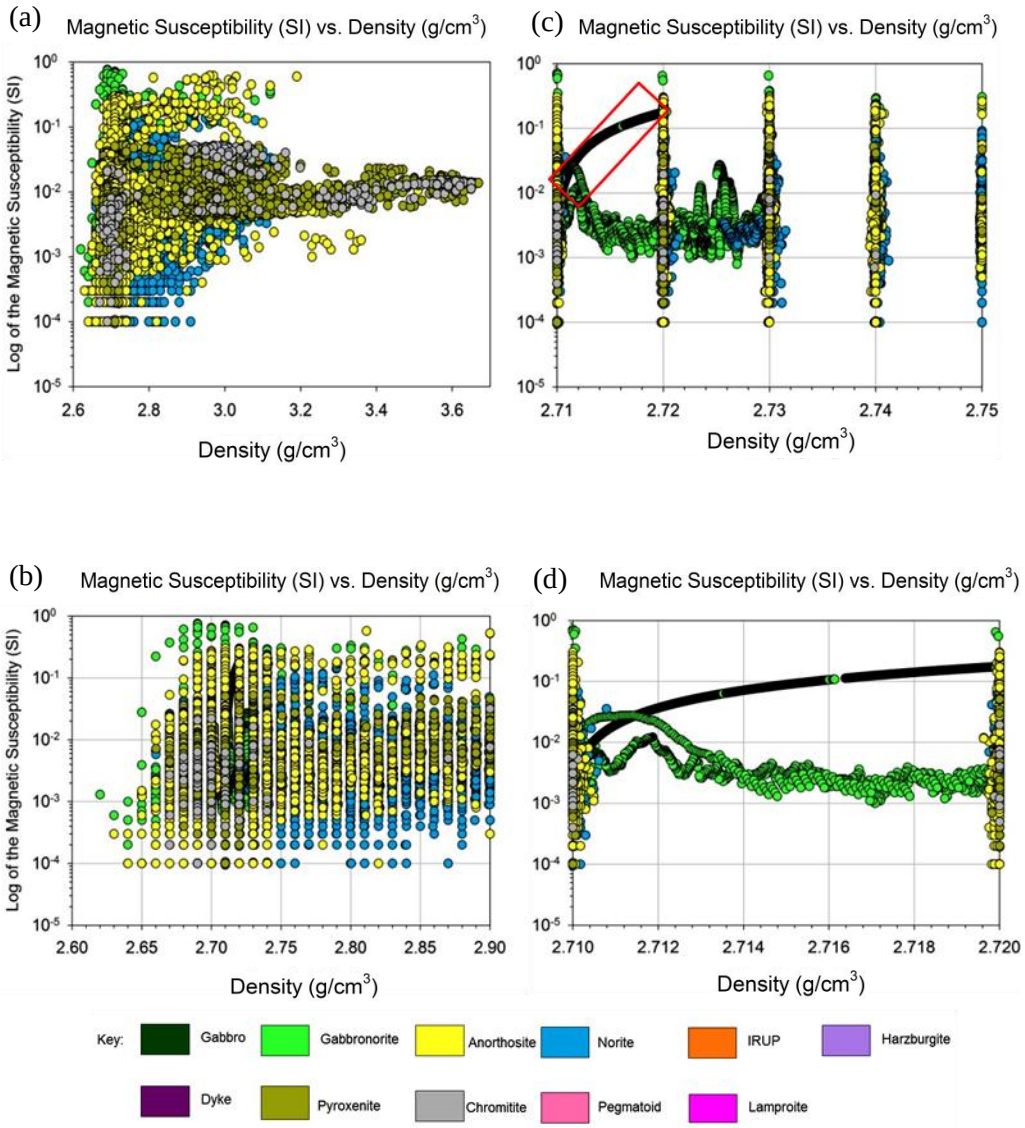

Figure 2.21 Plots of the magnetic susceptibility (SI) vs density (g/cm^3) for borehole SILO1 on a semi-log scale. The density data are shown at ranges of (a) 2.6-3.65 g/cm^3, (b) 2.71-2.75 g/cm^3, (c) 2.60-2.90 g/cm^3 and (d) 2.71-2.72 g/cm^3.

There is no full understanding as to why this occurs, even following consultation with logging engineers and analysts. The effect described above may due to digital data storage when an incorrect dynamic range is selected for a piece of instrument. Data which such as these have been excluded in further data analysis as it may introduce biases and errors, especially in the statistical analysis. A log analyst may not always closely study a wireline log to be able to identify problematic data; however these can be easily observed in a scatter plot and probed further. These data are however, acceptable for simple

identification of horizons of interest for mining purposes, but not for such a detailed scientific study.

2.6.5 Zero and Negative Values

Several boreholes contain negative or zero values in the magnetic susceptibility data. Zero values may be attributed to values falling below the instrument detection limit while negative values have been attributed to a baseline of the dynamic range of the instrument being set to zero or too close to it (Chatfield, pers. comm). Figure 2.22 shows several values below zero, from borehole OV589. The total number of data points which are negative are 20221 (202.2 m) out of 38283 (328.8 m), which is 52% of the dataset. This has been observed to varying degrees in OV525, OV589, CH7, VO2 and SILO1.

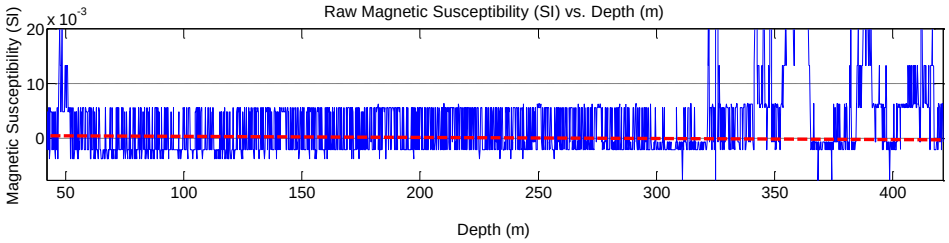

Figure 2.22 Magnetic susceptibility (SI) vs. depth (m) for borehole OV589. Data points shown below the red line are negative.

2.6.6 Data at Geological Contacts

Although the data are sampled at 1 cm, all data in the region of 3 cm lends itself to measurement in density logs. Some spurious data have been observed at geological boundaries between layers with a large density contrast. Thin layers in particular are influenced by layers in their vicinity. The density of the thinner pyroxenite, chromitite and harzburgite layers tends to be under reported if they are surrounded by layers of lower densities. Conversely, layers of lower densities may have their values over reported. This feature is once again most easily observed in a scatter plot. Borehole DB136 has been selected in order to illustrate this feature. Figure 2.23a and b shows the data points of interest, in a red colour.

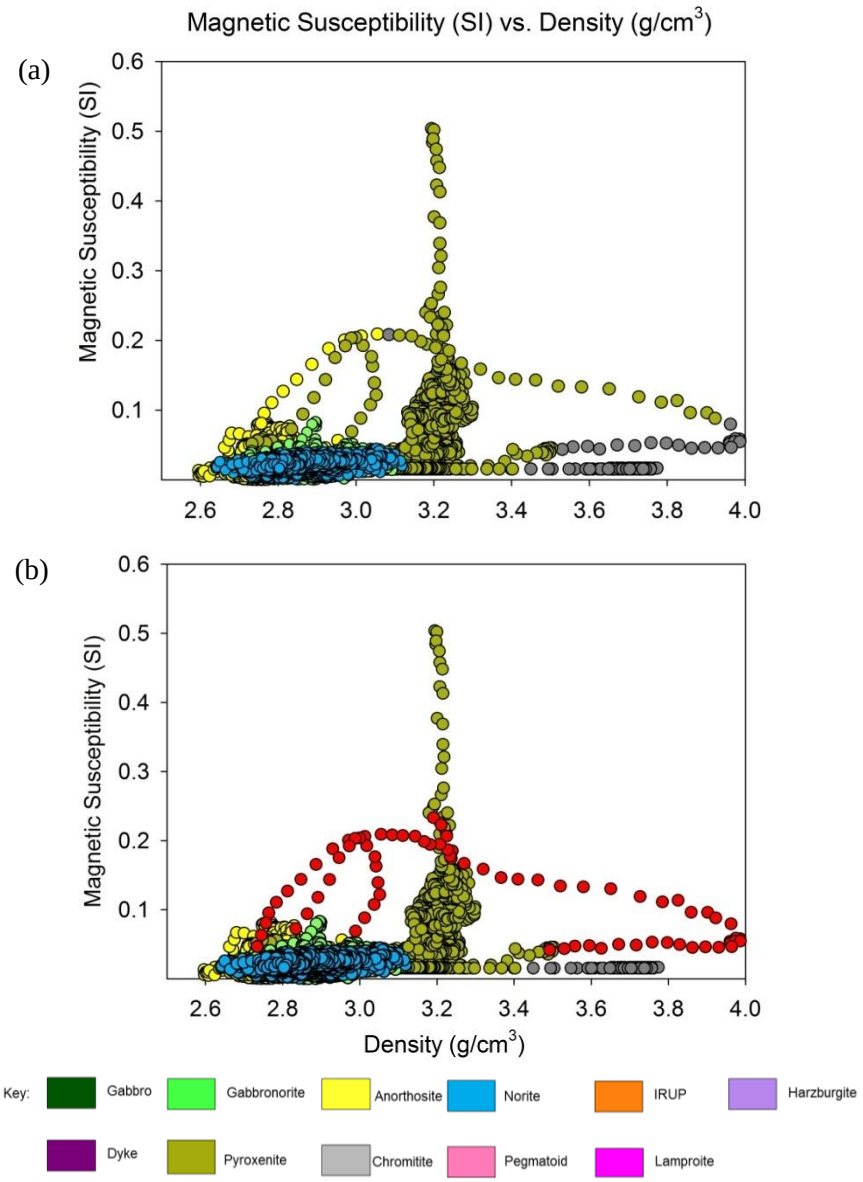

Figure 2.23 (a) Plot of the magnetic susceptibility (SI) vs density (g/cm^3) for borehole DB136. The image in (b) shows several data points mark in red, which have been observed to correspond to geological contacts.

These data points generally deviate from the visible clusters associated with each of the lithologies. This is more pronounced in the density data with fairly constant magnetic susceptibility. A similar effect is observed in the chromitites, which shows some data points with a range of densities from 3.4-4 g/cm^3. These outliers are not characteristic of the actual lithology and found to lie at geological boundaries. These are plotted on the density log in Figure 2.24. It is clear that these data are associated with sharp changes in densities. This feature is also observed in boreholes SO2, KLG52, BY60 and DB135

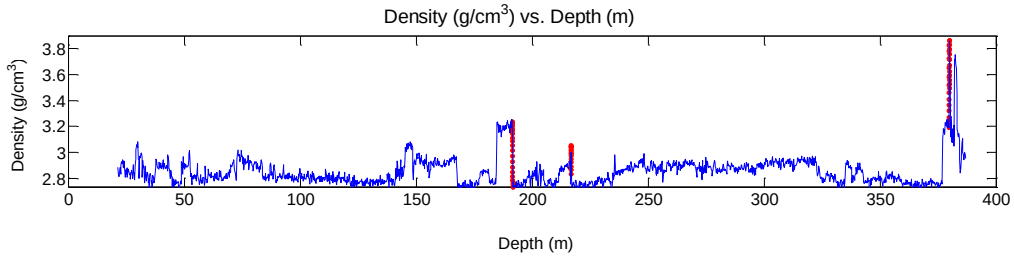

Figure 2.24 Density (g/cm^3) vs. depth (m) for borehole DB136, showing the data points marked red in Figure 2.23 (b) superimposed on it. These data points plot exactly on the geological contacts.

2.6.7 Summary

A variety of data issues have been outlined. These are most easily investigated using a scatter plot between physical properties. This simple tool can be used to highlight peculiarities which may be present before interpretation. The table below summarizes all of the data amassed for the project, and indicates which data was used for further data analysis (with a tick) and those which were discarded (with a cross), based on the quality control discussed above (Table 2.4).

Table 2.4 Summary of boreholes in the BC. As before, WL and EL beneath the name of the mine indicate the location of the mine in the limbs of the BC i.e. Western or Eastern Limb.

Mine	Borehole ID	Density	Magnetic Susceptibility	Comment
Amandelbult WL	EL56	✓	✗	Data resolution issues in magnetic susceptibility
	EL57	✓	✗	Data resolution issues
	AB39	✗	✗	Truncated decimal places in density
	AB42	✗	✗	Truncated decimal places in density
Union WL	SK59A	✓	✗	-Data resolution issues in magnetic susceptibility
	G11	✗	✗	-No lithology log -Borehole direction unknown
Styldrift WL	VO2	✗	✗	-2634/71284 magnetic susceptibility values are either values zero or negative -Truncated decimal places in density
	SO2	✓	✓	
	SILO1	✗	✗	-10000/71286 magnetic susceptibility values are either values zero or negative -Truncated decimal places in density
RPM WL	KLG19	✗	✗	-Data resolution issues in magnetic susceptibility -Truncated decimal places in density
	KLG52	✓	✓	
	KLG8	✓	✗	Data resolution issues in magnetic susceptibility
Der Brochen EL	DB136	✓	✓	
	DB135	✓	✓	
	RM123	✓	✓	
Booysendaal EL	BY60	✓	✓	
	BY62	✗	✗	Data resolution issues in density and magnetic susceptibility
	BY63	✓	✓	
Lebowa EL	CH7	✗	✗	-No lithology log -22000/128000 magnetic susceptibility values are either values zero or negative -Data resolution issues in magnetic susceptibility

CHAPTER 3: DATASETS

A general description of the BC is given as well as the boreholes and where they lie in the stratigraphy. The boreholes have been logged by contractors to Anglo Platinum Ltd. The supplied geological logs record changes in lithology, the stratigraphy in which they fall and their thicknesses. Where possible, marker horizons have also been identified. The various boreholes with which this project is concerned have mainly intersected the MZ and CZ of the RLS of the BC. Although these boreholes do not intersect the UZ, MaZ and LZ, general descriptions for these are included for completeness. The physical properties for various lithologies are summarized and discussed using histograms and scatter plots and their application for quality control of geological logging and physical property logs.

3.1 Overview of the Stratigraphy and Lithology Logs

The general stratigraphy of the BC and its main lithologies are shown in Figure 3.1. The MaZ forms the base of the RLS (although not across the entire BC) and is composed mainly of norite with minor pyroxenite (Eales and Cawthorn, 1996; Cawthorn et al., 2006). The exposure of the MaZ in the Northern Limb is poor, but shows a similar composition to the exposures in the Eastern and Western Limbs. Van der Merwe (2008) has estimated the thickness to range from a few centimetres to tens of meters, and is seen to be intrusive with the rocks surrounding it.

The LZ has a total thickness of 1.3 km and is composed of harzburgites and pyroxenite units. Chromitite bodies within units have been recorded by both Cawthorn et al. (2006) in the Eastern and Western Limbs as well as by Van der Merwe (2008) in the Northern Limb. This unit crops out only in the northern part of the Eastern Limb, the south-western part of the Western Limb, and the southern portion of the Northern Limb (Eales and Cawthorn, 1996).

The overlying CZ is characterised by magmatic cycles of pyroxenite, chromitite, norite and anorthosite (Cawthorn et al., 2006). A Lower CZ has been recognise and is characterised by the first appearance of cumulate plagioclase (Cawthorn and Walraven, 1998). The predominantly ultra-mafic Lower CZ consists of pyroxenites and harzburgites; while the Upper CZ comprises of mostly of anorthosite, norites and pyroxenites. This zone has an estimated thickness of 1300 m. This zone has been identified by Eales and Cawthorn (1996) to crop out in the Western and Eastern Limbs,

but does not at the southernmost part of the Eastern Limb. It is present south of Potgietersrus in the Northern Limb (Figure 1.1). These rocks encompass large deposits of PGE's and chromite. The Merensky Reef, which is mined extensively, contains significant PGE mineralization. Several groups of chromitite horizons have been identified and subdivided to form the Lower, Middle Group and Upper Group chromitites. These are considered "markers", and together with many others are distinct rocks which are laterally extensive. Another notable marker in zone is the Bastard Reef, which is similar to the Merensky Reef but barren in PGEs.

The MZ overlies the CZ and shows very limited lithologies. This Zone shows thick homogeneous successions of gabbro, norites and gabbronorites. It is devoid of chromitite layers and reaches an estimated 2.2 km in thickness in the Western Limb and 3.1 km in the Eastern Limb (Cawthorn et al., 2006). A Porphyritic Gabbro Marker (PGM) has been identified as a marker in this zone, and comprises of course-grained gabbro. Studies by von Gruenewaldt (1973), Molyneux (1974) and others have found a reversal in geochemical data and petrographic evidence supporting a dramatic change in magma processes. This is at the level of an orthopyroxenite layer identified 2000-2500 m above the base of the MZ. This layer is continuous and identified least in the Western and Eastern Limbs, and is referred to as the Pyroxenite Marker. Mitchell (1990) subsequently subdivided the MZ into the LMZ below this marker, and the Upper MZ above it. The Giant Mottled Anorthosite is taken to mark the base of the MZ (De Klerk, 1995; Eales 2002) although some authors prefer to place the boundary at the top of the Merensky Reef (Kruger, 2005).

The final sequence is the UZ, is described as the most extensive zone by Cawthorn et al. (2006). It consists of ultramafic dunites and pyroxenites, and mafic norites, gabbros, anorthosites and magnetite-rich diorites (Cawthorn et al., 2006). This unit has a thickness of up to 2 km across the BC. The boreholes are discussed below for the Western and Eastern Limbs.

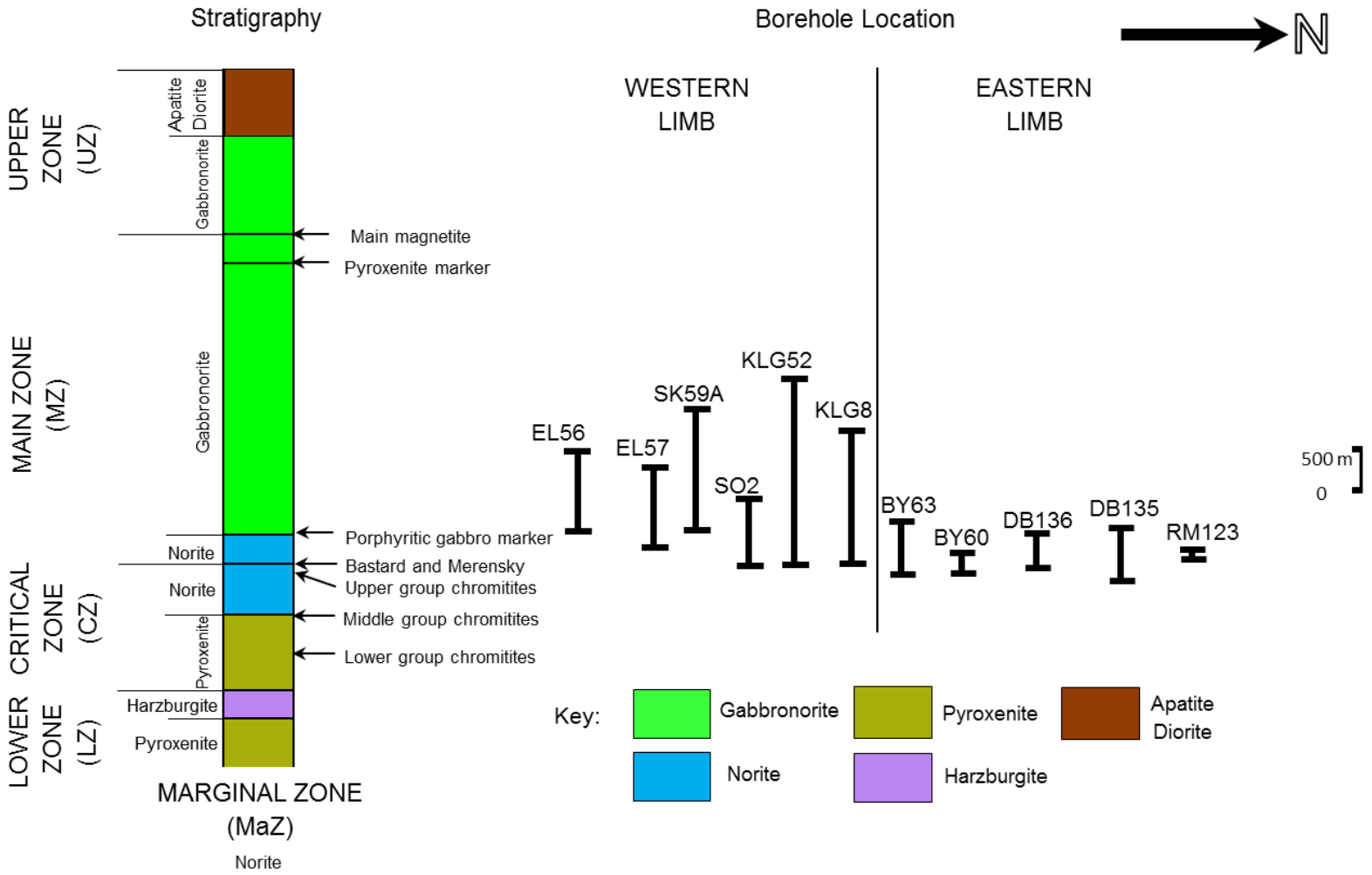

Figure 3.1 Simplified stratigraphic column of the BC, showing various markers as well as the approximate positions of the boreholes used in this project. Thicknesses of the various units shown are drawn to scale for the Western Limb (adapted from Clarke et al. 2009).

3.1.1 The Western Limb of the BC

Six boreholes from the Western Limb (Figure 3.2) are discussed below.

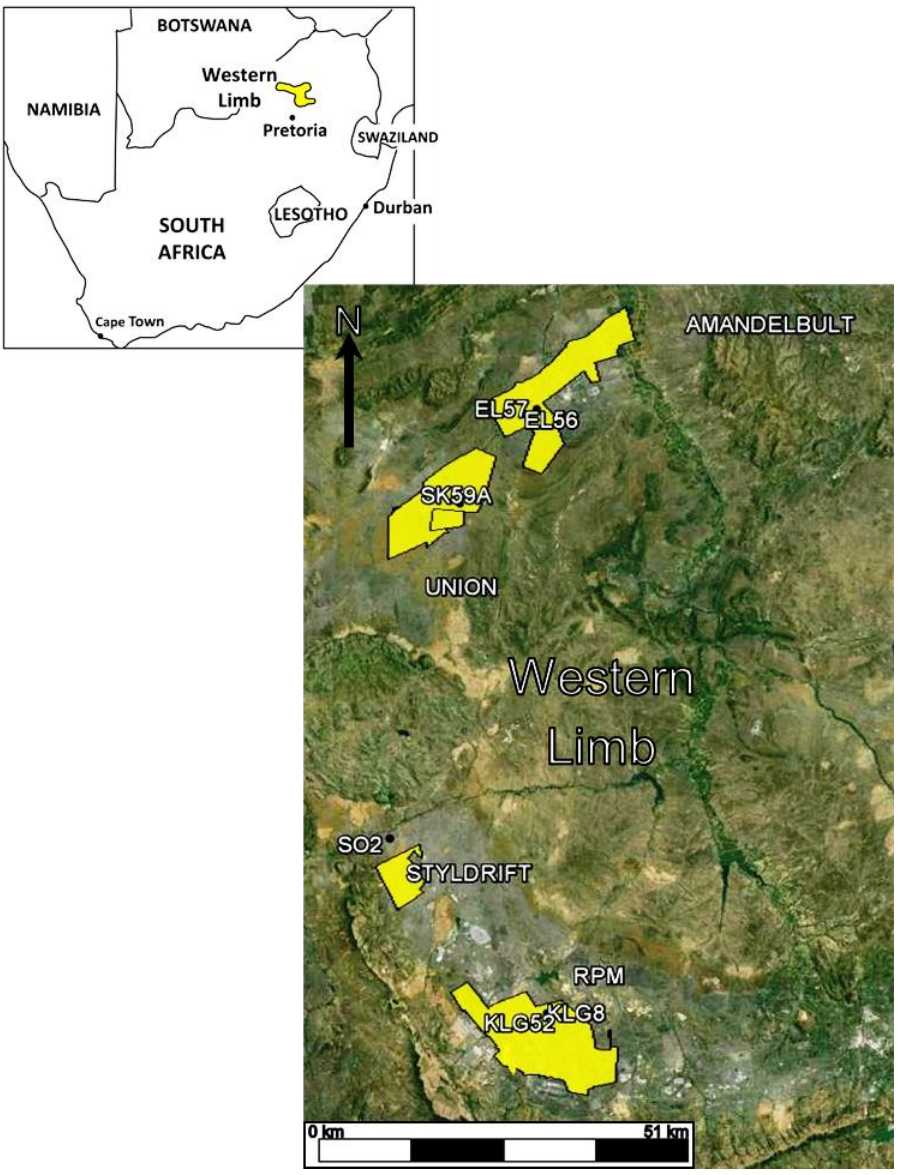

Figure 3.2 Google Earth image showing outlines of mining operations and locations of boreholes EL56, EL57, SK59A, SO2, KLG8 and KLG52 in the Western Limb.

The lithology logs for the first three northernmost boreholes EL56, EL57 and SK59A are shown in Figure 3.3. The white sections in the logs indicate that there is no core.

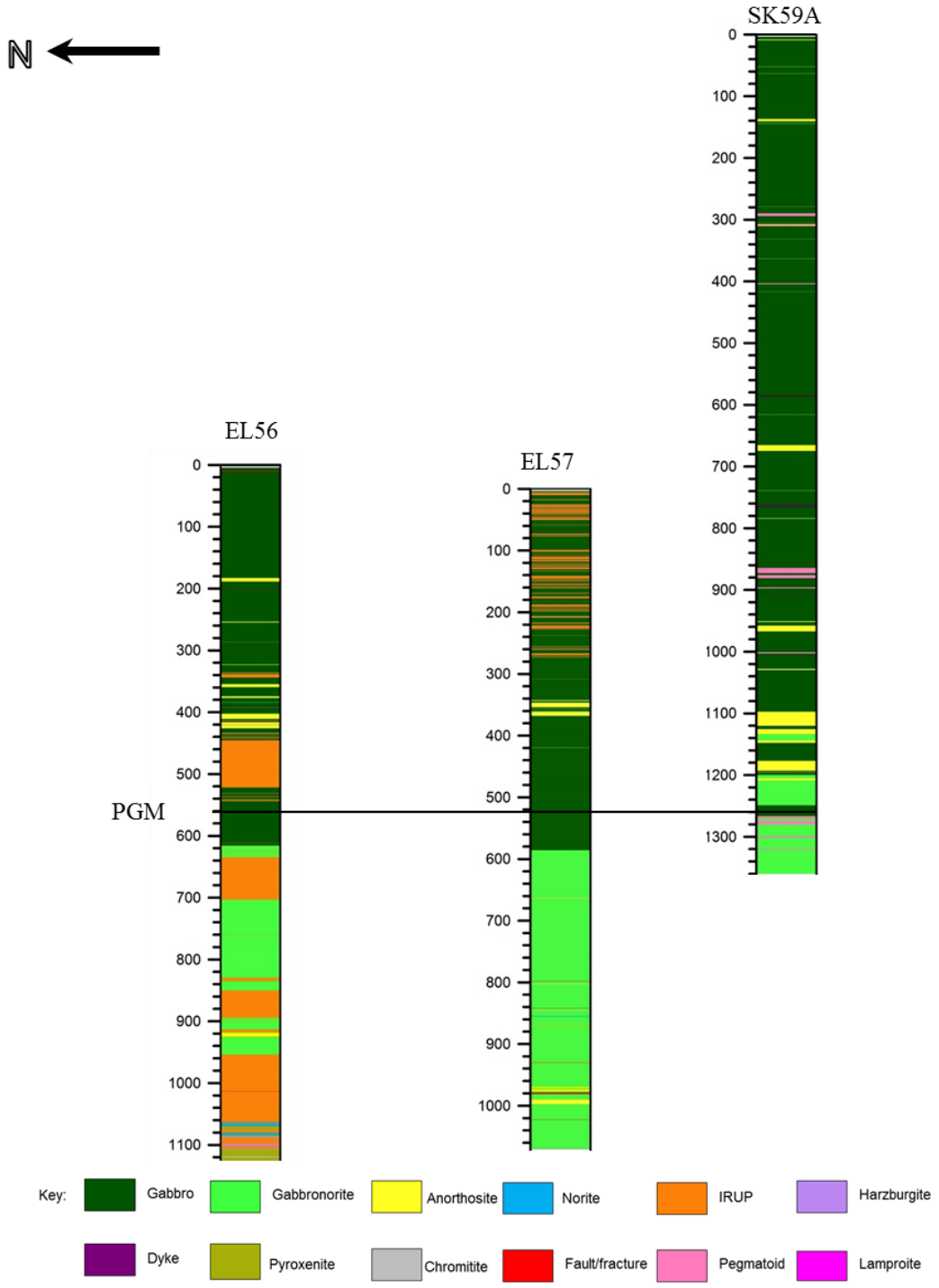

Figure 3.3 Lithology logs for boreholes EL56, EL57 and SK59A. The black solid line indicates the approximate location of the PGM (Porphyritic Gabbro Marker) used to align the boreholes.

The Porphyritic Gabbro Marker identified in all of these boreholes is used to align them. EL56 consists mostly of MZ rocks with minor CZ rocks. The exact location of the start of the CZ is unknown. However, the Bastard Reef has been intersected implying there are CZ rocks. The log consists of gabbros to a depth of ~620 m depth which have been

interrupted by iron-rich ultramafic pegmatoids (IRUPs). These are discordant pipe-like bodies which contain sulphides (Eales and Cawthorn, 1996). These are not the focus of this study, but the processes involved in the formation of these rocks are contested and have been discussed by several authors (Wagner, 1929; Cameron and Desborough, 1964; Viljoen and Scoon, 1985). The gabbros are followed by layers of gabbronorites until ~960 m. These layers are also interrupted by IRUPs. The thin section of CZ lithologies consists of pyroxenite and harzburgite layers with minor anorthosite and IRUP layers. EL57, which is separated by 1.9 km from EL56, shows similar features. This borehole has also intersected IRUPS, although much thinner than in EL56. The IRUPs in this borehole occur as "stringers" within gabbros from the top of the borehole to approximately 280 m. Gabbros are intersected until a depth of 580 m after which there is a transition to gabbronorites until the end of the borehole. These boreholes are relatively homogeneous. SK59A, which is 15 km from EL57, consists mostly of gabbros from 0-1120 m with stringers of pegmatoid, anorthosite and dykes. The three boreholes show similar lithologies due to their close proximity, and are relatively homogeneous. In general they contain thick units of gabbro until the PGM, below which gabbronorites are observed. Thin anorthosite layers occur sporadically within these units.

The lithology logs for the three boreholes in the southern part of the Western Limb in Figure 3.2; SO2, KLG52 and KLG8 are shown in Figure 3.4. The Bastard Reef has been identified in all of these boreholes, and they are shown aligned using this marker. Borehole SO2 shows lithologies which change from gabbronorite and norite in the MZ, to anorthosite layers towards the CZ. The CZ consists predominantly of norite with thinner layers of anorthosites, pyroxenite and chromitites. Dyke stringers and intrusive lamproites are also present sporadically throughout the log. Lamprophyres have been seen before in the BC, and have been documented by Leeb-Du Toit (1986). Borehole KLG52 shows thick homogenous units in the MZ. The CZ consists mainly of anorthosite and norites, with minor pyroxenite layers and stringers of pegmatoid. A pegmatoid similar to that observed in SK59A is also present, as well as layers of lamproite at approximately 340 m.

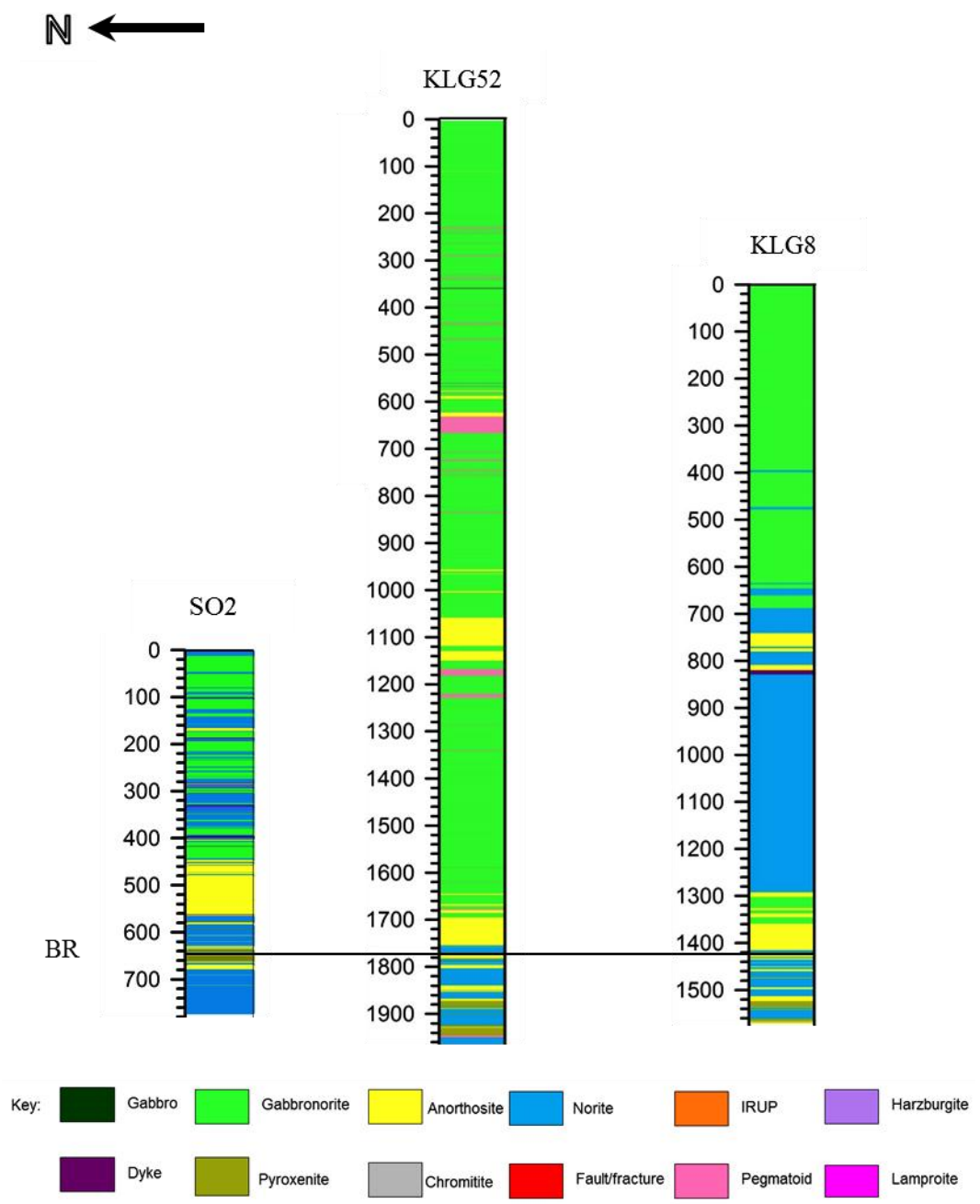

Figure 3.4 Lithology logs for boreholes SO2, KLG52 and KLG8. The black solid line indicates the approximate location of the BR (Bastard Reef) used to align the boreholes.

Borehole KLG8 consists mainly of gabbronorite from 0-680 m with intermittent norite layers. Norites become dominant from 680 m, but eventually the rocks become more anorthositic and gabbronoritic towards the MZ-CZ boundary. This borehole shows the thickest non-interrupted layer of norite, which reaches ~500 m thickness. The CZ consists mostly of thinner layers of norite, with minor pyroxenite and anorthosite.

3.1.2 The Eastern Limb of the BC

Five boreholes from the Eastern Limb (Figure 3.5) are discussed below.

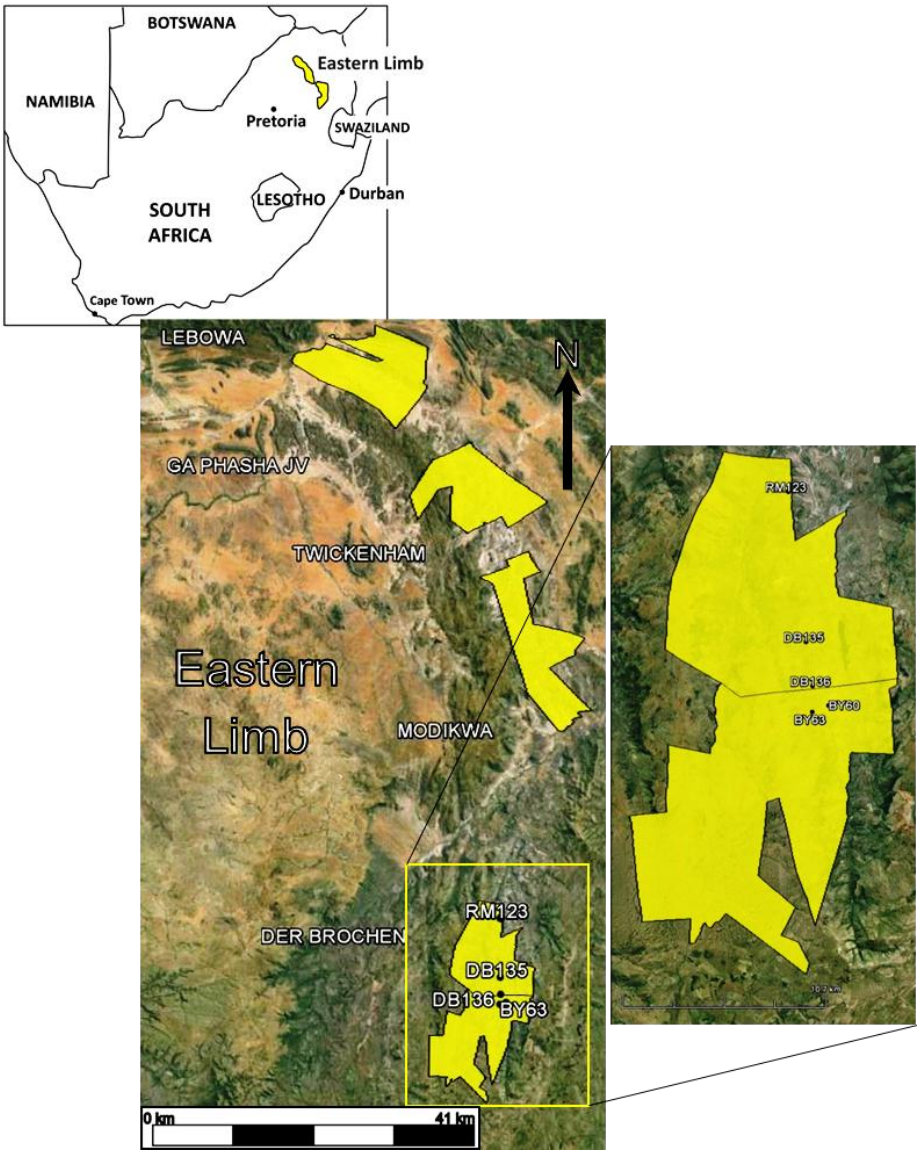

Figure 3.5 Google Earth image showing outlines of mining operations and locations of boreholes RM123, DB135, DB136, BY63 and BY60 in the Eastern Limb.

The lithology logs are shown in Figure 3.6, from north to south along strike. The first three boreholes RM123, DB135 and DB136 have been aligned using the UG2 marker horizon. Borehole RM123 is approximately 300 m shorter than all of the other boreholes from Der Brochen, DB135 and DB136, and 400 m lower in elevation. As a result, the Giant Mottled Anorthosite is not intersected in this borehole. This marker is seen in

DB135, DB136 and BY60, and has been inferred in BY63. RM123 is homogeneous, made up entirely of CZ rocks consisting of norite and anorthosite.

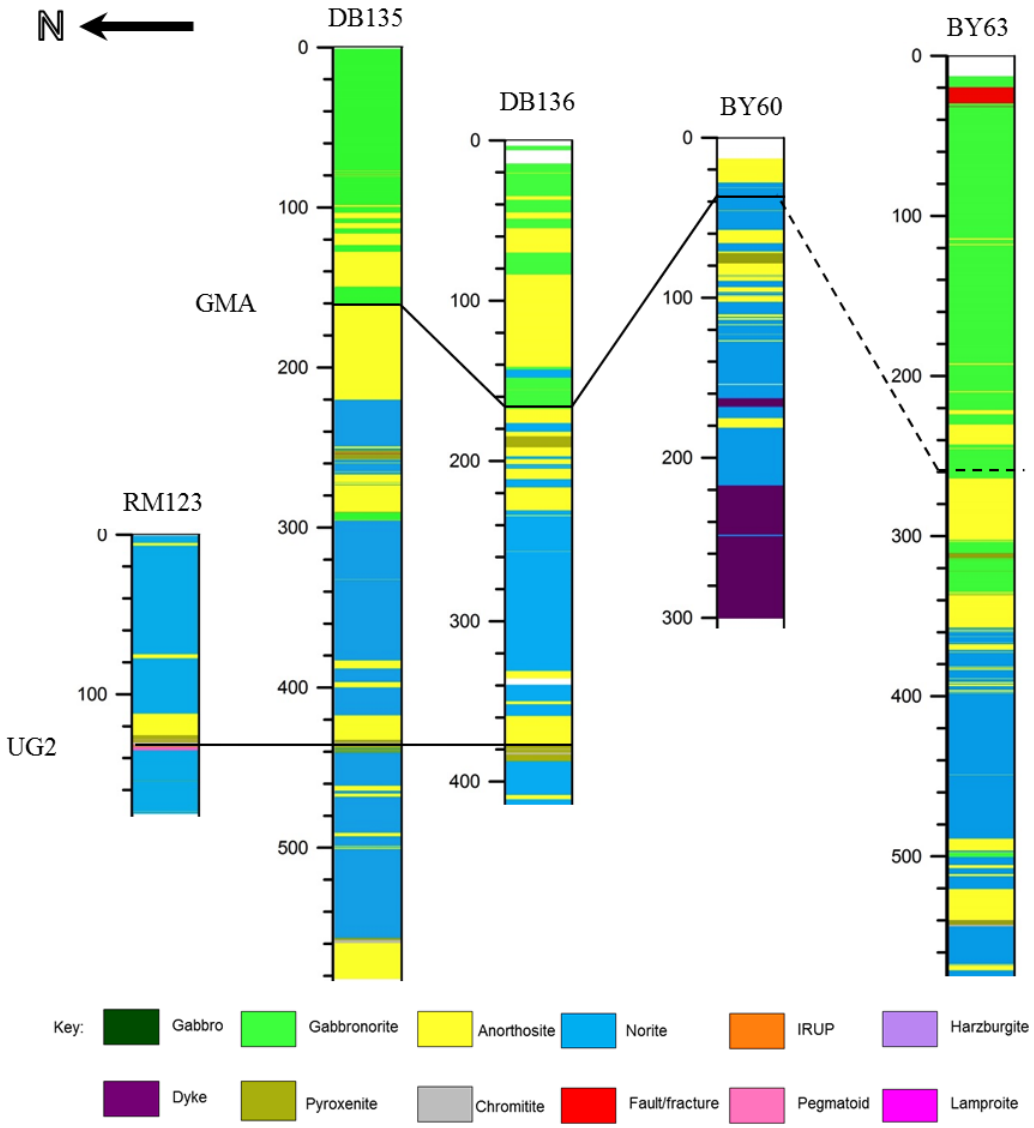

Figure 3.6 Lithology logs for boreholes RM123, DB135, DB136, BY60 and BY6. The black solid line indicates the approximate location of the UG2 used to align RM123, DB135 and DB136. The stippled line between BY60 and BY63 is the location of the inferred GMA (Giant Mottled Anorthosite).

Some pegmatoids have been identified at the level of the UG2. Borehole DB135 has both LMZ rocks as well as Upper CZ rocks. The MZ rocks show thick layers of gabbronorite and anorthosite. In contrast, the CZ rocks consist predominantly of norite and anorthosite with minor pyroxenite and chromitite. Borehole DB136, which is 2 km away from this, has similar lithologies. The MZ shows gabbronorite and thick anorthosite layers (up to 60 m), and the CZ show layers of pyroxenite and chromitite with thick units of norite.

Borehole BY60 begins in the mottled anorthosites that define the Giant Mottled Anorthosite, and therefore shows the Upper CZ only. This borehole consists of thinner layers of norite and anorthosites, and is not unique in any way from DB135 and DB136 except that a 50 m thick dyke is intersected towards the end of the borehole. The Giant Mottled Anorthosite is absent in BY63 but has been inferred based on the lithologies identified in boreholes BY60, DB136 and DB135 which are in close proximity to this hole. The lithology log shows a thick section of gabbronorite from the 0-320 m, followed by norite up to a depth of 580 m. The succession of layers is strikingly similar to KLG8, which was observed to consist of homogeneous layers of gabbronorite and norites in Figure 3.6.

3.1.3 Summary

The boreholes have intersected similar sections and markers which has allowed them to be correlated to some extent. The boreholes in the Western Limb are evidently much longer, and intersect a larger part of the MZ then those of the Eastern Limb, which have sampled thicker CZ successions. Although each borehole is unique in layering, some general features have been observed. The MZ generally contains thick homogeneous units of gabbro and gabbronorite. Gabbros have only been observed in the northern Western Limb, typically above the PGM. The CZ shows small scale layering, and thick layers are less common.

3.2 Physical Property Histograms Based on Lithology

Several histograms are examined for the various lithologies studied above. The density and magnetic susceptibilities were extracted for each borehole hole from their .las files and combined into one database. The frequency histograms represent the combined lithologies for all of the boreholes. The mean, standard deviation and the total number of data points are also shown. The mean ($\bar{x}$) was calculated using,

$$\bar{x} = \frac{1}{n}\sum_{i=1}^{n} x_i, \qquad 3.1$$

where n is the total number of data points and x_i are the observations. The standard deviation (σ) was calculated in MATLAB which uses the formula,

$$\sigma = \sqrt{\frac{1}{n-1}\sum_{i=1}^{n}(x_i - \bar{x})^2}\,. \qquad 3.2$$

The histograms for density and magnetic susceptibility are presented below.

3.2.1 Density Histograms

The density histogram for gabbros in Figure 3.7a shows that the observations are asymmetric, with a mean of 2.91 g/cm^3. The gabbronorites in Figure 3.7b, have the same mean density, but shows a bimodal distribution. The modes correspond to densities of 2.90 g/cm^3 and 3.50 g/cm^3 respectively. The density histogram for anorthosites in Figure 3.7c shows an approximately normal distribution similar to the one seen for gabbros. The histogram for pyroxenites in Figure 3.7d has three modes character, associated with densities of 3.10 g/cm^3, 3.50 g/cm^3 and ~4.0 g/cm^3. The chromitites in Figure 3.7e show a large polymodal variation in density, from approximately 2.60 g/cm^3 to 4.30 g/cm^3 and more scatter. The histogram is long tailed, asymmetric and skewed towards higher densities. These data show the highest density observed in samples. A mode of close to 3.70 g/cm^3 is probably the best representative value for the densities rather than the calculated mean of 3.64 g/cm^3. The norite data Figure 3.7f are unimodal, with an average density of 2.86 g/cm^3, which show the lowest observed average density. This is unexpected, since these are more mafic and should have a higher density than anorthosites. This discrepancy is being attributed to misidentification, since it is easy to confuse leuconorites (which are not uncommon) for anorthosites and vice versa in hand specimen. This is primarily because leuconorites have a plagioclase content of 80-90 %, which is close to that of anorthosites of 90-100% (Seabrook, 2005). This data shows a strong clustering around the mean.

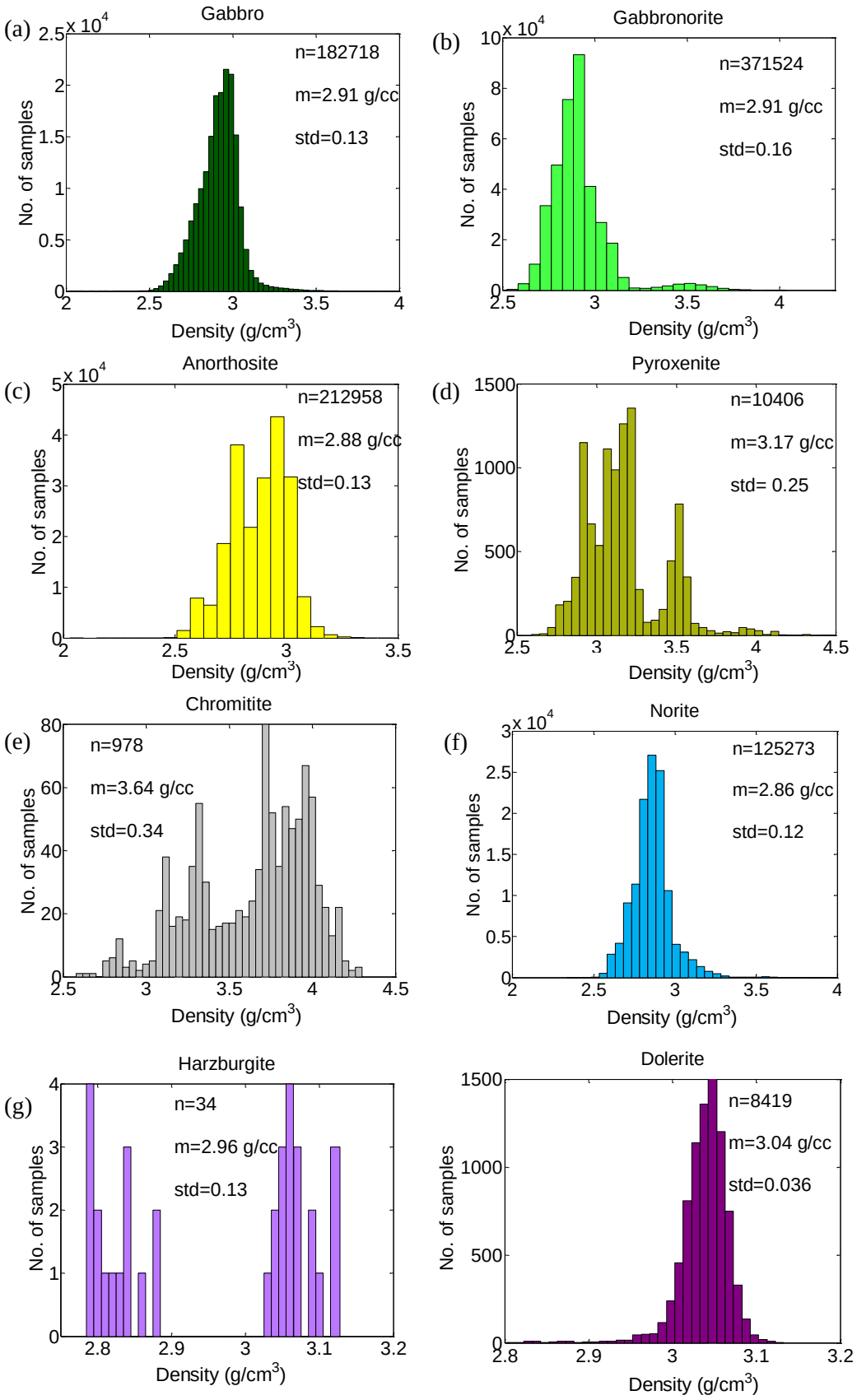

Figure 3.7 Continued

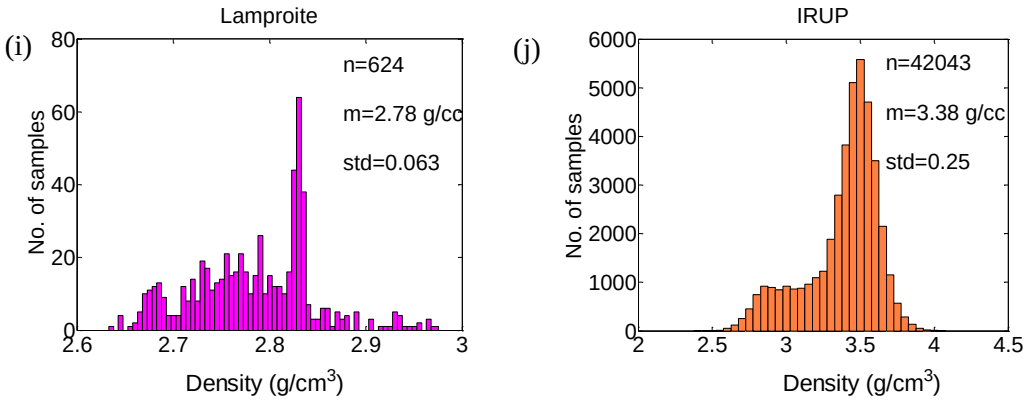

Figure 3.7 Density histograms for (a) Gabbro, (b) Gabbronorite, (c) Anorthosite, (d) Pyroxenite, (e) Chromitite, (f) Norite, (g) Harzburgite, (h) Dolerite, (i) Lamproite, and (j) IRUP. The symbols "n", "m" and "std" denote the total number of data points, mean and standard deviation respectively.

The harzburgite data shown in Figure 3.7g shows two easily distinguishable distributions; between approximately 2.80-2.90 g/cm^3 and 3.01-3.11 g/cm^3. The distribution with the lower densities is from the borehole SO2 while the distribution of higher densities is from KLG52. This may point to weathering of the harzburgites in SO2. Figure 3.7h shows a unimodal distribution for dolerites, with the data clustered around a mean of 3.04 g/cm^3. The lamproite show an asymmetric distribution in density and a mode of 2.84 g/cm^3 (Figure 3.7i). The IRUP have a bimodal density distribution with modes of 2.58 g/cm^3 and 3.50 g/cm^3 (Figure 3.7j). The density histogram for the combined lithologies is shown in Figure 3.8. The density histogram for the combined lithologies is shown in Figure 3.8.

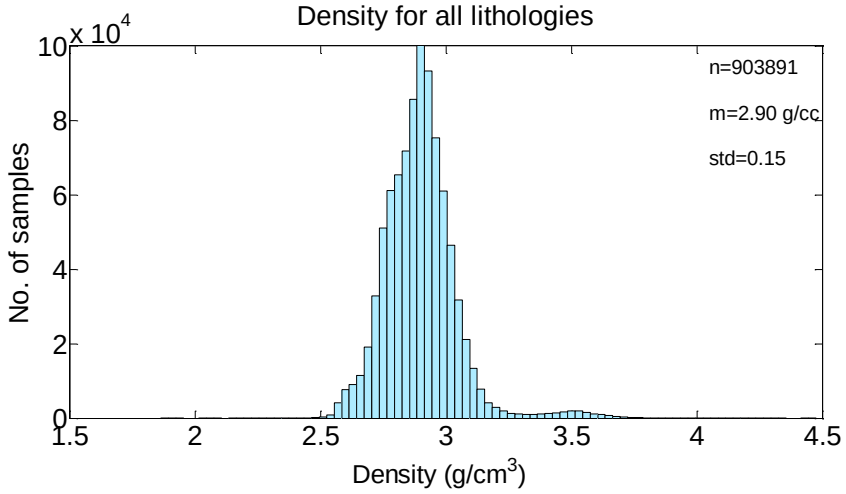

Figure 3.8 Density histogram for all lithologies.

The histogram is clearly bimodal, with modes of 3.0 g/cm^3 and 3.50 g/cm^3. The samples predominantly lie between approximately 2.5 g/cm^3 and 4 g/cm^3.

3.2.2 Magnetic Susceptibility Histograms

Histograms for the magnetic susceptibilities of lithologies are shown in Figure 3.9. Although magnetite (ferrimagnetic) is an accessory mineral in these rocks, it contributes to the measured rock magnetic susceptibility (Henkel, 1976, Kukkonen and Peltoniemi, 1998). Studies by Letts (2007) and Hattingh (1983) have revealed magnetite lamellae in plagioclase and pyroxene grains in the MZ. Mafic paramagnetic minerals also contribute to this (Kukkonen and Peltoniemi, 1998). Previous studies across different mafic rocks have shown that the magnetic susceptibility tends to be highly variable (e.g. BC- Hatting, 1991; Insizwa Sill, South Africa- Ferré et al., 2002; Proterozoic sills, Ontario, Canada- Middleton, 2004). These variations mostly reflect ferric minerals as well as grain size changes (Ferré et al., 2009). This is also evident across each of the properties for the lithologies studied here. In general, the histograms are asymmetric and skewed towards lower values, unlike those of the densities which tend to show uni- or bimodal behaviour. This makes the averages calculated for these histograms less representative of the various lithologies, since statistics are not Gaussian. The mode is a better representative value. The log of the frequencies is used for easier display. Figure 3.9a clearly shows that the magnetic susceptibility is skewed towards lower values in gabbronorites.

This data shows the highest variability in magnetic susceptibility, with a significant number of observations at the high end of the magnetic susceptibility. A similar trend is observed in anorthosite, although these data show a more flat distribution in Figure 3.9b. There are some outliers shown with data susceptibilities in the range of 2-3 SI. Figure 3.9c shows that the chromitite data have a bimodal distribution. The second of the distribution indicates that the data may have some enrichment in magnetite. The pyroxenite distribution in Figure 3.9d shows an asymmetric distribution of susceptibilities up to 2 SI. Figure 3.9e shows the histogram for harzburgite. This is generally a smaller dataset, and smaller bins than those displayed produce counts or frequencies of 1 and 0. Half of the samples have susceptibilities of approximately 0.007-0.011 SI, with smaller occurrences present but at much larger susceptibilities. Figure 3.9f shows a distribution for norite samples, which is similar to that observed for pyroxenites in trend as well as the range of susceptibilities. The dolerites shown in Figure 3.9g shows a strong clustering about a mean value of 0.027 SI. Finally, the lamproites data shows bimodality.

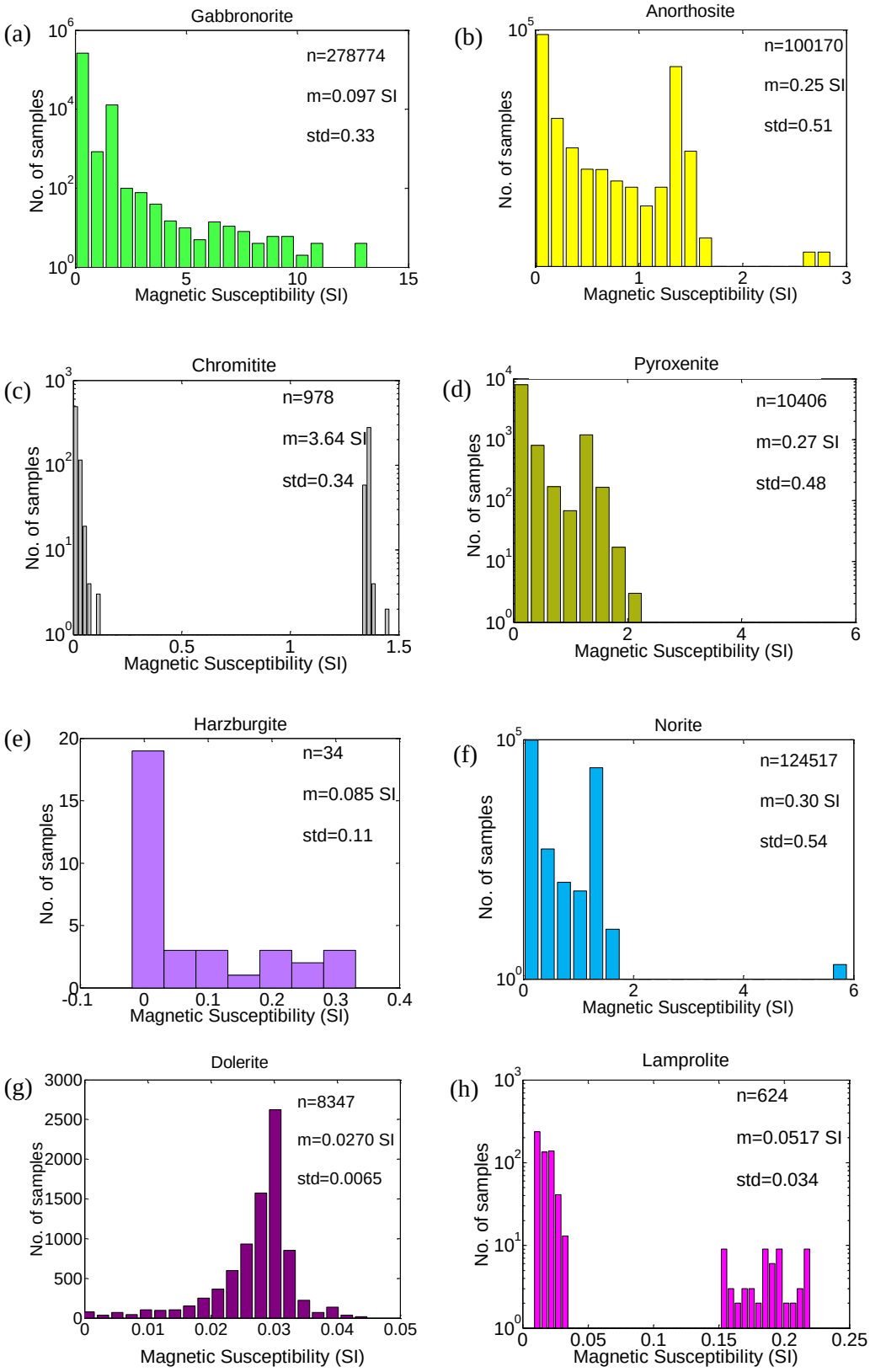

Figure 3.9 Magnetic susceptibility histograms for (a) Gabbronorite (semi-log scale), (b) Anorthosite (semi-log scale), (c) Chromitite (semi-log scale), (d) Pyroxenite (semi-log scale), (e) Harzburgite, (f) Norite (semi-log scale), (g) Dolerite and (h) Lamproite (semi-log scale).

Neither of these distributions are Gaussian and they show dissimilar shapes. The magnetic susceptibility histogram for the combined lithologies is shown in Figure 3.10. The histogram is long tailed, with most of the data points at the low end of the scale and fewer data points at higher susceptibilities.

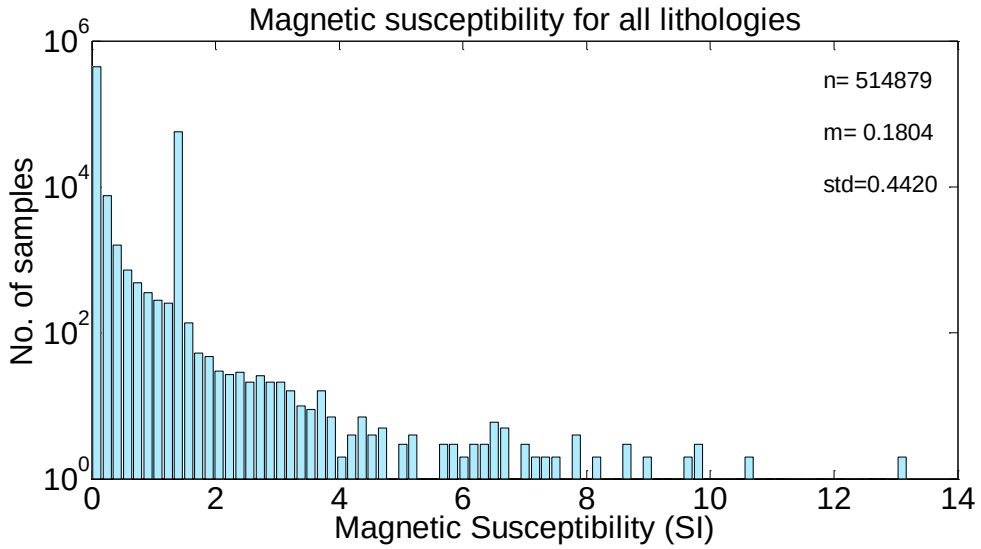

Figure 3.10 Magnetic susceptibility histograms for all lithologies on a semi-log scale.

3.2.3 Summary

The data show a variety of distributions. In general, the density data show uni- and to a lesser extent bimodal distributions. This is with the exception of chromitite data which are skewed towards higher density values. The unimodal distributions tend to be symmetric and closely clustered around the mean in some instances, an indication of smaller variance and standard deviation. The mean density values are representative of the lithologies shown. In the case of the bimodal distribution, the modes associated with the peaks are better estimators. The more felsic rocks (anorthosite and norites) show the lowest densities, while the ultramafic (pyroxenite and harzburgites) rock show higher values, which is an expected result. Possible misidentification between norite and anorthosites has also been identified based on the rock physical properties. This makes histograms an easy quality control measure for geological logs. The magnetic susceptibility data show non-Gaussian statistics, which makes the mean a poor estimate of the representative physical property for the rocks. There is often scattering across several orders of magnitude. The distributions of magnetic susceptibility tend to be long tailed, and skewed towards low values.

These wireline data can be compared to hand specimen data compiled by the Council for Geoscience (CGS) as well as a study by Cawthorn and Spies (2003), who developed a linear relationship between plagioclase content (with Anorthite content of 80% or An_{80}) and rock density, to an accuracy of 2.9 % plagioclase. This tool can be used in rocks where plagioclase and pyroxene are the dominant minerals. Since percentage plagioclase content is not known in the data at hand, theoretical values were used from Seabrook (2005) for anorthosite, norite and gabbronorite which are based on chemical analyses from whole rock chemistry. These values are shown in the Table 3.5. The mineral propositions have been estimated.

Table 3.5 Proportions of plagioclase and orthopyroxene in anorthosite, norite, gabbronorite and feldspathic pyroxenite with %MgO and and Al_2O_3. Opx and cpx are orthopyroxene and clinopyroxene respectively.

Lithology	**% Plagioclase**	**%Orthopyroxene**	**%MgO**	**%Al_2O_3**
Anorthosite	90-100	0-10	<4	>27
Norite (including leuconorite and melanorite)	30-80	20-70	2.5-20	10-27
Gabbronorite	55-75	25-45 (opx and cpx)	6-10	16-24
Feldspathic pyroxenite	10-30	70-100	>20	3-10
Gabbro (including leucogabbro and melagabbro)	35-65	35-65 (cpx)	-	-

Values for plagioclase and %Al_2O_3 can then be compared to the relationship established by Cawthorn and Spies (2003) to calculate values for density, shown in Figure 3.11.

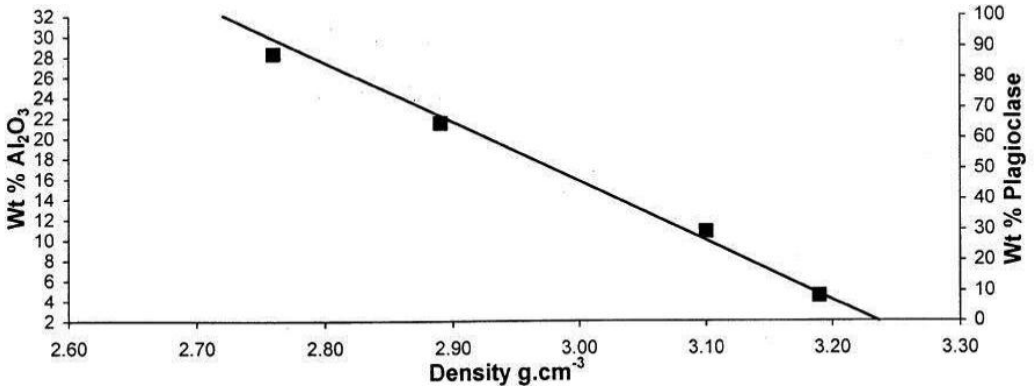

Figure 3.11 Relationship between %Al_2O_3 and % plagioclase and rock density established by Cawthorn and Spies (2003).

The range of density values for this project, those calculated from Cawthorn and Spies (2003) as well as the compilation from CGS are shown in Figure 3.12. The wireline data show large variations in each of the lithologies, followed by the CGS data. Values calculated using Cawthorn and Spies' (2003) method show a much narrower range in density. The large scatter in the wireline log data may be due to misidentification of lithologies and alterations since these measurements are made in situ. Also, the wireline data are sampled more closely and more likely to reflect heterogeneity caused by alteration as opposed to usually pristine hand samples.

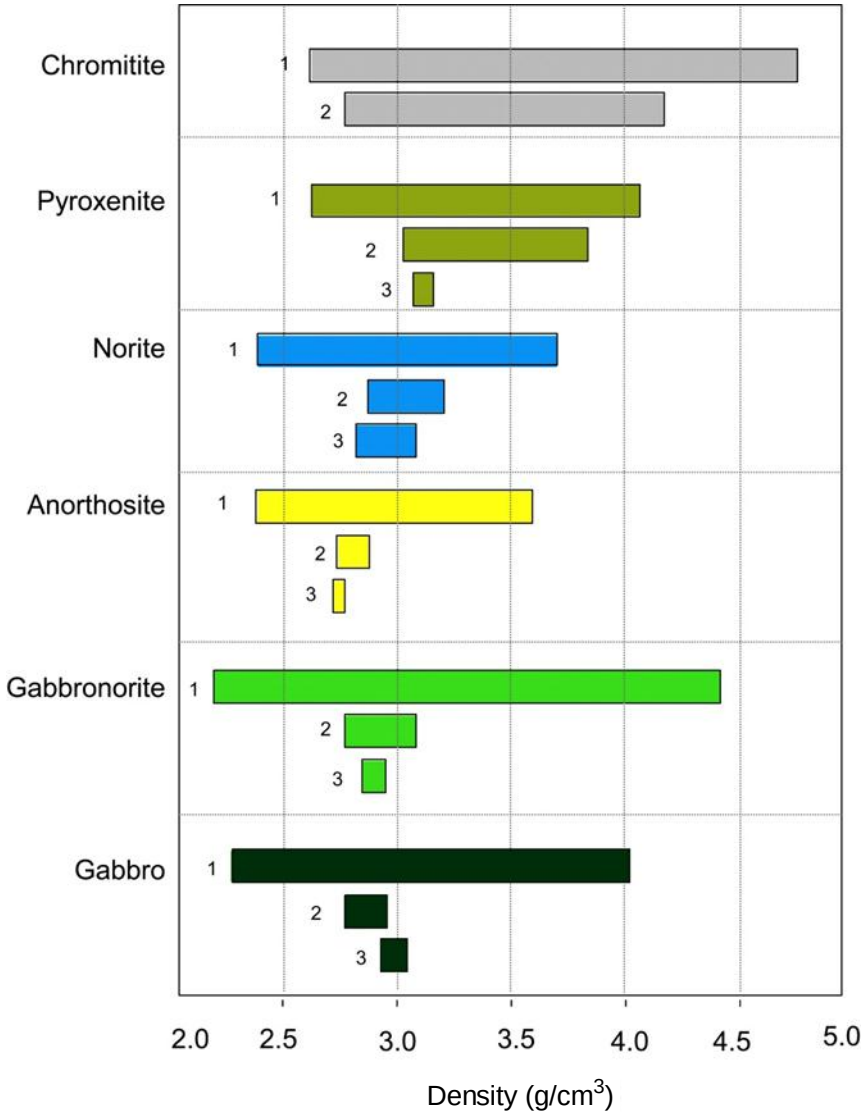

Figure 3.12 Ranges for rock densities obtained from borehole data acquired for this project (1), the compilation of physical properties from the CGS (2) and those calculated using the method by Cawthorn and Spies (2003) (3).

3.3 Cross-Correlation Plots

Scatter plots have been created for several boreholes to study the relationships between the density and magnetic susceptibilities for each of these lithologies. The extent of correlation is descried below, which is only possible in boreholes in which both of the density and magnetic susceptibility have been deemed "usable" (see Chapter 2.6). A semi-log scale is used where appropriate; in order to better display the magnetic susceptibility data. The scatter plots do not include rocks which have intruded into the BC rocks, i.e. pegmatoid, lamproite and dolerite.

3.3.1 The Western Limb of the BC

Styldrift- SO2

The scatter plot for lithologies for borehole SO2 are shown in Figure 3.13.

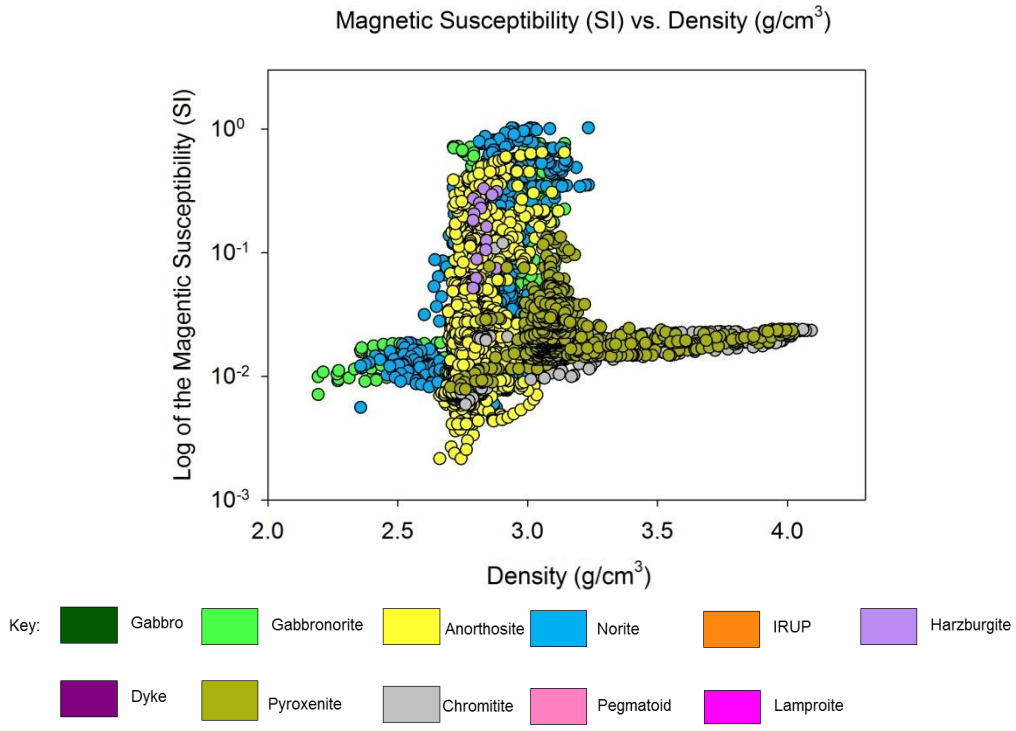

Figure 3.13 Scatter plot of magnetic susceptibility (log scale) vs. density for the borehole SO2.

The general trend is a large variability in magnetic susceptibility across several orders of magnitude. The physical properties for anorthosite, norite and gabbronorite have similar ranges which makes it difficult to discriminate the lithologies based on the physical property measurements. The densities generally fall into the ranges of 2.5-3.0 g/cm^3, and

magnetic susceptibilities in 10^{-3}-1 SI. The harzburgites have a surprisingly lower than expected magnetic susceptibility and density. However these data are from a thin layer which compromises the accuracy of the physical property measurements. Noteworthy are the chromitite data which have densities of 2.5-4.2 g/cm^3. The lower end of the densities can be explained by the thinness of these layers. The magnetic susceptibilities show an average magnetic susceptibility of 10^{-2} SI. The pyroxenite data have densities which predominantly lie between 3.0 g/cm^3 and 4.0 g/cm^3, and susceptibilities of 10^{-2}-10^{-1} SI.

RPM- KLG52

The densities of gabbronorite, norite and anorthosite in KLG52 lie predominantly between 2.6 g/cm^3 and 3.4 g/cm^3 (Figure 3.14).

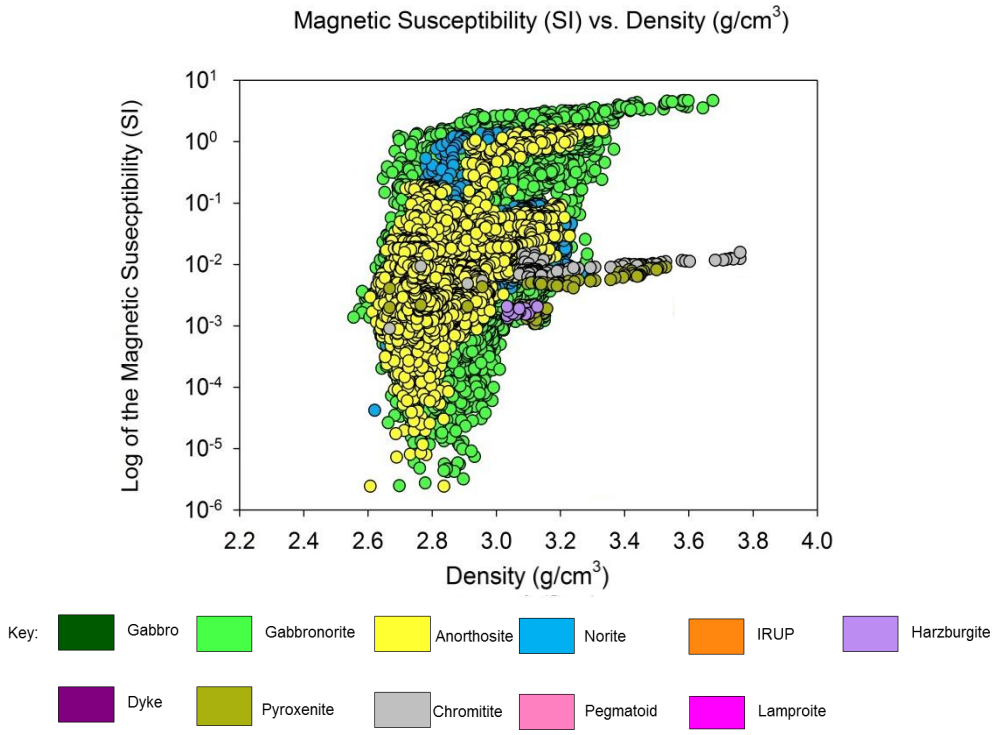

Figure 3.14 Scatter plot of magnetic susceptibility (log scale) vs. density for the borehole KLG52.

The magnetic susceptibilities of these lithologies span more than seven orders of magnitude. The densities for harzburgite are fairly constant, lying between 3.0 g/cm^3 and 3.2 g/cm^3, and magnetic susceptibility of approximately 10^{-3} SI. The chromitite and pyroxenite have similar physical properties with a larger scatter in density from 2.6 g/cm^3 to 3.0 g/cm^3 and an average magnetic susceptibility of close to 10^{-2} SI.

3.3.2 The Eastern Limb of the BC

Booysendaal- BY63

The anorthosite, norite and gabbronorite are well constrained, predominantly falling in ranges 2.45-2.9 g/cm^3 in density and 10^{-5} to 10^{-2} SI in magnetic susceptibility in Figure 3.15.

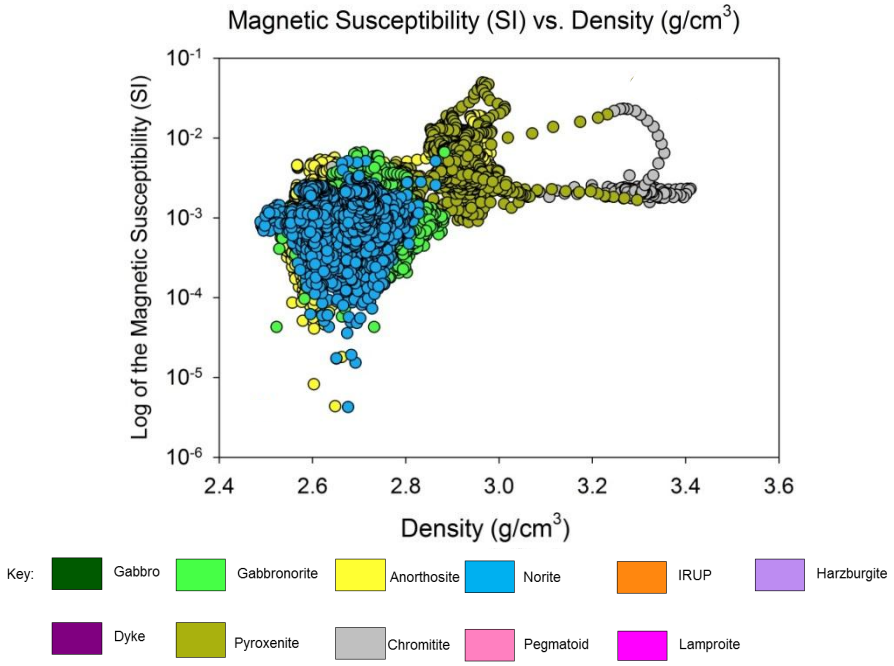

Figure 3.15 Scatter plot of magnetic susceptibility (log scale) vs. density for the borehole BY63.

The pyroxenites show higher densities of over 2.90 g/cm^3 as well as higher magnetic susceptibilities >10^{-3} SI. The chromitites show much more scatter in density than the other lithologies, but little scatter in magnetic susceptibility. The densities are still underestimated however, and do not reach expected values. This borehole shows relatively good clustering of pyroxenites and chromitites.

Booysendaal- BY60

The lithologies for BY60 shown in Figure 3.16 spans a smaller range in density and magnetic susceptibility than observed previously, with strong clustering.

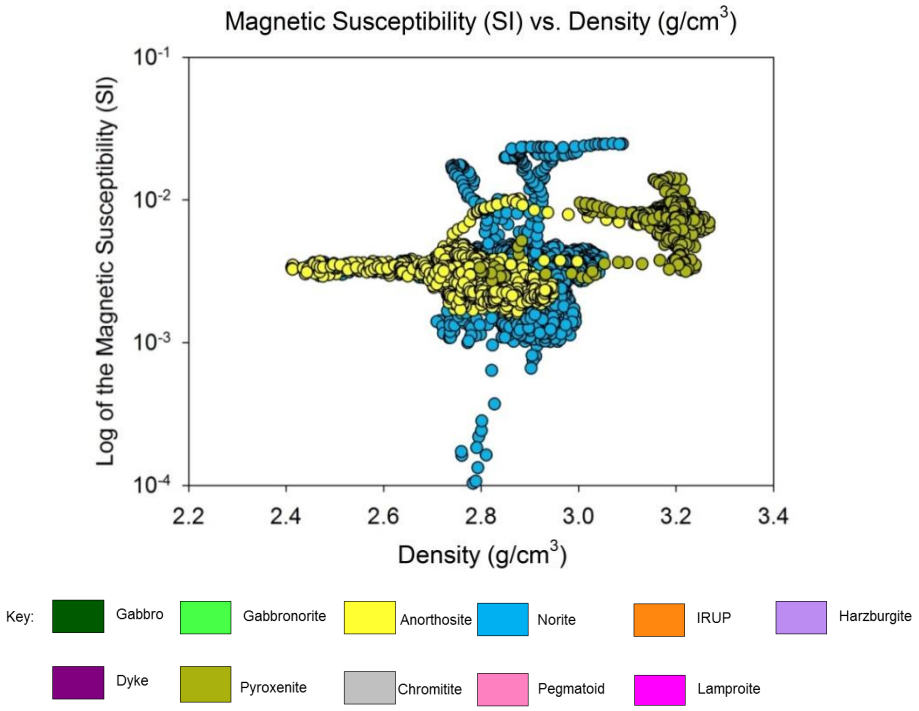

Figure 3.16 Scatter plot of magnetic susceptibility (log scale) vs. density for the borehole BY60.

The variation in magnetic susceptibility is only two orders of magnitude, as opposed to the 4-7 observed previously. The anorthosite only varies by one order of magnitude in magnetic susceptibility and has considerably less scatter. The density range is also slightly more confined than seen previously. The physical properties in the anorthosite and norite lie in the same range as seen previously, although the norites have more data points in the higher density ranges. These lithologies lie between 2.4 g/cm^3 and 3 g/cm^3. The pyroxenites have a well-defined range, and are easily distinguishable from the other lithologies based on their physical properties. These generally have a density of 3.0-3.3 g/cm^3, and fall into magnetic susceptibility range of between 10^{-3} and 10^{-2} SI, which is the same as those seen previously in KLG52.

Der Brochen- DB136

This borehole, like DB135, shows some scatter but also clustering of the various lithologies according to physical property in Figure 3.17.

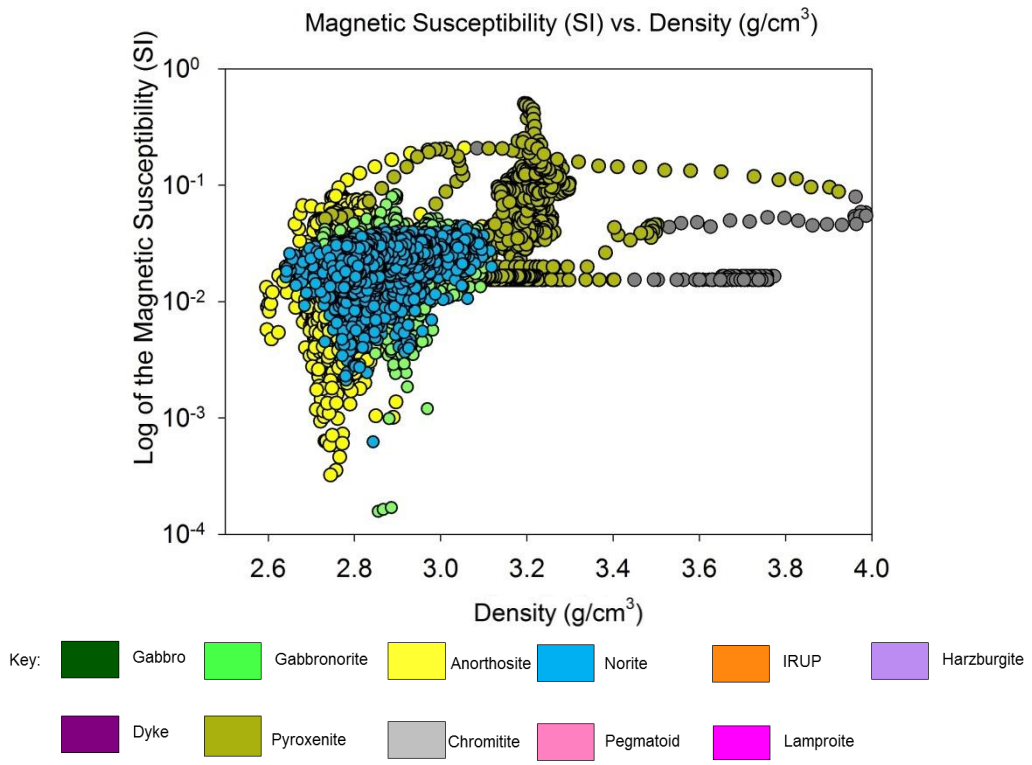

Figure 3.17 Scatter plot of magnetic susceptibility (log scale) vs. density for the borehole DB136.

The anorthosites show variable magnetic susceptibility, across several orders of magnitude. The density however is well constrained and falls between 2.5-2.8 g/cm^3. Gabbronorite can be distinguished from anorthosite to some extent, even though there is overlap. However it almost completely overlaps with norites, making them difficult to differentiate. The norites and gabbronorites show higher densities up to close to 3.2 g/cm^3, with similar magnetic susceptibilities of 10^{-3}-10^{-1} SI. The pyroxenite data have well constrained densities between 3.0-3.4 g/cm^3, although some scattering is present. The chromitites show large variability in density, but this is probably influenced by layer thickness.

Der Brochen- DB135

The pyroxenite and chromitite form distinct clusters making them differentiable based on their physical properties (Figure 3.18).

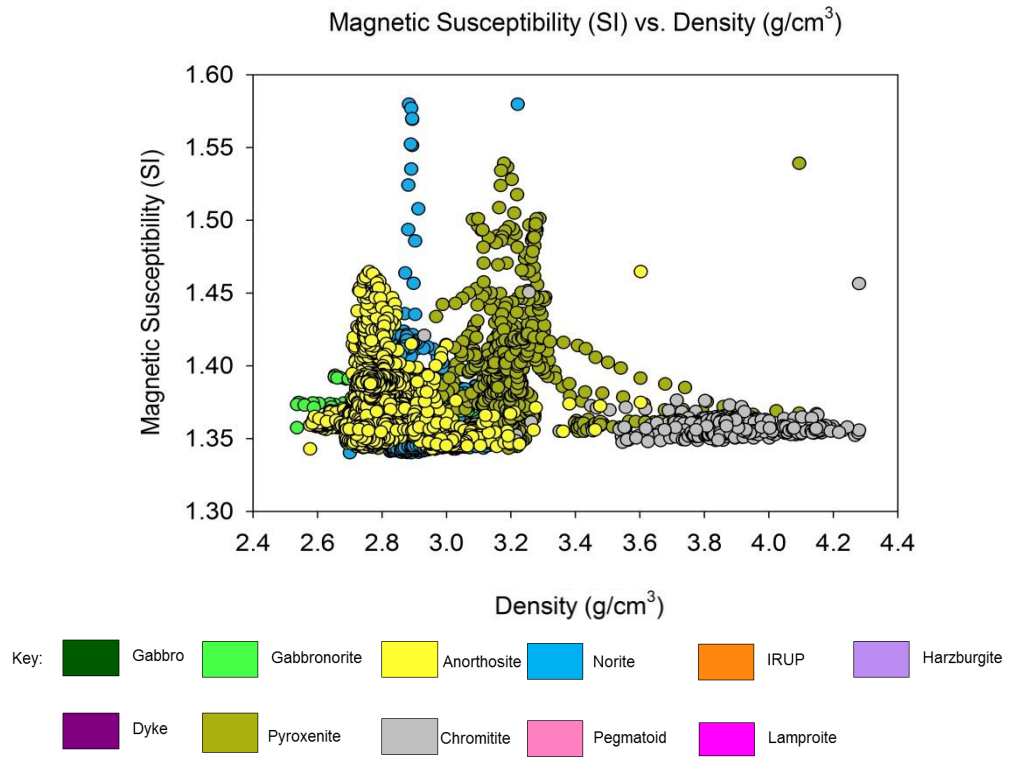

Figure 3.18 Scatter plot of magnetic susceptibility vs. density for the borehole DB135.

The pyroxenites fall within a narrow range in density of 3.0-3.4 g/cm^3 and magnetic susceptibility between 1.35 and 1.55 SI. Chromitites span values of 3.4-4.4 g/cm^3 in density and an almost constant 1.35 SI in magnetic susceptibility. The anorthosites, norite and gabbronorite show an overlap in physical properties, with densities which predominantly fall between 2.6-3.0 g/cm^3 and magnetic susceptibilities of 1.35-1.45 SI.

Der Brochen- RM123

There is considerable scatter in the physical properties of chromitites and pyroxenites, and not the distinct clustering observed before in Figure 3.18. Chromitites and pyroxenites show similar density ranges from 2.8 g/cm^3 to 4 g/cm^3. The magnetic susceptibility for these lithologies is approximately constant, with values of 10^{-4} SI on average, which is two orders of magnitudes smaller than observed previously in DB136 for example. The anorthosite and norite mostly have densities of 2.7-3.0 g/cm^3, and magnetic susceptibilities in the range of 10^{-6}-10^{-4} SI, although there are some data points of norite with susceptibilities down to 10^{-7} SI.

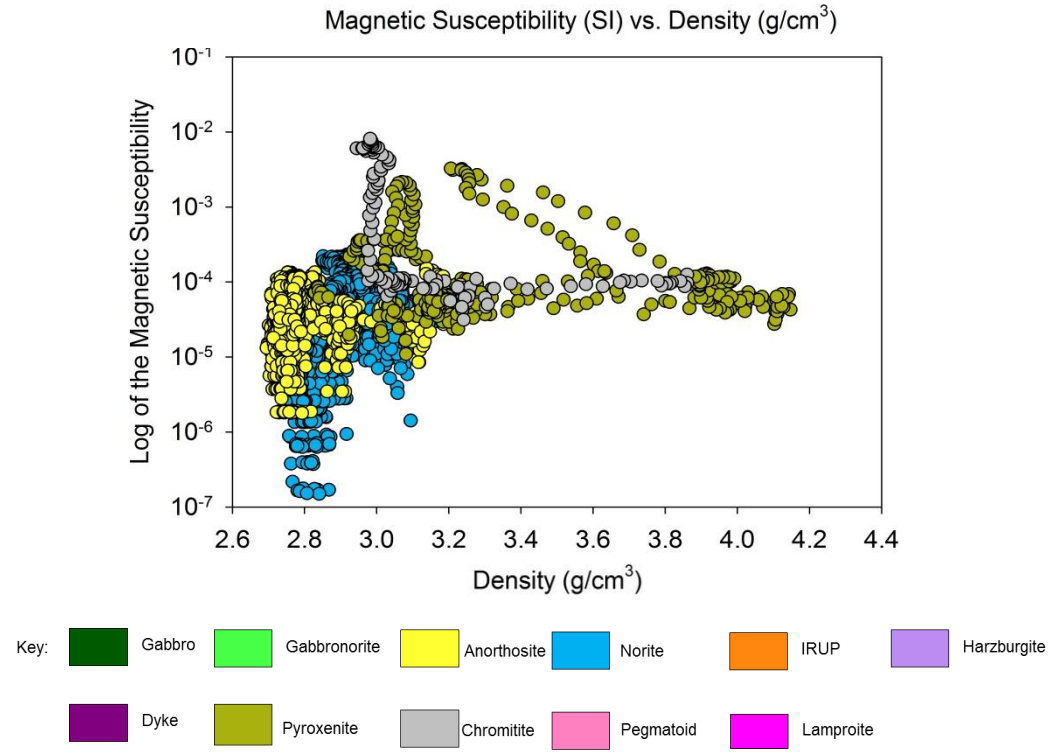

Figure 3.19 Scatter plot of magnetic susceptibility (log scale) vs. density for the borehole RM123.

3.3.3 Summary

Variations in density and magnetic susceptibility in lithologies has been attributed by Ashwal et al. (2005) and Fullagar (1999) to changes in modal abundance i.e. variations in the percentage of pyroxenite and plagioclase. The variability in the magnetic susceptibility is probably due to the amount of accessory magnetite. While some boreholes show data with variations up to 7 orders of magnitude (e.g. KLG52), some data show only a single order of magnitude (e.g. DB135). The density data however, generally show small variations within a lithology, and when there is scatter, it is in the thinner chromitite and pyroxenite layers. This is the influence of layer thickness as outlined in Chapter 2.6 has also been observed. Pyroxenites and chromitites produce spurious data points which do not reflect the actual physical properties accurately. This effect is easily observed in scatter plots, as seen in borehole RM123 for example. Another important observation has been the physical property contrasts across lithologies. It is not always possible to discern the various lithologies, especially norites and gabbronorites, whose ranges in physical properties have been shown to consistently overlap. Pyroxenite and chromitites, and to a lesser extent anorthosites, appear to be more constrained in terms of physical properties compared to the other lithologies, and are easily distinguishable from the other lithologies based on clustering. The extent to which lithologies can be

distinguished solely from their physical properties is investigated in the next chapter using cluster analysis.

CHAPTER 4: CLUSTER ANALYSIS

Cluster analysis is a method used to recognize groups or patterns in large datasets (Peña et al., 1999). It describes various techniques used for assigning observations to groups in datasets, which make them easier to study. Scatter plots shown in Chapter 3 for various boreholes have revealed some clusters in the data which often correlate with lithology. This suggests that some lithology types are distinguishable based on their densities and magnetic susceptibilities although overlapping between lithologies also occurs. Although not a major focus of this thesis, cluster analysis can be used as a step towards creating a tool that allows for the automatic detection of major changes in physical properties of rocks which may indicate changes in mineralogy or grading in the rock not easily visible in hand specimen. It can be used as a quality control measure for the lithology log. This can help highlight layers of interest which can be mistakenly misidentified or omitted during geological logging. The aim of carrying out this investigation is to therefore investigate the feasibility of accurately representing a lithology log from rock physical properties. There are numerous ways of classifying data e.g. expectation-maximization methods, principal component analysis, fuzzy clustering, neural network etc. The *k*-means was chosen as it is the most widely used and is computationally efficient and robust. The MATLAB code used to implement this is in APPENDIX A1.

4.1 *k*-Means Classification

One of the most popular used methods in cluster analysis is *k*-means classification (Bottou and Bengio, 1995; Peña et al., 1999; Kogan, 2007; El Agha and Ashour, 2012). This is an unsupervised clustering method in which no a priori information such as a class label is given to the data and they are studied in an exploratory fashion (Lange et al., 2005; Jain, 2010; Mythili and Madhiya, 2014). This method was apparently derived by several different scientists in varying fields, with the earliest work in the literature by Steinhaus (1956). Since its invention 50 years ago there have been over one thousand clustering algorithms proposed. However this method of classification still remains the most widely used due to its flexibility, easy implementation and proven experimental success over the years (Jain, 2010).

The *k*-means classification technique works by partitioning data points into pre-existing clusters in a data set. This technique falls under the clustering methods collectively known as “optimization-partitioning techniques”, in which an optimized solution is

reached when a particular clustering criterion is met. These type of clustering algorithms generally consider each data point in a dataset to be a cluster centre, and then merges it with neighbouring data points to form bigger and bigger clusters iteratively (El Agha and Ashour, 2012). This method has found applications in data mining, data compression, vector quantification as well as pattern recognition and classification (Alsabti et al., 1997; Ackermann et al., 2010). It is also used to help initialize computationally costly algorithms such as Gaussian mixture algorithms amongst others (Bottou and Bengio, 1995; Peña et al., 1999). The classification of data points is based on their similarity, which is measured as their relative distances from the cluster mean (El Agha and Ashour, 2012). The cluster means are representative reference points for each cluster, also referred to as centroids. The algorithm achieves this by iteratively trying to minimize the sum of the distances between the centroid of a given cluster and the neighbouring points.

4.1.1 Distance Metrics

There are several distance measures which can be used for a classification scheme. All distance (D) metrics in R^p dimensional space satisfy the following, for observations x, y and z (Seber, 1984):

- $D(x, y) \geq 0$, for all ($\forall$) x and y
- $D(x, y) = 0$, when $x = y$
- $D(x, y) = D(y, x)$, $\forall$ x and y
- $D(x, z) \geq D(x, y) + D(y, z)$, $\forall$ x, y and z

The most popular are the Minkowski and the cosine distances which are discussed below. A complete list of distance and correlation measures is given by Cormack (1971). The Minkowski distance metric or L_p norm is given by Jain (2010),

$$D(x, y) = \left\{ \sum_{j=1}^{p} |x - y|^p \right\}^{\frac{1}{p}}. \quad 4.1$$

The L_2 norm or Euclidean is the Minkowski distance for $p = 2$. The L_1 norm or city block is the Minkowski distance for for $p = 1$ (Cormack, 1971). The cosine distance is given by Liu et al. (2012),

$$D(x,y) = \sum_{j=1}^{p} (1 - \cos(x,y)) \,. \qquad 4.2$$

Analysing synthetic data with these three metrics has shown that the L_2 and L_1 norm give similar results while the cosine distance is unsuitable. See APPENDIX A2 for comparisons. The metric that was chosen for data analysis is based on the L_2 norm which is implemented in MATLAB using the squared Euclidean distance, also referred to as the error function (Faber, 1994) or the square-error criterion (Peña et al., 1999). Minimizing this in a cluster minimizes the spread of data points and improves the quality of a classification scheme. The error function of a cluster (E_i), and is given by (Faber, 1994),

$$E_i = \sum_{i=1}^{k} \sum_{j=1}^{n_i} \left| x_{ij} - u_i \right|^2 \qquad 4.3$$

where x_{ij} is the *j*th data point in cluster *i*, n_i is the number of data points in any given cluster *i*, *k* is the number of centroids chosen, and u_i is the centroid of the *i*th cluster. The sum of errors E_i is minimized with each iteration of the *k*-means algorithm, and the optimal solution to the classification is reached when E_i for all clusters reaches a minimum. The input data set for a *k*-means classification can be multi-dimensional, where each data point represents several measured quantities or components. The corresponding centroids can therefore also then have several components as R^p dimensional space is specified by the number of data sets used. This means that the *k*-means analysis of magnetic susceptibility and density defines a two-dimensional real space R^2.

4.1.2 Convergence

With each iteration of the classification, the reference points to each cluster are moved in order to converge to a solution where the error function is minimized. This occurs in two steps:

- The initial step is to partition the data points into *k* initial clusters. The choice of these initial reference points is chosen at random (El Agha and Ashour, 2012) and data points are then assigned to these clusters based on the initial classification (Faber, 1994). A data point x_{ij} is assigned to the *i*th cluster (C_i), with centroid u_i, if it is closest to it in space (Faber, 1994). The

mathematical condition for this is adapted from Alsabti et al. (1997) and is given by

$$C_i = \{x_{ij}: |x_{ij} - u_i| \leq |x_{ij} - u_i'| \; \forall \; 1 \leq i \leq k\}. \quad 4.4$$

C_i is therefore the set of all points x_{ij}, whose distance from the centroid u_i is smaller than the distance between any other centroid u_i' belonging to another cluster C_i'. This is known as the assignment step.

- Once the initial clusters have been calculated, the mean of each of the clusters are calculated using Alsabti et al. (1997),

$$u_i' = \frac{1}{|C_i'|} \sum_{x_{ij} \epsilon C_i'} x_{ij} \, . \quad 4.5$$

The initial reference points in the assignment step of the algorithm for each of the clusters are then moved to new positions, which are the positions of the mean. This is the update step. The error function is then calculated to determine the spread of the points in each cluster.

Convergence is reached if there is no change in cluster means anymore, i.e. when the error function is cannot be minimized any further (Peña et al., 1999). The number of iterations required for convergence is said to be in the order of hundreds or thousands depending on the size of the dataset, the number of clusters, and the distribution of the dataset (Alsabti et al., 1997). Bad assignment of initial reference points can be overcome since the algorithm reaches an optimal solution iteratively. This may not always to be case however, and convergence to local minima cannot be fully avoided in all cases (El Agha and Ashour, 2012). To mitigate this, each classification scheme was computed 100 times using different initial random centroids and the partitioning which produced the lowest E_i was selected as the final result and sub-optimal solutions were discarded. More often than not, the various classifications showed similar convergence properties, which is an indication of the robustness of this algorithm.

4.1.3 Choosing "*k*"

Choosing the number of partitions is difficult when clusters are not obvious and there are no perfect mathematical criteria for this. The number of clusters is not always well-defined in this project, since the data sets are large and not all clusters are easily visible by eye. Therefore several values for *k* were experimented with, where maximum value of *k* was taken to the number of unique lithologies in the borehole since these are the data used for comparison. The best partitions were chosen for further discussion.

4.1.4 Computational Time

The computational time of the *k*-means algorithm is proportional to the number of data points in a given data set (Alsabti et al., 1997; El Agha and Ashour, 2012). This algorithm is therefore relatively slow for very large datasets. Several authors have come up with variants of this algorithm which produce results which are comparable to the *k*-means algorithm but with a much faster computation time. Computation time for each iteration of the *k*-means algorithm has been summarized by Alsabti et al. (1997) as the following:

- The time required to perform the assignment step is $O(nmk)$, where O is the order.
- The time required to perform the update step is $O(nm)$.
- The time required for calculating the error function is $O(nm)$.

4.1.5 Synthetic Data

Synthetic datasets have been generated to illustrate how the classification occurs, first using simple circular clusters, and then cluster distributions similar to those in Chapter 3.3. In the following discussion, the term "cluster" is used to describe groups visible in the generated data, and "class" to describe the group in which they have been placed. Figure 4.1a shows three easily identifiable circular clusters. Figure 4.1b shows results obtained using *k*-means classification.

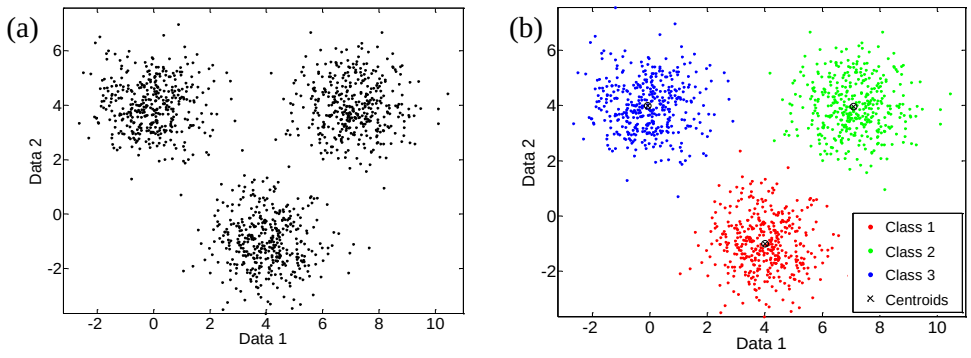

Figure 4.1 (a) Cross-plot between two arbitrary measurements, with three visible clusters. (b) *k*-Means classification has been able to allocate the clusters into three different groups. The centroids for each of them are indicated as crosses.

Convergence is reached after five iterations for these classes whose calculated centroids are indicated as black crosses. The three clusters have been allocated to different classes showing the success of the algorithm in differentiating the groups of data.

Chapter 3.3 showed cluster shapes, which may be elliptical, i.e. elongate in magnetic susceptibility or density. The latter is typically seen in gabbronorite, anorthosite and norite and the latter in the case of chromitites and pyroxenites. A combination of elliptical and circular clusters is used to test how robust the classification is. Figure 4.2a shows three clusters; two ellipsoidal and one circular.

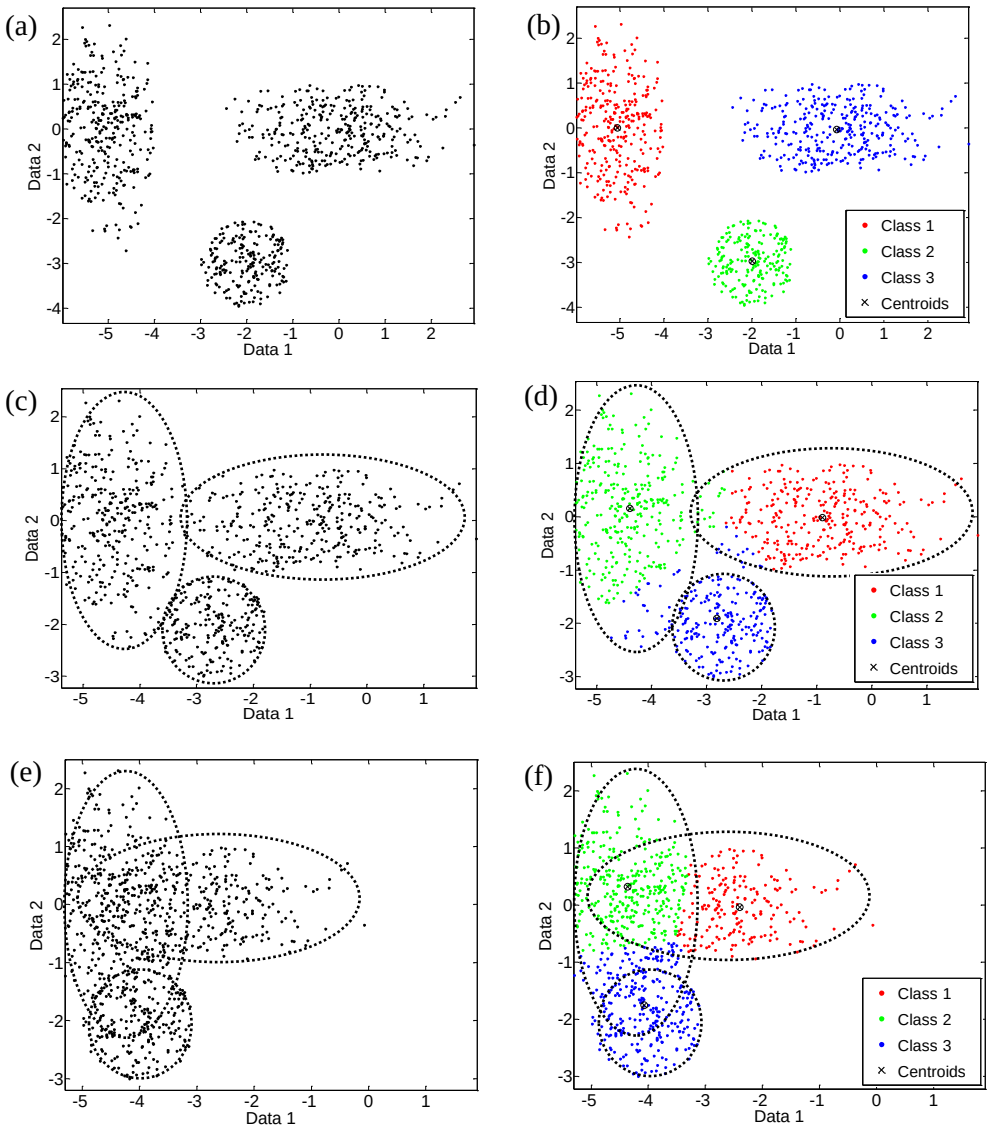

Figure 4.2 The series of images (a), (c) and (e) shows cross-plots between two arbitrary measurements, with three visible clusters. Two of the generated clusters are elliptical and the third is circular. These clusters have different distances of separation and the *k*-Means classification results for these are shown next to them, in (b), (d) and (f). The centroids for each of them are indicated as crosses. Details are in the text.

These are distinct and separated in space. Figure 4.2b shows that the various clusters have been classified into different groups. Figure 4.2c shows the same clusters, but separated by a smaller distance to test the classification resolving power when centroids are closer together. The results in Figure 4.2d show that the classification has been able to resolve the different groups, although not perfectly. In the last set of images Figure 4.2e and Figure 4.2f the clusters have now been superimposed and the clustering is no longer visible by eye as before. The classification is unable to resolve them successfully but the data are still grouped even with no visible clusters, which indicate that the algorithm

partitions the data irrespective of the existence or non-existence of clusters. It can therefore already be anticipated that the classification scheme may not be able to resolve clusters which overlap in physical properties (density and magnetic susceptibility). The physical property contrasts between anorthosite, norite, gabbronorite and gabbro are not only small but overlap, as demonstrated by Figure 3.12. Chromitites and pyroxenites can be distinguished from each other as well as the abovementioned lithologies based on physical properties, but these represent a small proportion of the lithology logs. These factors therefore lead to clusters which overlap and make it impossible for the algorithm to group the rocks accurately. However as the results will show, the algorithm performs reasonably well for boreholes in the Eastern Limb. These boreholes typically consist of norite, anorthosite, pyroxenite and chromitite only.

Since the physical property logs have depth information each of the classified data points also has a known depth. The results of the classification can therefore be plotted with depth and the distribution of classes with depth cane be compared with the actual distribution of lithologies with depth. An example is shown in Figure 4.3, which shows each of the allocated classes in Figure 4.2 plotted with depth.

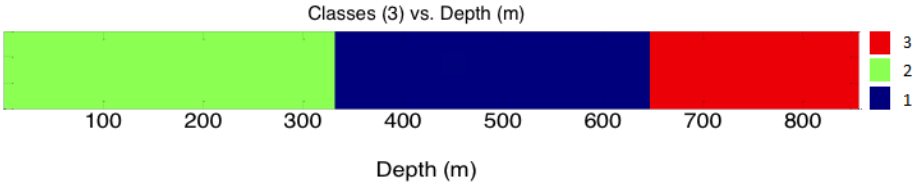

Figure 4.3 The various classes are shown with respect to depth indicated as different colours. This example uses the clusters identified in Figure 4.2b.

This could then be compared to a lithology log to assess the success of classification and to highlight discrepancies which may exist. The synthetic data are normally distributed which is ideal for classification (Fullagar, 1999). The histograms produced from real data in Chapter 3.2 have shown that density data may be bimodal, and the magnetic susceptibility may be long-tailed and flat. It is therefore not unreasonable to expect different distribution types in individual boreholes. However the classification done using only the density data did not considerably improve the classification. Both of the physical properties have therefore been used for classification in the results discussed below.

4.2 Results: *k*-Means Cluster Analysis

This section evaluates the accuracy with which lithological rocks of the BC can be represented using their rock physical properties. The results of the *k*-means classification are studied using scatter plots of clustered data in conjunction with the scatter plots for each of the boreholes. The scatter plots from Chapter 3.3 are presented again but with rocks which are intrusive in the BC included to allow for a better comparison with the lithology logs.

4.2.1 The Western Limb of the BC

Styldrift- SO2

Figure 4.4 shows the scatter plot for SO2 and the classification obtained for two, three and four-classes. Figure 4.4b shows that the first class groups the anorthosites, gabbronorites, and norites. The second class also contains data from these lithologies but includes chromitite. Figure 4.4c shows that the second class has grouped lithologies with magnetic susceptibilities >0.4 SI, which consists mostly of data points related to the dyke. The third class contains data from gabbronorite, norite, anorthosite and pegmatoid whose susceptibilities are <0.4 SI and densities <3.0 g/cm^3. The first class contains chromitite; however it is mixed with pyroxenite, anorthosite and norite. These data have densities >3.0 g/cm^3 and magnetic susceptibilities <0.4 SI. Figure 4.4d shows that the data previously classified in the third class in Figure 4.4c has been partitioned into two. The pyroxenite and chromitite data are grouped into the third class.

Figure 4.5 shows the lithology log and classification schemes for two, three and four classes and their distribution with depth. Figure 4.5b shows the results for two classes. The second class contains dyke stringers (e.g. 100 m) and thin chromitite layers (~640 m and 660 m). The first class contains all of the other lithologies. These lithologies grouped in this manner since there are large physical property contrasts between lithologies in the second and first classes. The three-class partitioning in Figure 4.5c does not show a considerable difference to Figure 4.5b but is almost completely able to isolate the chromitite layers, with the exception of the pegmatoid layer at 680 m and the thin pyroxenites at between 600 m and 650 m.

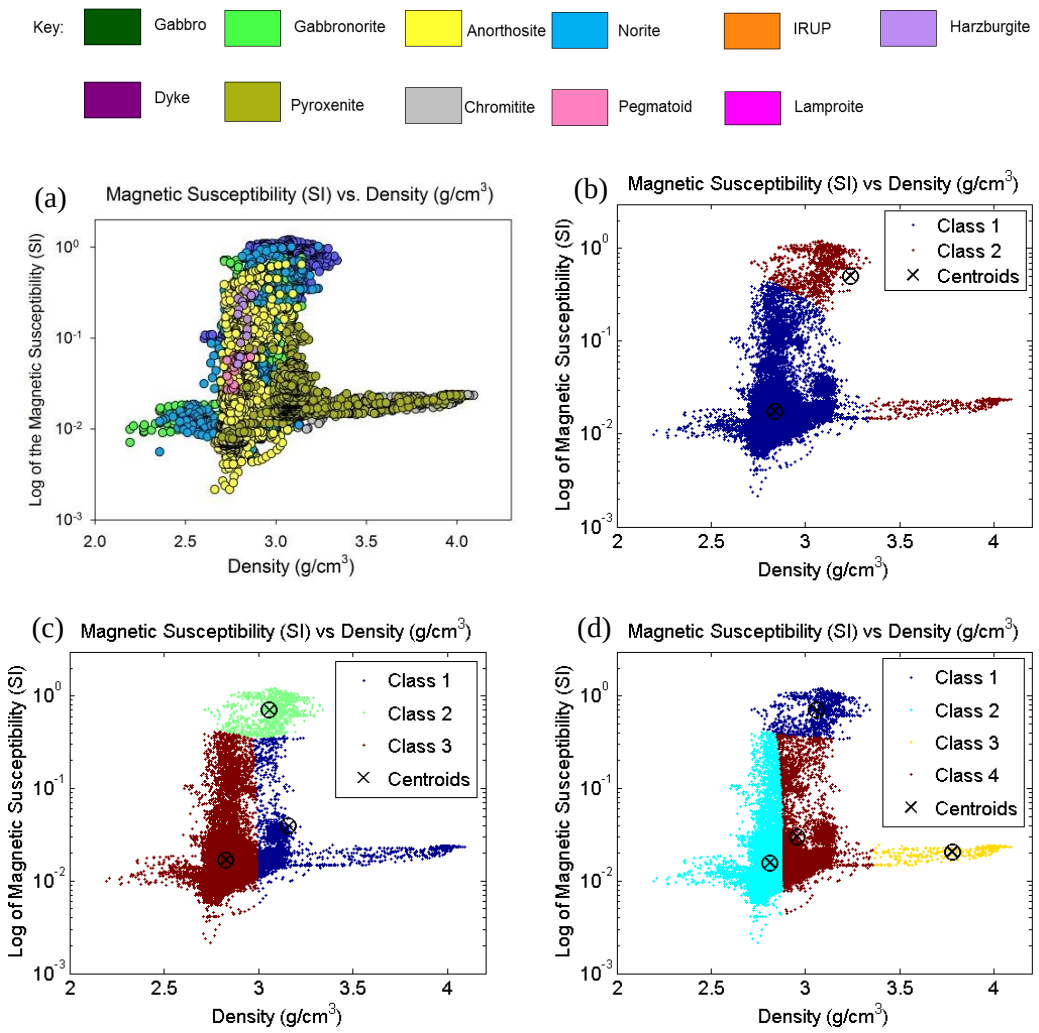

Figure 4.4 (a) Scatter plot of magnetic susceptibility (log scale) vs. density for the borehole SO2. Scatter plots of the *k*-Means classification for (b) two classes, (c) three classes and (d) four classes.

The four-class partitioning in Figure 4.5d does not improve the classification considerably. This scheme is not able to accurately reflect the lithology log but the chromitite in the third class are distinguished from the pegmatoid.

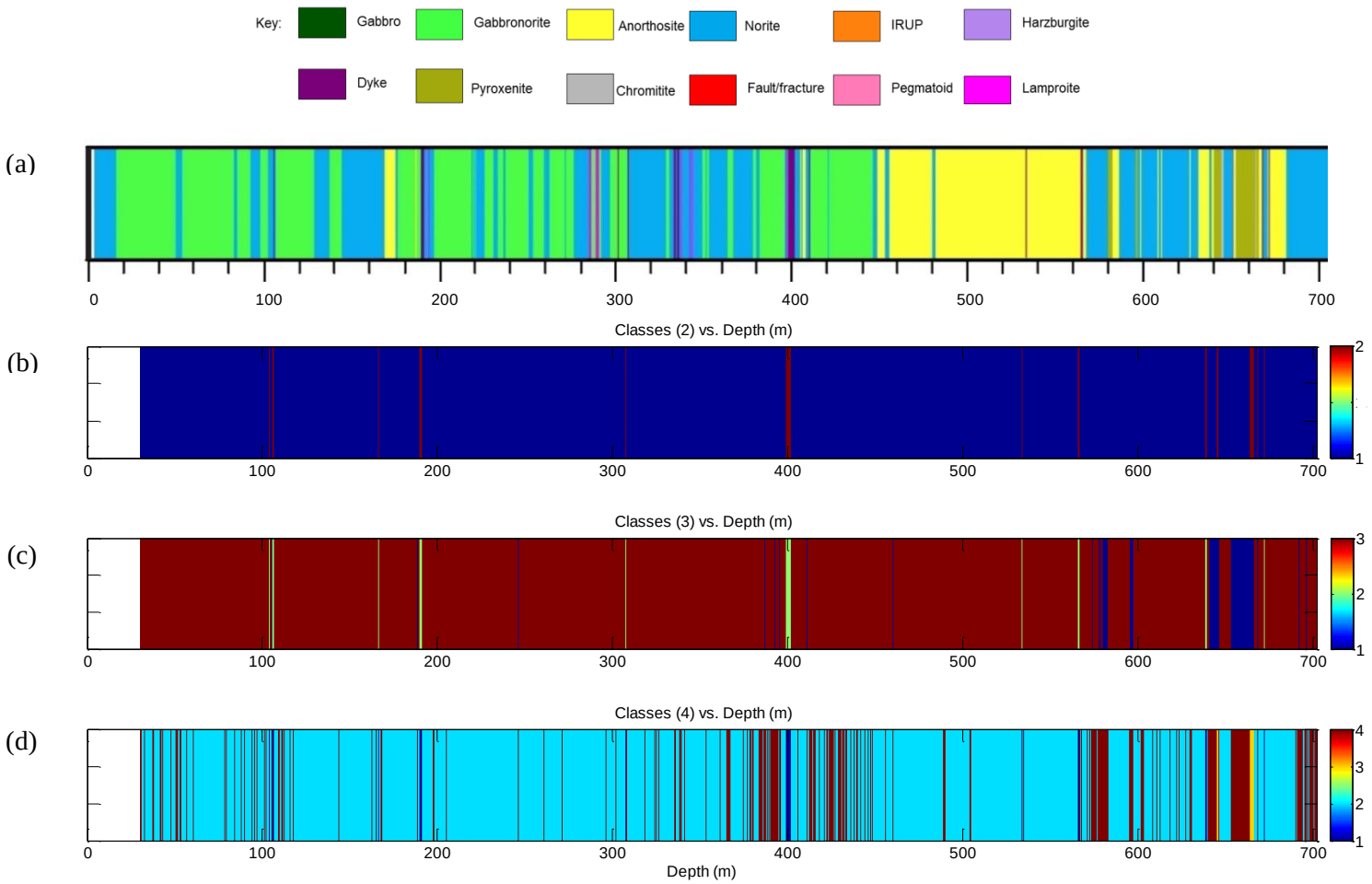

Figure 4.5 (a) Lithology log for borehole SO2. *k*-Means classification using density and magnetic susceptibility classification for (b) two, (c) three and (d) four classes.

RPM- KLG52

Figure 4.6 shows the scatter plot for KLG52 and the classification obtained for two, three and four classes.

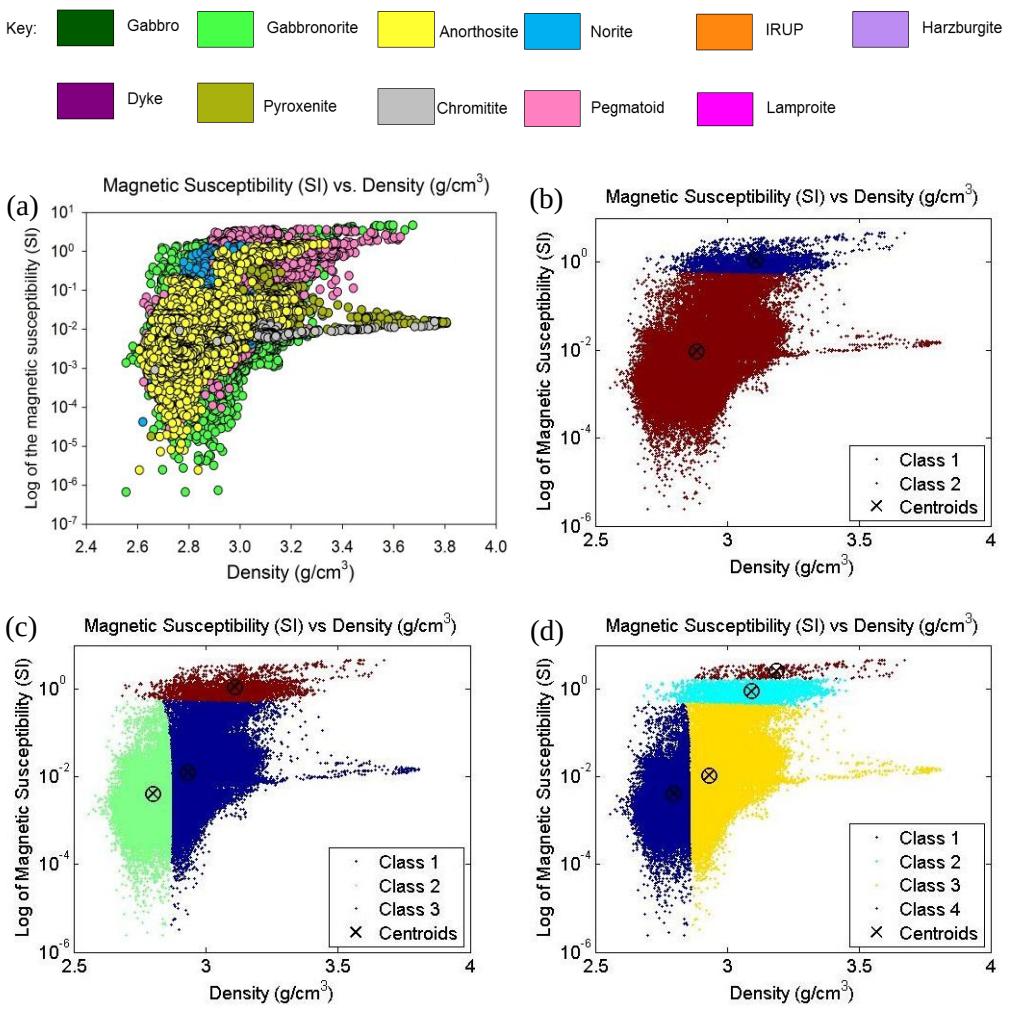

Figure 4.6 (a) Scatter plot of magnetic susceptibility (log scale) vs. density for the borehole KLG52. Scatter plots of the *k*-Means classification for (b) two classes, (c) three classes and (d) four classes.

The data in Figure 4.6a show that the physical properties for gabbronorite, anorthosite and norite overlap. The classification scheme for two classes in Figure 4.6b shows that the first class contains the least amount of data points, containing pegmatoid, gabbronorite and anorthosite. These data have densities larger than approximately 1 SI with densities of 2.6-3.7 g/cm^3. The rest of the data has been allocated to the second class, which consists predominantly of gabbronorite since this is the dominant lithology. Figure 4.6c shows that the abovementioned first class is the second class in this classification

scheme and remains unchanged. The rest of the data are partitioned into the second class with densities of 2.6-2.8 g/cm^3 and magnetic susceptibilities of 10^{-6}-1 SI. The rest of the data is placed in the first class. The data in the various classes contain a mixture of lithologies. The four-class partitioning scheme in Figure 4.6d shows that the third class in Figure 4.6c is partitioned into two, but does not show considerable changes otherwise.

Figure 4.7 shows the lithology log and classification schemes for two, three and four classes and their distribution with depth. Figure 4.7b shows that the classification separates some of the thin pegmatoid layers and part of the gabbronorites to form the second class, which constitutes about 2% of the borehole. The first class contains the rest of the lithologies, mixing gabbronorite, anorthosite, norite and the pegmatoid layers. Figure 4.7c shows the three-class partitioning. The pyroxenite layers at ~1840 m and 1860 m have been placed in the first class. The third class contains the least data, and consists mainly of pegmatoid stringers. A four-class partitioning is shown in Figure 4.7d, which shows that the classification is increasingly complicated and does not reflect the lithology log. The pyroxenite layers have not been isolated in the classifications discussed.

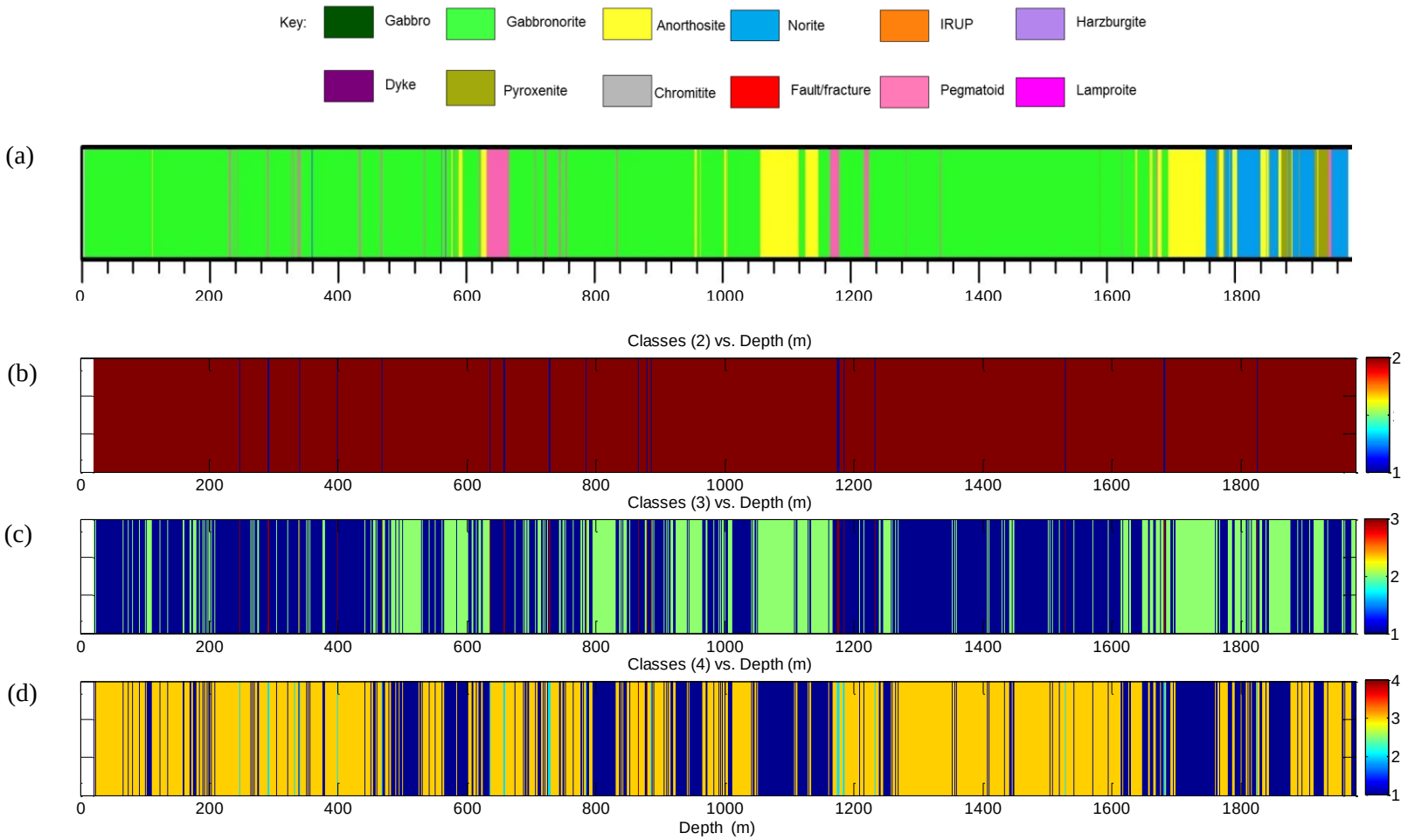

Figure 4.7 (a) Lithology log for borehole KLG52. *k*-Means classification using density and magnetic susceptibility for (b) two, (c) three and (d) four classes.

4.2.2 The Eastern Limb of the BC

Booysendaal- BY63

Figure 4.8 shows the scatter plot for BY63 and the classification obtained for two, three and four classes.

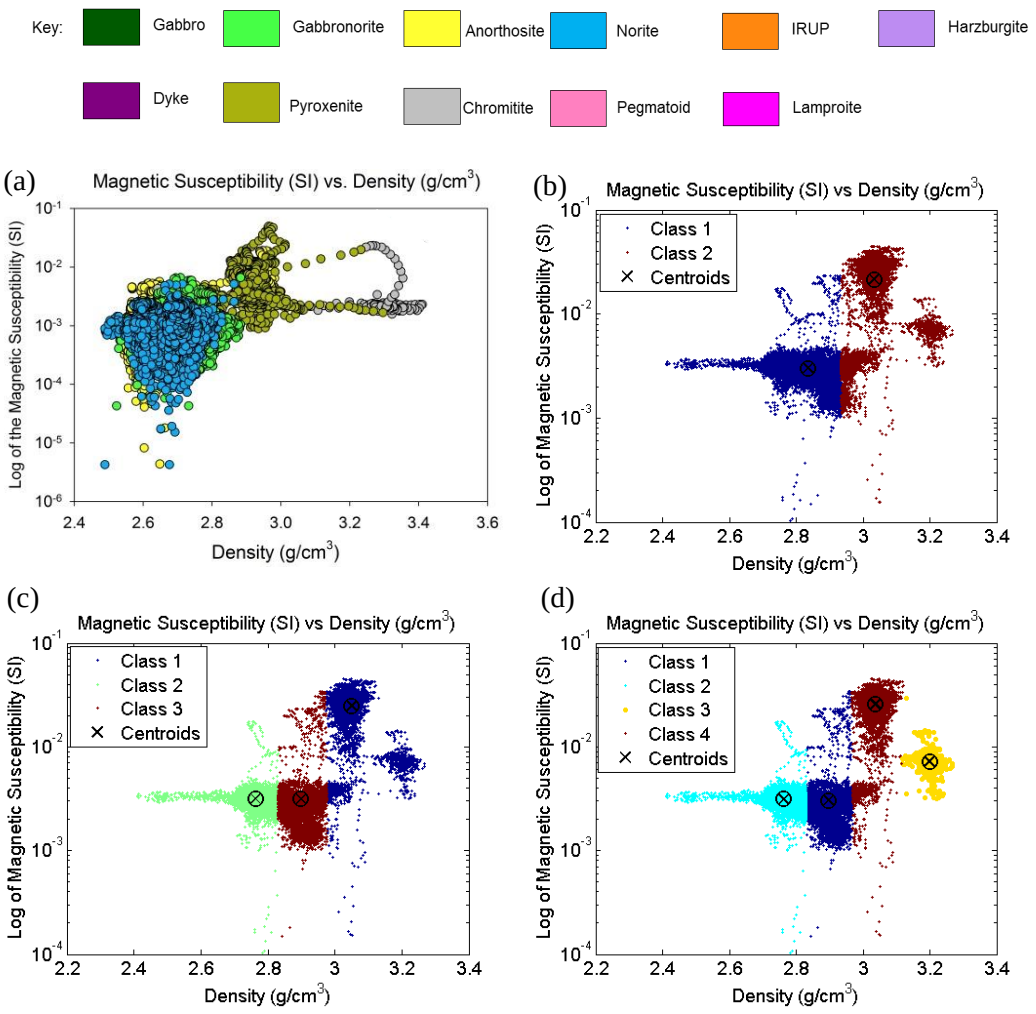

Figure 4.8 (a) Scatter plot of magnetic susceptibility (log scale) vs. density for the borehole BY63. Scatter plots of the *k*-Means classification for (b) two classes, (c) three classes and (d) four classes.

This boreholes shows visible clusters in Figure 4.8a of pyroxenite and chromitite, with overlap in the physical properties for anorthosite, anorthosite and gabbronorite. Figure 4.8b shows the classification scheme for two classes, with data points with densities >2.7 g/cm^3 being allocated to class one, and those with smaller densities in the second class. The first class consists mostly of gabbronorite and norite, with minor pyroxenite and chromitite. The second class contains norite and anorthosite. Figure 4.8c shows an

improved classification, with pyroxenite and anorthosite placed in the third class which better reflects the lithology log in Figure 4.8a. The first class contains anorthosite, norite and gabbronorite with densities <2.6 g/cm^3. Figure 4.8d shows that an increase to the number of partitions does not improve the classification considerably.

Figure 4.9 shows the lithology log and classification schemes for two, three and four classes and their distribution with depth. Figure 4.9a shows that this borehole contains thick units of gabbronorite until a depth of approximately 260 m, after which anorthosite and norite layers become more dominant. This is partly reflected in the two-class partitioning shown in Figure 4.9b, which shows that at depths shallower than 260 m, the first class is dominant and contains mostly gabbronorites. At shallower depths the second class is dominant and consists mostly of norite with minor anorthosite. The three-class scheme in Figure 4.9c does not show major differences to that observed in Figure 4.9b, but shows that the second class contains the anorthosite layer at ~340 m in Figure 4.9a, and the pyroxenite layer at a depth of 540 m. The only other pyroxenite layer which is at a depth of 310 m has been placed in the first class. The classification in Figure 4.9d is complex and does not accurately reflect the lithology in Figure 4.9a.

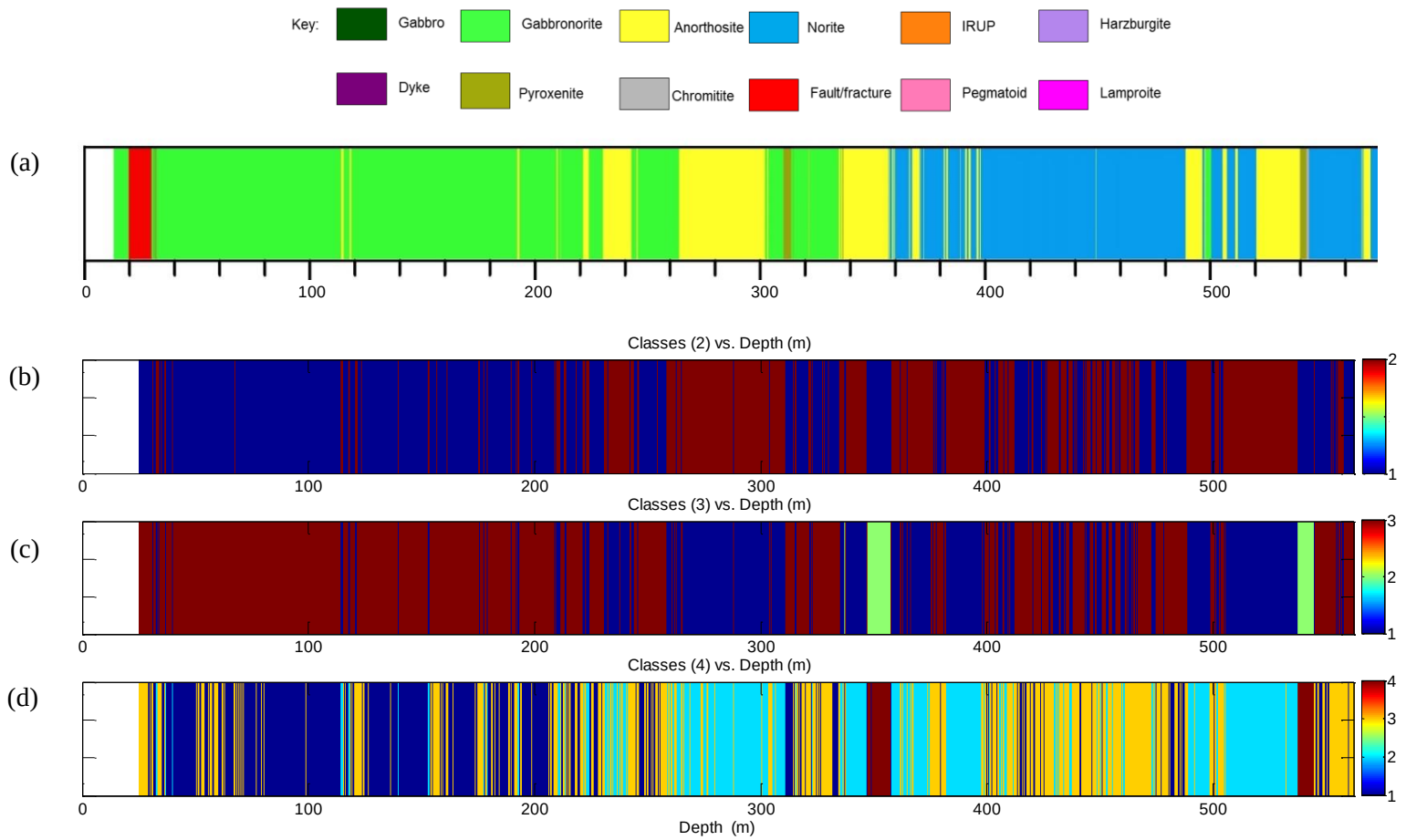

Figure 4.9 (a) Lithology log for borehole BY63. *k*-Means classification using density and magnetic susceptibility for (b) two, (c) three and (d) four classes.

Booysendaal- BY60

Figure 4.10 shows the scatter plot for BY60 and the classification obtained for two, three and four classes.

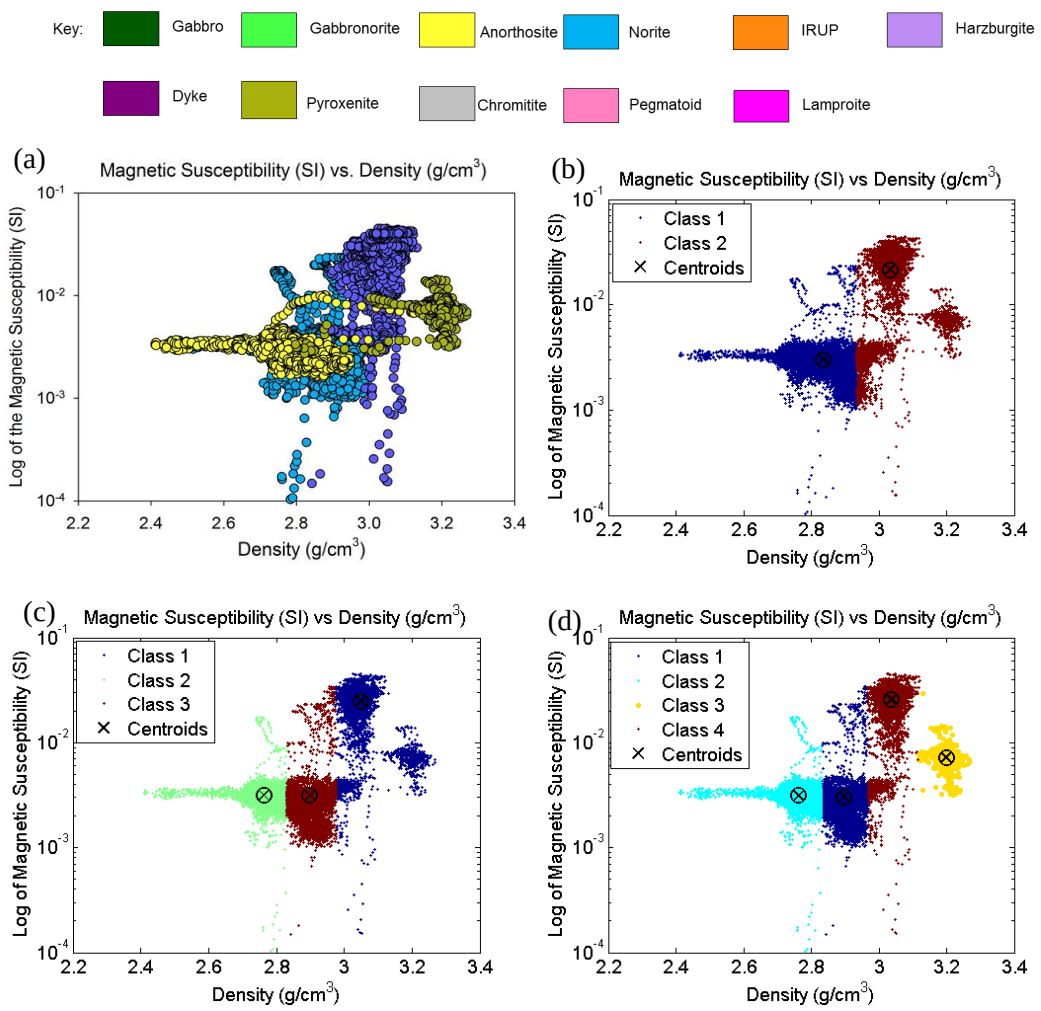

Figure 4.10 (a) Scatter plot of magnetic susceptibility (log scale) vs. density for the borehole BY60. Scatter plots of the *k*-Means classification for (b) two classes, (c) three classes and (d) four classes.

This borehole shows clear visible clusters in Figure 4.10a, although there is some overlap in norite and anorthosite, the dyke and pyroxenite layers are easily distinguishable. The two-class partitioning shown in Figure 4.10b shows that the first class contains anorthosite and norite data with densities <2.95 g/cm^3. The pyroxenite and dyke have been grouped into the second class and contain data points with have densities >2.95 g/cm^3. The pyroxenite and dyke are still grouped together in the three-class partitioning in Figure 4.10c, although this class now only contains densities that are larger than 3.0

g/cm^3 which increases the quality of the classification. The second class contains data less 2.8 g/cm^3 and has grouped anorthosite and norite. The third class has intermediate densities of 2.8-3.0 g/cm^3, and contains predominantly norite. The final classification in Figure 4.10d does not show major changes with respect to Figure 4.10c, but shows that the pyroxenite are completely isolated from the dykes.

Figure 4.11 shows the lithology log and classification schemes for two, three and four classes and their distribution with depth. BY60 has intersected a thick dyke towards the end of the borehole, and the results discussed below show the classification are able to separate the dyke from the rest of the lithologies. Figure 4.11b shows that the second class contains most of the dykes and to a lesser extent norite, as well as the pyroxenite layer at a depth of 75 m. The second class contains all of the other lithologies. The classification scheme in Figure 4.11c begins to reflect the lithology log, as a comparison with Figure 4.11a shows that the first class contains the dyke and pyroxenite layer, the second class is made up predominantly of norite and the third class contains anorthosite. The same is true for Figure 4.11d which shows complete isolation of the pyroxenite layer into the third class, thereby separating it from the dyke which is placed in the fourth class.

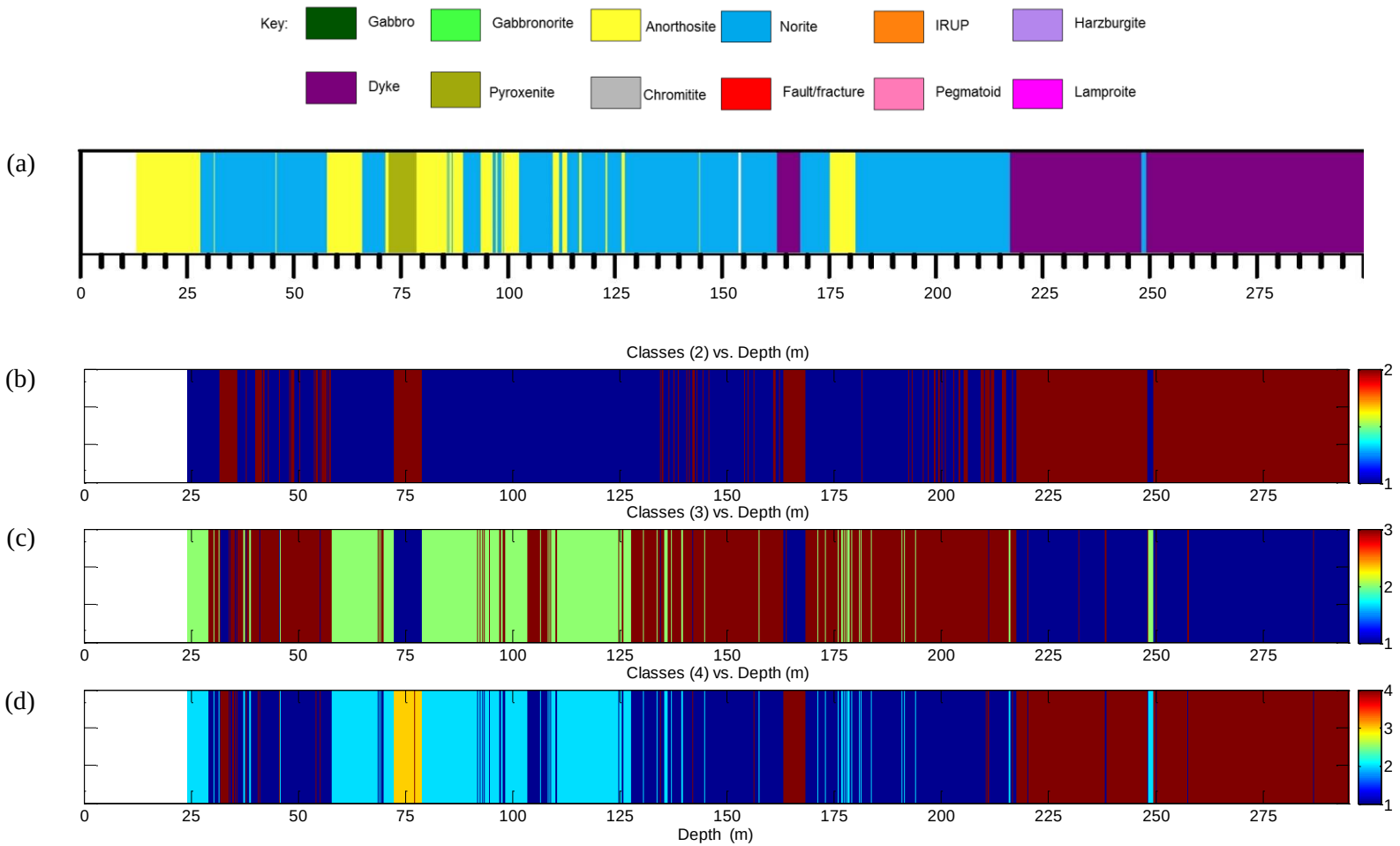

Figure 4.11 (a) Lithology log for borehole BY60. *k*-Means classification using density and magnetic susceptibility for (b) two, (c) three and (d) four classes.

Der Brochen DB136

Figure 4.12 shows the scatter plot for DB136 and the classification obtained for two, three and four classes.

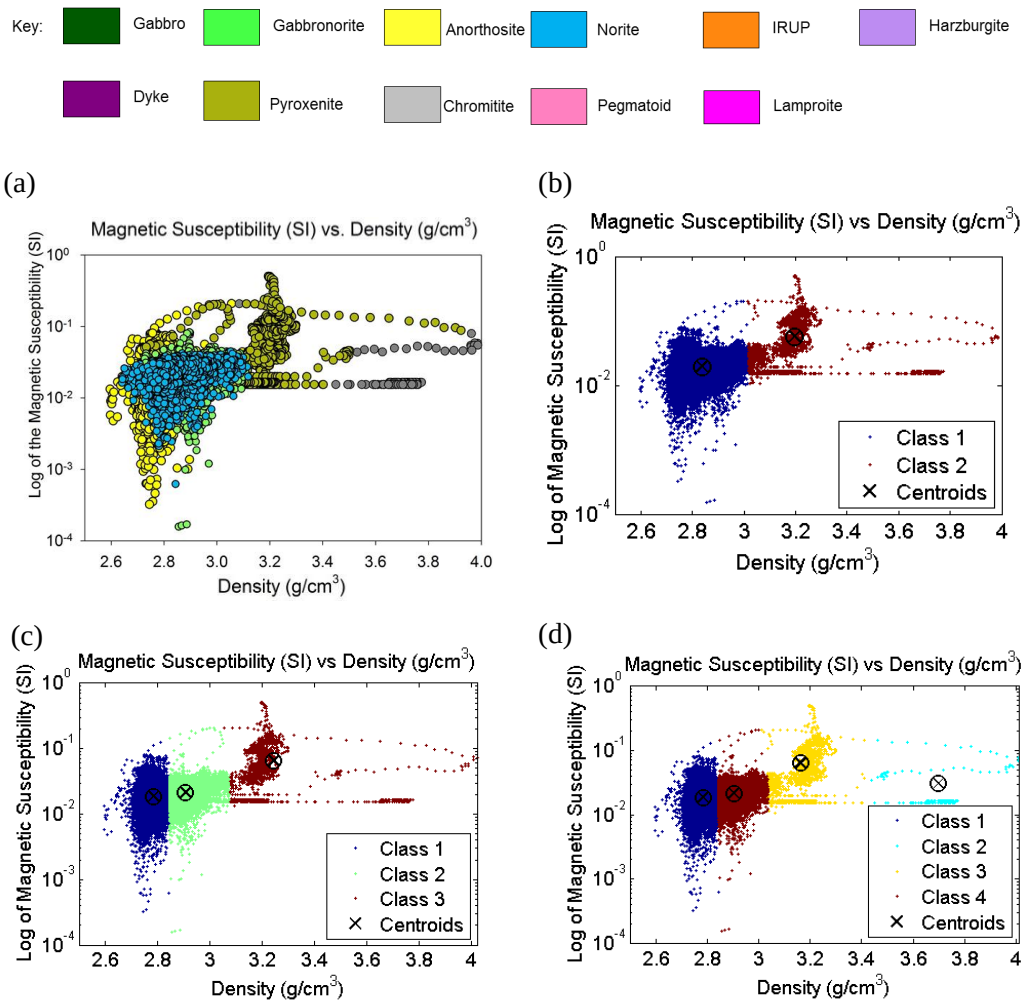

Figure 4.12 (a) Scatter plot of magnetic susceptibility (log scale) vs. density for the borehole DB136. Scatter plots of the *k*-Means classification for (b) two classes, (c) three classes and (d) four classes.

Figure 4.12a shows clustering according to lithologies, which is also evident in the classification schemes. Figure 4.12b shows that the pyroxenite and chromitite have been grouped into the second class, which contains all the data that have densities larger than 3.0 g/cm^3. The first class consists of gabbronorite, norite and anorthosite, all of which have densities below 3.0 g/cm^3. The three-class partitioning in Figure 4.12c shows that the pyroxenite and chromitite are grouped together into the third class, which has data points with densities larger than 3.05 g/cm^3. The first class consists mostly of anorthosite

with minor norite which have densities that are smaller than 2.8 g/cm^3. The second class groups norite and gabbro, which have densities of 2.8-3.0 g/cm^3. The scheme shown in Figure 4.12d does not show major differences to that in Figure 4.12c, but shows that the improvement in the classification of pyroxenite and chromitite. These data have been allocated to groups of three and two respectively. The data in all of the other groups are still mixed in terms of lithology.

Figure 4.13 shows the lithology log and classification schemes for two, three and four classes and their distribution with depth. The classification shown in Figure 4.13b shows that the second class contains the pyroxenite and chromitite layer package at a depth of 380 m, the pyroxenite layer at 185 m as well as gabbronorite at a depth of approximately 140 m. This is scheme is clearly able to isolate the pyroxenite layers which was also observed in BY60. The three-class partitioning shown in Figure 4.13c shows that the anorthosite layers in the borehole are mostly placed in the first which accurately reflects the lithology log. This is with the exception of some norite layers which are placed in this class towards the end of the borehole. The gabbronorite and norite have been placed in the second class and although these lithologies are mixed in the same class, they correlate with the lithology log. This classification has also been successful in isolating the pyroxenite and chromitite from the rest of the lithologies, contained in the third class. Figure 4.13d shows that the classification scheme does not change significantly. Both the three- and four-class schemes accurately map the lithologies.

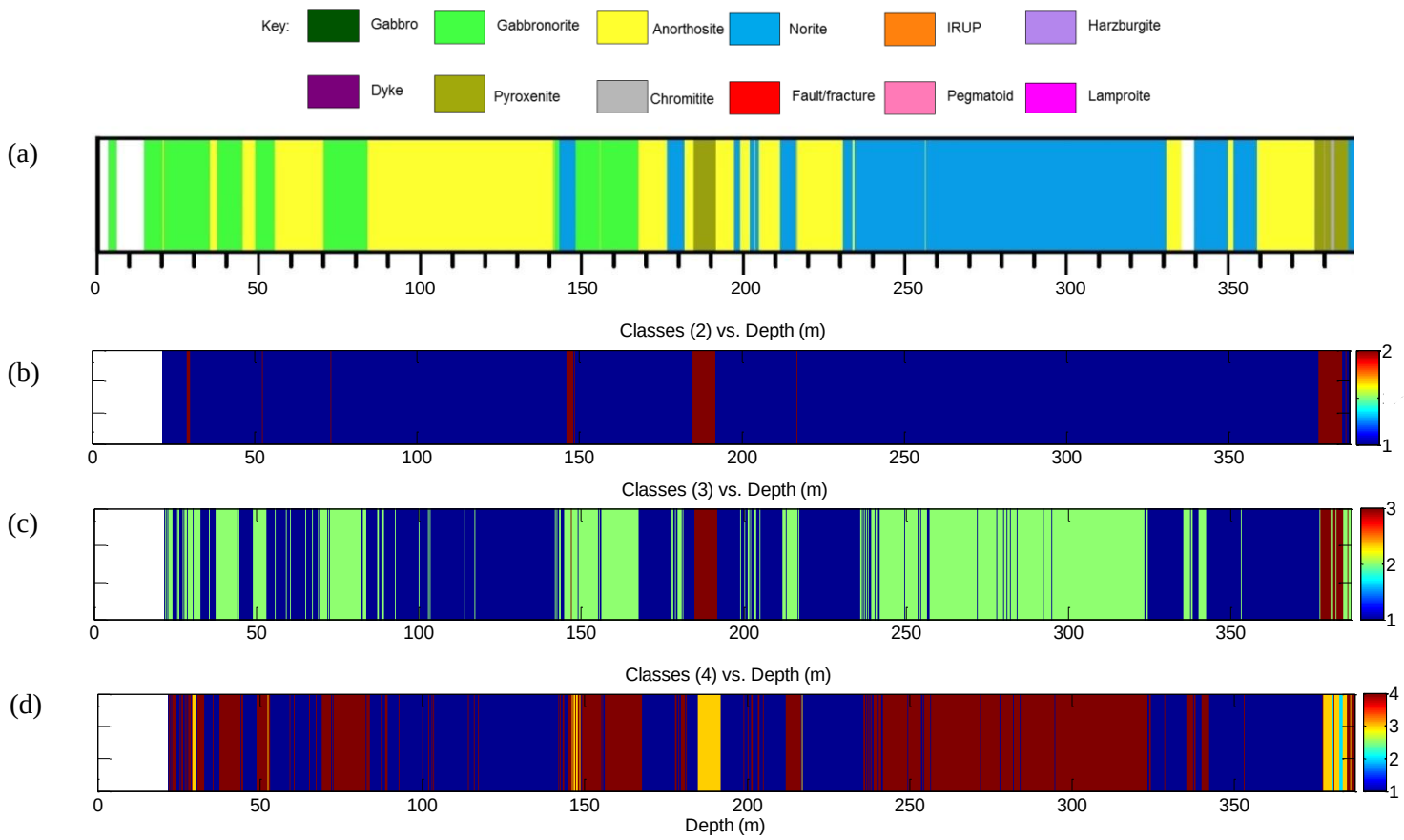

Figure 4.13 (a) Lithology log for borehole DB136. *k*-Means classification using density and magnetic susceptibility for (b) two, (c) three and (d) four classes

Der Brochen- DB135

Figure 4.14 shows the scatter plot for DB135 and the classification obtained for two, three and four classes.

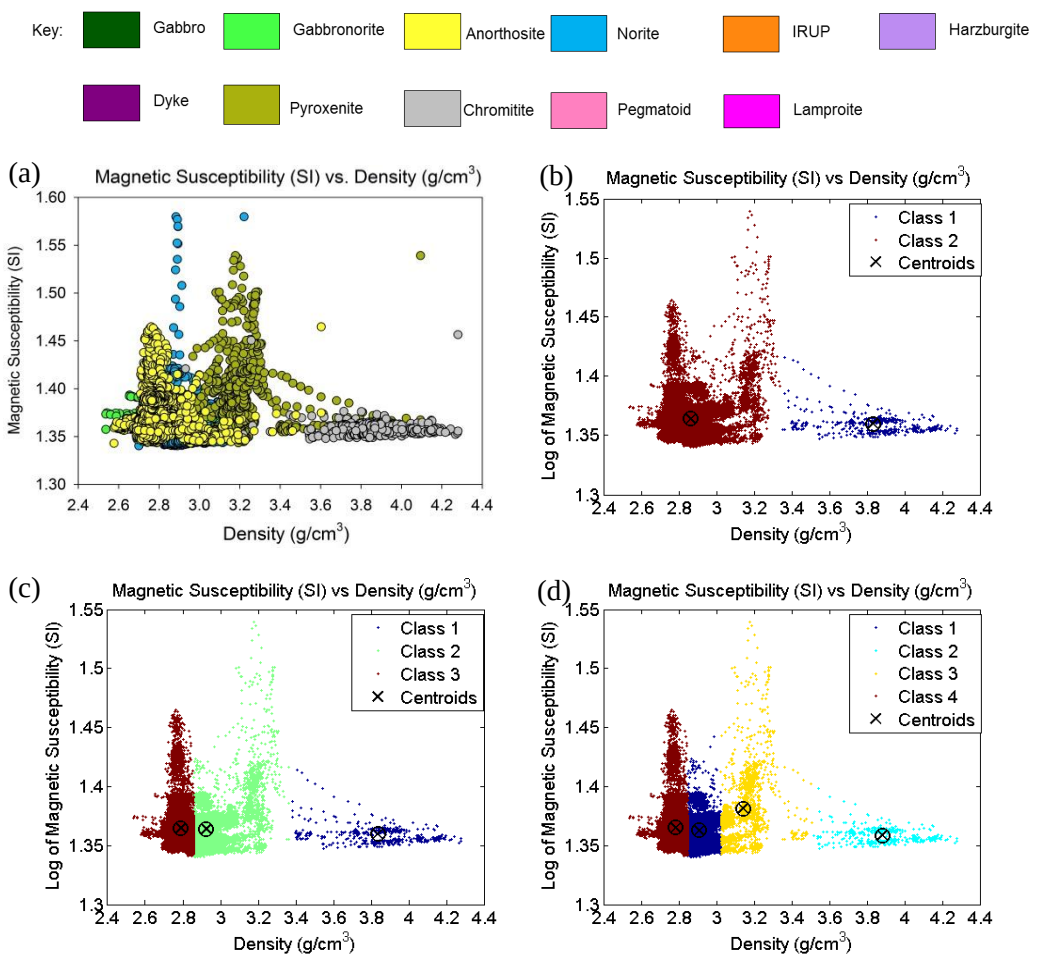

Figure 4.14 (a) Scatter plot of magnetic susceptibility (log scale) vs. density for the borehole DB135. Scatter plots of the *k*-Means classification for (b) two classes, (c) three classes and (d) four classes.

Figure 4.14a shows clustering of the various lithologies as seen previously in BY60, BY63 and DB136. The second class in Figure 4.14b contains chromitite with a small number of pyroxenite data points. The pyroxenite is grouped with all of the other lithologies in the second class which contains data points with densities smaller than 3.3 g/cm^3. The first class in Figure 4.14b does not change in Figure 4.14c and still groups the chromitites. The second class consists mostly of gabbronorite, norite and pyroxenite. These data lie between densities of 2.9-3.4 g/cm^3. Data with densities smaller than 2.9 g/cm^3 have been grouped into the first class and consist mostly of anorthosite and minor norite. The second class in Figure 4.14c is partitioned into two to form the first and third

classes. However these contain the same lithologies as previously. The first class contains densities of 2.7-3.0 g/cm^3, and the third class from 3.0-3.5 g/cm^3. The quality of the classification of chromitite is improved, showing less mixing with data from pyroxenite.

Figure 4.15 shows the lithology log and classification schemes for two, three and four classes and their distribution with depth. Figure 4.15a shows that the first class maps the chromitite layers at depths of 440 m and 555 m. The second class contains the gabbronorite, anorthosite, norite and pyroxenite. Figure 4.15c shows that for the first 220 m the classification scheme is identical to the lithology log. At depths below this, the third class is able to show the location of the anorthosite almost accurately, while the second class contains the gabbronorite and norite. The first class has once again accurately classifies the chromitite layer at a depth of 555 m and in the layer within the pyroxenite package 430-440 m. Figure 4.15d shows that the quality of the classification improves as the third class is able to isolate the pyroxenite layers at depths of approximately 250 m, 435 m and 55 m in the four-classification scheme. However a thin section of norite at a depth of 200 m has also been classified in the same group. This classification scheme almost accurately reflects the lithology log; except that the gabbronorite layers at the top of the borehole are not sufficiently separated from the norites at depth. Further increasing the number of clusters is unable to achieve this.

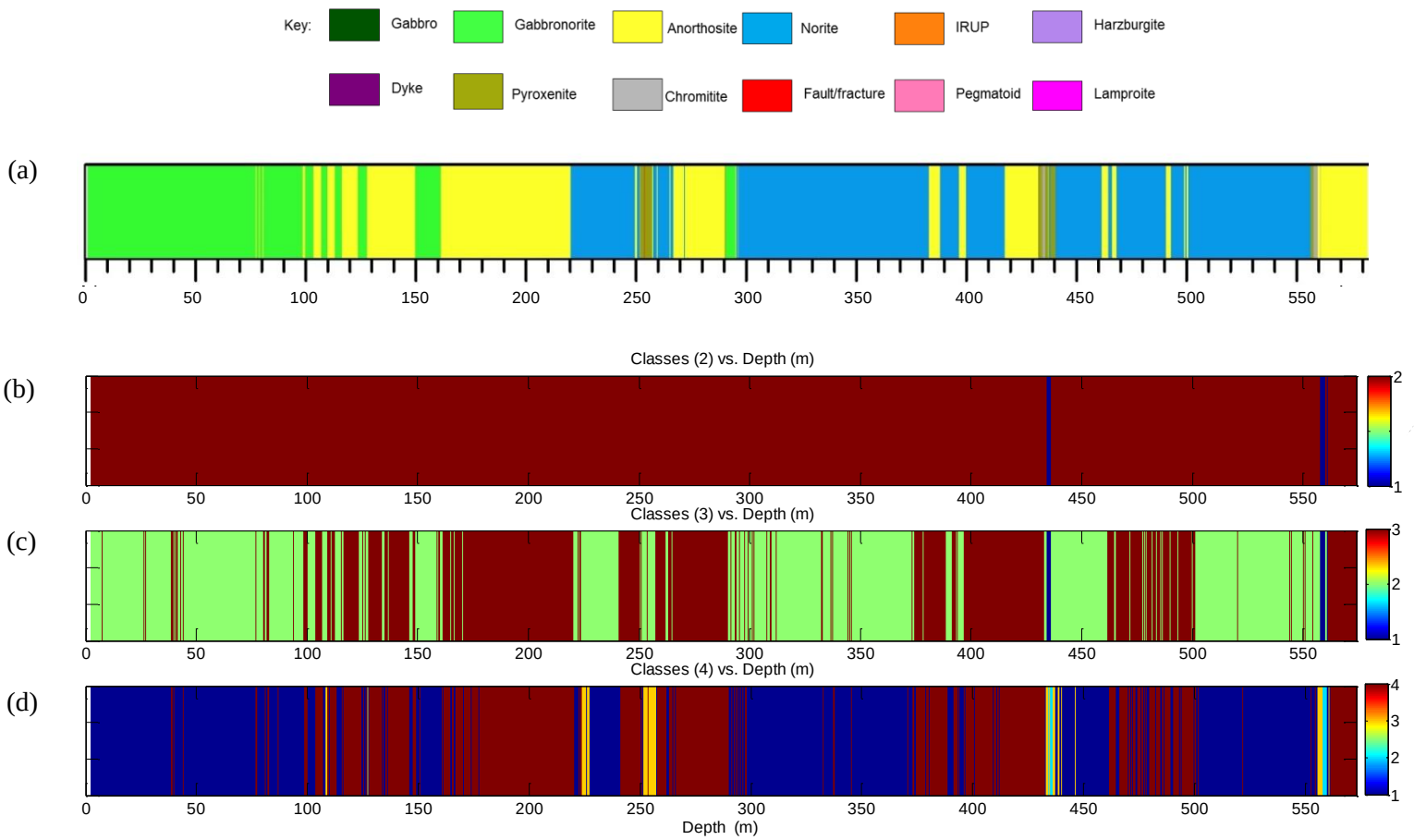

Figure 4.15 (a) Lithology log for borehole DB135. *k*-Means classification using density and magnetic susceptibility for (b) 2 and (c) 3 and (4) classes.

Der Brochen- RM123

Figure 4.16 shows the scatter plot for RM123 and the classification obtained for two, three and four classes.

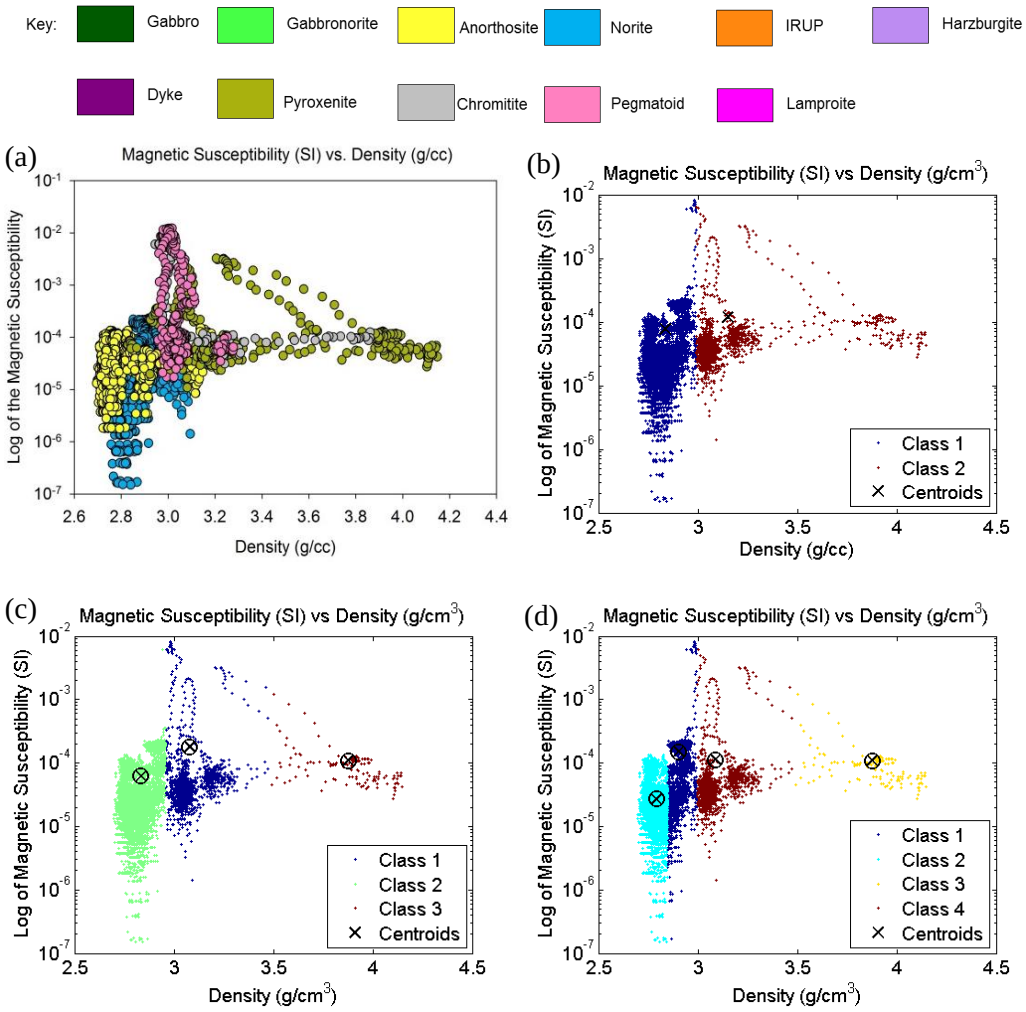

Figure 4.16 (a) Scatter plot of magnetic susceptibility (log scale) vs. density for the borehole RM123. Scatter plots of the *k*-Means classification for (b) two classes, (c) three classes and (d) four classes.

The first class in Figure 4.16b has grouped pyroxenite, chromitite and pegmatoid, which have densities larger than approximately 3.0 g/cm^3. The rest of the data with densities smaller than 3.0 g/cm^3 has been grouped together, consisting of norite and anorthosite. The three-class partitioning in Figure 4.16c is similar to that in Figure 4.16b significantly, with the exception of the third class which accurately groups the chromitite data without mixing it with the other lithologies.

Figure 4.17 shows the lithology log and classification schemes for two, three and four classes and their distribution with depth. This is the most simple of the logs presented above since it consists predominantly of two lithologies; norite and anorthosite. Figure 4.17b shows that the classification scheme has broadly classified the lithologies (norite and anorthosite) above the pyroxenite layer at approximately 125 m into the second class, and lithologies (norite and pegmatoid) below it in the first class. Figure 4.17c shows minor changes to Figure 4.17b, with the exception of the chromitite layers at depths of 128 m and 132 m which have been allocated to the third group. The four classes in Figure 4.17d do not reflect the log.

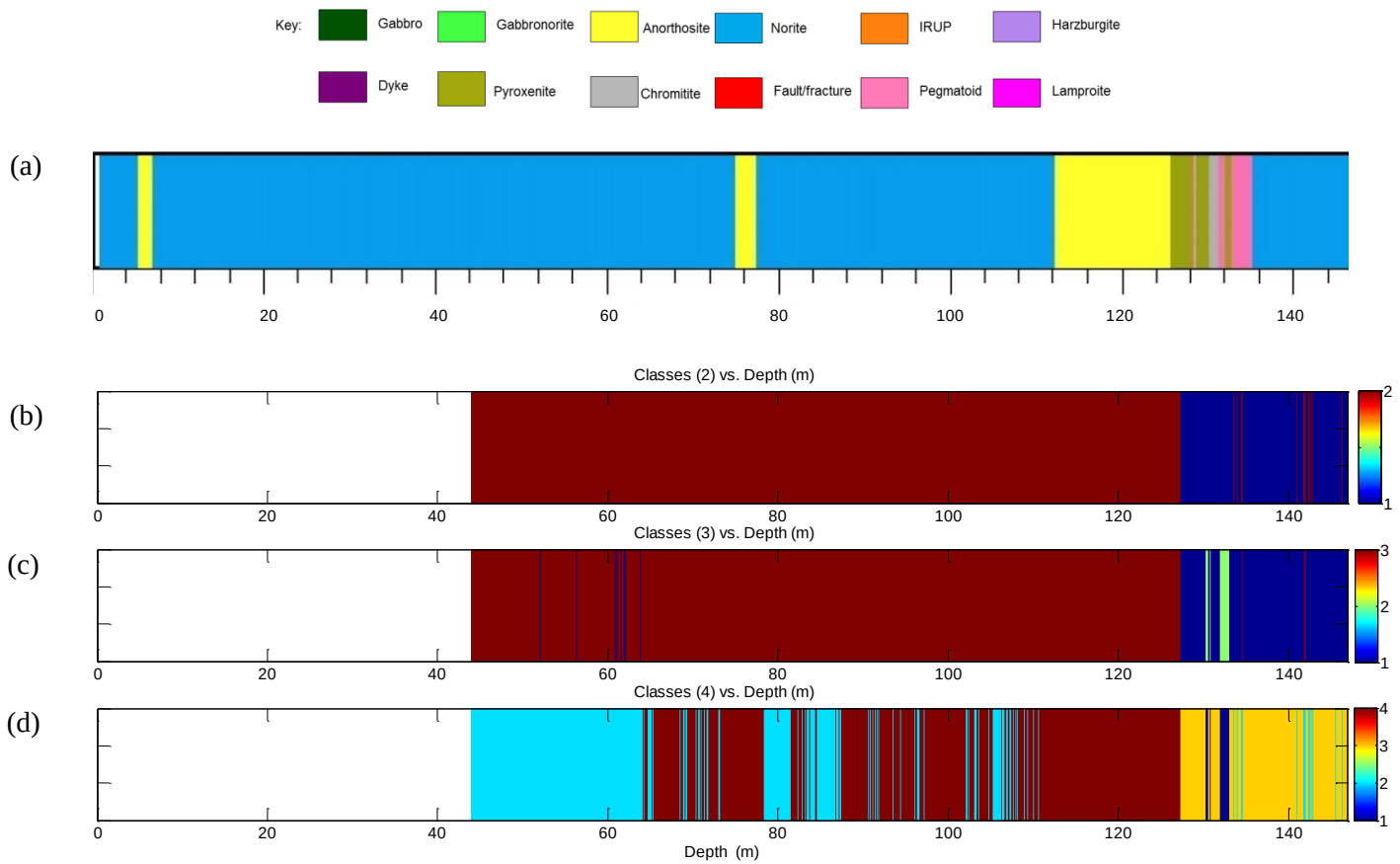

Figure 4.17 (a) Lithology log for borehole RM123. *k*-Means classification using density and magnetic susceptibility for (b) two, (c) three and (d) four classes.

4.3 Summary

Some degree of correlation between rock physical properties and the Lithology logs has been achieved using *k*-means classification. This is particularly true for the Eastern Limb whose scatter plots of density and magnetic susceptibility show visible clusters according to lithology. However the classification has not been effective in all of the boreholes and often becomes complicated and an inaccurate representation of lithology log. The following observations have been made:

- *Class number:* The influence of class number is clearly observed. While an increase in the number of classes generally allows for lithologies to be differentiated and partitioned into different classes, the classification becomes increasingly complicated for classes more than 3 or 4. Cluster boundaries are predominantly vertical, which is due to the data being elongate in the magnetic susceptibility across several orders of magnitude.

- *Heterogeneities:* Increasing the class number has shown to often place a single continuous lithology type into different classes. This may be due to localized heterogeneities produced by subunits or grading. A good example of this is borehole RM123, which appears to be lithologically homogeneous, but whose classification shows that there are strong enough physical property changes in the norite that different clusters arise. Geological logging errors may also result in these discrepancies between the lithology log and the classification. However this cannot be fully ascertained as there is no access to lithology cores.

- *Physical property contrasts:* The classification has also been able to show that there is not always a large enough density and magnetic susceptibility contrast to produce sensible classes out of the data. These mafic rocks represent a continuum in the change in mineralogy and hence a change in physical properties. Gabbronorite and norite for example are commonly grouped together, which is not ideal. Pyroxenites and chromitites, and to a lesser extent anorthosites, can be classified separately from the other lithologies.

The overall results show *k*-means analysis can be used as an interpretation tool for borehole geophysics, although it should be exercised with caution. Classifications which are able to reflect the general changes in lithology occur in DB136, DB135 and BY60, which are three out of the seven boreholes presented. However, one important outcome has been the detection of chromitite and pyroxenites. These have obvious significance in BC as these are the layers of interest in mining.

In the borehole SO2 only the chromitite layer at a depth of 665 m has been accurately classified while the others have been grouped with other lithologies. The chromitite layer in BY63 at a depth of 540 m has not been accurately classified since it is not adequately separated from pyroxenite and anorthosite. In borehole DB135 the chromitite layer at a depth of 430 m was successfully identified in the two, three and four class partitioning schemes. The chromitite layer in borehole DB136 at a depth of 380 m is only successfully classified in the four class partitioning. Finally, the chromitite layers in borehole RM123 at depths of 130 m and 132 m have both been detected in both the three and four class partitioning.

The pyroxenite layers borehole SO2 at depths of ~580 m, 590 m, 600 m and 660 m have not been accurately grouped. In borehole KLG52, those at depths of 1840 m and 1860 m have also not been successfully classified since they have been mixed with gabbronorite, norite, anorthosite and pegmatoid. The pyroxenite layer in borehole BY60 at a depth of 75 m has been accurately classified using only the four class partitioning. The only other borehole from Booysendaal is BY63, which has not accurately classified the pyroxenite layers at depths of 310 m and 540 m. These are not only placed in different classes, they are also mixed with gabbronorite, anorthosite and to a lesser extent chromitite. The borehole DB135 showed accurate classification (with a four class partitioning) of a total of three pyroxenite layers (at depths of 250 m, 435 m and 555 m) even though the data were mixed with some data from norite. Similarly, borehole DB136 has accurately classified pyroxenite layers at depths of 185 m and 375 m in a three class partitioning. The pyroxenites in borehole RM123 are grouped with pegmatoid and gabbronorite, making this a poor classification. This tool can therefore be used as a way of confirming the location of chromitite and pyroxenite layers to support lithology logging but probably not independent of the lithology log and since these results depend highly on the user-selected cluster number *k* at run time.

CHAPTER 5: BACKGROUND - WAVELET ANALYSIS

This chapter gives the theoretical background to wavelet and wavelet-based semblance analysis which are used to study cyclicity in physical property data. A brief introduction to wavelet and Fourier analysis is given and the motivation of the using the former over the latter. The codes which have been developed are tested using synthetic data, to study cyclicity in individual datasets as well as correlations across multiple datasets. Finally, some studies which are similar to this are discussed.

5.1 Fourier Analysis

The usual starting point to discussing wavelets is to discuss Fourier analysis. Fourier analysis is the process of breaking a signal down into sine waves of varying frequencies and amplitude and is commonly used technique for extracting the frequency components of a signal. Wavelet transforms (WT) also work by way of decomposition but produce "shifted and scaled versions" (Misiti et al., 1997) of the input wavelet. While the Fourier transform (FT) produces sine waves of infinite extent, wavelets are irregular in shape, asymmetric, and have a finite extent (Misiti et al., 1997, Pan et al., 2008). The FT and its inverse of a continuous signal $x(t)$ is given by Prokoph and Barthelmes (1996),

$$H(f) = \int_{-\infty}^{\infty} x(t) e^{-2\pi i f t}\, dt, \tag{5.1}$$

where $i = \sqrt{-1}$, f is frequency and t is time or position. Since geophysical data are discrete and finite, the discrete FT (DFT) is more appropriate. For a discretely sampled signal $x(t_n)$ with a total of N consecutive samples the DFT is given by Pan et al. (2008),

$$H_n(f_n) = \sum_{n=0}^{N-1} x\,(t_n) e^{-\frac{2\pi i n k}{N}}, \tag{5.2}$$

where $k = 0,1,..,N-1$ and f_n are the discrete frequencies. The inverse transform is,

$$x(t_n) = \sum_{n=0}^{N-1} H_n(f_n)\, e^{\frac{2\pi i n k}{N}}. \tag{5.3}$$

Fourier analysis, although a powerful tool, suffers from several drawbacks. When moving from the space-time domain to the frequency domain, information on the time or position of an event is lost. This method also assumes stationary data and is therefore unsuitable

for non-stationary datasets i.e. where the frequency changes with time (Grinsted et al. 2004; Prokoph and Bilali, 2008). These types of events are of interest in this project which makes Fourier analysis unsuitable. The conventional way of computing the FT described by the equations above was first modified by Gabor (1946). This is referred to as the short-time or windowed Fourier transform (WFT) (Rioul and Vetterli, 1991). It aims to address the shortfalls of the FT by using a window which analyses portions of the data at a time in a window of finite extent (Prokoph and Barthelmes, 1996; Pan et al., 2008; Sifuzzaman et al., 2009) (Figure 5.1).

Figure 5.1 Computation of Fourier analysis using windows of the same size (Misiti et al., 1997).

The WFT of a signal with a window $g(t)$ centred at time or position t' is,

$$H_w(t', f) = \int_{-\infty}^{\infty} x(t) g(t - t') e^{-2\pi i f t}\, dt. \qquad 5.4$$

However this method's precision is limited depends on the size of the window used for computation. It is also inherently problematic since only a single window size can be used for all frequencies, whereas smaller windows would be better suited for high frequencies and larger windows for lower frequencies (Prokoph and Agterberg, 1999; Prokoph and Bilali, 2008).

5.2 Wavelet Analysis

Wavelet analysis is a better tool for characterizing multi-scale features in data. This method addresses the shortfalls of both the FT and WFT analysis by using windows with varying sizes for different frequencies. The concept of a wavelet was introduced by in 1982 by Jean Morlet for the analysis of seismic signal analysis (Kumar and Foufoula-Georgia, 1994; Labat, 2005; Sifuzzaman et al., 2009). Narrow windows are used for high frequencies while wider windows are used for lower frequencies (Prokoph and Agterberg, 1999) (Figure 5.2).

Figure 5.2 Wavelet analysis: an input signal is transformed using windows of varying sizes (Misiti et al., 1997).

The benefit of using this tool is that the time or position information of events is not lost when a WT is taken. This allows for the frequency information of a signal to be studied with respect to time or position. Since then, it has undergone several developments and has been used in various fields outside geophysics (Kumar and Foufoula-Georgia, 1994). The advantage of wavelets in geophysics has been in the analysis of non-stationary data, the analysis of multi-scale and transient phenomena, for the detection of singularities and signal compression. Some of the earliest applications of wavelet analysis in earth sciences have been in the study of atmosphere turbulence, noise reduction, land surface topography, sea-floor bathymetry, sea surface temperature variation, paleoclimatology using oxygen isotopes and sea-level fluctuations (Kumar and Foufoula-Georgia, 1994; Labat, 2005). The wide range of applications of the WT since its inception shows the robustness of this method for delineating underlying poorly understood geological or geophysical processes. There are two main types of WTs: the discrete wavelet transforms (DWT) and the continuous wavelet transform (CWT) (Grinsted et al., 2004). The DWT has been described as being suited for filtering and compressing data, and the CWT to highlight trends, discontinuities or periodicity (Prokoph and Barthelmes, 1996, Misiti et al., 1997, Prokoph and Agterberg, 1999; Grinsted et al., 2004). Since this project aims to characterise cyclic vertical variations in density and magnetic susceptibility measurements, the CWT will be used. The CWT is defined by Mallet (2009) as,

$$C(u,s) = \int_{-\infty}^{\infty} x(t) \frac{1}{\sqrt{s}} \psi^* \left(\frac{t-u}{s} \right) dt, \qquad 5.5$$

where u is a displacement in the horizontal direction, s the scale parameter, and ψ is called the "Mother" wavelet. The scaling parameter s stretches and compresses the wavelet for small and large values respectively (Prokoph and Barthelmes, 1996). The displacement parameter u shifts the wavelet, hence delaying or advancing it. The symbol * implies complex conjugate. The equation shows that the CWT is the convolution between a function *x(t)* (the signal) and the complex conjugate of the wavelet ψ^*, which is

being shifted and scaled. Figure 5.3a shows a wavelet (shown in red) at the beginning of a signal (shown in black). The wavelet is translated through the signal (Figure 5.3b) by changing the parameter *u* until the wavelet reaches the end of the signal. The wavelet is then stretched by changing the parameter *s*, and this process is repeated (Figure 5.3c).

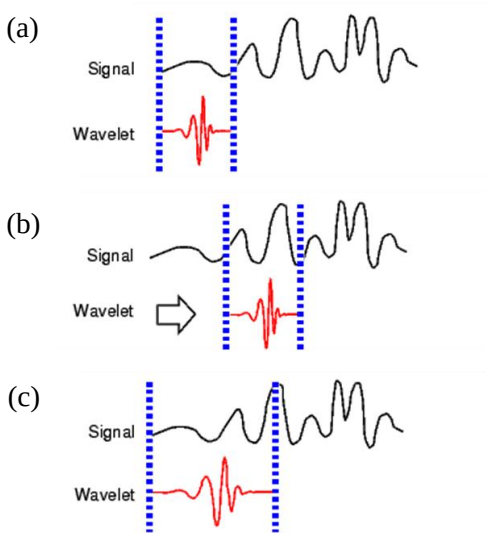

Figure 5.3 (a) Shows the initial position of a wavelet which is being convolved with a signal. (b) The wavelet is advanced to a new position, until the end of the signal is reached. (c) The wavelet is stretched and translated through the data once more. This process is repeated until the WT is calculated at all scales selected by the user (Misiti et al., 1997).

There are several types of wavelets, each with varying mathematical properties (Misiti et al., 1997; Cooper and Cowan, 2008). The wavelet that will be used in this project to analyse datasets will be the Morlet wavelet. This wavelet is the most popular for quantifying cyclicity as it has the optimum localization (Labat, 2005). This means that it achieves the best possible frequency and space-time resolution. The equation of the real Morlet wavelet is given by Misiti et al. (1997) as,

$$\psi(x) = C\, e^{-\frac{x^2}{2}} cos5x \qquad 5.6$$

This wavelet has a complex version, which is symmetrical and infinitely regular, given by (Misiti et al., 1997),

$$\psi(x) = \frac{1}{\pi f_b}\, e^{2\pi i f_c x}\, e^{-\frac{x^2}{f_b}}, \qquad 5.7$$

where f_b is the frequency bandwidth, and f_c is the centre of frequency of the wavelet. These will be chosen as one and one respectively since this makes the scale of the CWT

equivalent to the wavelength of the input signal. Figure 5.4a and b show the real and complex parts of the Morlet wavelet.

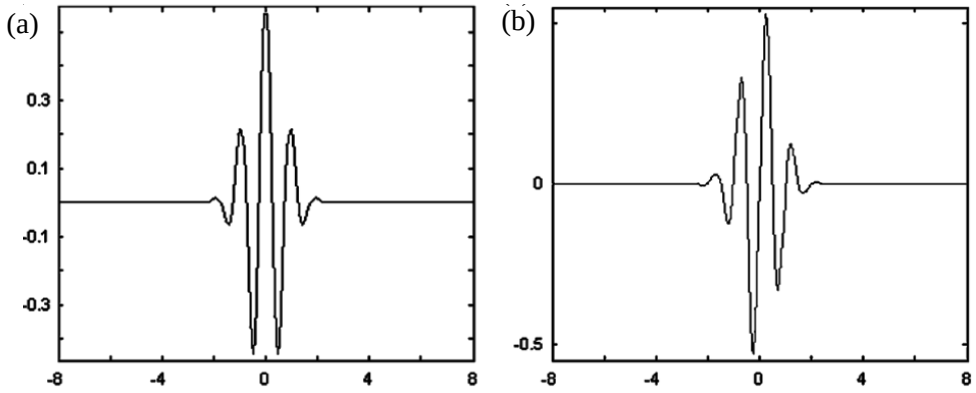

Figure 5.4 (a) Real part of the complex Morlet wavelet. (b) Imaginary part of the complex Morlet wavelet (Cowan and Cooper, 2003).

5.3 Wavelet-based Semblance

Semblance analysis is used to compare similarities between two datasets based on phase. It can be calculated using the real (R) and imaginary parts (I) of the FT of the datasets. Semblance S is defined by Cooper and Cowan (2008) as,

$$S(f) = \cos\theta(f) = \frac{R_1(f)R_2(f) + I_1(f)I_2(f)}{\sqrt{R_1^2 + I_1^2}\sqrt{R_2^2 + I_2^2}}, \tag{5.8}$$

where f is the frequency. It therefore has a maximum value of 1 and a minimum value of -1. A value of 1 corresponds to perfect correlation, 0 to no correlation and -1 to anti-correlation. Although this method allows for correlation between datasets, a much better result can be achieved using wavelet-based semblance, which has all the advantages of the WT. Wavelet-based semblance analysis is calculated from the cross-wavelet transform (XWT).

The XWT compares the WT of two datasets, and is given by,

$$C_{1,2} = C_1 \times C_2^*, \tag{5.9}$$

whose complex modulus (also known as the cross-wavelet power) is given by,

$$P = |C_{1,2}|. \tag{5.10}$$

The phase of the datasets is given by,

$$\theta = \tan^{-1}\left(\frac{I(C_{1,2})}{R(C_{1,2})}\right). \quad 5.11$$

Cooper and Cowan (2008) have found that the local phase angle does not give good results. This semblance is calculated from this by calculating the cosine of this quantity,

$$S = cos^{n}(\theta) \quad 5.12$$

Where *n* is a non-zero odd integer. While the semblance contains phase information, the cross-wavelet power contains amplitude information.

The theory outlined above can be used for two datasets, but is not suitable for multiple datasets. For multiple datasets (>2), a correlation factor for *N* datasets can be calculated using (Cooper, 2009),

$$MRL(t,\lambda) = \frac{\sqrt{(\sum_{i=1}^{N} R(C_{i,t,\lambda}))^2 + (\sum_{i=1}^{N} I(C_{i,t,\lambda}))^2}}{\sum_{i=1}^{N}\left|C_{i,t,\lambda}\right|}. \quad 5.13$$

This is known as the mean-resultant length (*MRL*), and calculates the correlation between *N* datasets at a time *t* (or position) and wavelength λ. The *MRL* gives an indication of the average direction of a set of vectors. When closely spaced, they are correlated and the calculated MRL has a similar length as the constituent vectors and is nearly equal to their sum, and is large. When vectors are dispersed, they have a small MRL due to their large dispersion, and are therefore uncorrelated. The maximum value for *MRL* is 1 when datasets are perfectly correlated and 0 when they are not correlated. Figure 5.5 shows the two datasets consisting of three vectors with different dispersions.

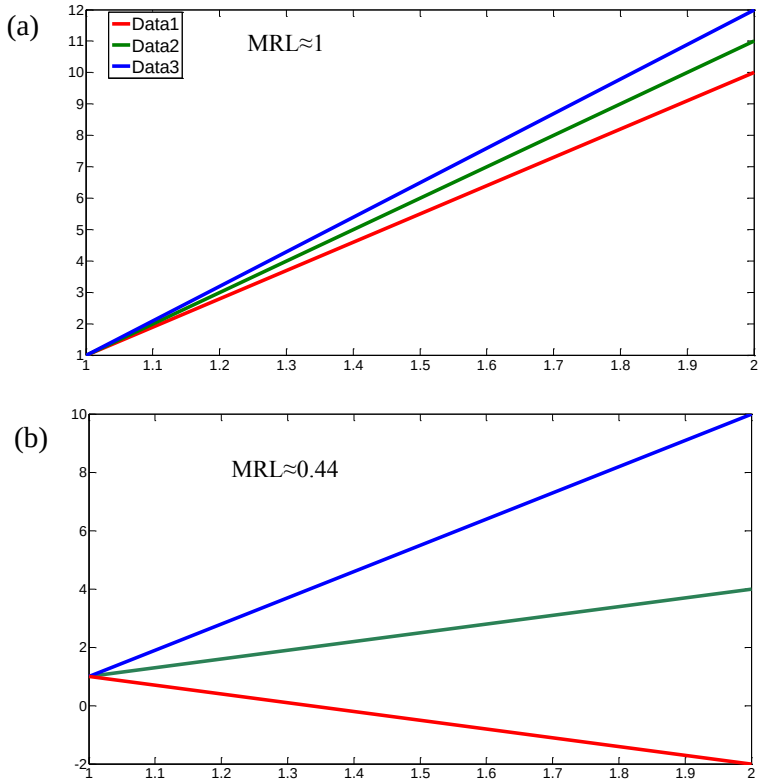

Figure 5.5 Two different plots of three sets of datasets with different dispersions. The MRLs are approximately (a) 1 and (b) 0.44.

The data with the least amount of dispersion shown in Figure 5.5a has the highest correlation, with an MRL of approximately 1. The data shown in Figure 5.5b have less correlation as they are dispersed, and have a MRL of 0.44.

5.4 Application to Synthetic Data

This section shows the results from the application of the abovementioned mathematical techniques to synthetic datasets. See Appendix B for the MATLAB programs used to compute the power spectrum and wavelet analysis.

5.4.1 Power Spectrum

Although this project will use wavelet analysis to study the wavelength of cyclicities, Fourier analysis can be used as an independent check of the integrity of the coding using synthetic data. This is achieved using the power spectrum (P_ω). The power spectrum or spectral analysis is a Fourier-based technique for calculating how frequencies in a dataset contribute to the entire signal. This is given by Labat (2005),

$$P_\omega = \left| \int_{-\infty}^{+\infty} x^2(t)\, e^{-2\pi i \omega t}\, dt \right|^2, \qquad 5.14$$

where ω is the angular frequency. Figure 5.6a shows a sine wave with two components and the power spectrum is shown below it in Figure 5.6b.

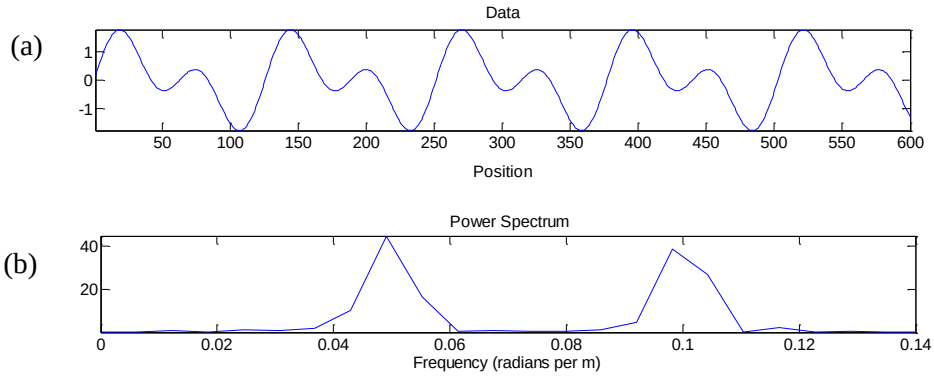

Figure 5.6 (a) Sine curve with of two frequencies. (b) Power spectrum of the sine curve.

The sine curve in Figure 5.6a has a long wavelength component with a shorter wavelength superimposed. The two distinct peaks shown in Figure 5.6b correspond to frequencies of approximately 0.05 and 0.1 radians per second and wavelengths of 125.66 m and 69.13 m.

5.4.2 Continuous Wavelet Transform

This section studies the result of taking the CWT of a dataset. The sinusoids are used to illustrate both how the frequency content can be calculated and studied with position. This method is also able to detect cyclicity that is not necessary present throughout a dataset. Figure 5.7a shows a sine wave with two frequency components identical to that in Figure 5.7a. Figure 5.7b shows the real part of the CWT of the data.

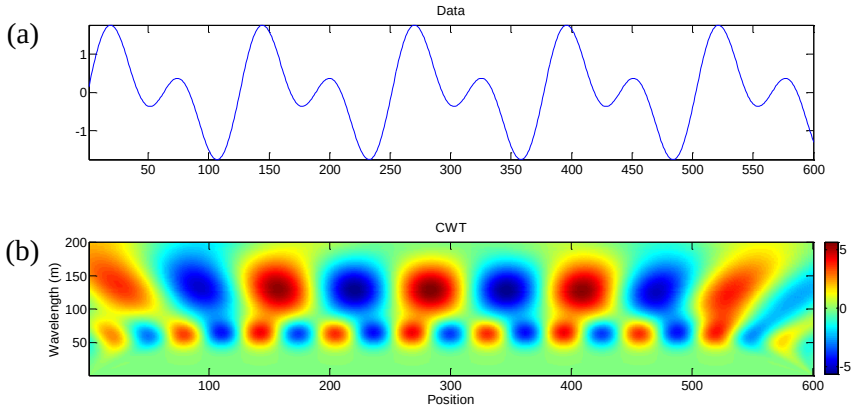

Figure 5.7 (a) Sine curve with two frequencies. (b) CWT of the data, showing two frequencies.

Figure 5.7b above shows the success of the method in revealing the different wavelength components of the dataset with respect to position. These two regions with maxima and minima correspond to wavelengths of approximately 125 m and 70 m. The computation of the power spectrum showed the wavelengths of the signal to be approximately 125.66 m and 69.81 m in wavelength. These values are in the same range as those obtained from computing the CWT, suggesting that the two methods are in agreement. Figure 5.8 shows the ability of wavelet analysis to detect a non-stationary signal.

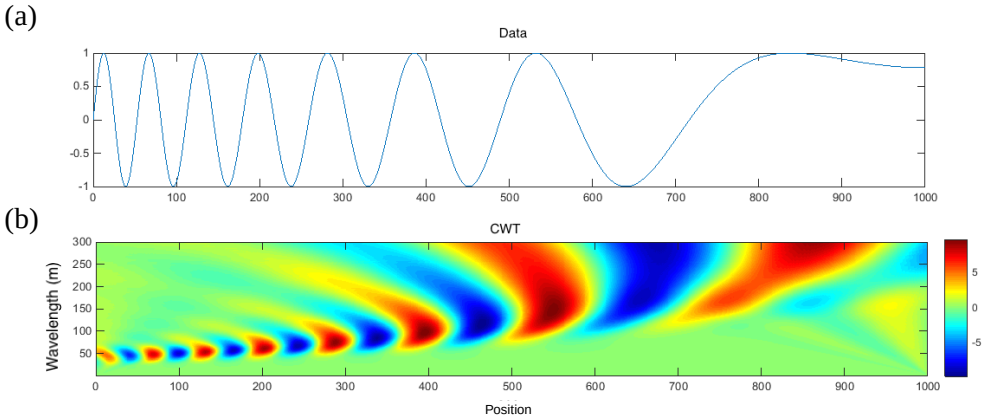

Figure 5.8 (a) Non-stationary sine curve. (b) CWT of the data showing a signal with changing frequency.

The signal in Figure 5.8a consists of a sine curve with constant amplitude (non-attenuating) but changing frequency. At zero position (Figure 5.8b) the signal shows a wavelength of 20m, which changes steadily with a change in position. At a position of 0.9 m the wavelength is close to 250 m. The change in wavelength is mapped accurately with every change in position.

5.4.3 Wavelet-based Semblance Analysis

Semblance Analysis for Two Datasets

Two sine waves can be correlated using semblance. This technique will be useful for comparing the WT from individual boreholes in different locations in the BC. Since wavelength is plotted as a function of position, semblance analysis allows for changes in wavelength of the datasets to be studied as a function of position. Figure 5.9a and c show two sine curves with identical wavelengths of 130 m and 70 m but with a phase shift.

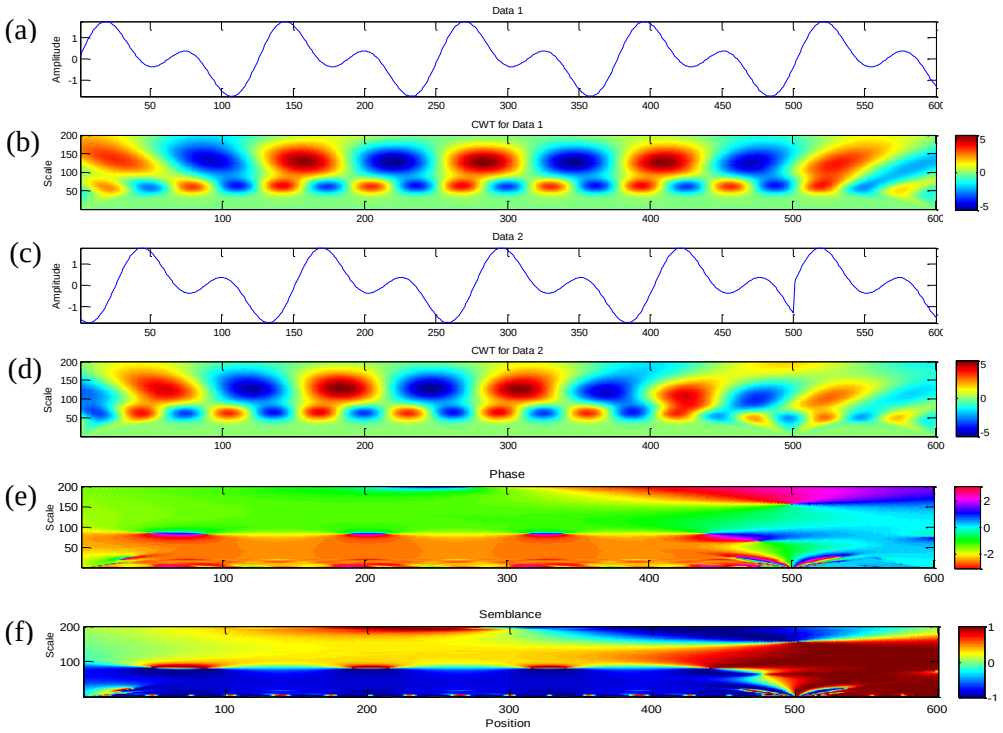

Figure 5.9 (a) Sine curve with two frequencies (Data 1). (b) Real part of the CWT of Data 1. (c) Sine curve with two frequencies (Data 2) advanced by 100 m with a large phase change at 500 m. (d) Real part of the CWT for Data 2. (e) The phase angle. (f) Semblance analysis of Data 1 and 2.

The sine curve in Figure 5.9c has been advanced by 100 m and has a large phase change at 500 m. The sine waves have been constructed such that the short wavelength components present in both of these datasets do not correlate with each other from 0 m to 500 m. After 500 m, these signals are then in phase again. The anti-correlation is symbolised by the maxima of the first dataset aligning with the minima of the second datasets (see Figure 5.9b and d). The anti-correlation of the small wavelength signal can also be seen in the image of the local phase Figure 5.9e. This image shows a red region colour across the 70 m wavelength until 500 m. The semblance analysis (Figure 5.9f) that corresponds to this region shows a broad blue patch which is an indication of anti-correlation i.e. $S = -1$. Following the large phase change at 500 m the small wavelength component is then correlated again, symbolised by the red region in the plot of the semblance. The long wavelength component of the data shows a positive correlation which is stronger after 500 m when there is a large change in the phase of the second dataset. The two signals being correlated is shown by the yellow region, which corresponds to $0 \leq S \leq 1$. This is then replaced by a predominantly red region which represents the long wavelength features becoming perfectly correlated thereafter.

5.5 Similar Studies

One of the earliest applications of wavelet analysis to borehole data is by Prokoph and Barthalmes (1996). They applied wavelet analysis to a gamma-ray log (sampled at 10 cm) of the Kirchrode Well 1/91 to understand the geological processes during the sedimentation of the Cretaceous North German Basin. The 275 m thick sedimentary package covers an almost complete transgressive-regressive sedimentation cycle, spanning a time interval of 2.4 Ma. It consists primarily of marlstones, with silty layers. Their results are shown in Figure 5.10. They were able to identify cyclic, non-cyclic and chaotic units in the sedimentary package, having modelled the physical property characteristics of each of these units. The chaotic units are ones which have no cyclicity but have high intensity at all wavelengths. These were interpreted as being at depths of 207-235 m, at the base of the sequence. The chaotic units are said to have been deposited during low-sea level and during early stages of sea-level rise (transgression).

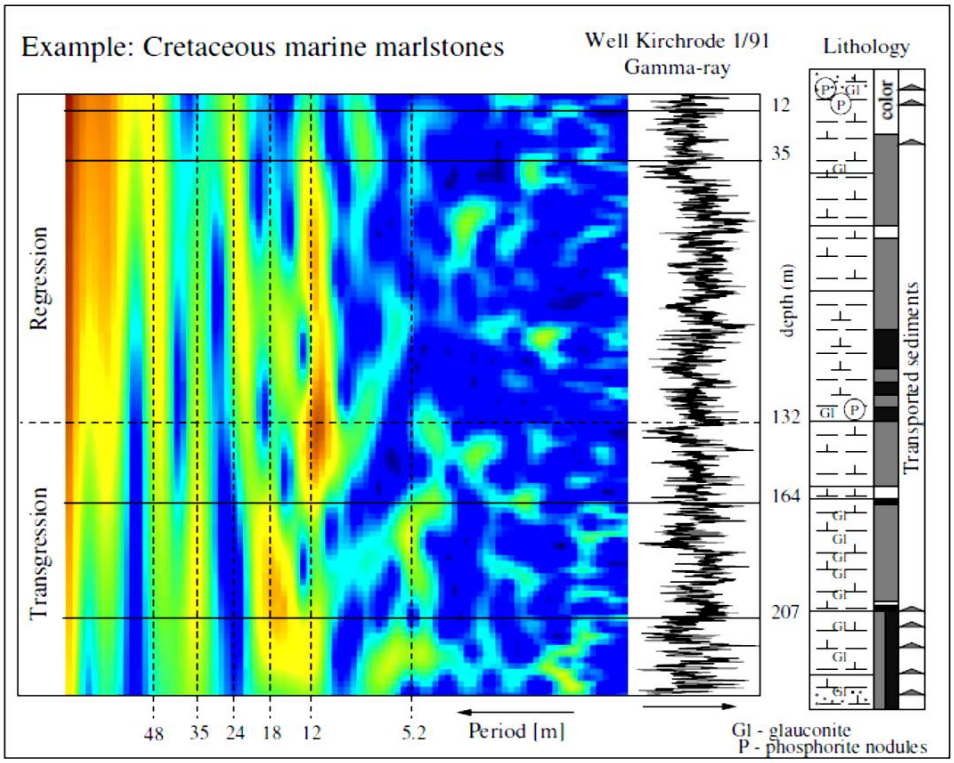

Figure 5.10 CWT of the gamma-ray log of the Kirchrode Well 1/91, the measured gamma-ray dataset, and the lithological log (Prokoph and Barthalmes, 1996).

This unit is overlain by a period of stable sedimentation which produces distinct cyclicity at wavelengths of 16-35 m at depths of 163-207 m, and 12 m between 35 m and 163 m. Stable sedimentation is said to be associated with the relatively high sea-level, during late

periods of transgression and early regression. A non-stationary dataset such as this is not uncommon in geophysics according to Grinsted et al. (2004). Their results are supported by a spectral analysis of the data, which shows the same frequencies as those of the WT with the exception of wavelengths longer than 80 m. This discrepancy is not explained.
Prokoph and Agterberg (1999) also used natural gamma-ray logs to study cyclicity in sedimentation in the Western Canada basin using the CWT method. This study was undertaken to study sediment accumulation at a resolution that conventional biostratigraphy, chronostratigraphy or sequence stratigraphy cannot provide. Instead of using Fourier methods to support the interpretation as Prokoph and Barthalmes (1996), they used a sonic log. They were able to determine a sedimentation rate of 5-7 cm per 1000 years in mudstone and 29 cm per 1000 years in sandstone using the CWT method. The gamma-ray and sonic logs showed agreement. Like Prokoph and Barthalmes (1996), they applied wavelet analysis to synthetic data first, but emphasis in this study was placed on the limitations of the method at small wavelengths for noisy data.

They then followed this study with one in offshore eastern Canada, in the oil-source (black shales) rocks of the Egret Member, Jeanne d'Arc Basin (Prokoph and Agterberg, 2000). This time a much more extensive dataset of seventeen gamma-ray logs were used of the 55-227 m thick succession. This study showed that not only can the application of wavelet analysis to physical property data be used to quantify cycles; it can be used to detect discontinuities. Prokoph and Agterberg (2000) were able to detect cycles of 2.8 m in the western part of the basin, which gradually increases to 24 m in the eastern part of the basin. This was possible from a good distribution of gamma-ray logs in their study area. They interpreted discontinuities in the CWT as faults or unconformities, or a decrease in oil content. This study shows the importance of a good spatial distribution of datasets in order to characterise changes in cyclicity across a large area, which this project aims to achieve.

Rampino et al. (2000) have attempted to analyse the Permian-Triassic (PT) boundary, a well-known extinction event in the earth's history, using wavelet analysis. This study used a 300 m core of dolomitized limestones, marls and shales from the Carnic Alps in Austria, which document this event. Evidence of this event is supported by changes in fauna and a negative sharp change in the carbon isotopes which is said to be observed globally. Together with carbon isotope studies, they used measurements of physical rock properties much like the studies described before. They were able to quantify the rate of

sedimentation across this P-T boundary, which they estimated to be 10-11 cm per 1000 years from density logs, showing that sedimentation was continuous from the late Permian to early Triassic.

Cowan and Cooper (2003) have also applied the wavelet method to chemical sedimentary rocks. Unlike the studies outlined above, they used the magnetic susceptibility of the rocks (sampled at 1 cm) instead of the gamma-ray logs. These rocks are from the Brockman Iron Formation from the Hamersley Basin in western Australia, and consist of a series of shales, volcanic rocks, dolomite and banded-iron formations (BIF). Their measured magnetic susceptibility data were also found to be non-stationary in the borehole used, similar to the study by Prokoph and Barthalmes (1996) and by Webb et al. (2008). Variations in magnetic susceptibility were found to be across different lithological units, as well as within individual units, much like the study of Webb et al. (2008). Cowan and Cooper (2003) found the variations in bulk magnetic susceptibility in the banded-iron formation (BIF) units were a function of thickness, composition and the magnetite to hematite ratio. A high magnetite to hematite ratio results leads to high magnetic susceptibility measurements, since magnetite is more strongly magnetic than hematite is.

Cowan and Cooper (2003) used both the CWT and DWT. The CWT was used to quantify layering like the studies by Prokoph and Barthalmes (1996), Prokoph and Agterberg (1999, 2000) and Rampino et al. (2000), while the Haar wavelet for the DWT was used to segment between each of the 17 observed BIF units. Figure 5.11 below shows how Cooper and Cowan (2003) smoothed and discretised their data to highlight changes in lithologies while retaining their boundaries.

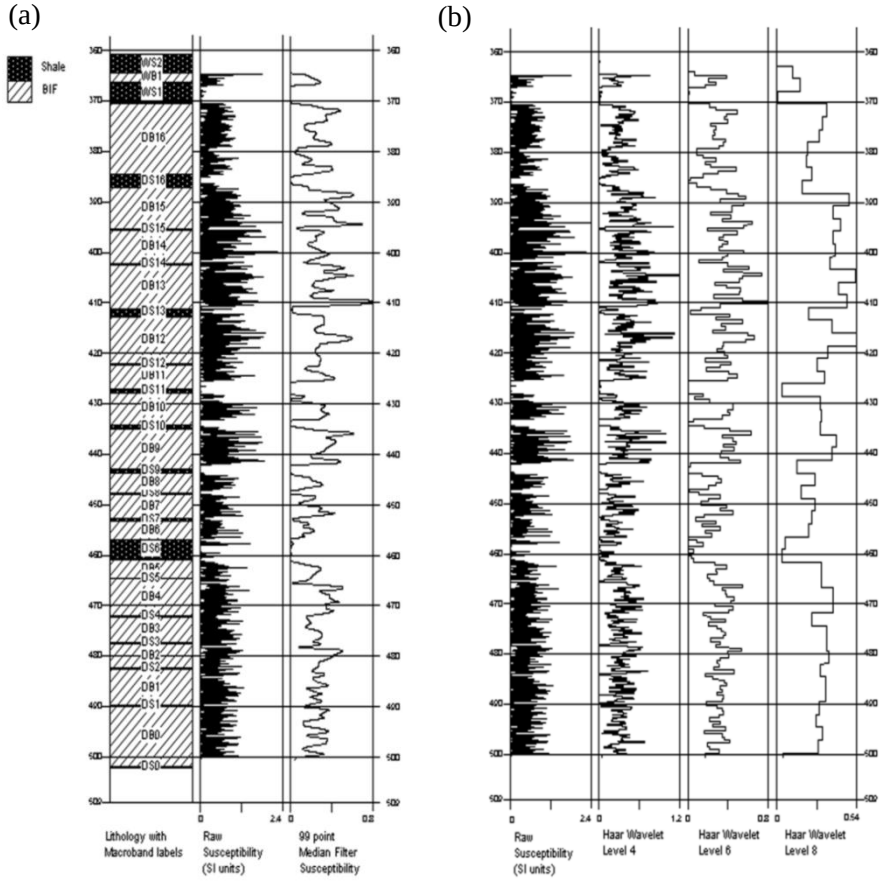

Figure 5.11 Lithological log, measured magnetic susceptibility data and the median filtered data. A median filter has been used to smooth the data without compromising edges. (b) Shows the data and the Haar WT of the data at approximation levels 4, 6 and 8 (Cowan and Cooper, 2003).

The raw data shows a course structure with high frequency fluctuations superimposed. The median filtered data shown in Figure 5.11a shows the coarse variations in magnetic susceptibility present in the data while retaining the edges. The median filtering was done using a 99 point moving window which computes the median across the dataset and is a popular filter for preserving edges in a dataset. Figure 5.11b is shown for comparison where various levels of Haar wavelets have been applied using DWT. They used the DWT to filter their magnetic susceptibility log into lower resolution (low-pass filtering) and higher-resolution (high-pass filtering) components. These are commonly referred to as approximation (cA) and detail (cD) components respectively (Pan et al. 2008). The first filtered results are referred to as level 1, but this can be done iteratively to produce several components. Cowan and Cooper (2003) chose to use level 4, 6 and 8 of the approximation detail.

According to their study high approximation levels of the Haar filter reveal the coarser structure of the data (longer wavelength), while lower levels are able to reveal small-scale structure in the magnetic susceptibility data of the BIF units (see Figure 5.11b). Having shown the ability of the DWT to closely match lithological boundaries, Cowan and Cooper (2003) then studied the trends in the data using the CWT shown in Figure 5.12.

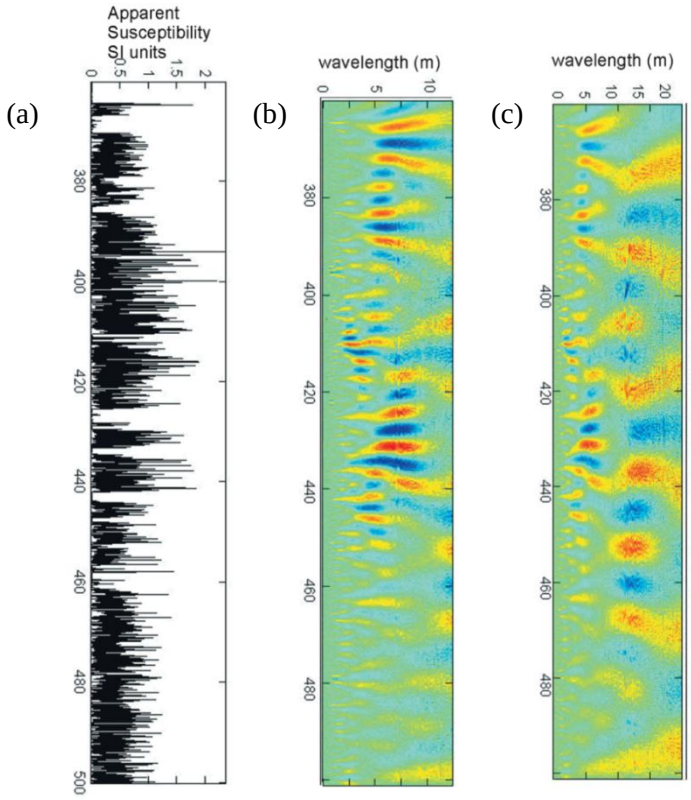

Figure 5.12 (a) Measured magnetic susceptibility data. Figure (b) and (c) show the wavelet analysis for the measured data at different scales of 1-10 m and 10-20 m respectively (Cowan and Cooper, 2003).

Their results show a 15 m wavelength, which ranges in intensity (most intense at ~400 m) and is present almost throughout the section. A wavelength of ~5 m is seen from 360-420 m and then increases to 7 m from 420 m-440 m. It then decreases in amplitude making it difficult to interpret beyond this depth.

Pan et al. (2008) also used both the CWT and DWT like Cowan and Cooper (2003) but combined wavelet analysis with Fourier methods. This apparently allowed them to detect stratigraphic interfaces in a more accurate way then is allowed by computing the WT and doing conventional well log analysis. They carried out a three step process; by calculating both the CWT and DWT, the spectral analysis, followed by a logarithmic transform

successively. Their results of their WT of self-potential (SP) data are shown below (Figure 5.13). Figure 5.13b shows four zones of interest in this study, which are oil sands of the M-formation. These zones have been interpreted as representing different depositional environments. Each of these zones has relatively low SP values compared to the rest of the log.

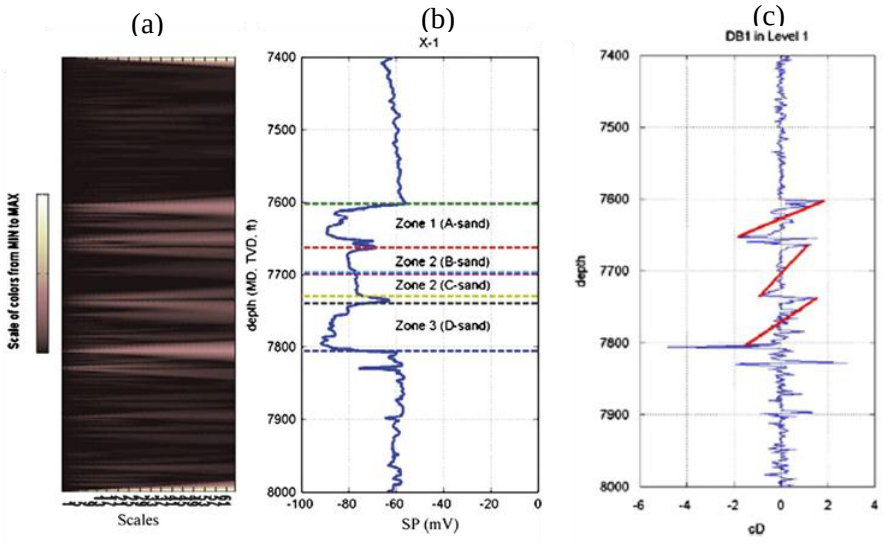

Figure 5.13 CWT for the measured data. (b) Measured SP data for borehole X-1. (c) Plot of the wavelet coefficients of the DWT, for the first approximation level (see text for details) (Pan et al., 2008).

Although these are clearly shown in the SP data, the Pan et al. (2008) could not clearly delineate these zones in the CWT of the data shown in Figure 5.13a. They used the DWT using the Haar wavelet like Cowan and Cooper (2003), to produce the level 1 cA and cD components of their SP and gamma-ray logs. Figure 5.13c shows DWT coefficients for the cD of the SP data, which are able to show the zones of interest better than what was achieved with the CWT. The red lines indicate where each of the zones which have been detected using the DWT. The analysis of the gamma-ray logs was done in a similar fashion to this.

One of the most recent studies in wavelet analysis has been by Verma et al. (2012). This study is one in the petroleum sciences like previous studies by Prokoph and Agterberg (2000) and Pan et al. (2008), interested in identifying interfaces between lithologies. The study takes place in the Cold Lake area of Alberta, analysing a suite of gamma-ray, SP, resistivity, density, and neutron porosity logs. This study uses the Haar wavelet similar to the study by Cowan and Cooper (2003) and Pan et al. (2008), but using the CWT instead.

In addition to this, they calculate the S-transform on some of their dataset, a technique that combines the WFT and the WT. They used this method to analyse noisy density and neutron porosity logs, after applying a median filter to the data. The results of their wavelet analysis on resistivity data are shown below (Figure 5.14).

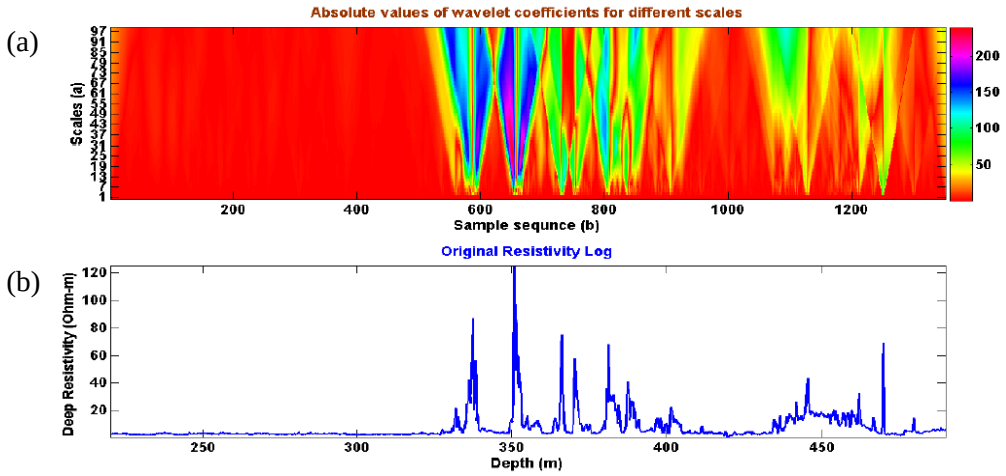

Figure 5.14 (a) Absolute value of the calculated wavelet coefficients for resistivity data. (b) The measured resistivity data (Verma et al., 2012).

They were able to interpret lithological boundaries, which correspond to high wavelet coefficient values. These boundaries are associated with abrupt changes in well log properties which can be observed in Figure 5.14b.

The literature shows that there have been several studies applying the WT method. This method is has been used to quantify sediment accumulation, sedimentary cycles, detect lithology boundaries discontinuities in stratigraphy (e.g. faults and unconformities). However the literature is sparse on wavelet analysis applied to borehole data in magmatic rocks with the exception of the study by Webb et al. (2008) for studying emplacement processes. More so, no comparative studies have been done using the wavelet-based semblance analysis following its use by Cowan and Cooper (2003).

CHAPTER 6: RESULTS - WAVELET ANALYSIS

The results of the CWT of density and magnetic susceptibility data of the Western and Eastern Limb of the BC are presented in this chapter. Where possible, the MZ-CZ boundary (top of the GPA) or the marker closest to it has been indicated in order to show the cyclicity in the data with respect to the major stratigraphic subdivisions of the BC. The data are presented as the lithology log, the physical property log and the CWT of the respect log. The data for the Northern Limb BV-1 borehole by Ashwal et al. (2005) is also presented. A table is presented summarizing all of the various wavelengths observed from individual boreholes. Several boreholes in which coincident markers have been observed are compared using wavelet-based semblance analysis.

6.1 The Western Limb of the BC

6.1.1 Amandelbult

Density Data– EL56

The lithology log, density data (downsampled to 100 cm) and the CWT of the density data are shown in Figure 6.1. The density log in Figure 6.1b has distinct regions of high density values which correspond to IRUPs in the lithology log, observed at depths of 410-510 m, 620-700 m, 850-900 m and 970-1100 m. The average density contrast between the IRUPs and the surrounding country rock is 0.5-1 g/cm^3. The wavelet transform of the density data shown in Figure 6.1c reveals cyclicity in the data at a wavelength of 500 m which decreases linearly to 400 m at a depth of 500 m. Cyclicity is present at a wavelength of 200 m in Figure 6.1d which is consistent but decreases gradually until it reaches 150 m with depth. This signal becomes progressively intense with increasing depth. Figure 6.1e shows a wavelength of 80-100 m which increases in intensity with increasing depth. This wavelength decreases to 60 m at a depth of 1000 m but shows consistency throughout the borehole. There are much smaller wavelengths than these, which are better observed in Figure 6.1f. It becomes more difficult to make observations at this scale, since there is cyclicity at several wavelengths, with varying intensities. For this reason, the image histogram has been thresholded. This figure shows a wavelength of 50 m from a depth of 200 m which decreases to 40 m at a depth of 400 m and decreases in intensity from here on until 600 m. This wavelength shortens steadily from a depth of 1155 m where it reaches a minimum of 30 m. There is also a consistent 20 m wavelength, which is present throughout and most clearly discernible at depths of 300-400 m, 500-550 m and 800-900m.

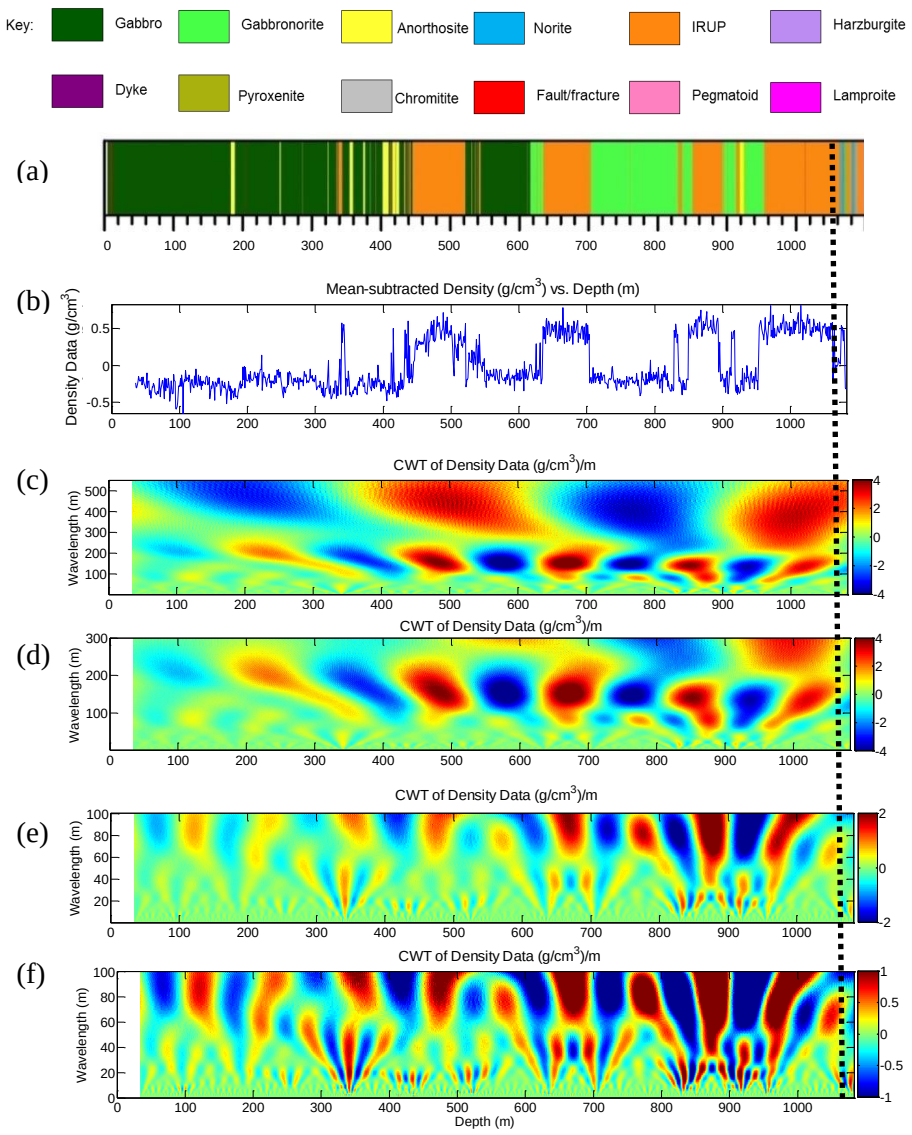

Figure 6.1 (a) Lithology log for borehole EL56. (b) Mean-subtracted density data (g/cm^3) vs. depth (m). CWT of the density data shown on a scale of (c) 1 to 550 m, (d) 1 to 300 m, (e) 1 to 100 m and (f) 1 to 100 m with the image histogram thresholded. The black stippled line shows the approximate location of the Bastard Reef.

The cyclicity in this borehole is observed on several scales, some of which show consistency throughout the borehole. There is no significant difference in wavelengths observed in the MZ and those in the CZ (below the Bastard Reef marker). The signals tend to also increase in intensity with increasing depth. In addition to this, cyclicity at smaller wavelengths is pervasive across both Bushveld rocks and IRUPs. This suggests that the signature of the signal from the replaced rocks has been preserved even following replacement by IRUPs.

Density Data– EL57

The lithology log, density data (downsampled to 100 cm) and the CWT of the density data are shown in Figure 6.2. The effect of the IRUPs on the density log is obvious in the first 280 m (Figure 6.2b). The rest of the log appears homogeneous with variations smaller than 0.4 g/cm^3. Figure 6.2c shows a consistent 450 m wavelength signal with a slight decrease in wavelength with depth. The intensity of this signal does not change significantly but is more intense and dispersed where the IRUPs have been intersected. Figure 6.2d shows a signal with a wavelength of approximately 200 m from the top until 600 m where it then shortens to approximately 150 m. The signal intensity decreases away from the IRUPs. This image also shows a 60 m wavelength seen until 400 m and again from 800 m to 1000 m. The intensity of this signal falls between 400-800 m, but Figure 6.2e shows that it is present at this depth when the histogram of the image is thresholded. There are smaller wavelength features at wavelengths of 30 m and 20 m consistent throughout the borehole. There are wavelengths even shorter than this but they are complex at these very small scales.

Multi-scale cyclicity is observed similar to EL56. Cyclicity is seen to occur in thick units of gabbros and gabbronorite. Interestingly, the 200 m wavelength signal discussed above changes at roughly the gabbro-gabbronorite contact (~600 m). The detection of this boundary is not obvious in the density log, but there is a change in the wavelength of the cyclicity of the data. Lastly, even with the interruption of the IRUPS in the top 280 m of the borehole, the cyclicity can still be observed in the country rocks.

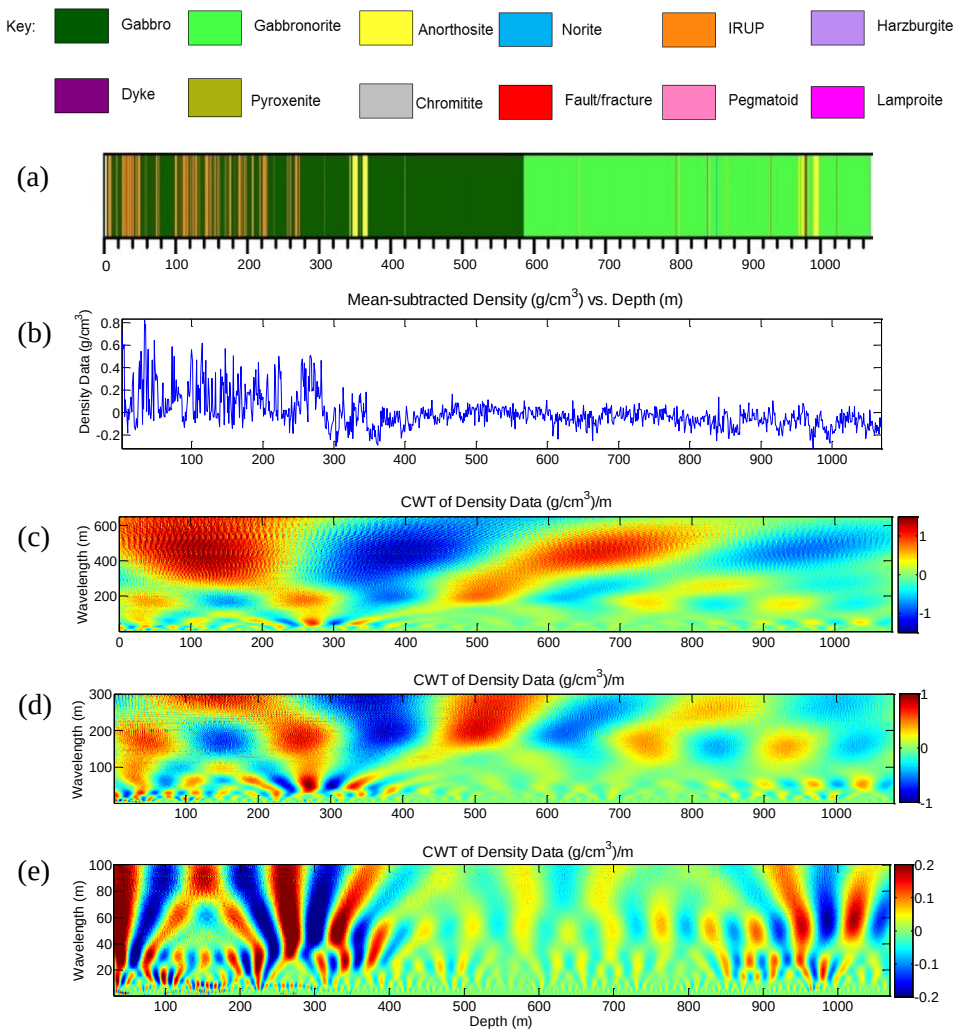

Figure 6.2 (a) Lithology log for borehole EL57. (b) Mean-subtracted density data (g/cm^3) vs. depth (m). CWT of the density data shown on a scale of (c) 1 to 650 m, (d) 1 to 300 m and (e) 1 to 100 m with the image histogram thresholded. There is no record of the CZ.

6.1.2 Union

Density Data– SK59A

The lithology log, density data (downsampled to 100 cm) and the CWT of the density data are shown in Figure 6.3. The stringers of pegmatoid have large density contrasts with the surrounding gabbros and gabbronorites. This is most clearly seen in Figure 6.3b at depths of ~880 m and ~1300 m. Other than the observed larger densities associated with the pegmatoids, the density log appears relatively homogeneous with minor changes with depth.

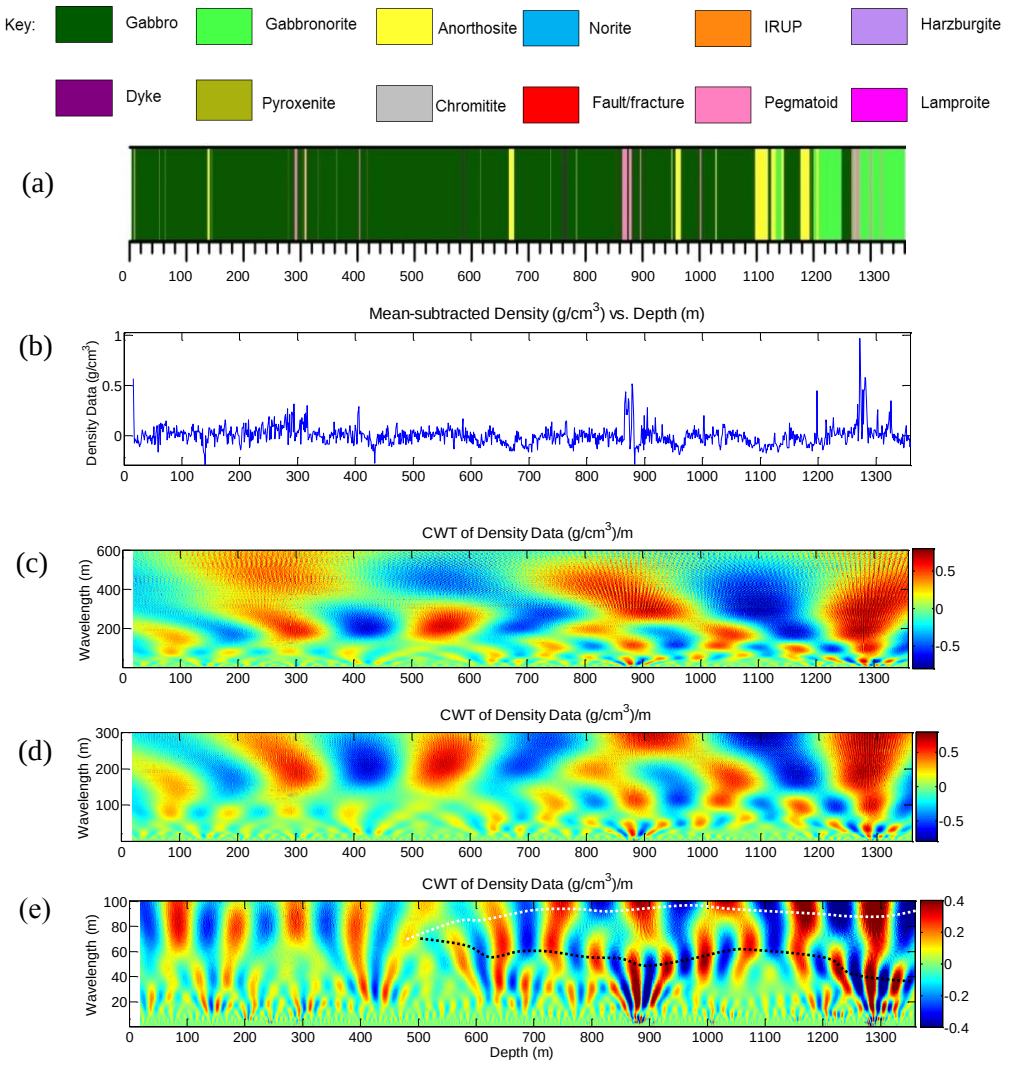

Figure 6.3 (a) Lithology log for borehole SK59A. (b) Mean-subtracted density data (g/cm^3) vs. depth (m). CWT of the density data shown on a scale of (c) 1 to 600 m, (d) 1 to 300 m and (e) 1 to 100 m. There is no record of the CZ. Stippled lines are discussed in the text.

Figure 6.3c shows a 500 m wavelength which decreases gradually with increasing depth until reaching approximately 400 m. Figure 6.3d shows cyclicity at a wavelength of 150 m which increases to 200 m at a depth of 700 m before decreasing back to 150 m. This wavelength seems to also "break" into two at a depth of 700 m to form signals with wavelengths of 250 m and 150 m. Figure 6.3e shows wavelengths smaller than 100 m which show a complex relationship with depth. These show variable intensity and changes in the wavelength with depth. Cyclicity at 80 m can be seen to a depth of 400 m but becomes unclear between 500-550 m depth. The signal splits and decreases to a

wavelength of 60 m which undulates with depth before steeply approaching a wavelength of 40 m, indicated by the black stippled line. The 40 m wavelength can also be seen vaguely at shallower depths between 100 m and 200 m, 350-400 m and 600-900 m depths. The white stippled line shows the 60 m wavelength increase to 100 m and stays constant from approximately 750-1100 m before falling to 80 m towards the end.

Cyclicity is multi-scale and although it is consistent, it shows more changes with depth than the boreholes previously discussed. This is especially true at small scales (< 80 m). Lastly, cyclicity is observed both within lithologies and across them.

6.1.3 Styldrift

Density Data– SO2

The lithology log, density data (downsampled to 20 cm) and the CWT of the density data are shown in Figure 6.4. This borehole is thinly layered, and does not contain thick homogeneous units seen before. The measured density data in Figure 6.4b contains several spikes 100 m apart, at depths of approximately 100 m, 200 m, 300 m and 400 m in the MZ. These are spatially associated with dyke stringers in Figure 6.4a. The spikes in the CZ are associated with chromitite and pyroxenite layers. This borehole suffers from edge effects, therefore only the data up to 630 m has been used for the CWT. Figure 6.4c shows cyclicity at a wavelength of approximately 130 m (at 100 m) which increases to 140-160 m. The intensity of this wavelength increases with depth from the MZ towards the rocks of the CZ. A 80 m wavelength can be vaguely seen from 300 m depth onwards, and is not clearly discernible towards the top of the borehole. Figure 6.4d shows cyclicity at 50 m wavelength which decreases sharply towards the bottom of the borehole from a depth of 500 m and reaches approximately 20 m.

Cyclicity on several scales has been observed in borehole SO2 some of which are consistent throughout the borehole.

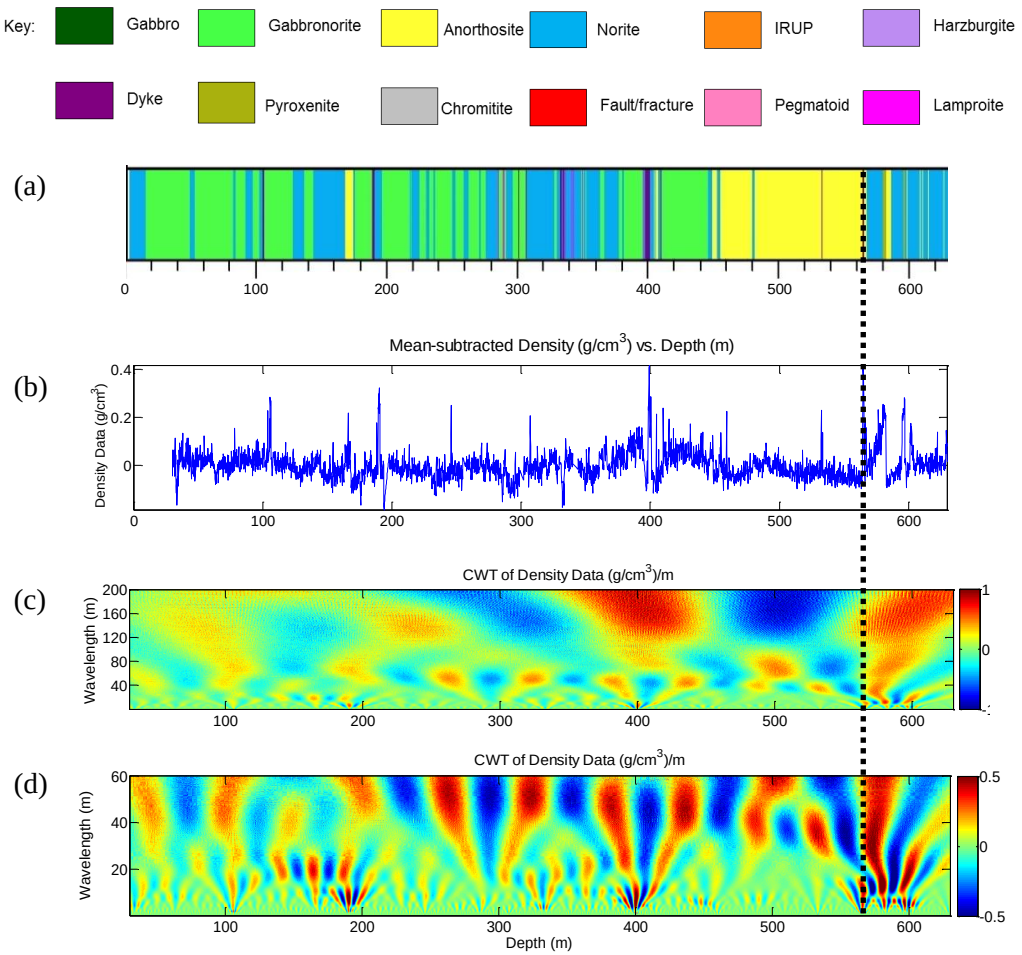

Figure 6.4 (a) Lithology log for borehole SO2. (b) Mean-subtracted density data (g/cm^3) vs. depth (m). CWT of the density data shown on a scale of (c) 1 to 200 m and (d) 1 to 60 m. The black stippled line shows the approximate location of the MZ-CZ boundary.

While some of the shorter wavelength signals have been observed to end abruptly, the longer wavelengths are consistent across both lithology boundaries as well as the MZ-CZ boundary. The steep change in the cyclicity at a wavelength of 50 m may document the MZ-CZ transition.

Magnetic Susceptibility Data– SO2

The lithology log, magnetic susceptibility data (downsampled to 20 cm) and the CWT of the susceptibility data are shown in Figure 6.5. These show large amplitude spikes of up to 4 SI. A close study of both Figure 6.5b and c shows that these spikes are associated with dykes stringers and lamproites. Although these spikes create edge effects in the

CWT, the cyclicity can be observed when the histogram of the image has been sufficiently thresholded.

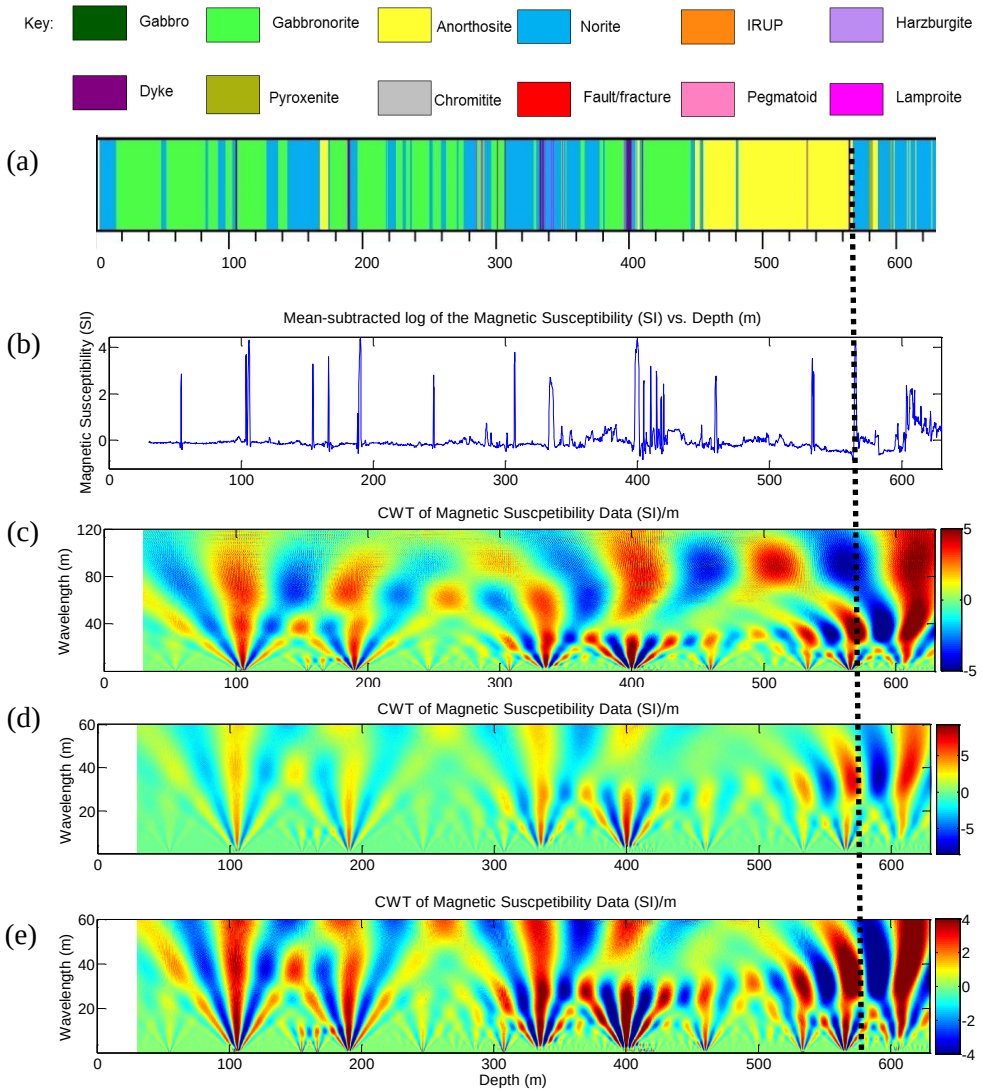

Figure 6.5 (a) Lithology log for borehole SO2. (b) Mean-subtracted log of the magnetic susceptibility (SI) vs. depth (m). CWT of the magnetic susceptibility data shown on a scale of (c) 1 to 120 m, (d) 1 to 60 m and (e) 1 to 60 m with the image histogram thresholded. The black stippled line shows the approximate location of the MZ-CZ boundary.

Cyclicity is observed in Figure 6.5c at a wavelength that starts off as 80 m until a depth of 200 m. It then breaks up to form two wavelengths of 90 m and 60 m between 200 m and 350 m. These wavelengths then merge and return to 90 m for the remainder of the borehole. Figure 6.5d shows a wavelength of 40 m wavelength, whose continuity can be better studied in Figure 6.5e. This wavelength is visible until 200 m. A 20 m wavelength can be seen until 450 m, before increasing steeply to 45 m. The continuity of this

wavelength is not clear from just studying Figure 6.5d, but the continuity is shown in Figure 6.5e. A 10 m wavelength is also seen, although it is not clearly visible throughout the borehole. The edges obscure some features which may be present.

The density and magnetic susceptibility data for SO2 show similarities in cyclicity at wavelengths of 80 m, 20 m and 10 m. While some wavelengths in the density data generally become longer with depth, wavelengths in the magnetic susceptibility data shorten with depth.

6.1.4 RPM

Density Data– KLG52

The lithology log, density data (downsampled to 100 cm) and the CWT of the density data are shown in Figure 6.6. This type of lithology log is ideal since it has thick homogenous units in the MZ. The density data in Figure 6.6b shows some variation although it is generally less than 0.4 g/cm^3. It also shows some spikes, some of which are associated with dykes and pegmatoids. In the CZ the higher densities are associated with pyroxenites, and the lower values with norites and anorthosites. Cyclicity is seen at a wavelength of 400 m which increases to 500 m and then decreases back to 400 m in Figure 6.6c. Figure 6.6d shows cyclicity at a wavelength of 275 m which decreases to ~250 m (800 m depth) before increasing back to 275 m and remaining fairly constant. This image also shows a 75 m wavelength which increases to approximately 100 m at a depth of ~1200 m. The signal then becomes unclear, but can be studied in Figure 6.6e which shows its continuity. Cyclicity is also present at 150 m wavelength up to a depth of 400 m, after which it seems to be replaced by the abovementioned 275 m wavelength. There is also cyclicity at smaller wavelengths but are more complex with clearer signals at wavelengths of 40-60 m but this shows great variation with depth.

This borehole shows non-stationary multi-scale cyclicity even though the lithology log consists mostly of thick gabbronorite units.

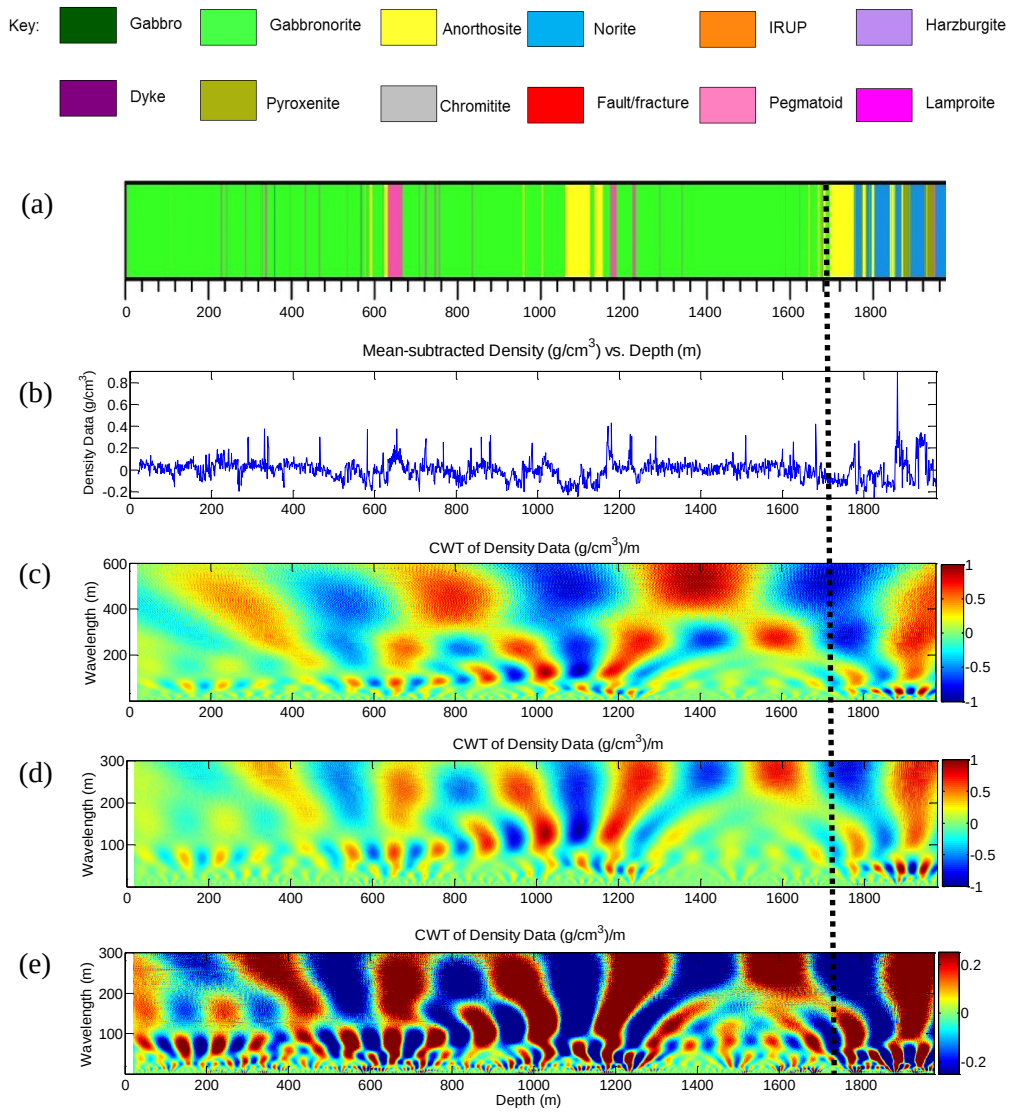

Figure 6.6 (a) Lithology log for borehole KLG52. (b) Mean-subtracted density data (g/cm^3) vs. depth (m). CWT of the density data shown on a scale of (c) 1 to 600 m, (d) 1 to 300 m and (e) 1 to 300 m with the image histogram thresholded. The black stippled line shows the approximate location of the MZ-CZ boundary.

Magnetic Susceptibility Data- KLG52

The lithology log, magnetic susceptibility data (downsampled to 100 cm) and the CWT of the susceptibility data are shown in Figure 6.7. The magnetic susceptibility log is shown in Figure 6.7b and is visibly noisy. Some of the spikes in this data are spatially associated with stringers of the pegmatoids and dykes. However they are also seen within units of gabbronorite of the MZ when compared to the lithology log in Figure 6.7a. The anorthosite and gabbronorite layers show a much smoother response.

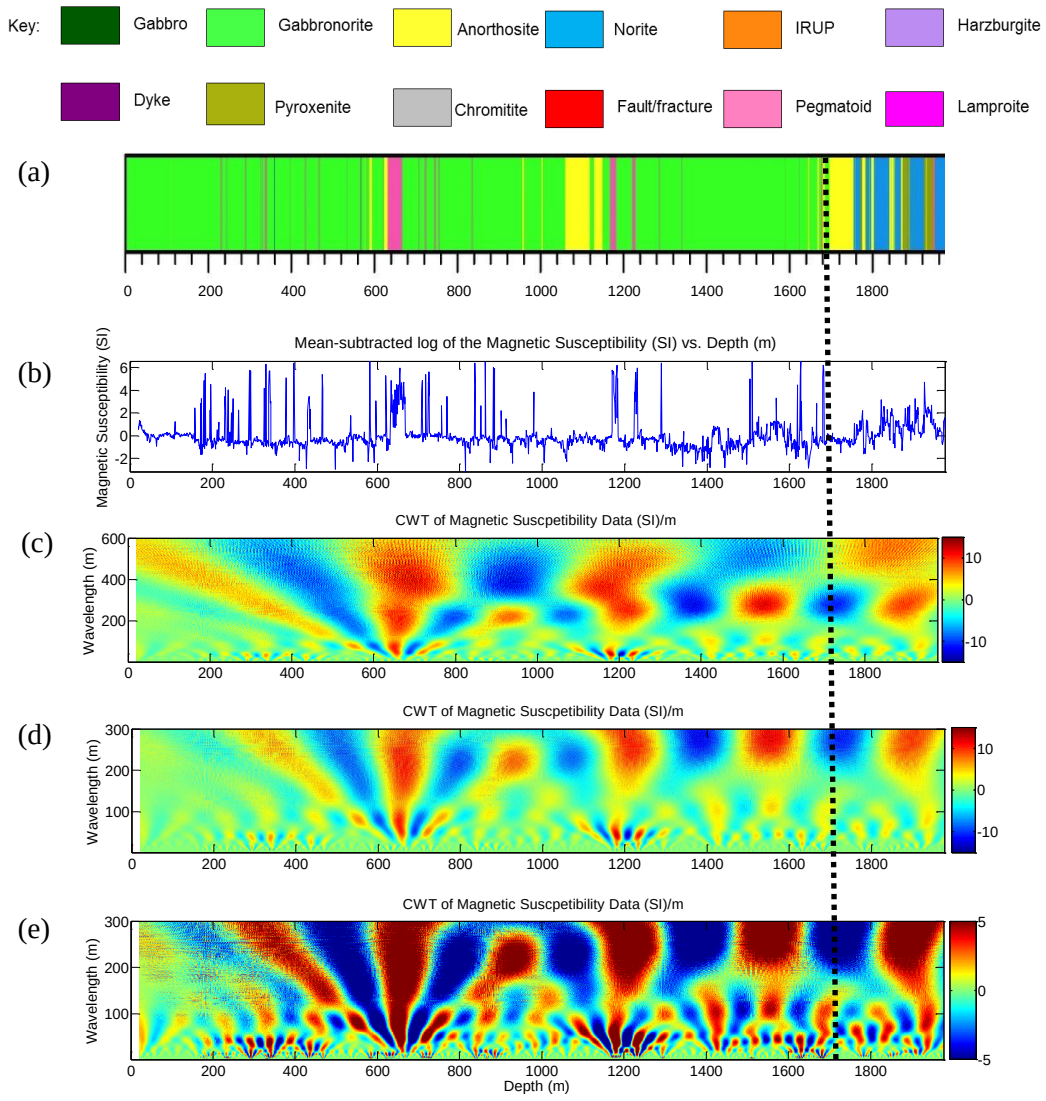

Figure 6.7 (a) Lithology log for borehole KLG52. (b) Mean-subtracted log of the magnetic susceptibility data (SI) vs. depth (m). CWT of the magnetic susceptibility data shown on a scale of (c) 1 to 1000 m, (d) 1 to 300 m and (e) 1 to 300 m with the image histogram thresholded. The black stippled line shows the approximate location of the MZ-CZ boundary.

Figure 6.7c shows consistent cyclicity at a wavelength of 400 m from a depth of 400 m, which increases to 500 m and then remains constant with depth. Figure 6.7d shows a 200 m wavelength from a depth of 250 m which shows a linear increase to 250 m gradually with depth. This image also shows an 80-100 m wavelength with changing intensity. This wavelength is seen clearer when the image histogram is thresholded in Figure 6.7e, and is consistent throughout. Wavelengths of 50 m and 20 m are also observed. The cyclicities in this borehole are consistent and multi-scale. The thick layers of gabbronorite also document cyclicity within them. The density and the magnetic susceptibility show the

same cyclicities at a wavelength of 400 m. The cyclicity is seen to be consistent across the MZ-CZ without disturbance at this stratigraphic boundary.

Density Data– KLG8

The lithology log, density data (downsampled to 100 cm) and the CWT of the density data are shown in Figure 6.8.

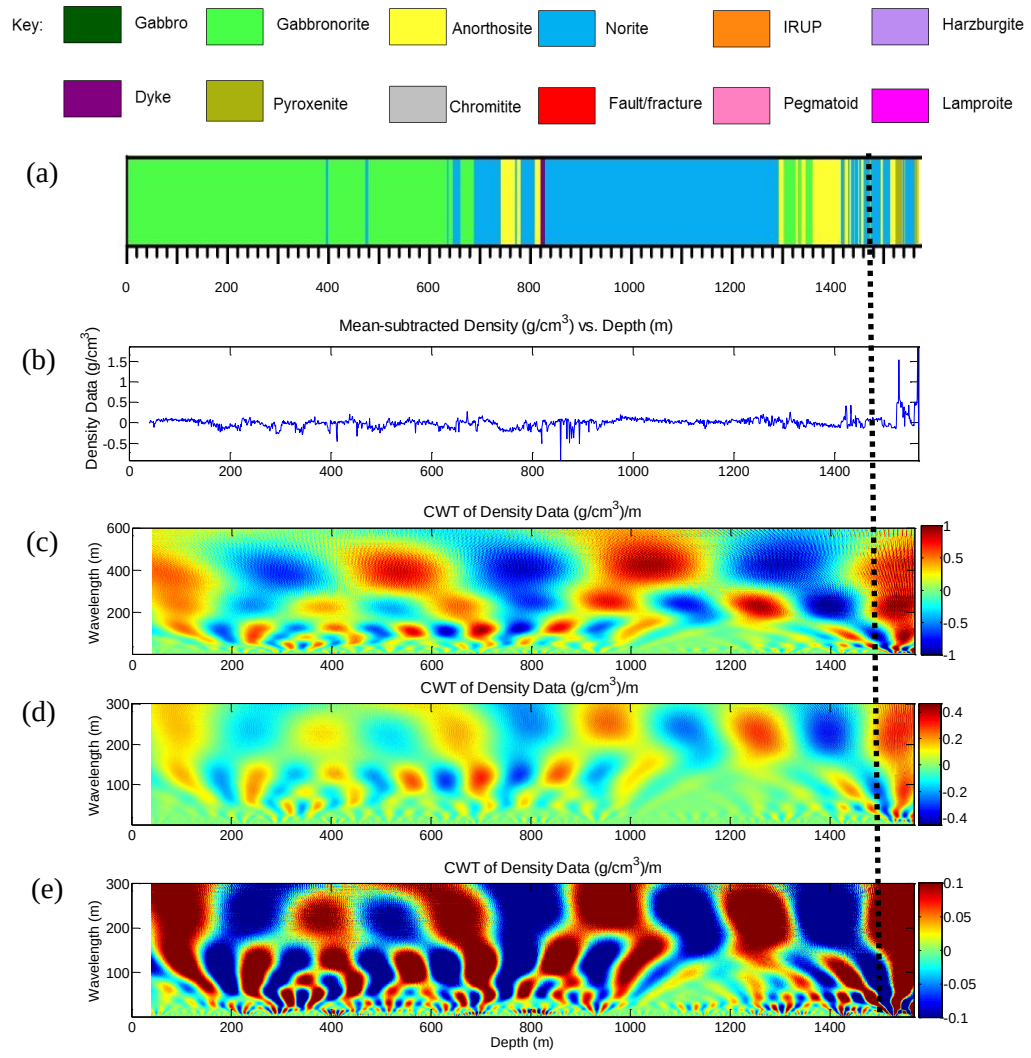

Figure 6.8 (a) Lithology log for borehole KLG8. (b) Mean-subtracted density data (g/cm^3) vs. depth (m). CWT of the density data shown on a scale of (c) 1 to 600 m, (d) 1 to 300 m (e) and 1 to 300 m with the image histogram thresholded. The black stippled line shows the approximate location of the MZ-CZ boundary.

The density data shown in Figure 6.8b is homogeneous, reflecting the homogeneity of the lithology log. Generally, there is no distinct density contrast between the gabbronorites, norites and the anorthosite layers. Larger density values observed in the CZ are associated

with pyroxenite layers. The wavelet analysis of for this data shown in Figure 6.8c has a consistent cyclicity at a wavelength of 400 m, which increases steadily in wavelength towards the CZ to 450 m, before decreasing back to 400 m. Cyclicity is also seen at 250 m wavelength in Figure 6.8d whose wavelength increases to approximately 275 m at 1000 m depth, before decreasing back to 250 m. Figure 6.8d shows cyclicity at wavelengths of 100 m which increases to approximately 125 m wavelength at 1000 m depth and falls to 100 m from 1400 m onwards. It loses intensity at 1000–1400 m but is still present as shown in Figure 6.8e whose histogram has been thresholded. This image also shows cyclicity at 50 m and 25 m which are consistent with depth, but are complicated and change in intensity with depth as seen in previous boreholes.

The density data for borehole KLG8 shows the multi-scale cyclicity observed before, and wavelet analysis has revealed cyclicity in homogeneous layers of norites and gabbronorites. The cyclicity is also seen to be consistent across lithology boundaries and with depth. This is with the exception of the 125 m wavelength was seen to change in intensity with depth towards the CZ. The wavelengths studied generally increase in wavelength and intensity towards the CZ. However no obvious changes in cyclicity across the MZ-CZ boundary have been observed.

6.2 The Eastern Limb of the BC

6.2.1 Booysendaal

Density Data– BY63

The lithology log, density data (downsampled to 20 cm) and the CWT of the density data are shown in Figure 6.9. The contact between the Bastard Reef and gabbronorite is observed in the density data, although not clearly since this is a thin layer. An unusual anomaly is seen at a depth of approximately 320 m associated with an anorthosite layer in Figure 6.9a. A density contrast of up to 0.6 g/cm^3 of pyroxenite with anorthosite and norite are also seen at a depth of approximately 540 m.

Figure 6.9c shows cyclicity at a wavelength of approximately 120 m which decreases linearly to 100 m.

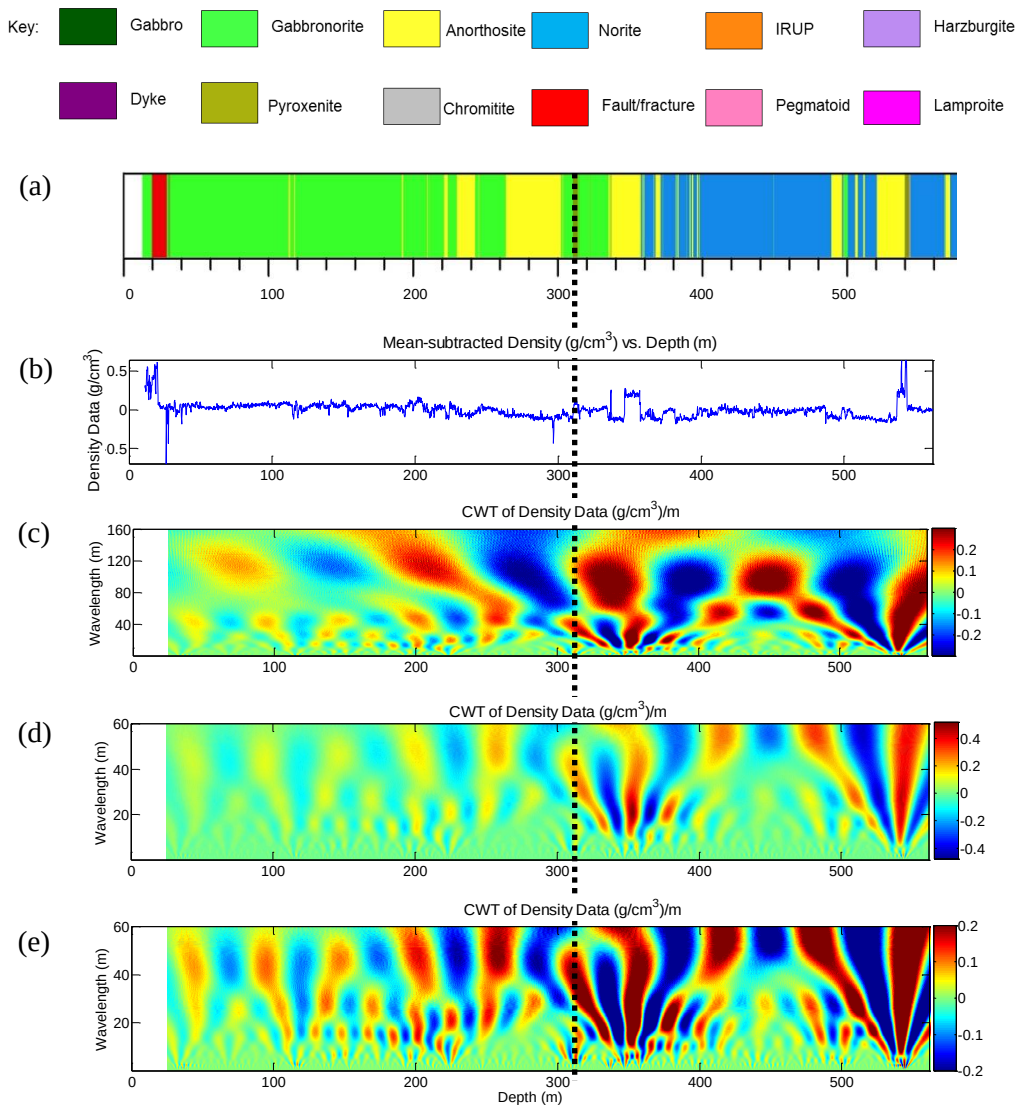

Figure 6.9 (a) Lithology log for borehole BY63. (b) Mean-subtracted density data (g/cm^3) vs. depth (m). CWT of the density data shown on a scale of (c) 1 to 160 m with the image histogram thresholded, (d) 1 to 60 m and (e) 1 to 60 m with the image histogram thresholded. The black stippled line shows the approximate location of the Bastard Reef marker.

Figure 6.9d shows a wavelength of approximately 50 m whose intensity increases with depth and whose wavelength increases to 60 m. Figure 6.9e shows the same image with the histogram thresholded to show smaller wavelength features. The shorter wavelengths are complicated, showing variable change in intensity and wavelength with depth. It shows wavelengths of approximately 20-30 m which is consistent through depth. There is also a 10-20 m wavelength which is clearly seen at depths of 100-250 m, 300-410 m and from 480 m onwards.

A linear decrease in wavelength is seen in the density data as well as in the cyclicity at wavelengths of 200-180 m and 120-100 m. Cyclicities are also multi-scale as seen before, with wavelengths generally showing consistency with depth throughout the borehole. These are observed in thick sections of homogeneous gabbronorite and norite whose density data show cyclicity.

Magnetic Susceptibility Data– BY63

The lithology log, magnetic susceptibility data (downsampled to 20 cm) and the CWT of the susceptibility data are shown in Figure 6.10. Figure 6.10b shows a relatively homogeneous log of the susceptibility. Large values in susceptibilities are observed at depths of ~340 m and 540 m, which are associated with pyroxenite layers with a susceptibility contrast of 3 SI. The Bastard Reef also shows a subtle contrast in susceptibility with the surrounding gabbronorites. Figure 6.10c shows cyclicity at a wavelength of approximately 80 m at depths greater than 400 m. Figure 6.10d below it shows the same image with the histogram thresholded, which shows that this wavelength is diffuse and dominated by noise at shallower depths. The cyclicity is lost at these depths. Figure 6.10d also shows a consistent 60 m wavelength at the top of the borehole, which gradually decreases in wavelength to 20 m with increasing depth. Figure 6.10e shows shorter wavelengths which are generally not consistent throughout the borehole, at wavelengths of 15 m, 10 m and 5 m. This borehole does not convincingly show cyclicity in the 80 m wavelength at depths shallower than 400 m which consists mostly of gabbronorite. Cyclicity was seen the density data however, even though it was weak. The density and susceptibility data show common cyclicity at wavelengths of 60 m, 20 m and 10 m.

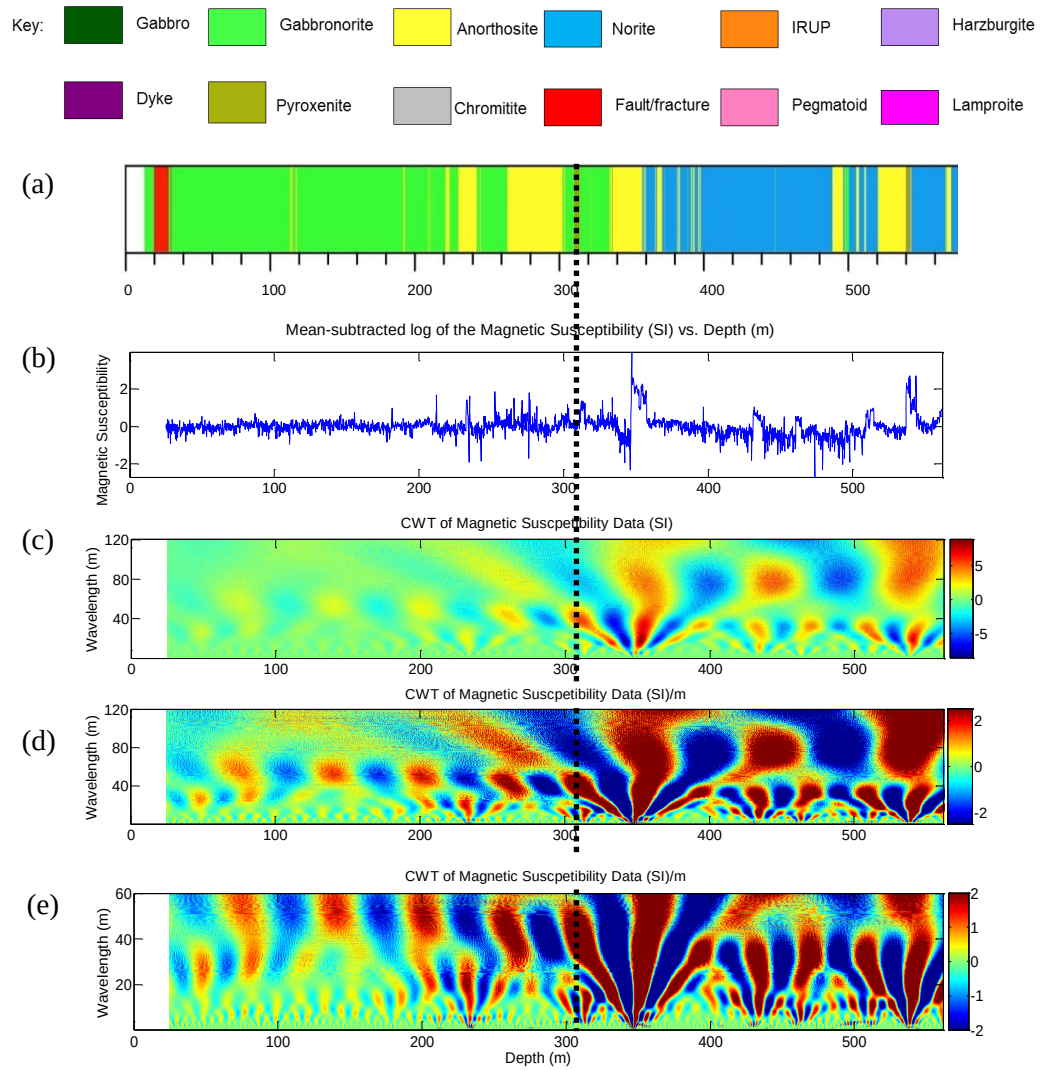

Figure 6.10 (a) Lithology log for borehole BY63. (b) Mean-subtracted log of the magnetic susceptibility data (SI) vs. depth (m). CWT of the magnetic susceptibility data shown on a scale of (c) 1 to 120 m, (d) 1 to 120 m with the image histogram thresholded and (e) 1 to 60 m with the image histogram thresholded. The black stippled line shows the approximate location of the Bastard Reef marker.

Density Data– BY60

The lithology log, density data (downsampled to 20 cm) and the CWT of the density data are shown in Figure 6.11. This core is made up entirely of CZ rocks consisting of norite, anorthosite and minor pyroxenite. The dolerite intrusion which has been intersected constitutes most of the borehole from approximately a depth of 225 m onwards (Figure 6.11a). The density is generally smaller for anorthosites, and larger for norites by up to approximately 0.2 g/cm^3 (seen clearly at a depth of 57.5 m) (Figure 6.11b). The large

density contrast of the pyroxenite from the surrounding anorthosites is observed at a depth of 75 m to be approximately 0.5 g/cm^3.

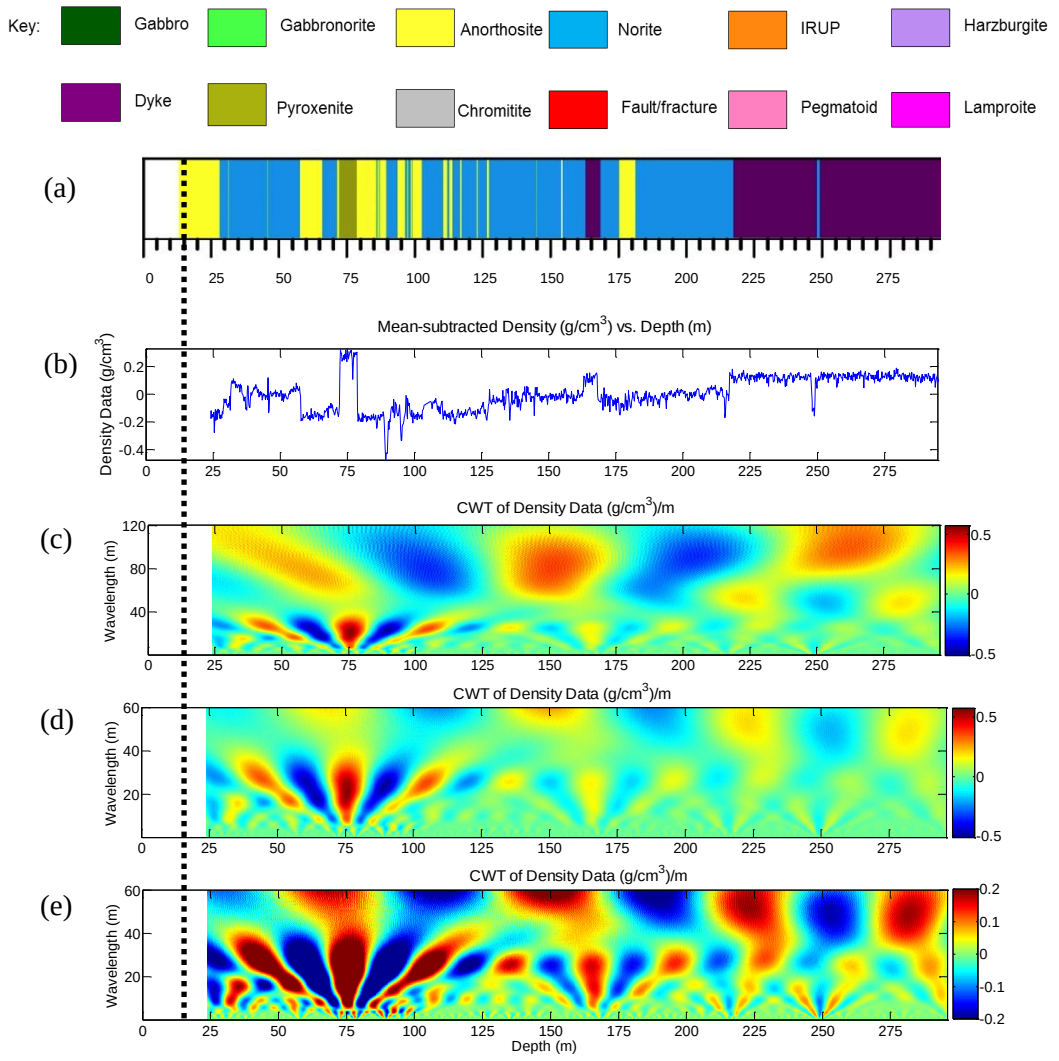

Figure 6.11 (a) Lithology log for borehole BY60. (b) Mean-subtracted density data (g/cm^3) vs. depth (m). (c) CWT of the density data shown on a scale of 1 to 120 m (d) 1 to 60 m and (e) 1 to 60 m with the image histogram thresholded. The location of the MZ-CZ boundary is indicated by the black stippled line.

The next significant density contrast is seen at a depth of 165 m, at the contact between the dolerite intrusion and the surrounding norites. The density log also maps the norite-dolerite contact at a depth of 215 m. There density log as whole has an increasing linear trend down the borehole. Figure 6.11c shows cyclicity at a wavelength of 80 m which increases to 100 m with increasing depth and is consistent throughout the borehole. Interestingly, it is seen to be unperturbed at the norite-dolerite contact at 215 m depth. The cyclicity is also constant through the dolerite, albeit increasing. This signal seems to

also “break-up” at a depth of 225 m, forming another wavelength of 45 m. This 45 m signal is only seen in the dolerite. Figure 6.11d shows cyclicity at a wavelength of 25 m, but this loses intensity gradually with increasing depth. Figure 6.11e whose histogram has been thresholded, shows that this wavelength is continuous throughout the borehole. This image also shows a wavelength of 10 m and 15 m with varying intensity with depth.

This data shows multi-scale cyclicity. The uniqueness of this borehole is that it has intersected a thick dolerite intrusion, whose density data also exhibits cyclicity similar to that of the host rocks. Interestingly though, a 45 m wavelength is seen, which is not present in the host rocks. The density log also easily maps the different lithology units in this borehole.

Magnetic Susceptibility Data– BY60

The lithology log, magnetic susceptibility data (downsampled to 20 cm) and the CWT of the susceptibility data are shown in Figure 6.12. Figure 6.12c shows the magnetic susceptibility of the data. The magnetic susceptibility is able to map the major lithology boundaries. These are seen to be at 75 m between the pyroxenite layer and the surrounding anorthosites, between the dolerite and the surrounding norites at 165 m and the contact between the dolerite and norite at 215 m. The magnetic susceptibility however, is not able to show the contacts between the anorthosite and norite. The susceptibility data shows a linear decrease in with depth until 215 m before the dolerite is encountered, after which there is an increase of 0.3 SI in susceptibility. Cyclicity in Figure 6.12c is at a wavelength of ~120 m, whose intensity increases with increasing depth towards the thick dolerite. A 50 m wavelength is also present, from 150 m until the end of the borehole. Figure 6.12d shows the presence of this wavelength at shallower depths (< 150 m). Cyclicity is also seen at a wavelength of 25 m which is consistent with depth although not clear at shallow depths. A 10 m wavelength is also present although not consistent at depth 200-250 m.

The cyclicity is multi-scale, although unlike the boreholes seen before, there is no consistent cyclicity at smaller wavelengths (<10 m). Also the cyclicity at longer wavelengths is seen to increase in wavelength as opposed to shorter wavelengths which decrease with depth. Intensity at depths shallower than 125 m is weak, in the weakly

magnetic norites and anorthosites. Common cyclicity is seen in both of these physical property data at wavelengths of 25 m and 10 m.

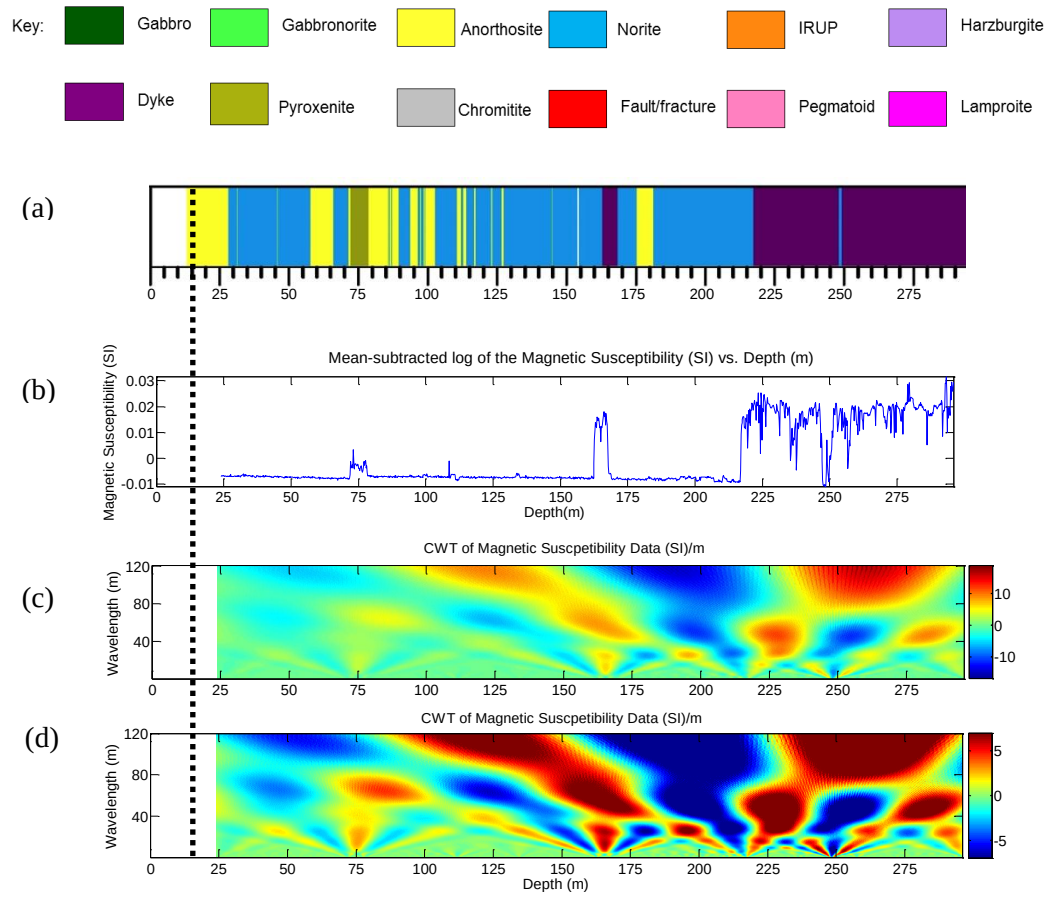

Figure 6.12 (a) Lithology log for borehole BY60. (b) Mean-subtracted log of the magnetic susceptibility data (SI) vs. depth (m). CWT of the magnetic susceptibility data shown on a scale of (c) 1 to 120 m, and (d) 1 to 120 with the image histogram thresholded.

6.2.2 Der Brochen

Density Data– DB136

The lithology log, density data (downsampled to 20 cm) and the CWT of the density data are shown in Figure 6.13. The first pyroxenite layer at a depth of 180 m shows a large density contrast of approximately 0.4 g/cm^3 with respect to the surrounding anorthosites. Pyroxenite and chromitite layers seen at a depth of approximately 370-385 m also show larger density values.

Figure 6.13c shows cyclicity at a wavelength of 100 m, which is consistent throughout the borehole with increasing intensity with depth. Figure 6.13d shows cyclicity at 50 m, which is consistent throughout the borehole but absent at depths of 30-50 m.

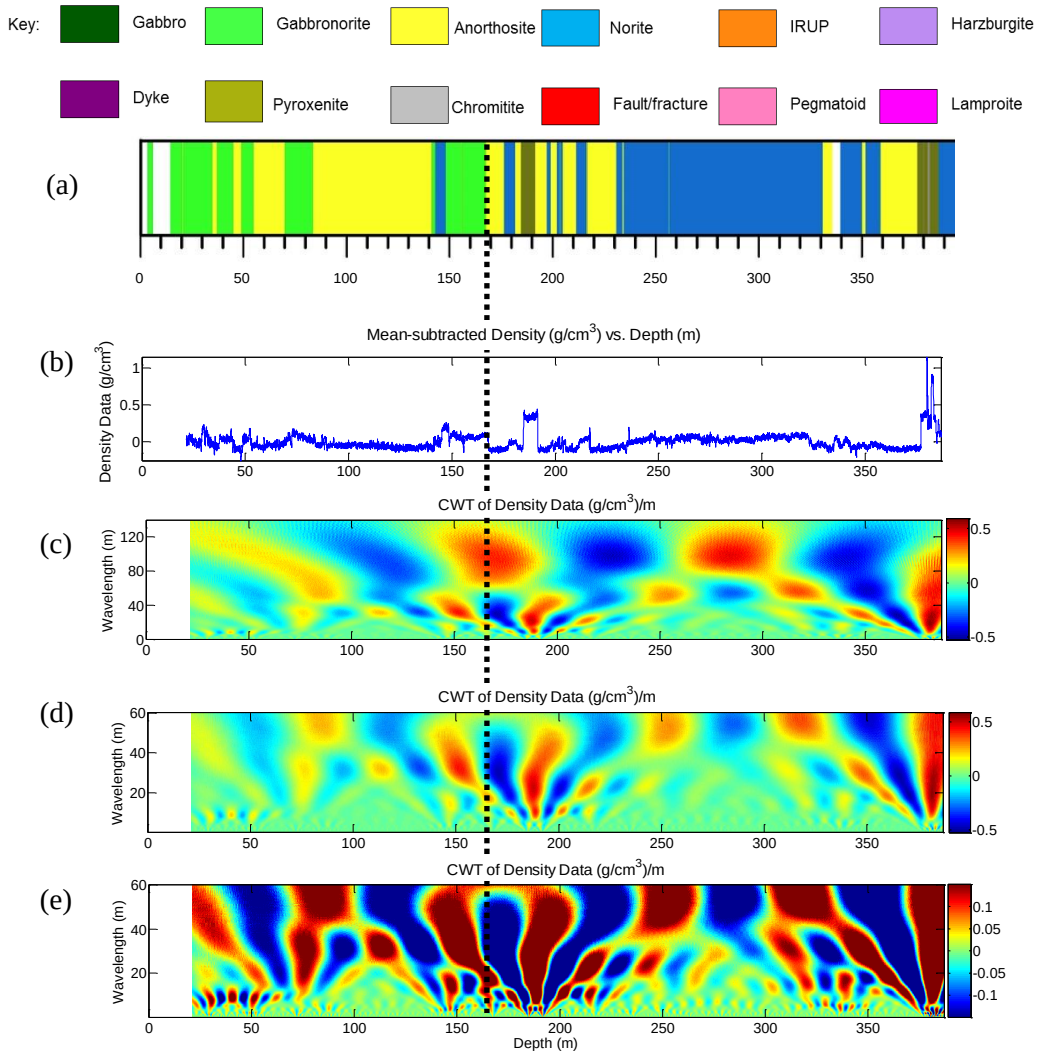

Figure 6.13 (a) Lithology log for borehole DB136. (b) Log of the mean-subtracted density data (g/cm^3) vs. depth (m). CWT of the density data shown on a scale of (c) 1 to 140 m with the image histogram thresholded, (d) 1 to 60 m and (e) 1 to 60 m with the image histogram thresholded. The black stippled line shows the approximate location of the MZ-CZ boundary.

This figure also shows a 40 m wavelength which decreases to 150 m and is not present at depths more than 200 m. Figure 6.13e shows that it is possibly replaced by a wavelength of 20 m from 200-300 m which then increases back to 30 m. This wavelength is also seen from the top of the borehole to a depth of 100m. Cyclicity is also present at wavelengths of 10 m, although it is not present at 75-130 m and 250-300 m. The cyclicity in the

density data shows no clear changes in wavelength across the lithology boundaries, nor are there significant changes across the MZ-CZ boundary. This data also shows replacement of one wavelength by another.

Magnetic Susceptibility Data– DB136

The lithology log, density data (downsampled to 20 cm) and the CWT of the density data are shown in Figure 6.14.

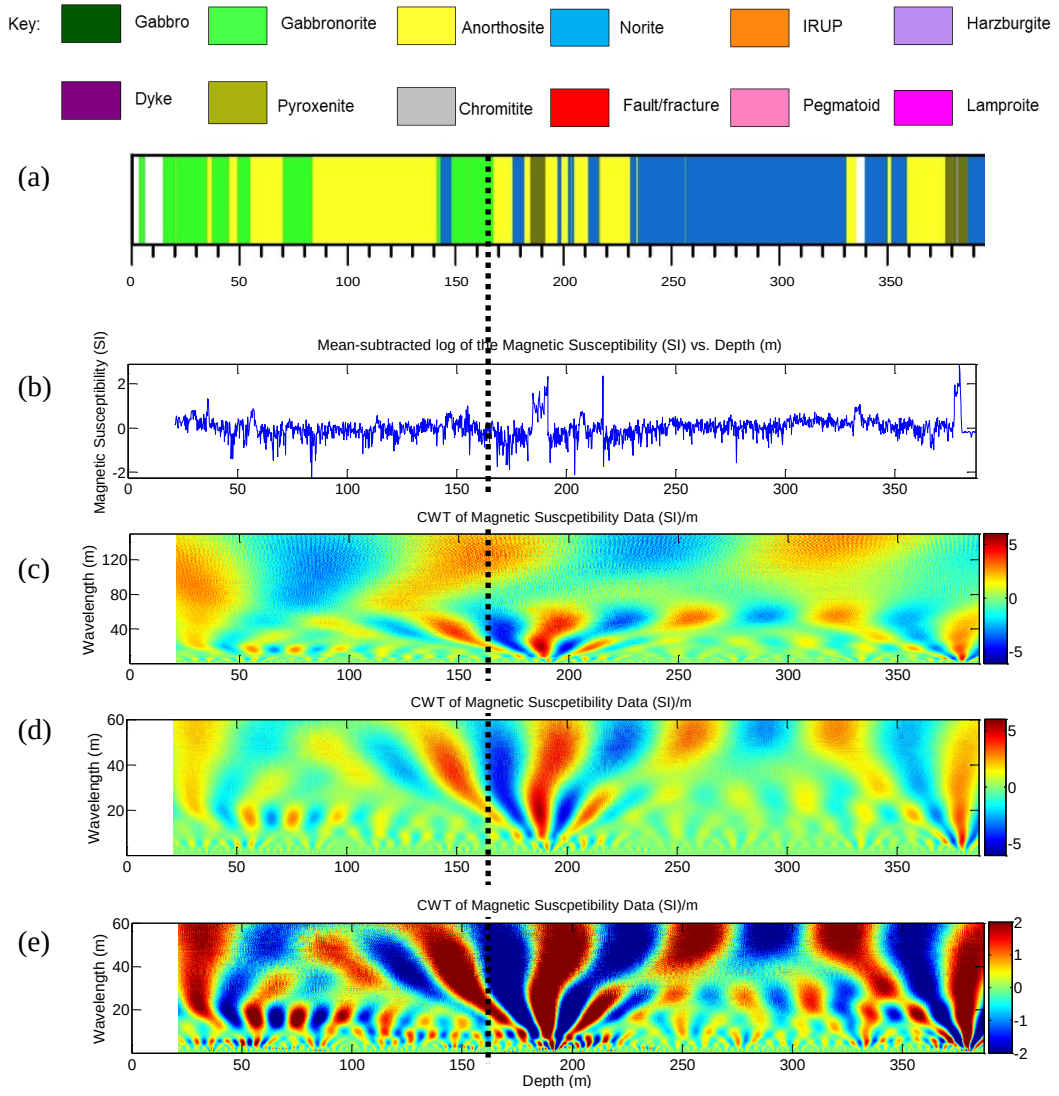

Figure 6.14 (a) Lithology log for borehole DB136. (b) Mean-subtracted log of the magnetic susceptibility data (SI) vs. depth (m). (c) CWT of the magnetic susceptibility data shown on a scale of 1 to 150 m with the image histogram thresholded, (d) 1 to 60 m and (e) 1 to 60 m with the image histogram thresholded. The black stippled line shows the approximate location of the MZ-CZ boundary.

The magnetic susceptibility log shown in Figure 6.14b shows some variations with no contrast between gabbronorites and anorthosites. The larger values are also associated with pyroxenite layers, which show a susceptibility contrast of 2 SI with respect to the anorthosite layers. Figure 6.14c shows cyclicity from a wavelength of 80 m, which increases to 120 m at a depth of approximately 150 m and is consistent. Figure 6.14d shows a wavelength of approximately 50 m towards the top of the borehole, which decreases to 40 m at a depth of 150 m before increasing back to 50 m. Figure 6.14e shows a wavelength of 20 m which loses intensity at depths of 250-325 m but is present at depths >325 m. Smaller wavelengths are complex but consistent throughout the borehole at wavelengths as small as 5m. There is generally no perturbation in cyclicity across the MZ-CZ boundary. The density and susceptibility data shows common cyclicity at wavelengths of 250 m, 150 m and 100 m.

Density Data– DB135

The lithology log, density data (downsampled to 20 cm) and the CWT of the density data are shown in Figure 6.15. The density log shows spikes which are spatially associated with a pyroxenite layer at 430 m and the chromitite layer at 560 m depth. Figure 6.15c shows cyclicity at a wavelength of 80 m at depths greater than 150 m with a low intensity at shallow depths. Figure 6.15d shows the same image with the histogram modified, which shows consistency of this wavelength at shallower depths. However it has a shorter wavelength of 60 m towards the top of the borehole. The 60 m wavelength is also seen from 300-500 m, but is obscured by edge effects in the data. Figure 6.15e shows a 30 m wavelength from a depth of 150 m onwards, which is not discernible at depths shallower than this. This image also shows a wavelength of 20 m at depths of 125-175 m, 250-300 m and from 400-525 m. Cyclicities at a wavelength of 10-15 m, are present although not consistent throughout the borehole. In particular, the MZ-CZ boundary can be detected solely on the intensity of the signal. The intensity of the cyclicity in the MZ is less than that in the CZ. The 30 m wavelength is almost exclusively present in the CZ and not the MZ this is density.

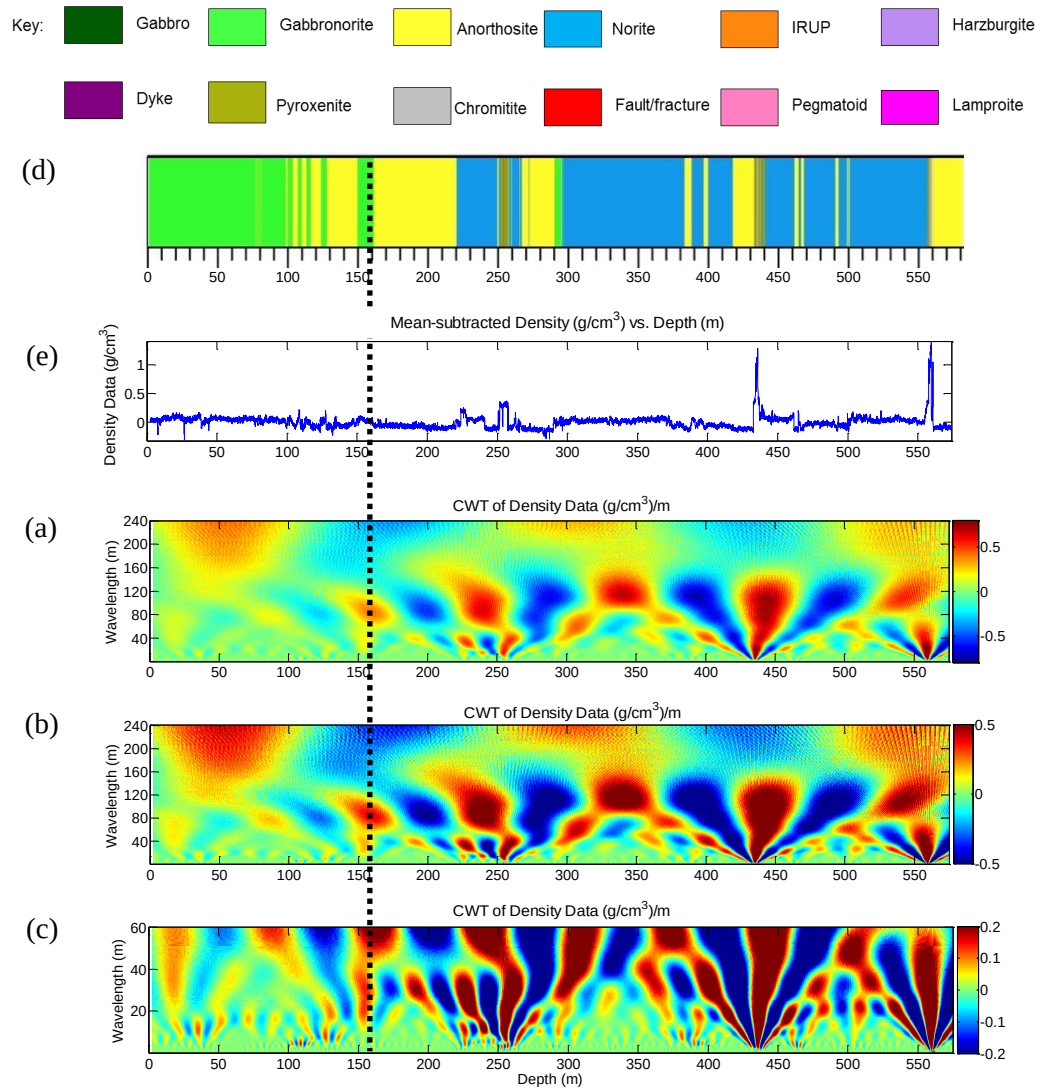

Figure 6.15 (a) Lithology log for borehole DB135. (b) Mean-subtracted density data (g/cm^3) vs. depth (m). CWT of the density data shown on a scale of (c) 1 to 240 m, (d) 1 to 240 m with the image histogram thresholded and (e) 1 to 60 m with the image histogram thresholded. The black stippled line shows the approximate location of the MZ-CZ boundary.

Magnetic Susceptibility Data– DB135

The lithology log, magnetic susceptibility data (downsampled to 20 cm) and the CWT of the susceptibility data are shown in Figure 6.16. The large susceptibilities in Figure 6.16b, which are mostly associated with pyroxenites at depths of ~250 m and 440 m. Cyclicity is present at a wavelength of 80 m which decreases in wavelength with increasing depth to 50 m. Figure 6.16d shows a 40 m wavelength which is only present at depths shallower than approximately 75 m (i.e. the MZ). Cyclicity at a wavelength of 25 m is also present at depths of 200-300 m and at depths greater than 400 m.

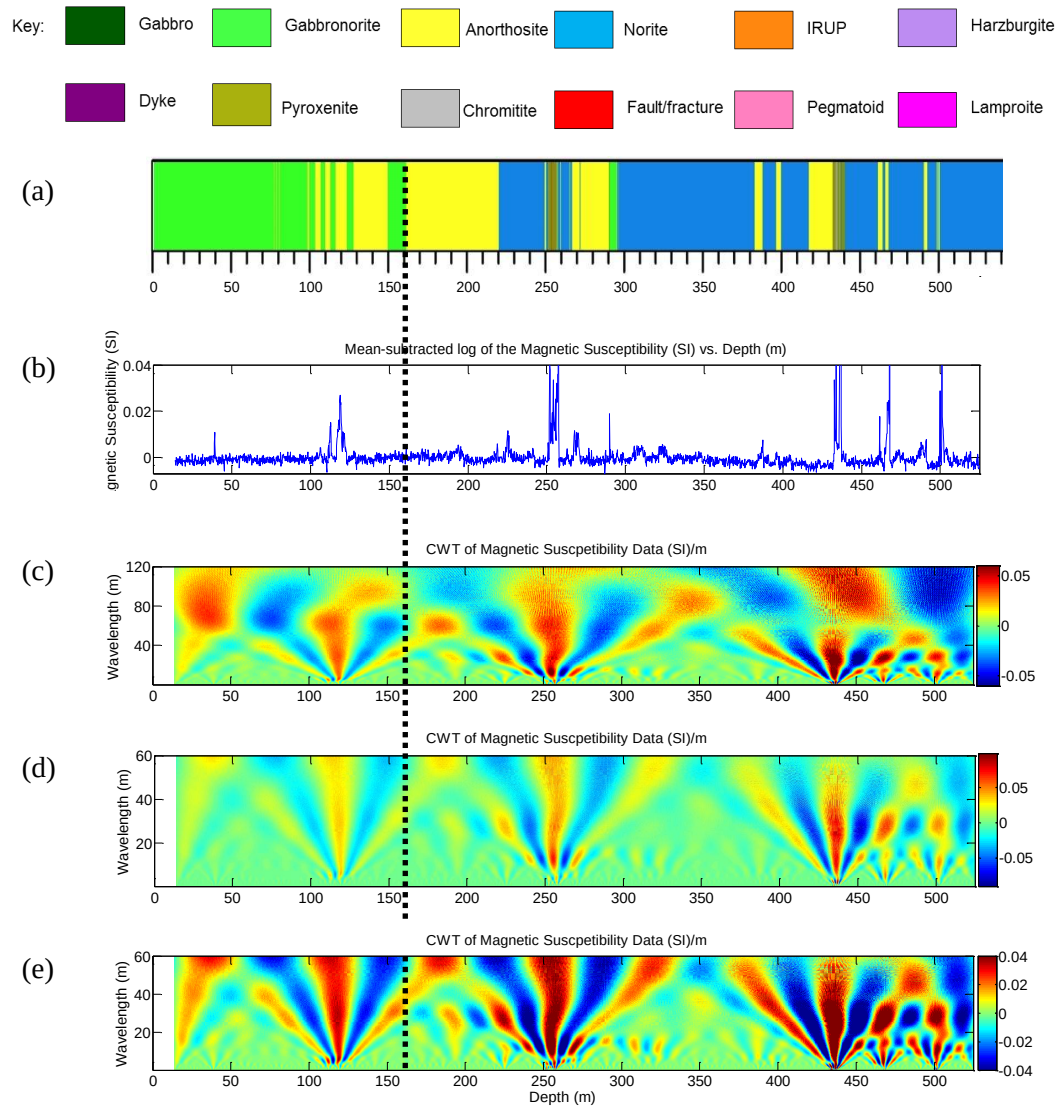

Figure 6.16 (a) Lithology log for borehole DB135. (b) Mean-subtracted log of the magnetic susceptibility data (SI) vs. depth (m). CWT of the magnetic susceptibility data shown on a scale of (c) 1 to 120 m with the image histogram thresholded, (d) 1 to 60 m with the image histogram thresholded and (e) 1 to 60 m with the image histogram thresholded. The black stippled line shows the approximate location of the MZ-CZ boundary.

Figure 6.16e below it shows the same image with the histogram thresholded, and shows this wavelength is probably present at depths shallower than 200 m. This figure also shows a wavelength of 15 m with varying intensity from 200 m depth until the end of the borehole. The CWT of the magnetic susceptibility data shows some edge effects, but is still able to provide valuable information on the cyclicity in the borehole where it is present. There are common wavelengths between density and magnetic susceptibility of

80 m and 15 m. While the 15 m wavelength is seen in both the MZ and CZ in the density data, it is almost exclusively in the CZ in the magnetic susceptibility.

Density Data– RM123

The lithology log, density data (downsampled to 10 cm) and the CWT of the density data are shown in Figure 6.17.

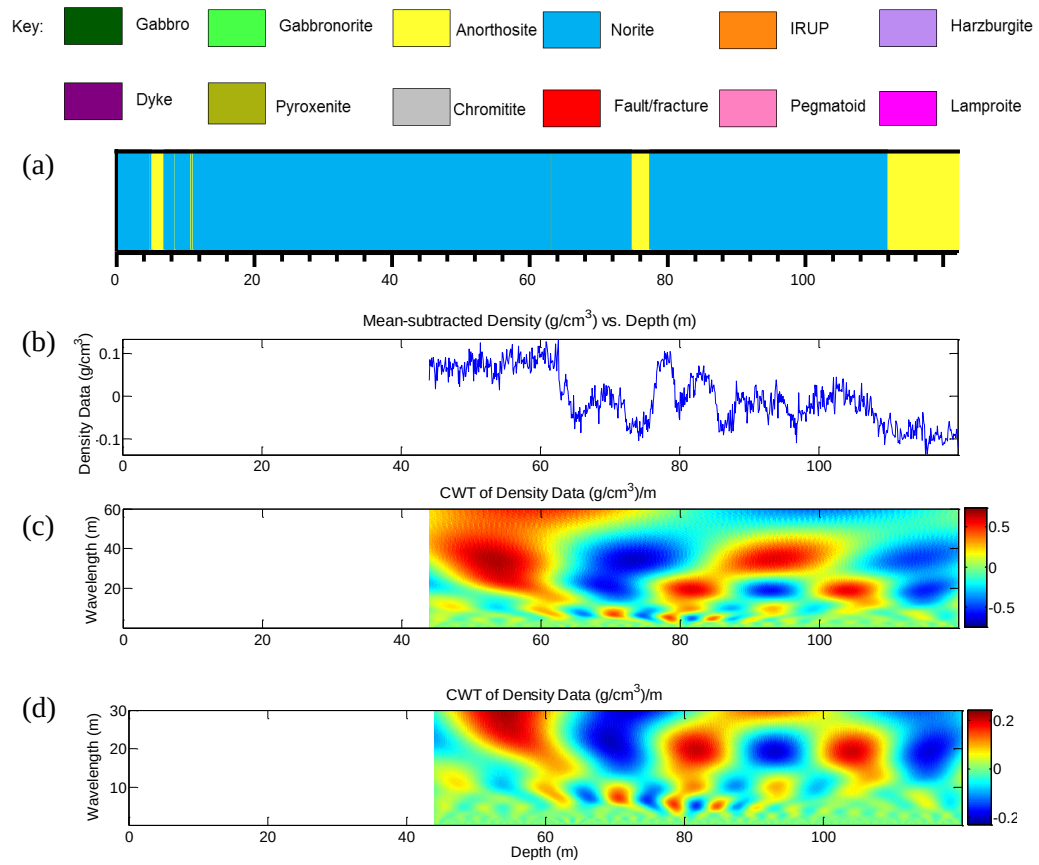

Figure 6.17 Lithology log for borehole RM123. (b) Mean-subtracted density data (g/cm^3) vs. depth (m). CWT of the density data shown on a scale of (c) 1 to 60 m and (d) 1 to 30 m.

This borehole is made up entirely of CZ norite and anorthosite (Figure 6.17a). The physical property logs of this borehole has only been analysed to a depth of approximately 120 m due to edge effects produced in the CWT. The density log shows that there are some variations in the density data within both of the lithologies (Figure 6.17b). Figure 6.17c shows cyclicity at wavelengths of ~40 m throughout the borehole. It does however break up at a depth of 70 m, to form a wavelength of 20 m. Figure 6.17d shows a 10 m wavelength which decreases in wavelength to 5 m at a depth of 90 m before losing intensity.

Magnetic Susceptibility Data– RM123

The lithology log, density data (downsampled to 10 cm) and the CWT of the Magnetic susceptibility data are shown in Figure 6.18. The magnetic susceptibility data is almost constant for the first ~20 m, before a sharp decrease at a depth of 65 m after which the data becomes is visibly noisy. Figure 6.18c shows cyclicity at wavelengths of 35-40 m. Figure 6.18d shows a 20 m wavelength, which is consistent with depth but decreases in intensity. Figure 6.18e shows that cyclicity at a wavelength of 5 m from 60 m onwards.

This borehole is able to show multi-scale cyclicity in both of the physical properties in seemingly homogenous units of norites and anorthosite. They also show cyclicity at common wavelengths of 40 m, 20 m and 5 m.

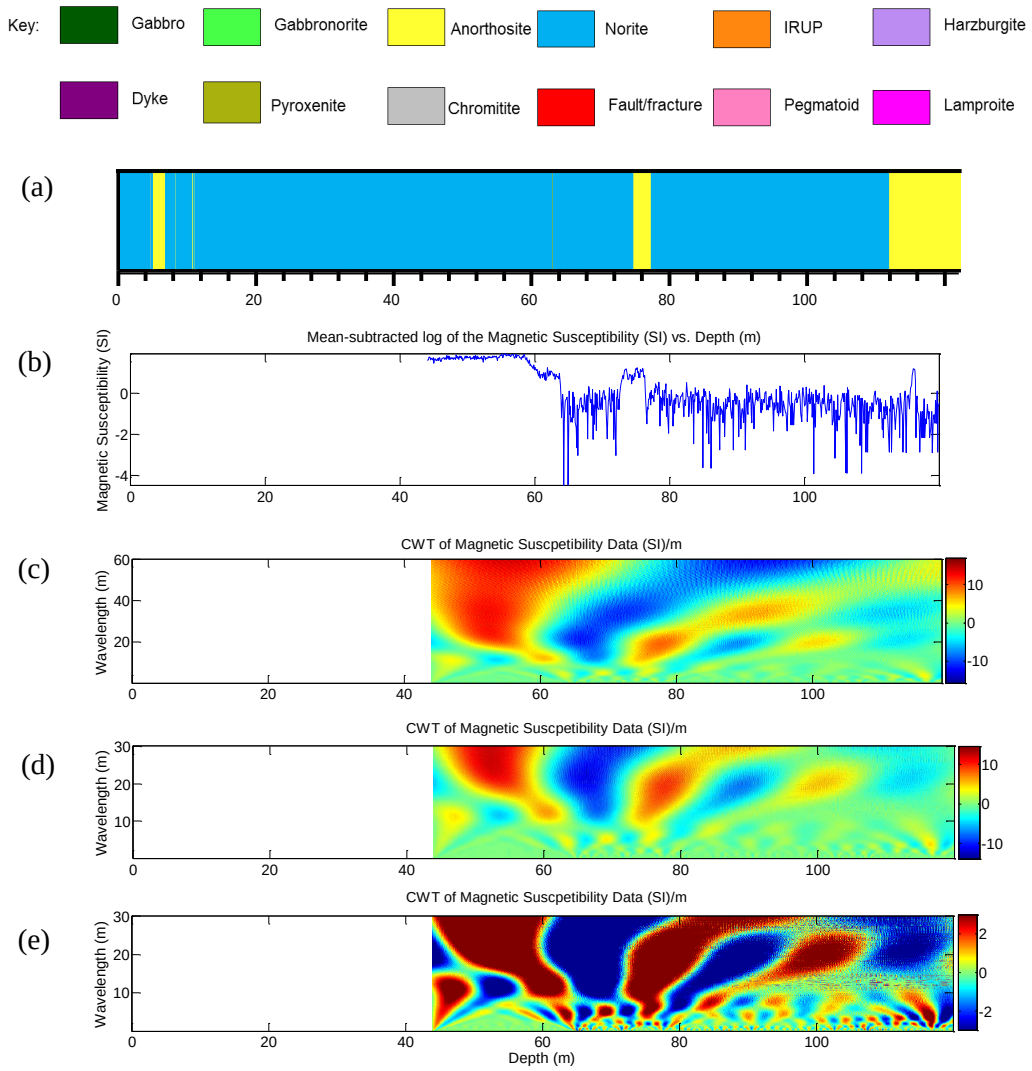

Figure 6.18 (a) Lithology log for borehole RM123. (b) Mean-subtracted log of the magnetic susceptibility data (SI) vs. depth (m). (c) CWT of the magnetic susceptibility data shown on a scale of 1 to 60 m, (d) 1 to 30 m and (e) 1 to 30 m with the image histogram thresholded.

6.3 The Northern Limb of the BC

6.3.1 Bellevue- BV-1

The only data available for the Northern Limb are the 2950 m continuous density and magnetic susceptibility measurements collected by Ashwal et al. (2005). They have provided density data sampled on average at 1.7 m. This borehole has intersected the UZ and part of the MZ. The lithology log for this borehole is shown in Figure 6.19a, and consists of granites and norites (enriched with magnetite) and thin anorthosite and magnetite layers. The MZ rocks are typical of those observed before, consisting of

norites, gabbros and anorthosites. An atypical (for the MZ) troctolite has also been intersected.

Density Data- BV-1

The density data in Figure 6.19b shows large variations due to the various layers enriched in magnetite in the UZ in the uppermost 1500 m. Below this density values are generally above 3 g/cm^3, making it possible to map the UZ and MZ. The CWT of the data shown in Figure 6.19c shows cyclicity at wavelengths of ~230 m, 150 m and 50 m. There is an obvious decrease in signal intensity in these results from the UZ to the MZ, which points to the influence of magnetite in signal intensity.

6.4 Summary of Dominant Wavelengths

Table 6.6 summarizes the wavelengths of the cyclicity which have been observed in each of the boreholes studied. These wavelengths have been separated into equal bins of 50 m and the occurrence of wavelengths in each borehole is indicated in blue (Table 6.7 and 6.8). The grey blocks indicate where there is no data. The influence of the length of the borehole and its influence on the longest wavelength signal that can be clearly observed in Table 6.7 and 6.8. The longer boreholes in the Western Limb have longer wavelength signals (>250 m) while the shorter Eastern Limb boreholes have wavelengths of <250 m. The most prominent wavelengths across the boreholes for the density data is between <150-100 m and <50 m, and <100-50 m and <50 m for the magnetic susceptibility.

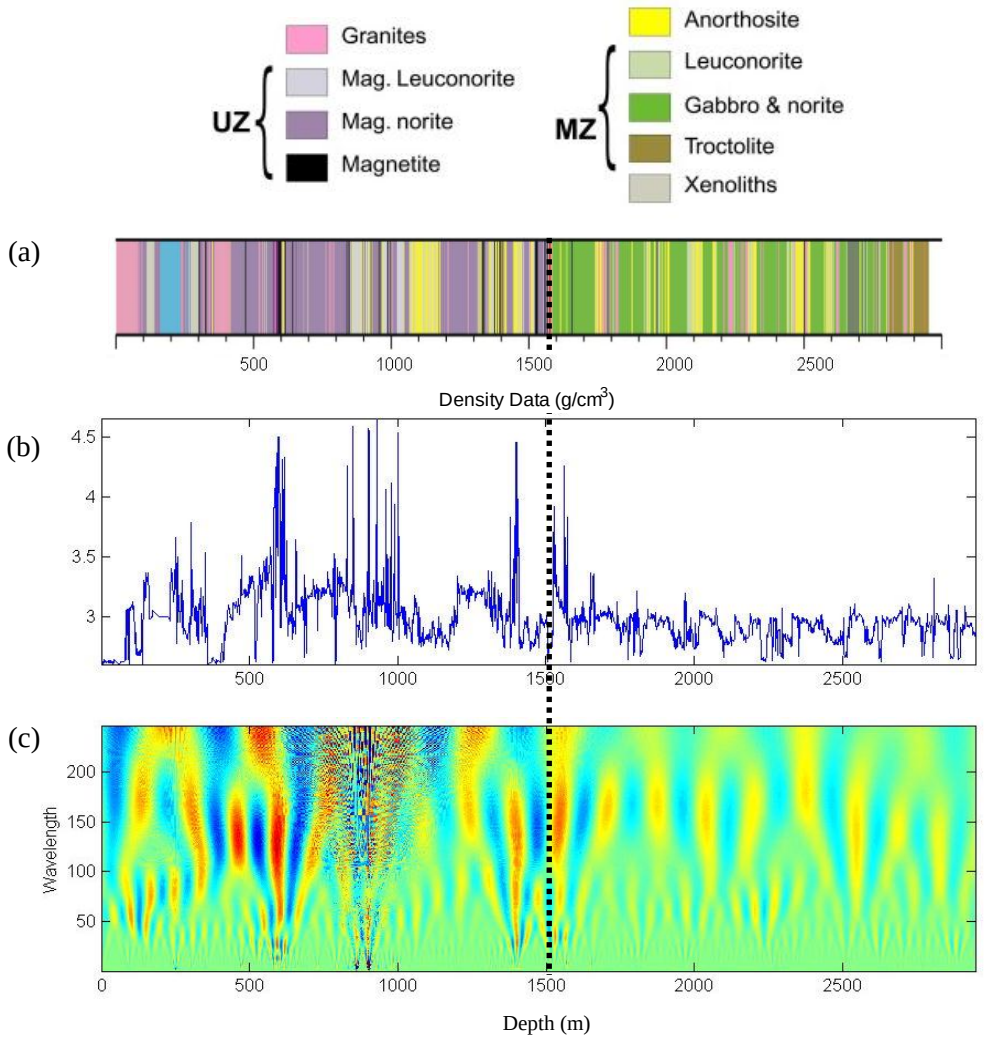

Figure 6.19 (a) Lithology log for borehole BV-1. (b) Mean-subtracted log of the magnetic susceptibility data (SI) vs. depth (m). (c) CWT of the density data shown on a scale of 1 to 250 m. The black stippled line shows the approximate location of the UZ-MZ boundary.

Table 6.6 Summary of the various wavelengths observed in the boreholes discussed. WL, EL and NL beneath the name of the mine indicates the location of the mine in the BC, i.e. Western, Eastern or Northern Limb. *Wavelength observed in dolerite.

Mine	Borehole ID	Wavelength (m)	
		Density	Magnetic Susceptibility
Amandelbult WL	EL56	500, 400, 200-150, 100-60, 50-40, 20	
	EL57	450, 200-150, 60, 30, 20	
Union WL	SK59A	500-400, 200-150, 100, 100-80, 80-40,	
Styldrift WL	SO2	160-130, 80, 50-20, 20, 30-20, 10	90, 80, 60, 40, 25-20, 10
RPM WL	KLG52	500-400, 275-250, 150, 125, 75, 100	500-400, 200-250, 100-80, 50, 20
	KLG8	450-400, 275-250, 150, 125-75, 100	
Booysendaal EL	BY63	120-100, 50, 30-20, 20-10	80, 60, 15, 10, 5
	BY60	80-100, 45*, 25, 15, 10	80, 60, 20, 15, 10, 5
Der Brochen EL	DB136	100, 50, 30-20, 5,10	80-120, 50-40, 20-25,20-10, 5
	DB135	80-60, 30, 20	80-50, 40, 25, 15
	RM123	40, 20, 15-10	40-35, 20, 10
Bellevue NL	BV-1	230, 150, 50	

Table 6.7 Summary of the wavelengths observed in density data. The "blue blocks" show the occurrence of the particular wavelength in a borehole.

Mine	Borehole ID	Wavelength (m)- Density									
		500-400	<450-400	<400-350	<350-300	<300-250	<250-200	<200-150	<150-100	<100-50	<50
Amandelbult WL	EL56	■	■				■	■	■	■	■
	EL57	■					■	■		■	■
Union WL	SK59A	■	■				■	■	■	■	■
Styldrift WL	SO2								■	■	■
RPM WL	KLG52	■				■		■	■		
	KLG8	■	■			■		■	■		
Booysendaal EL	BY63								■		■
	BY60								■		■
Der Brochen EL	DB136								■		■
	DB135									■	■
	RM123										■
Bellevue NL	BV-1						■	■			■

Table 6.8 Summary of the wavelengths observed in magnetic susceptibility data. The "blue blocks" show the occurrence of the particular wavelength in a borehole.

Mine	Borehole ID	Wavelength (m)- Magnetic Susceptibility									
		500-400	<450-400	<400-350	<350-300	<300-250	<250-200	<200-150	<150-100	<100-50	<50
Amandelbult WL	EL56										
	EL57										
Union WL	SK59A										
Styldrift WL	SO2										
RPM WL	KLG52										
	KLG8										
Booysendaal EL	BY63										
	BY60										
Der Brochen EL	DB136										
	DB135										
	RM123										
Bellevue NL	BV-1										

6.5 Wavelet-based Semblance Analysis- Western Limb of the BC

Wavelet-based semblance analysis is used to correlate the density and magnetic susceptibility data across boreholes. This will allow for wavelengths to be studied as a function of depth as well as spatially. Although different lithologies are compared in this analysis, this is not an important consideration since the cyclicity is generally pervasive across boundaries. Also, only borehole data which have coincident geological markers are discussed. The "depths" shown below are from the start of the height from which the physical properties are compared, to the bottom. The location of the marker horizon used to correlate the boreholes is indicated.

6.5.1 Amandelbult

EL56 and EL57

The lithology logs for boreholes EL56 and EL57 from Amandelbult are shown in Figure 6.20. Figure 6.21 shows the semblance analysis using the density data (downsampled at 100 cm) of these boreholes. These have been aligned using the PGM, allowing over 1000 m of the datasets to be compared. The most prominent feature is the positive correlation in Figure 6.21a at a wavelength of approximately 350 m at depths of 100-800 m, and shows anti-correlation everywhere else. Figure 6.21b shows a strong positive correlation at wavelengths of 150-200 m at depths of 150 m to the position of the PGM, below which there is anti-correlation. Positive correlation is also observed at a wavelength of 75-100 m from a depth of 320 m, which once again terminates at the PGM but reappears at depths of 900-1000 m. Other wavelengths which show correlation are also 50 m and at 20 m with less consistency than the abovementioned wavelengths.

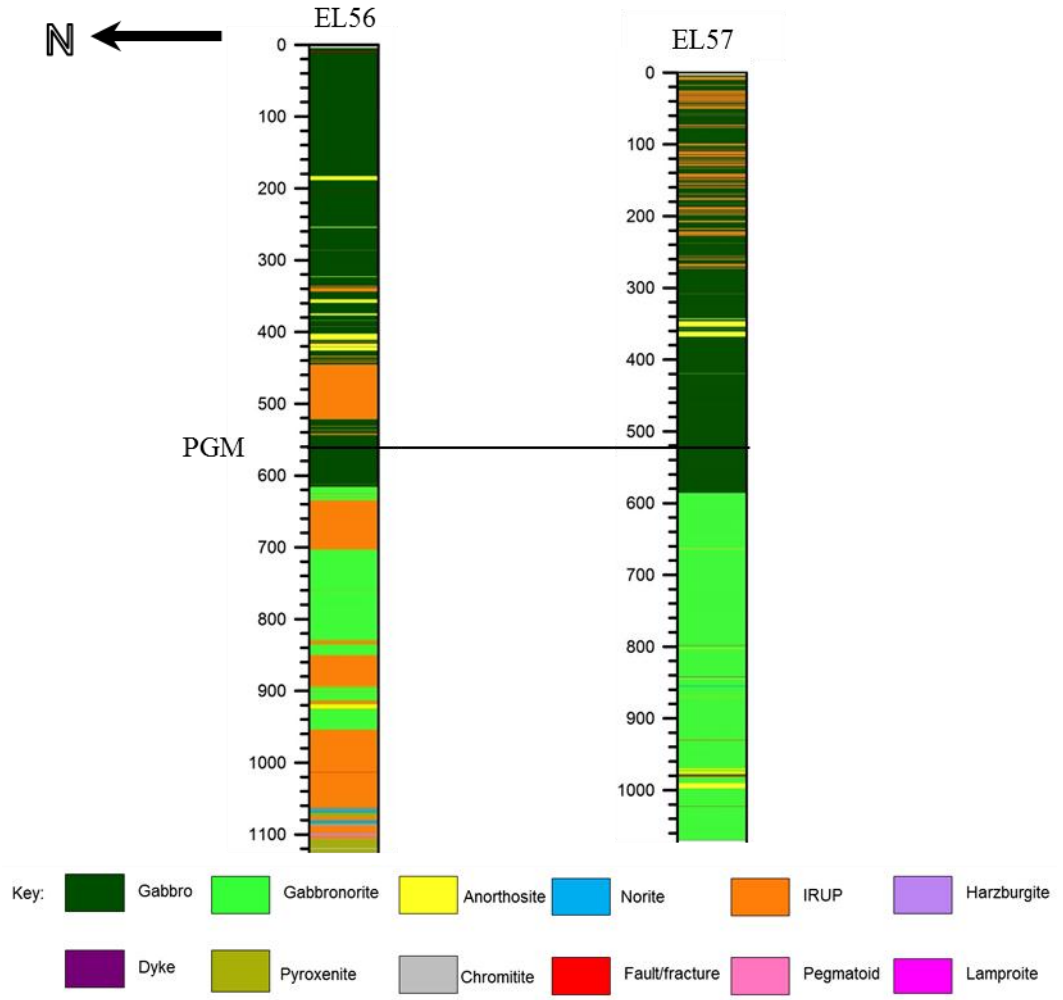

Figure 6.20 Lithology logs for boreholes EL56 and EL57. The black solid line indicates the approximate location of the PGM (Porphyritic Gabbro Marker) used to align the boreholes.

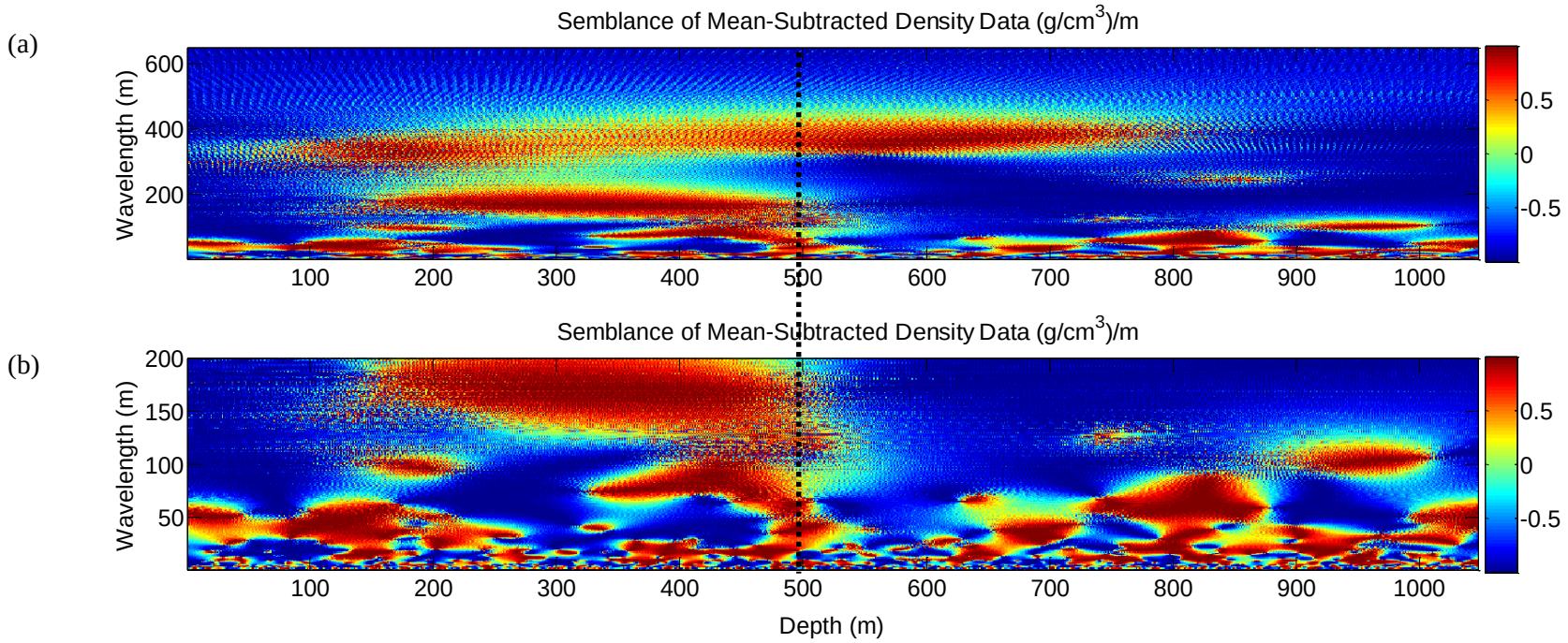

Figure 6.21 Semblance analysis of density data for boreholes EL56 and EL57 on a scale of (a) 1-650 m and (b) 1-300 m. The black stippled line shows the approximate location of the PGM (Pophyritic Gabbro Marker) used to align the boreholes.

6.5.2 Amandelbult and Union

EL56, EL57 and SK59A

The lithology logs for boreholes EL56 and EL57 from Amandelbult and SK59A from Union are shown in Figure 6.22.

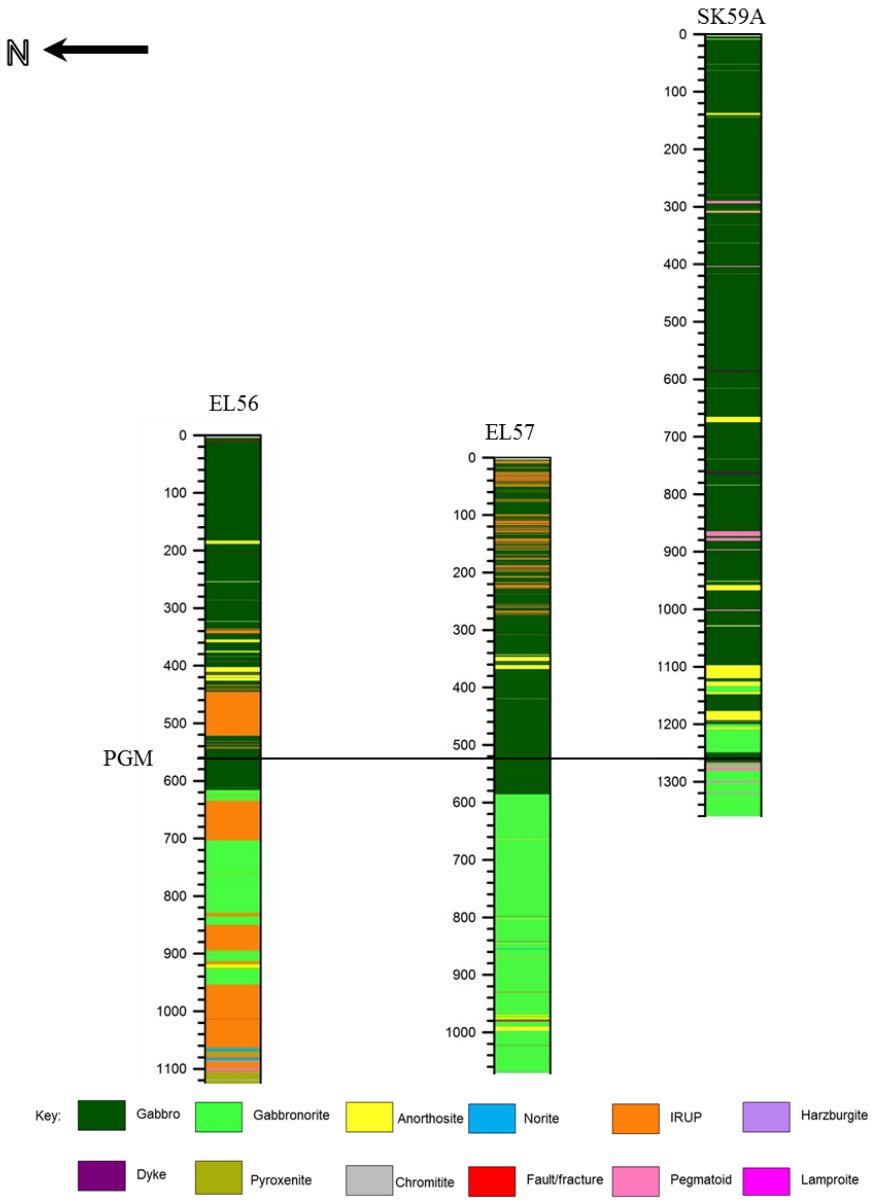

Figure 6.22 Lithology logs for boreholes EL56, EL57 and SK59A. The black solid line indicates the approximate location of the PGM (Porphyritic Gabbro Marker) used to align the boreholes.

Figure 6.23 shows MRL results for these boreholes for the density data downsampled at 20 cm. Over 550 m of density data of these boreholes can be compared. Figure 6.23a

shows that the three datasets correlate in a broad region of wavelengths longer than 160 m from approximately 50 m onwards until the end of the image. The most intense correlation is at depths of 200-400 m. Figure 6.23b shows that there is also correlation at a wavelength of 20-60 m at depths of approximately 0-200 m and 450-600 m. There are generally correlations at smaller wavelengths but these are more complex.

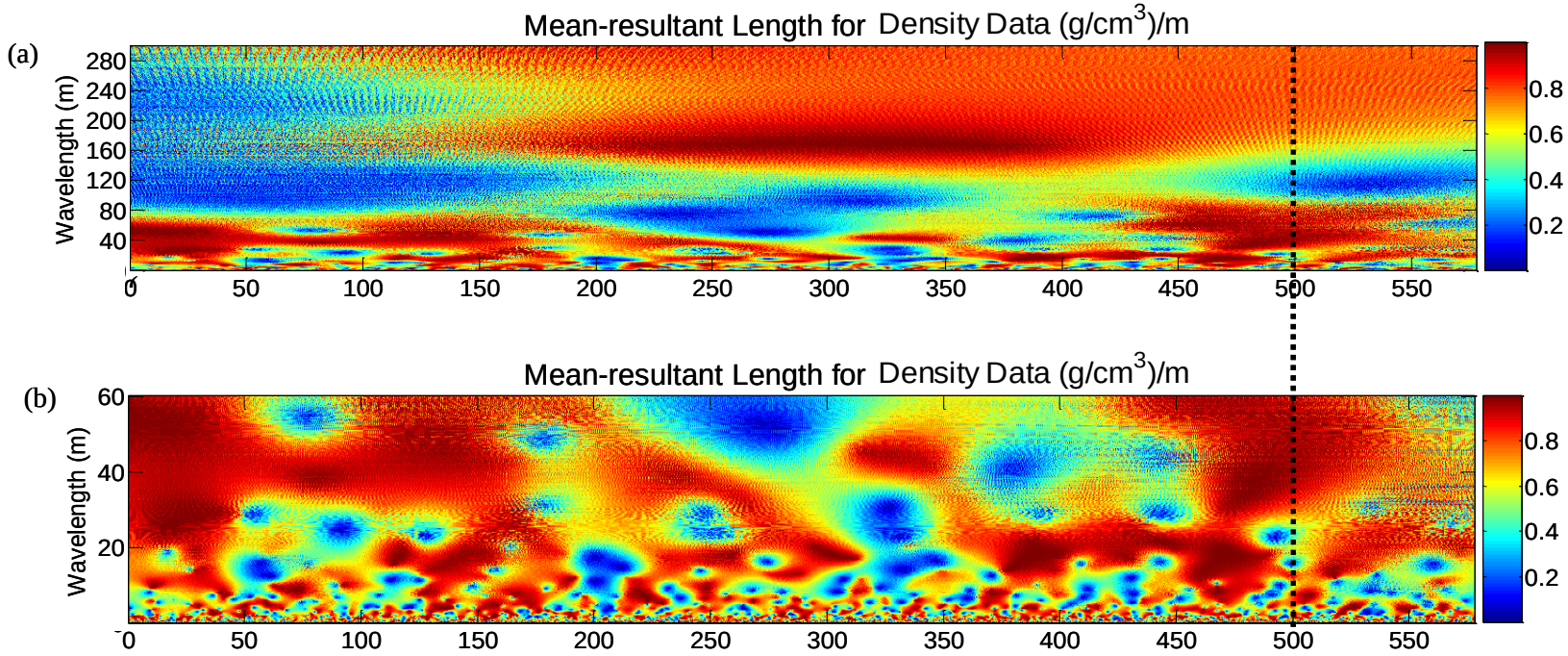

Figure 6.23 MRL of density data for boreholes EL56, EL57 and SK59A shown on a scale of (a) 1-300 m and (b) 1-60 m. The black stippled line indicates the approximate location of the PGM (Porphyritic Gabbro Marker).

6.5.3 RPM

KLG8 and KLG52

The lithology logs for boreholes KLG52 and KLG8 are shown in Figure 6.24.

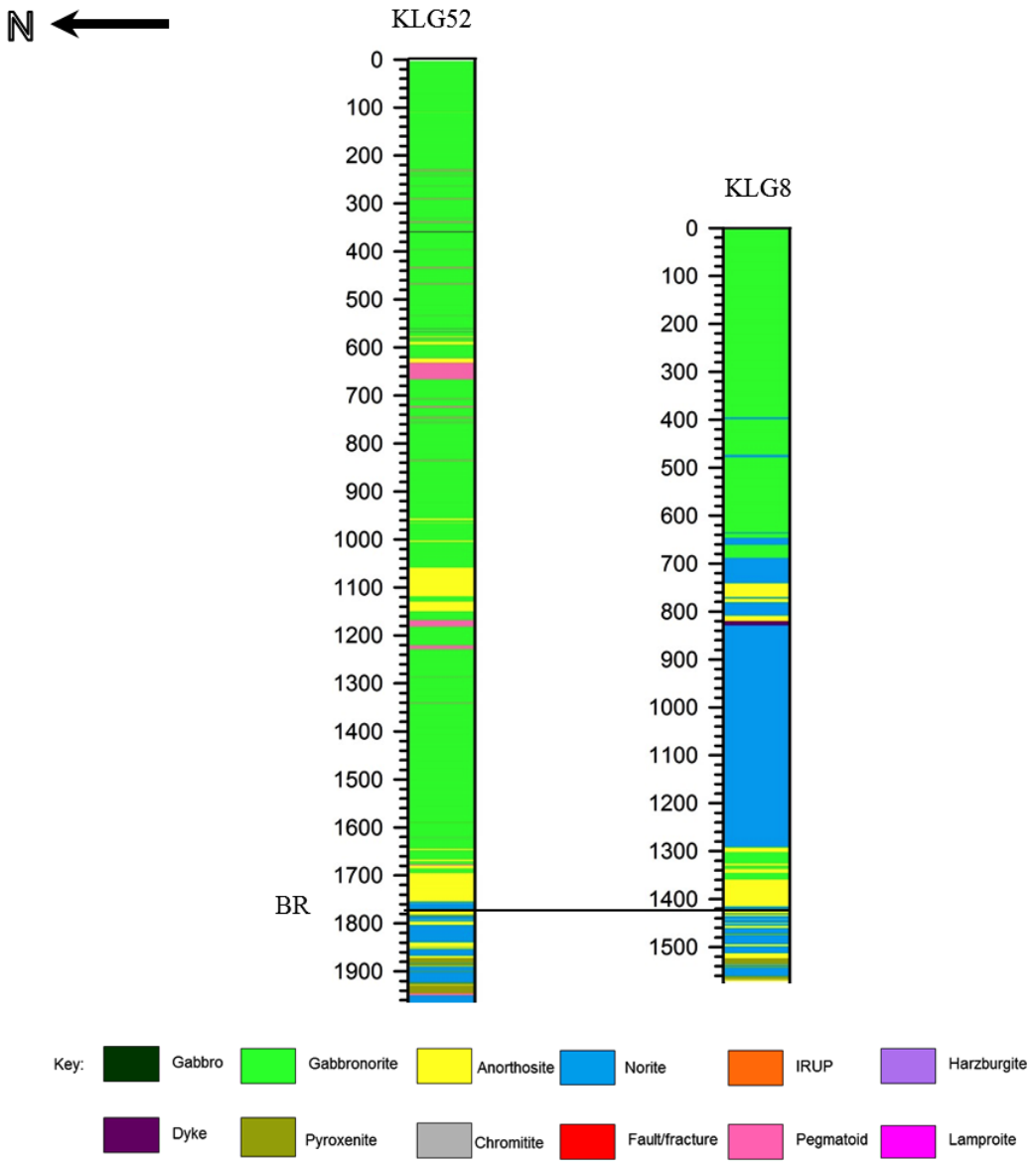

Figure 6.24 Lithology logs for boreholes KLG8 and KLG52. The black solid line indicates the approximate location of the BR (Bastard Reef) used to align the boreholes.

Figure 6.25 shows the semblance analysis for KLG8 and KLG52 using their density logs downsampled to 50 cm. Figure 6.25a shows that the image of the semblance is mostly red, an indication of positive correlation between the two datasets. Strong positive correlation at wavelengths in Figure 6.25a are observed at wavelengths of 250-400 m at

depths of 600-1300 m. Figure 6.25b shows that even at smaller wavelengths the data are predominantly positively correlated. The most intense positive correlations are seen at wavelength of 100-150 m which is consistent with depth except at depths of 800-1050 m. There is also correlation at a wavelength of 50-100 m from approximately 400-500 m and then again from depths of 1100-1500 m.

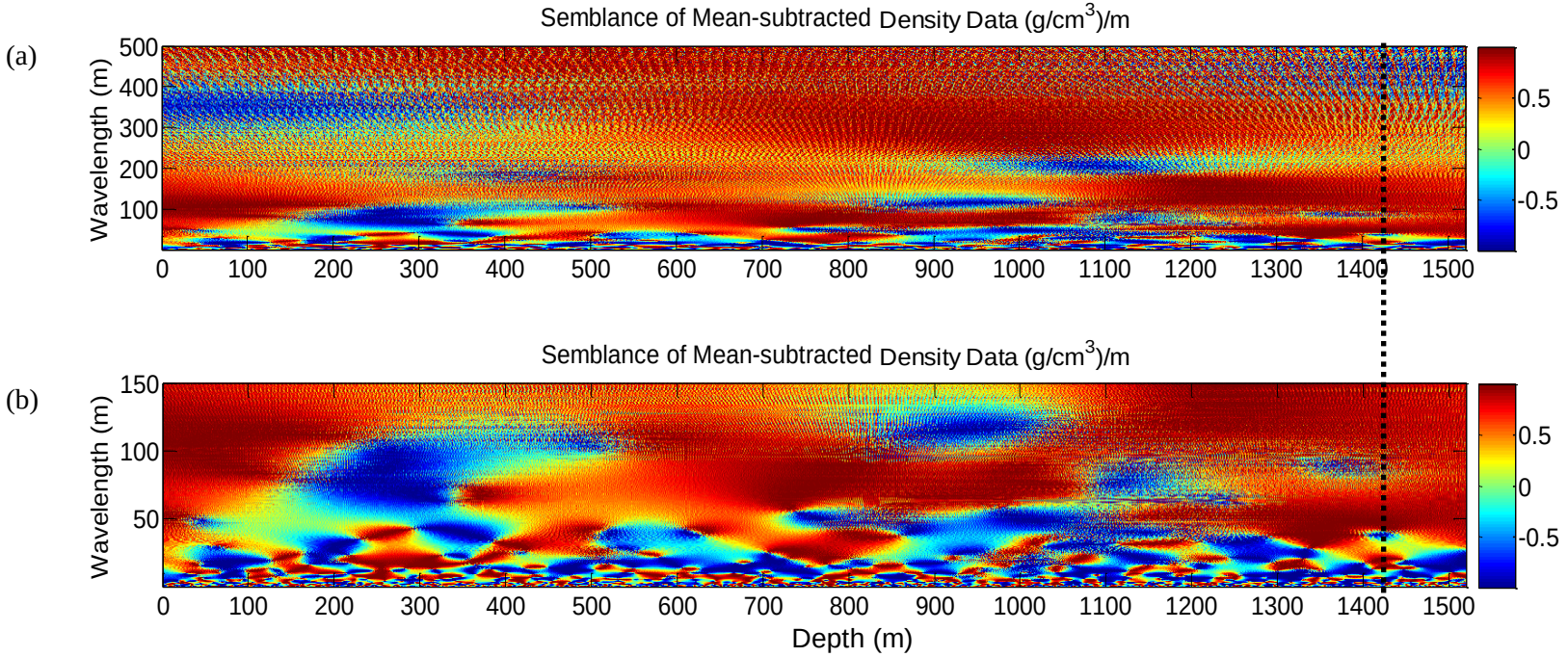

Figure 6.25 Semblance analysis of density data for boreholes KLG52 and KLG8 shown on a scale of (a) 1-500 m and (b) 1-150 m. The black stippled line shows the approximate location of the Giant Mottled Anorthosite used to align the boreholes.

6.5.4 Styldrift and RPM

SO2, KLG8 and KLG52

The lithology logs for boreholes SO2, KLG52 and KLG8 from Styldrift and RPM are shown in Figure 6.26.

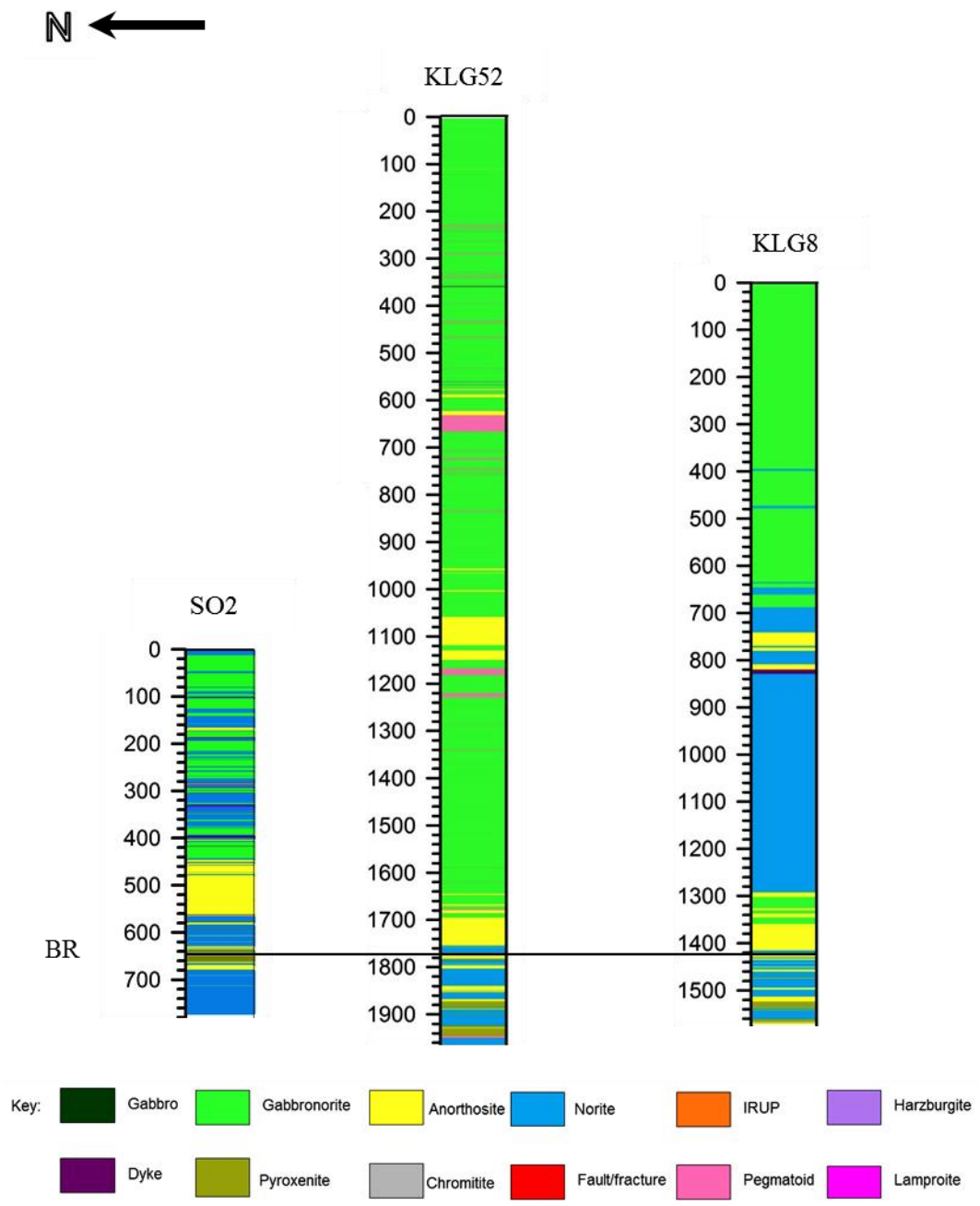

Figure 6.26 Lithology logs for boreholes for SO2, KLG8 and KLG52. The black solid line shows the approximate location of the BR (Bastard Reef) used to align the boreholes.

The marker which is being used to correlate the data is the Bastard Reef. These boreholes lie fairly along strike of each other. The MRL results for the density data (downsampled at 20 cm) for the three boreholes are shown below. Figure 6.27a shows strong correlation along wavelengths of 120-200 m which is almost consistent except at depths of 350-400 m. Wavelengths of 60-80 m in Figure 6.27b shows correlation which is consistent until the Bastard Reef where there is a break. This signal is then also observed after the Bastard Reef marker from 580 m to ~700 m. Figure 6.27c shows correlation at wavelengths of 20-40 m at depths of 0-120 m, 180-250 m, 300-350 m and after the Bastard Reef marker.

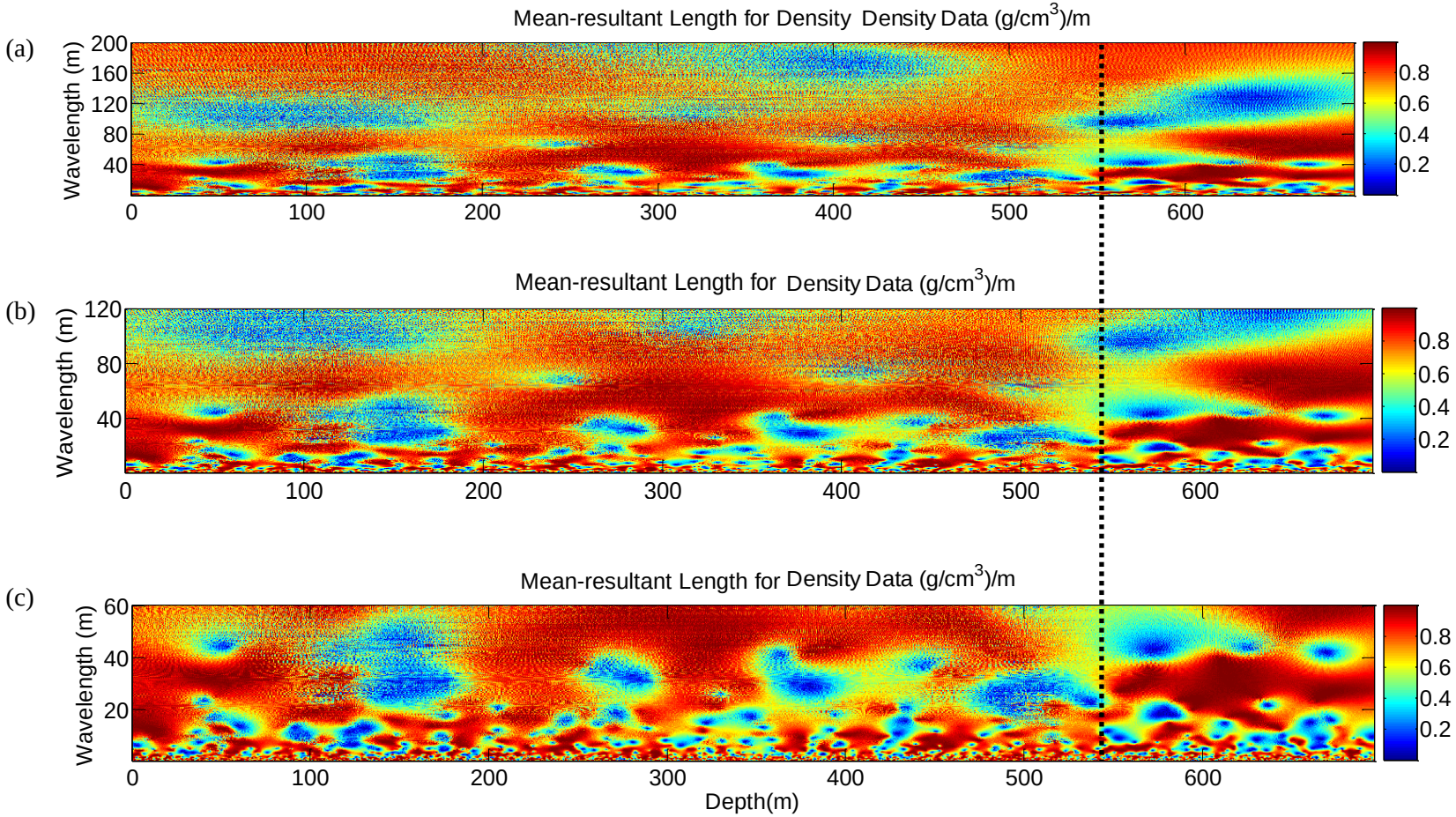

Figure 6.27 (a) Semblance analysis of density data for SO2, KLG52 and KLG8 shown on a scale of 1-200 m, (b) 1-120 m and (c) 1-60 m. The black stippled line shows the approximate location of the Bastard Reef used to align the boreholes.

6.6 Wavelet-based semblance analysis- Eastern Limb of the BC

6.6.1 Der Brochen

DB135, DB136 and RM123

The lithology logs for boreholes DB135, DB136 and RM123 from Der Brochen are shown in Figure 6.28.

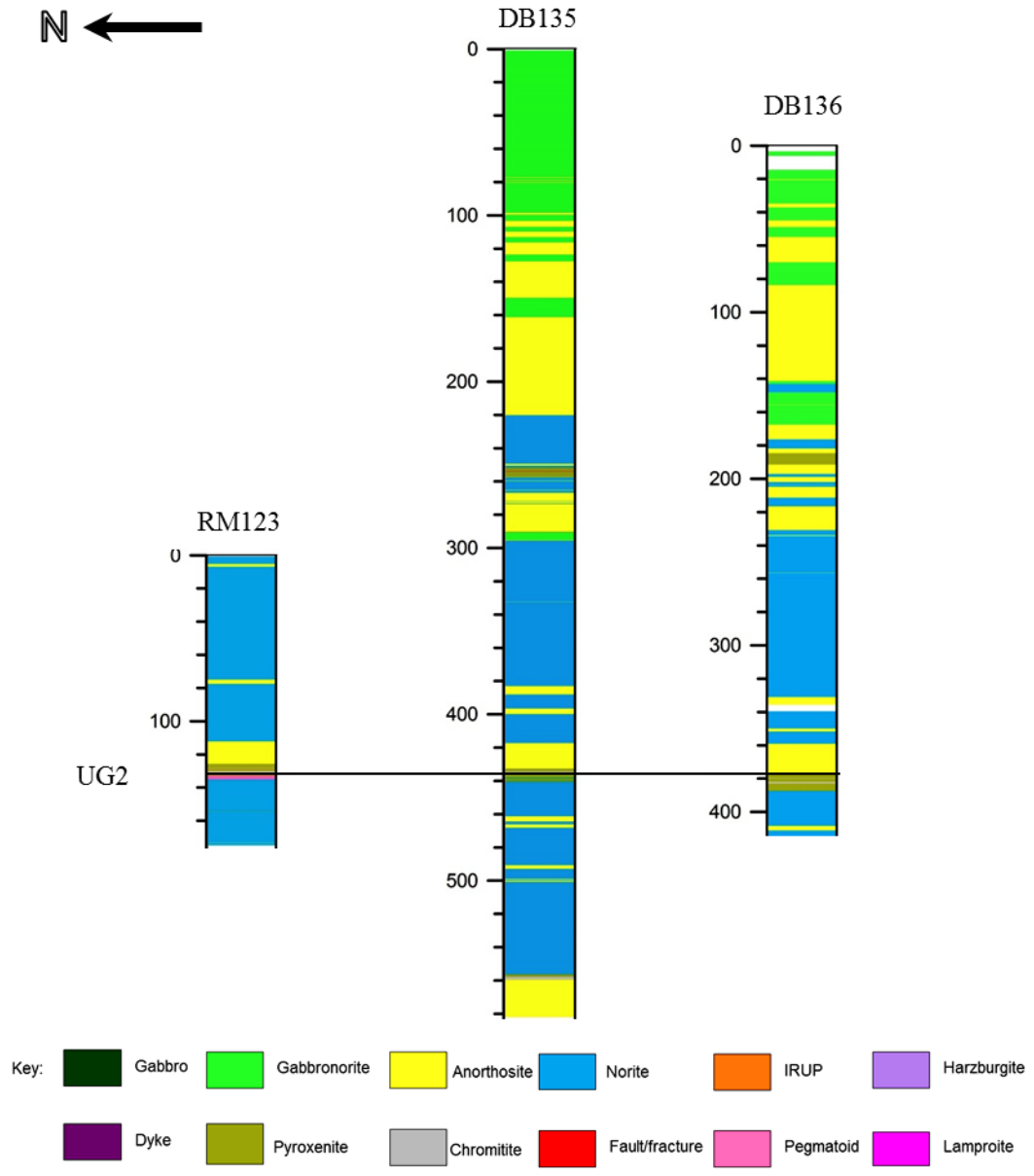

Figure 6.28 Lithology logs for boreholes DB136, DB135 and RM123. The black solid line shows the approximate location of the UG2 used to align the boreholes.

The MRL results for the density and magnetic susceptibility data (downsampled at 20 cm) for the three boreholes are shown in Figure 6.29. Figure 6.29a shows the MRL of the density data, which shows strong correlations at wavelength of 20-30 m which is consistent with depth. There is also correlation at wavelengths of 10-20 m which is consistent except at depths of 20-30 m, 40-50 m and >70 m. There is correlation at 5 m although it is less consistent. Figure 6.29b shows the MRL of the magnetic susceptibility data which shows that there is correlation at almost all wavelengths although with varying intensity. The most intense correlations are at wavelengths of 10-20 m, 20-30 m and 5-10 m.

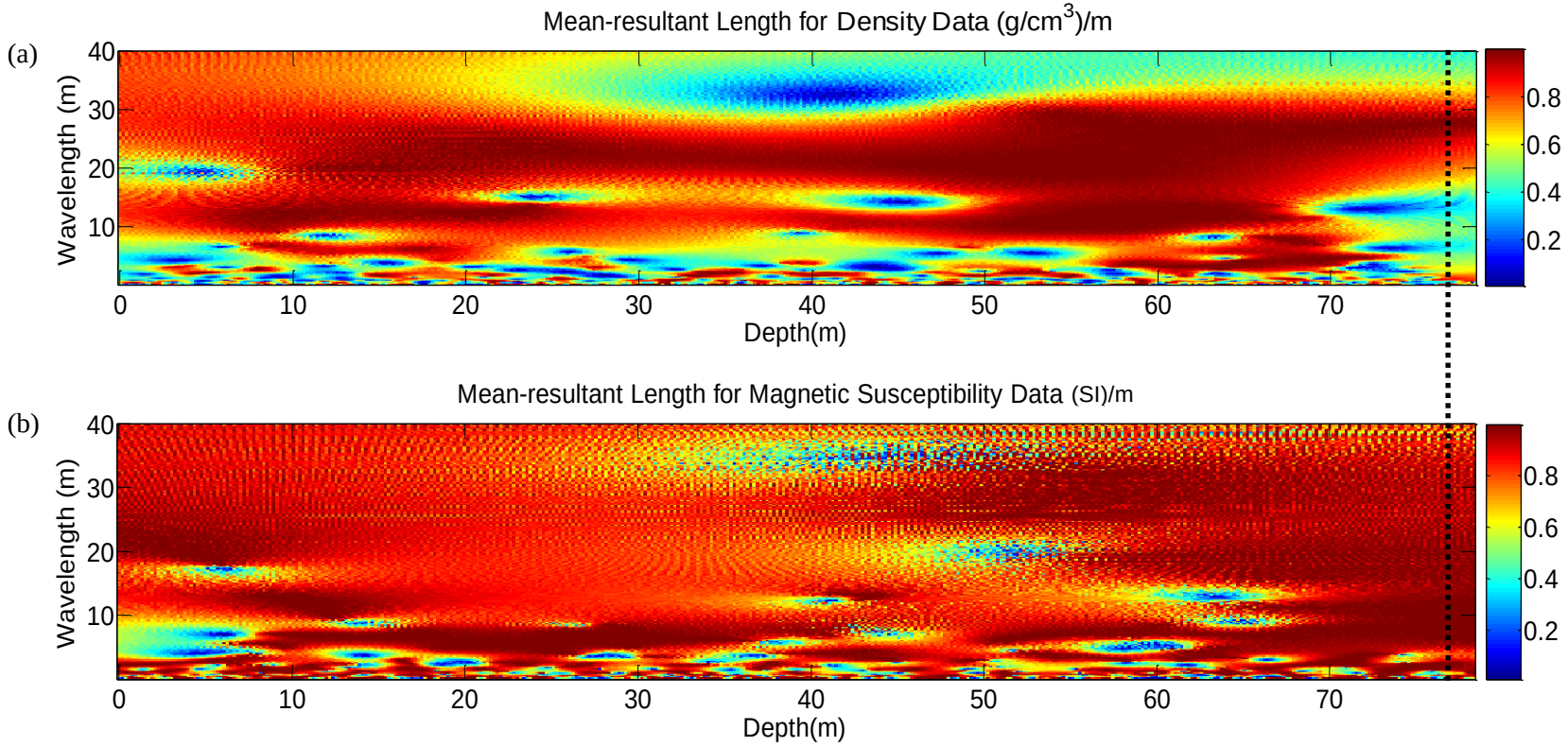

Figure 6.29 (a) Semblance analysis of density data for DB135, DB136 and RM123 shown on a scale of 1-40 m. (b) Semblance analysis of magnetic susceptibility data for DB135, DB136 and RM123 shown on a scale of 1-40 m. The black stippled line shows the approximate location of the UG2 used to align the boreholes.

6.7 Summary

Several observations have been made from the results of the wavelet analysis. There is no obvious uniqueness in the results obtained in the Western and Eastern Limbs of the BC. They both show a variety of wavelengths albeit that the Western Limb boreholes contain mostly MZ rocks while the Eastern Limb contains mostly CZ rocks. Also since the boreholes from the Western Limb are deeper, it makes it possible for longer wavelength signals to be studied. The cyclicity observed is pervasive across lithological boundaries, as well as within individual lithologies. Some of the longer wavelengths (>20 m) are not stationary with depth and a linear increase or decrease in wavelength is commonly observed. At smaller scales (wavelengths <20 m) the cyclicity in density and magnetic susceptibility are complex and commonly inconsistent with depth. The intensity of the magnetic susceptibility signal is commonly similar to that of density, suggesting that the same mechanism controls the intensity. This may therefore be a proxy for magnetite content. This is supported by the BV-1 borehole, which shows a decrease in the intensity of the CWT in the MZ compared to the UZ, where cumulus magnetite occurs. The change in intensity in the borehole BV-1 across the UZ and MZ boundary shows that this boundary is detectable using wavelet analysis (Figure 6.19). Replacement of one wavelength with another with depth is also not uncommon. Evidence of this has been observed in KLG52 (Figure 6.6) in the density data, for example. There are also break-ups of some signals into others, as seen in the density data of borehole SK59A (Figure 6.3).

The boreholes show strong correlations, which seem independent of the lithology types. This is somewhat expected since the cyclicity was seen to be pervasive across lithology boundaries. Boreholes in the northern Western Limb (Amandelbult and Union) show correlation in the density data at wavelengths >160 m and 20-60 m (Figure 6.23). Boreholes further south (Styldrift and RPM) show correlations at wavelengths of 120-200 m and 60-80 m in the density data (Figure 6.27). The cyclicity of the northern and southern boreholes cannot be compared easily, as although the stratigraphy may be coincident, there are no markers to align the boreholes. However, the wavelengths at which the northern and southern Western Limb boreholes correlate are similar. Der Brochen boreholes of the Eastern Limb show correlation in the density data at wavelengths of 10-20 m, 20-30 m and 5m and magnetic susceptibility at identical wavelengths to the density data (Figure 6.29). The major correlations across boreholes are summarized in Figure 6.30.

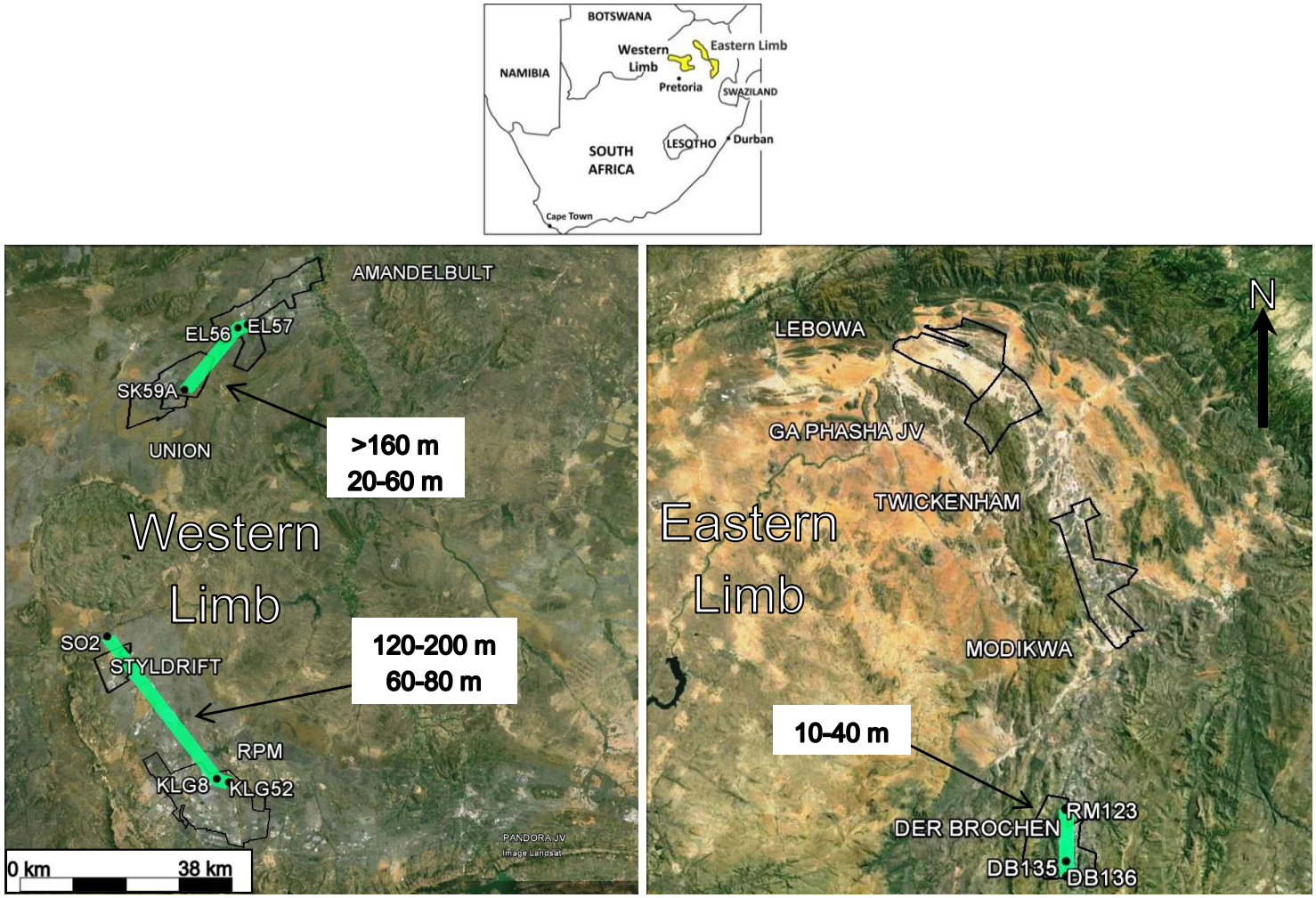

Figure 6.30 Google Earth image showing outlines of mining operations and locations of the boreholes. Lines (green) indicate the boreholes compared using the MRL and the dominant wavelengths that have been found to correlate. In the Western Limb these are from density data, and density and magnetic susceptibility in the Eastern Limb.

The important outcome is that positive correlations imply consistency in emplacement processes for several kilometres. At wavelengths smaller than 10 m the relationships between the boreholes become complex which could represent small scale differences in the data. The discussion chapter presents some of the features observed in the cyclicity and correlation studies closely, and what the process can be best attributed to.

CHAPTER 7: DISCUSSION

The quality of density and magnetic susceptibility logs studied in Chapter 2.6 revealed that some logs might have been subject to incorrect logging in practice. The most efficient manner of highlighting peculiarities is to study physical property logs plotted with depth in small sections and to produce a cross-correlation plot between two different physical properties. These tools have been formalized in this chapter into a workflow for evaluating the quality of physical property logs.

Cross-correlation plots between density and magnetic susceptibility in Chapter 3.3 have also been used to show how the different lithologies form clusters in space, which allows them to be differentiated solely on their physical properties. The *k*-means classification carried out in Chapter 4.2 investigated the possibility of automatically detecting these clusters, in order to create a semi-automatic approach to lithology logging. In some instances, good correlation has been found between the classification results and the lithology logs, with discrepancies being attributed to lithology misidentification and or lithology heterogeneities. Histogram plots for each of the major lithologies in Chapter 3.2 also highlighted possible misidentification. For these reasons, a workflow that makes use of physical property histograms, cross-correlation plots and *k*-means classification has been developed in order to mitigate the already subjective nature of geological logging.

The cyclicity in density and magnetic susceptibility logs in Chapter 6 has been shown to be pervasive throughout the boreholes studied in the BC. The cyclicity is studied at a smaller scale, within individual homogeneous layers for the major constituent lithologies of the BC including gabbro, gabbronorite, anorthosite and norite. A review of the typical types of layering identified in large layered intrusions including the BC is conducted in order to ascertain the kind of layering which may be responsible for the cyclicity observed. The emplacement of the BC is discussed as well as how wavelet analysis of density logs can be incorporated in the study of magmatic rocks.

7.1 Quality Control Workflows

Quality control criteria were evaluated in Chapter 2.6 and applied to density and magnetic susceptibility borehole data. The first proposed framework is for evaluating the quality of physical property data. The first step is to study a physical property log with depth in order to identify major variations and trends. The second step is to study the property log

in small sections allowing the interpreter to spot instrument problems and erroneous logging principles. The length of the section to be studied at a time will vary from dataset to dataset and on the quality of the data, but one tenth of the log proved to be sufficient in this project i.e. 100 m for a 1000 m long borehole. The final step is to produce a scatter plot, which is an effective way of evaluating data as it allows for two physical properties to be studied simultaneously. A proposed workflow for is shown in Figure 7.1.

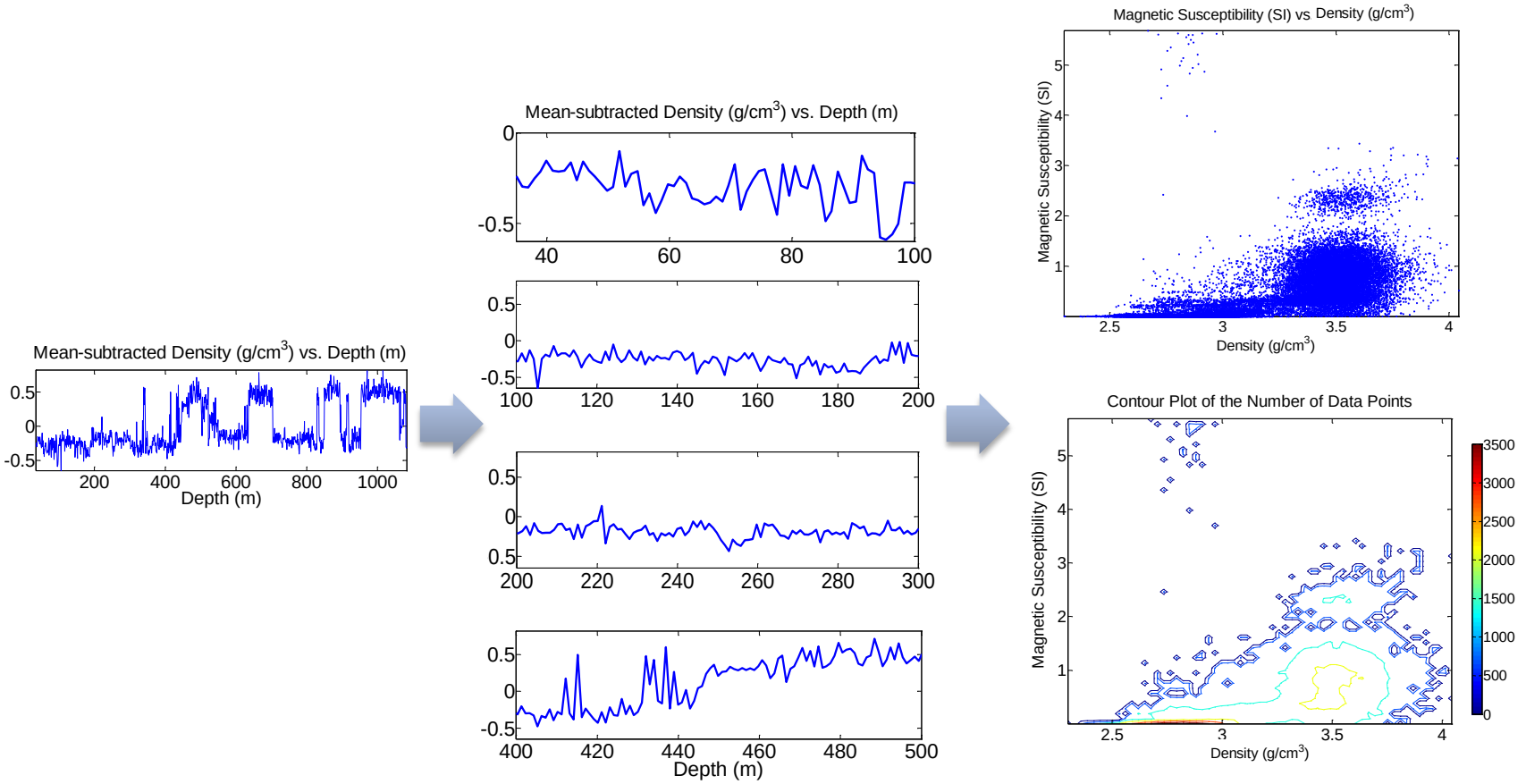

Figure 7.1 Workflow for assessing the quality of physical property logs for both density and magnetic susceptibility (left to right). The log shown in the first step is broken up into smaller sections (by depth), whose data quality can be assessed in the second step. The final step is to study the scatter plot. The plot below it shows the density of the data points.

The second workflow is for evaluating the quality of lithology logs. Due to the subjective nature of lithology logging, physical properties should be incorporated into this process to mitigate lithology logging errors. Pyroxenite, gabbro, gabbronorite, norite, anorthosite all have varying amounts of just two minerals, plagioclase and pyroxene, which makes them prone to misidentification during lithology logging. Histograms revealed misidentification of norite and anorthosite, while the k-means classification revealed large discrepancies when compared to the lithology logs (e.g. RM123 in Figure 4.17c and d). These two tools (histogram analysis and classification schemes) collectively highlight the deviation of observed lithologies and their expected physical property measurements. These methods are therefore collectively recommended to assist in geological logging. The first step is to plot a histogram of the available physical properties. The histograms will be useful if these data are multi-modal which could outright indicate the possible existence of different lithologies. The number of peaks may be used as an input into the *k*-means classification, which is the second step to be carried out in the framework. The classes should then be plotted with depth and referred to throughout the lithology logging process as a guide. This may not be important for mining companies since their real interest may be in pyroxenite and chromitite and not detailed changes in lithologies outside of those. However this may be useful to the academic community who can produce lithology logs. The suggested workflow is shown in Figure 7.2.

Both the workflows in Figure 7.1 and Figure 7.2 ensure that data of the best quality is used for further analysis and for causes of poor data quality to be isolated and investigated.

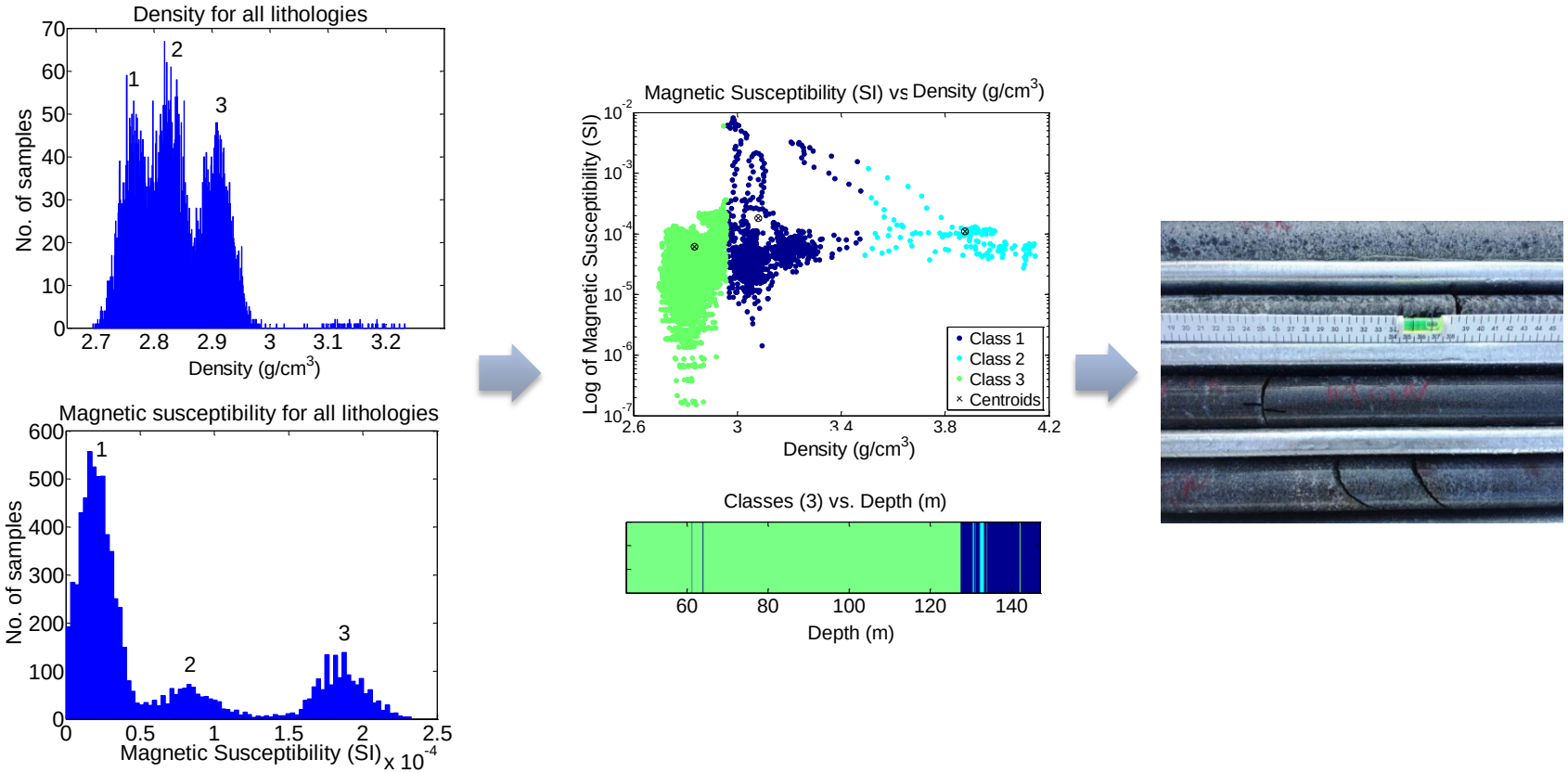

Figure 7.2 Workflow for using density and magnetic susceptibility data to assist in lithology logging (left to right). The first step is to study the histogram, whose peaks may suggest the number of types of lithologies present. Both the density and magnetic susceptibility histograms in this borehole show three peaks. The second step is to study the classification results and the final is to make actual observations on the core taking into account the histogram and classification results.

7.2 Cyclicity in Physical Property Data

This study aimed to determine whether cyclicity in density and magnetic susceptibility is present in the Western and Eastern Limbs of the BC and whether any information on the emplacement processes of the BC could be derived from this. The application of wavelet analysis has revealed multi-scale cyclicity in both the density and magnetic susceptibility. Some of the cyclical variations in physical property data are even visible in the density logs prior to the application of wavelet transforms. An example of this is shown for the borehole SO2 in Figure 7.3b, where the red stippled lines indicate prominent decreases and increases of density with stratigraphic height. Similar trends are also clearly visible in boreholes EL57 (Figure 6.2b), SK59A (Figure 6.3b), KLG52 (Figure 6.6b), KLG8 (Figure 6.8a), BY63 (Figure 6.9a) and BY60 (Figure 6.11a). Trends in the density data of increases followed by decreases with stratigraphic height are hereafter broadly referred to as 'reversals'.

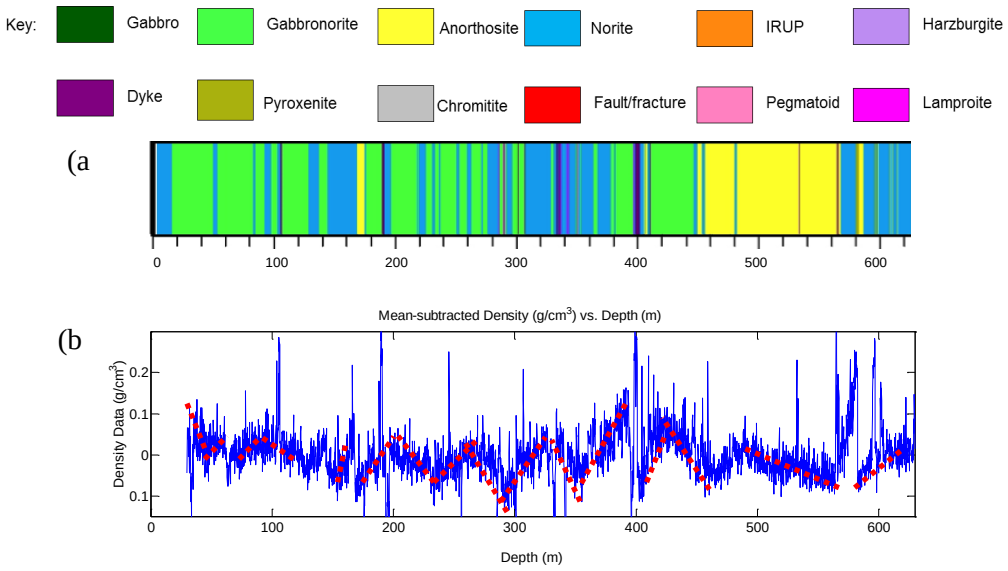

Figure 7.3 (a) Lithology log for borehole SO2. (b) Mean-subtracted density data (g/cm^3) vs. depth (m). The red stippled lines indicate prominent decreases and increases of density with increase in stratigraphic height. The black stippled line shows the approximate location of the MZ-CZ boundary.

Cyclicity studied in Chapter 6 has been studied in close relation to the lithology log. This has allowed the cyclicity to be observed across the MZ-CZ boundary, in intrusions into the BC, as well as across and within individual lithologies. Wavelengths are generally unperturbed at the MZ-CZ boundary. The exception to this is the borehole SO2 in which there is a steep change in wavelength from 50 m in the MZ to 20 m in the CZ. In addition

to this, wavelengths have been seen to occur exclusively in zones of the BC and not in others. An example of this can be seen in DB135, which shows cyclicity at a wavelength of 30 m the MZ that is absent in the CZ (Figure 6.15d and e). The MZ-CZ is also detectable in this borehole based on change in intensity in the wavelet transform of the density data. The wavelet analysis of the density data for the 85 m thick dolerite intrusion intersected in borehole BY60 shows a wavelength of 45 m not present in the BC host rocks (Figure 6.11c). The reversals in Figure 7.3b cross-cut lithological boundaries in Figure 7.3a. This is perhaps the feature which has been documented the most using the wavelet analysis, since it applies across all of the boreholes which were studied without exception. The signal across all lithology boundaries has been observed to be consistent or unperturbed across lithological boundaries for both density and magnetic susceptibility. In addition to this consistency, density and magnetic susceptibility data share common wavelengths across lithologies in most of the boreholes, suggesting that cyclicity in these properties is produced by the same geological processes.

7.2.1 Intralayer Cyclicity

Cyclicity also occurs within thick layers which have been logged as being lithologically homogeneous. This implies that there is a mineralogical control (changes in mineral proportions and or compositions) on the cyclicity. One thick section of each lithology type from the various logs has been selected to demonstrate intralayer cyclicity. The density data are used as they reveal the clearest reversals. These data have been downsampled to 10 cm from 1 cm in order to allow for the coarse structure in the data to be seen without the overprint of finer structure. Only the most obvious and prominent variations in density are indicated (red stippled lines). These together with other cyclical changes in the data are quantified using wavelet analysis. These changes in density are then related to the amount of relative change in the abundance of plagioclase (and pyroxene) as demonstrated in BC-type lithologies by Cawthorn and Spies (2003).

Gabbro- SK59A

The lithology log for borehole SK59A is shown in Figure 7.4a, and Figure 7.4b shows a section from 440 m to 580 m of gabbro. The density log for this part of the borehole is shown in Figure 7.4c and shows prominent increases followed by decreases in density of 0.1 g/cm^3 per 10 m. Gabbro by definition contains 65-35% plagioclase which results in densities of 2.95-3.05 g/cm^3. Density changes of 0.1 g/cm^3 imply a change in modal

abundance of plagioclase of 30 %. The indicated trends in density occur on the scale of approximately 10 m. This scale of cyclicity is evident in the wavelet analysis in Figure 7.4d, which also shows the presence of cyclicity at wavelengths of 20 m and 5 m.

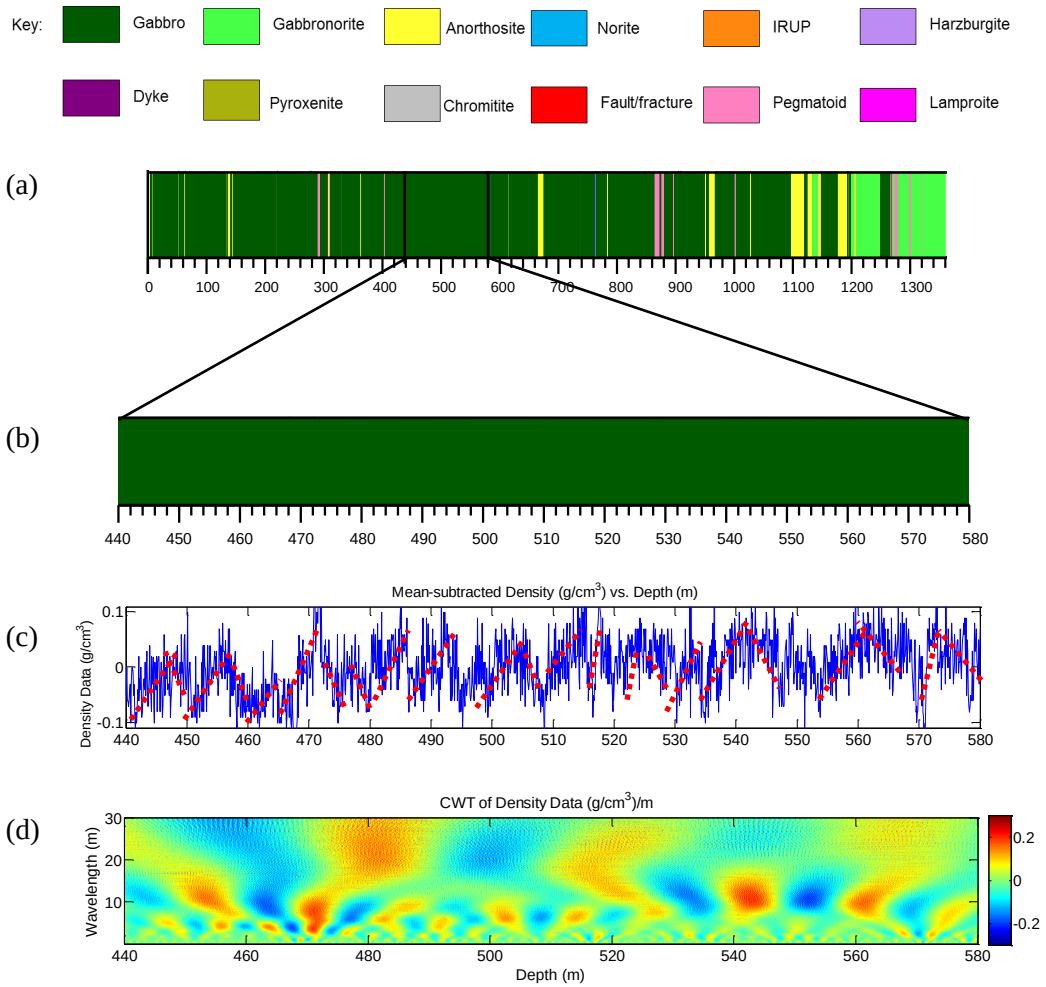

Figure 7.4 (a) Lithology log for borehole SK59A. (b) Gabbro layer for borehole SK59A from approximately 440 m to 580 m. (c) Mean-subtracted density data (g/cm^3) vs. depth (m). The red stippled lines indicate reversals in the density data. (d) CWT of the density data shown on a scale of 1 to 30 m.

Gabbronorite- KLG8

The lithology log for borehole KLG8 is shown in Figure 7.5a, and Figure 7.5b shows a 160 m thick gabbronorite layer from 170 m to 330 m.

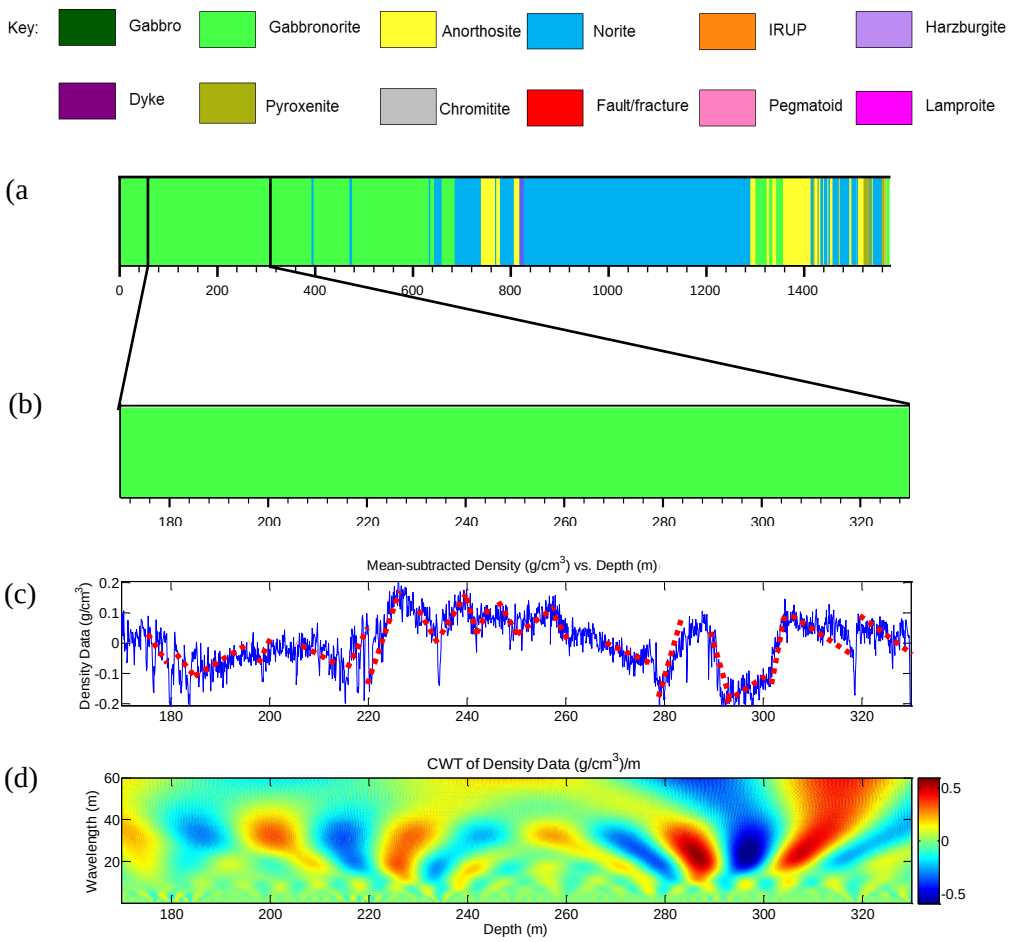

Figure 7.5 (a) Lithology log for borehole KLG8. (b) Gabbronorite layer for KLG8 from approximately 170 m to 330 m. (c) Mean-subtracted density data (g/cm^3) vs. depth (m). The red stippled lines indicate reversals in the density data. (d) CWT of the density data shown on a scale of 1 to 60 m.

The density log for this section of the borehole is shown in Figure 7.5c, which shows large variations in density of up to 0.3 g/cm^3. The trends observed in these data are not as finely periodic as in Figure 7.4c, and have a range of 0.1-0.3 g/cm^3. The wavelength of the variations also changes between the depths of 220 m and 260 m, showing a decrease. Alternatively these may be short wavelength components that emerge. Gabbronorite by definition contains 55-75% plagioclase which results in densities of 2.84-2.95 g/cm^3. Density changes of 0.1-0.3 g/cm^3 imply a change in modal abundance of plagioclase of 18% and 55% respectively. The wavelet analysis shows cyclicity at a wavelength of 30 m which becomes intense at a depth of 270 m associated with the large (0.3 g/cm^3) changes in amplitude. The change in the wavelength of the variations in the density data is observed as a 20 m wavelength in the wavelet analysis, which is clearest at these depths.

Anorthosite- DB135

The lithology log for borehole DB135 is shown in Figure 7.6a, and Figure 7.6b shows a 60 m thick anorthosite layer from 162 m to 220 m.

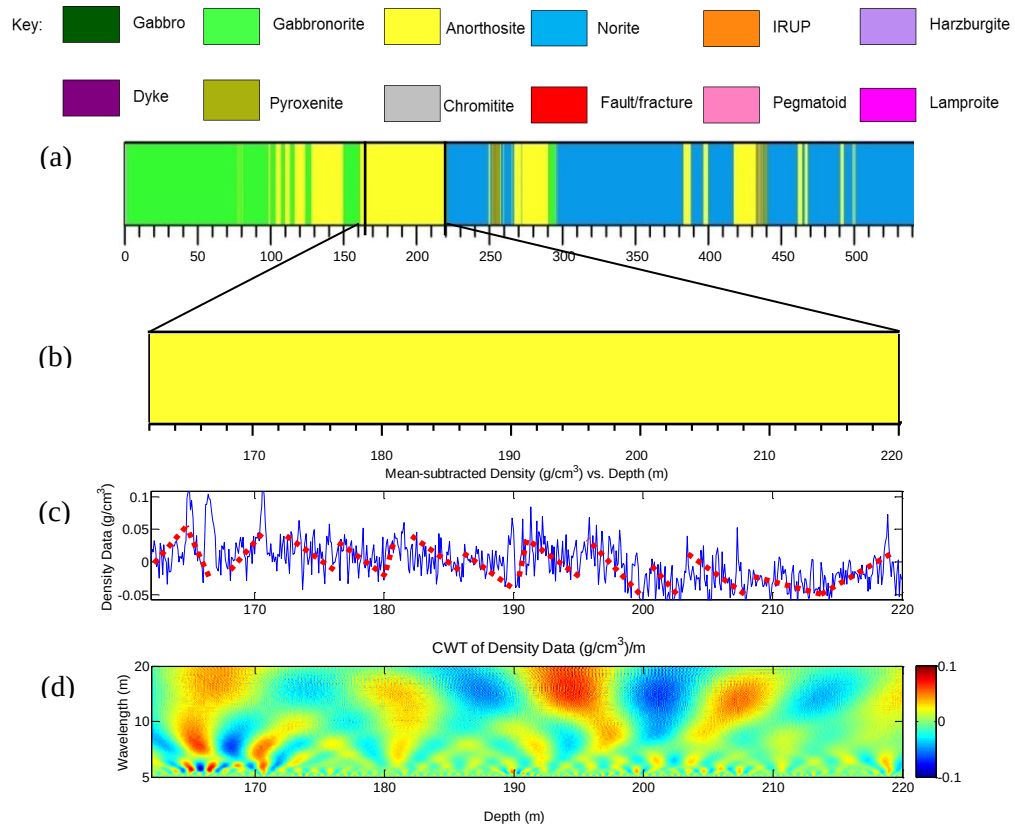

Figure 7.6 (a) Lithology log for borehole DB135. (b) Anorthosite layer for borehole DB135 from approximately 162 m to 220 m. (c) Mean-subtracted density data (g/cm^3) vs. depth (m). The red stippled lines indicate variations in the density data. (d) CWT of the density data shown on a scale of 5 m to 20 m.

The density log in Figure 7.6c shows mostly upward increases in density of approximately 0.05 g/cm^3 over 5-7 m. Anorthosite by definition contains 90-100% plagioclase, which results in densities of 2.72-2.77 g/cm^3. A density reversal of 0.05 g/cm^3 therefore implies a change in modal abundance of plagioclase of 10%. The wavelet analysis of the density data shown in Figure 7.6d shows some cyclicity within this anorthosite layer at a wavelength of ~15 m. A 7 m signal is also present and is most intense in the first 10 m of the borehole but consistent.

Norite- DB135

The lithology log for borehole DB135 is shown in Figure 7.7a, and Figure 7.7b shows a 70 m thick norite layer from 300 m to 370 m. Several cycles of density increasing and decreasing downwards of 0.05-0.1 g/cm^3 at depth intervals of 5-10 m (Figure 7.7c). There are dramatic changes in the log, including possible misidentification of this lithology from 330 m to 332 m which has been encircled. By definition norite contains 30-80% plagioclase, which results in densities of 2.82-3.0 g/cm^3. Density reversals of 0.05-0.01 g/cm^3 therefore imply a change in modal abundance of plagioclase of 13% and 2.6% respectively. The wavelet analysis shown in Figure 7.7d shows cyclicity at a wavelength of 10-15 m and at a 2.5 m wavelength that increases in intensity at depths of 325-335 m.

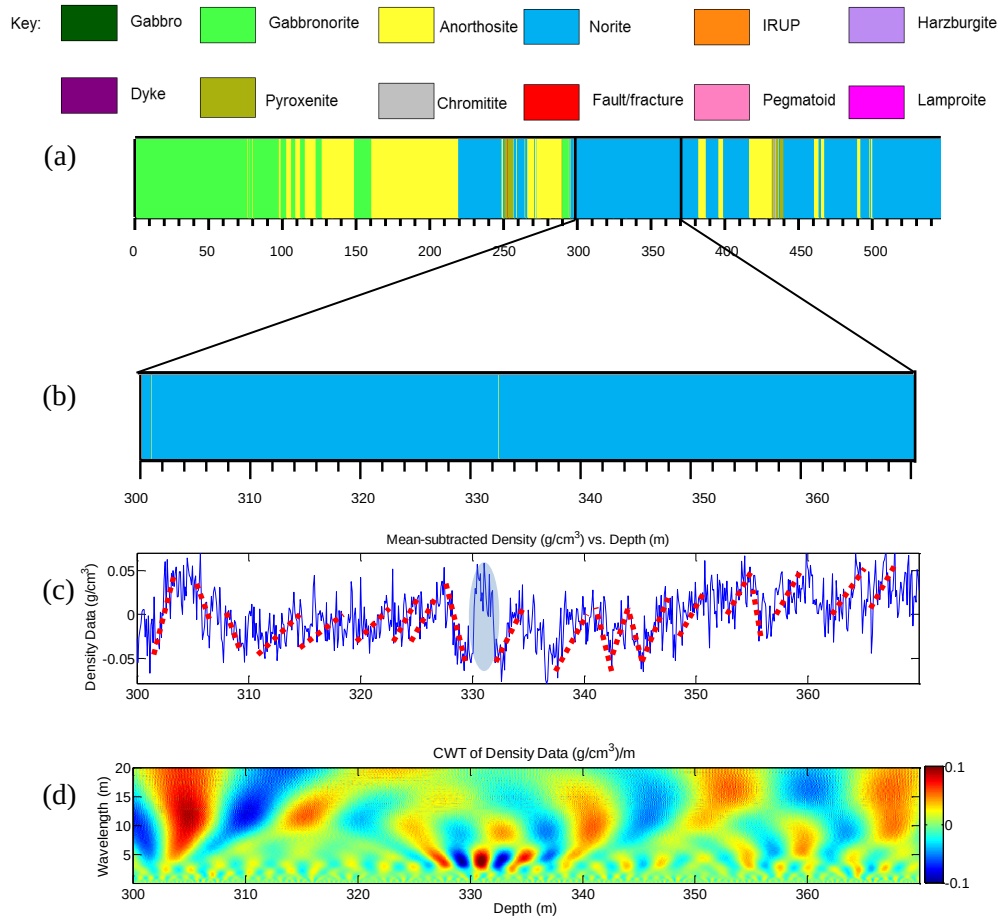

Figure 7.7 (a) Lithology log for borehole DB135. (b) Norite layer for DB135 from approximately 300 m to 370 m. (c) Mean-subtracted density data (g/cm^3) vs. depth (m). The red stippled lines indicate reversals in the density data and possible misidentification has been encircled. (d) CWT of the density data shown on a scale of 1 to 20 m.

Cyclicity studied within each of the dominant lithologies reveals that there are no unique features between interlayer and intralayer cyclicities. Similar features of multi-scale cyclicity, non-stationary variation and changes of signal intensity with depth observed in whole borehole analysis, are also present within layers. Periodicity in physical properties as observed using wavelet analysis is best attributable to a form of layering in the rock, which may or may not be macroscopically visible. Density data will most probably be the best indicator for processes occurring during layering, since it is the most consistent across logs, better constrained for each lithology type, and in general, of better quality, as summarized by Table 2.4. In addition to this, magnetite is an accessory mineral in the MZ and CZ. Forms of layering in layered intrusions are reviewed below.

7.3 Types of Layering

In the absence of isotopic, mineral composition and thin section data for the boreholes discussed, it is important to review various forms of layering observed in layered intrusions and their possible influence on the variations in physical property measurements.

7.3.1 Cryptic Layering

Layering that describes variations in mineral and whole rock composition is called cryptic layering, and is commonly not visible. Experiments have shown that the sodic (Na) end member of plagioclase forms under lower temperatures than the calcic (Ca) component. Similarly, the iron-rich (Fe) pyroxenes have lower crystallization temperatures than those which are magnesium (Mg) rich. Thus, mineral compositions indicate changes in temperature in a layered sequence (Wager and Brown, 1968). Since orthopyroxene is almost always present throughout the various layers, its composition has been studied extensively in the various zones of the BC using the Mg#, calculated using 100Mg/(Mg+Fe) (Eales and Cawthorn, 1996).

7.3.2 Phase Layering

Phase layering is a term used to describe the appearance or disappearance of certain phases in a layered sequence of rocks. This feature may be in response to either rejuvenation of magma or the formation of crystals from melt. An example of this is the disappearance of olivine in the lower part of the CZ at Union section and its reappearance in UG2 (Eales and Cawthorn, 1996).

7.3.3 Gradational Layering

Changes in modal abundances, mainly between plagioclase and pyroxene can produce layering where one increases while the other decreases towards contacts creating gradational layering. Gradational layering also describes changes in grain size, shape of individual crystals and rock fabric or texture. Grain size variations in the MZ were first investigated by Maier and Mitchell (1995). They observed upward increases in grain sizes in individual norite and gabbronorite units of the LMZ which they attributed to magma replenishment (addition) and differentiation. Textural layering exists in anorthositic and pyroxenitic rocks, which are said to commonly have bladed plagioclase crystals parallel to the layering (Eales and Cawthorn, 1996). The gabbroic rocks of the MZ studied by Ashwal et al. (2005) also showed weakly parallel alignment of tabular plagioclase to bedding.

7.3.4 Modal Layering

The last type of layering considered here is modal layering, which is not pervasive across the stratigraphy of the BC. Modal layering is most distinct in the CZ, although not always complete. This can consist of a succession of pyroxenite-norite-anorthosite from the base, to form what has been called a cyclic unit. These have varying thicknesses of 20 cm to 200 m, and most well developed in the Upper CZ (Cawthorn and Spies, 2003). The continuity of these cyclic units can extend for hundreds of kilometres laterally.

7.4 The Origin of Cyclicity

The disappearance or appearance of a cumulate mineral (e.g. orthopyroxene) can affect physical properties as the analysis is sensitive to edges or abrupt changes. Most of the boreholes from the Western Limb have intersected the MZ, where there are no observed cyclical changes in the appearance and disappearance of minerals as observed in Figure 7.8.

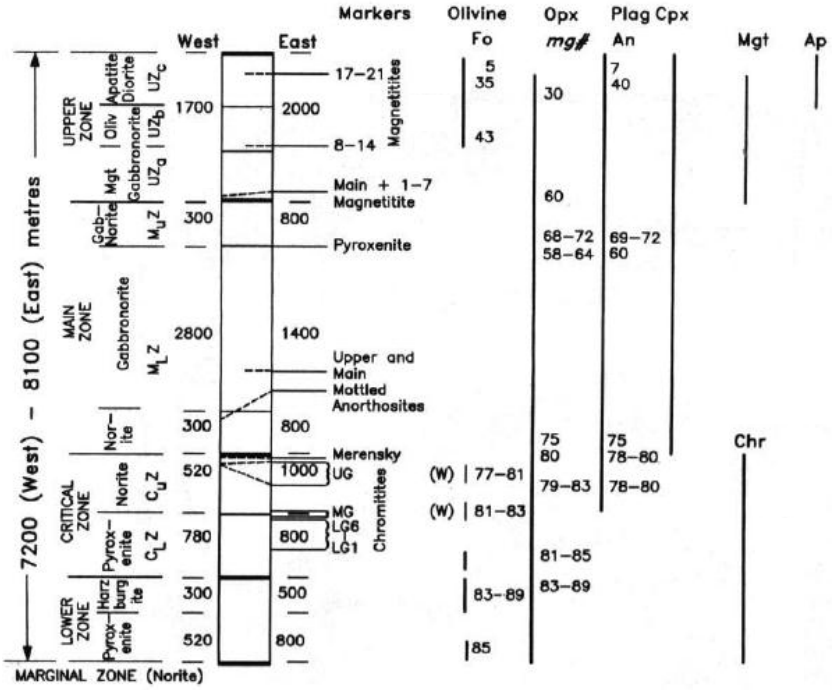

Figure 7.8 General stratigraphy of the BC showing phase layering of olivine, orthopyroxene, plagioclase, clinopyroxene, magnetite, chromitite and apatite. There are no visible appearances and disappearances of cumulate minerals in the MZ and Upper CZ which could drive the cyclicity observed in the physical property logs (data compiled by Eales and Cawthorn, 1996).

These data have been compiled by Eales and Cawthorn (1996) from studies by Cameron (1978, 1980), von Gruenewaldt (1973), Molyneux (1974), Teigler and Eales (1996) and Mitchell (1990). This image shows the chemical compositions of major constituent minerals and where they fall in the stratigraphy of the BC. The boreholes in the Eastern Limb intersect the Upper CZ in which there are appearances and disappearances of olivine. However, these have only been observed in the Western Limb at Union section. Therefore phase layering unimportant in the observed cyclicity.

Since there are no mineral compositions to accompany the boreholes which have been used, theoretical calculations can be made in order to ascertain whether cryptic layering may produce cyclicity in density readings and further reference can be made to other studies in the BC. Orthopyroxene end members of enstatite ($MgSiO_3$) and ferrosilite ($FeSiO_3$) have densities of 3.21 g/cm^3 and 3.96 g/cm^3, respectively. Clinopyroxene end members of diopside ($Mg_2Si_2O_6$) and hedenbergite ($Fe_2Si_2O_6$) have densities of 3.22 g/cm^3 and 3.56 g/cm^3, respectively. The fractionation trend for both ortho- and

clinopyroxene's Mg-rich end-members to the Fe-rich end members follows a linear trend, and should it be repeated, could follow a saw-tooth profile.

Since the Mg-rich member is less dense, the density increases towards the Fe-rich end members for the pyroxenes. Plagioclase end members of albite ($NaAlSi_3O_8$) and anorthite ($CaAl_2Si_2O_8$) have densities of 2.62 g/cm^3 and 2.76 g/cm^3, respectively. The evolution of plagioclase from its Ca-rich end-member to the Na-rich end member also follows a linear trend. Since the Ca-rich member is denser, the density decreases with an increase in Na content. Periodic reversals in these cryptic trends would thus produce a reversal in density. The mineral compositions used to calculate the density response to changing mineral compositions are based on data compiled by Eales and Cawthorn (1996) from studies by, Tegner et al. (2006) and Eales et al. (1990) for the Eastern and Western Limbs of the BC. These data are similar to those obtained by Ashwal et al. (2005) and Roelofse and Ashwal (2012) in the Northern Limb in terms of range. Only the values pertaining to the UMZ and Upper CZ have been considered for this analysis. The compositions and their associated densities are shown Table 7.9, which shows that the range in mineral compositions produce a significant change in density.

Table 7.9 Mineral compositions for plagioclase, ortho- and clinopyroxene from Eales and Cawthorn (1996) and their associated calculated densities. The difference between these is shown in the last column.

Mineral	**Mineral Composition**	**Density (g/cm^3)**	**Δ Density (g/cm^3)**
Plagioclase	An_{80} An_{50}	2.73 2.69	0.07
Orthopyroxene	Mg# 80 Mg# 50	3.36 3.59	0.34
Clinopyroxene	Mg# 85 Mg# 60	3.27 3.36	0.14

This is displayed graphically in Figure 7.9.

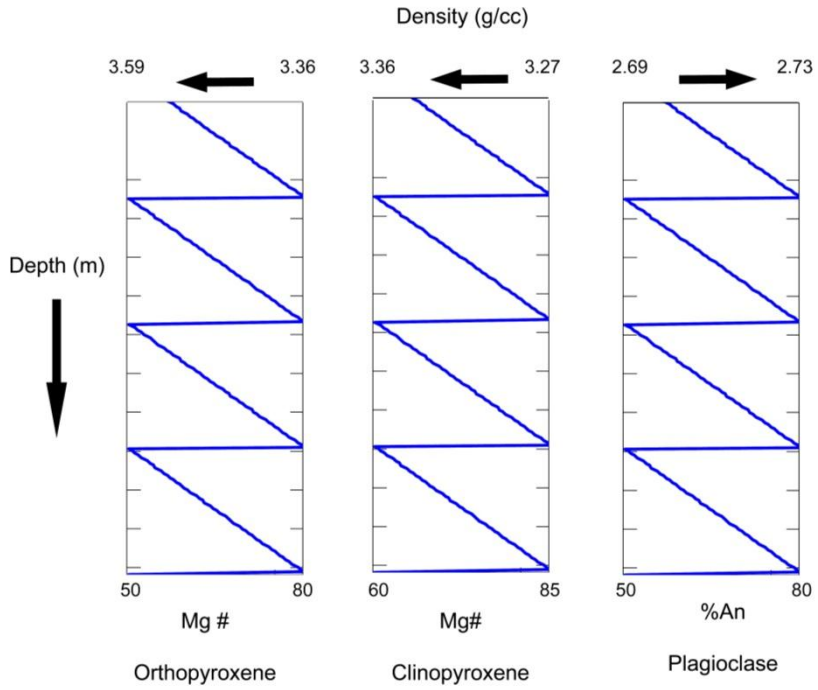

Figure 7.9 The trends show typical fractionation trends for orthopyroxene, clinopyroxene and plagioclase repeated cyclically and the associated density response. The ranges in mineral compositions used are from Eales and Cawthorn (1996). The arrows indicate the direction in which density increases based on changes in mineral composition.

The calculated densities for mineral compositions can be used to calculate whole rock densities for gabbro, gabbronorite, anorthosite and norite assuming constant modal abundance. The relative modal proportions of plagioclase and pyroxene for each of these lithologies used are based on the definitions shown previously in Table 3.1. The final calculated values are shown in Table 7.10.

Table 7.10 Lithologies and their associated minimum and maximum densities, calculated from mineral compositions. The last column shows the difference in the minimum and maximum densities.

Lithology	**Min. Density (g/cm^3) An_{80} Mg# 80 (Opx) Mg# 85 (Cpx)**	**Max. Density (g/cm^3) An_{50} Mg# 50 (Opx) Mg# 60 (Cpx)**	**Δ Density (g/cm^3)**
Anorthosite	2.67	2.74	0.07
Norite	2.81	3.08	0.28
Gabbronorite	2.84	2.98	0.14
Gabbro	2.97	3.05	0.08

The ranges of densities that can be achieved by changes in mineral compositions are not only significant but in fact comparable to those observed in Chapter 7.2.1. However, as the next section will demonstrate, changes in mineral compositions may not be the key driver to observed density changes. There are few studies in the BC which have both density readings as well as mineral compositions. The studies which do have this suite of data are by Ashwal et al. (2005) and Roelofse and Ashwal (2012) from the Northern Limb of the BC. Data by Ashwal et al. (2005) showed density reversals on the scale of 50-200 m, which in general do not correlate with mineral compositions (Figure 7.10). They did however observe reversals in chemical fractionation (e.g. an upward increase in Mg# of pyroxenes) which in some instance correlate with density e.g. 1900-2000 m. These reversals have been interpreted as "blending zones" between a new batch of added magma and a pre-existing "pile" of cumulate minerals (Ashwal, et al., 2005). However the upward increases in density in most instances correlate with an increase in the modal abundance of mafic silicates (olivine and pyroxenes) which is discussed further below.

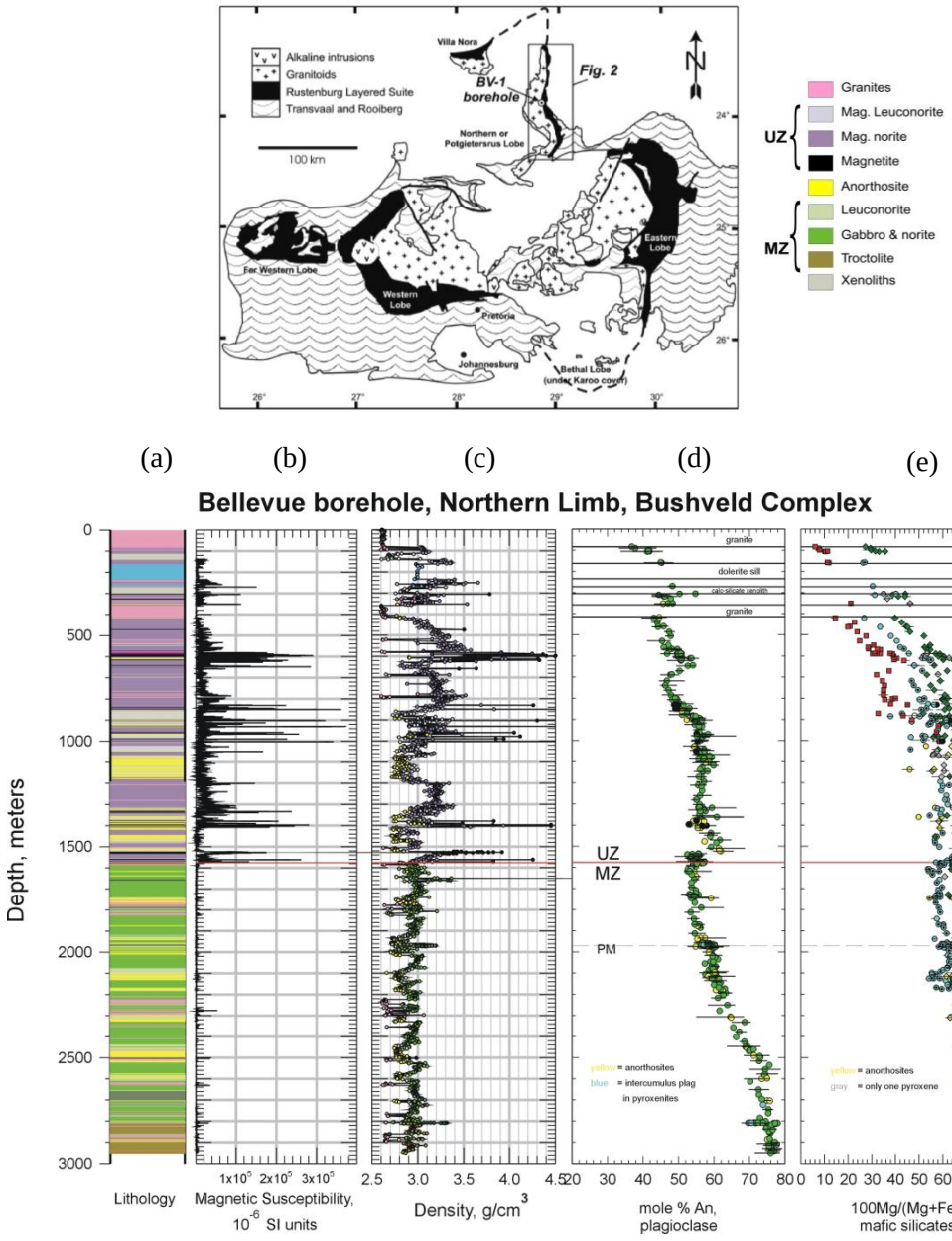

Figure 7.10 (a) Lithology for borehole Bellevue BV-1 in the Northern Limb. (b) Magnetic susceptibility log. (c) Density log. Chemical compositions for (d) plagioclase (%An) and (e) mafic silicate (Mg#). The reversals in density are not reflected in the mineral compositions (Ashwal et al., 2005).

Roelofse and Ashwal (2012) observed reversals in normal differentiation trends (similar to Ashwal et al., 2005) in Mg# (upward increase in Mg#), indicated in black arrows in Figure 7.11a.

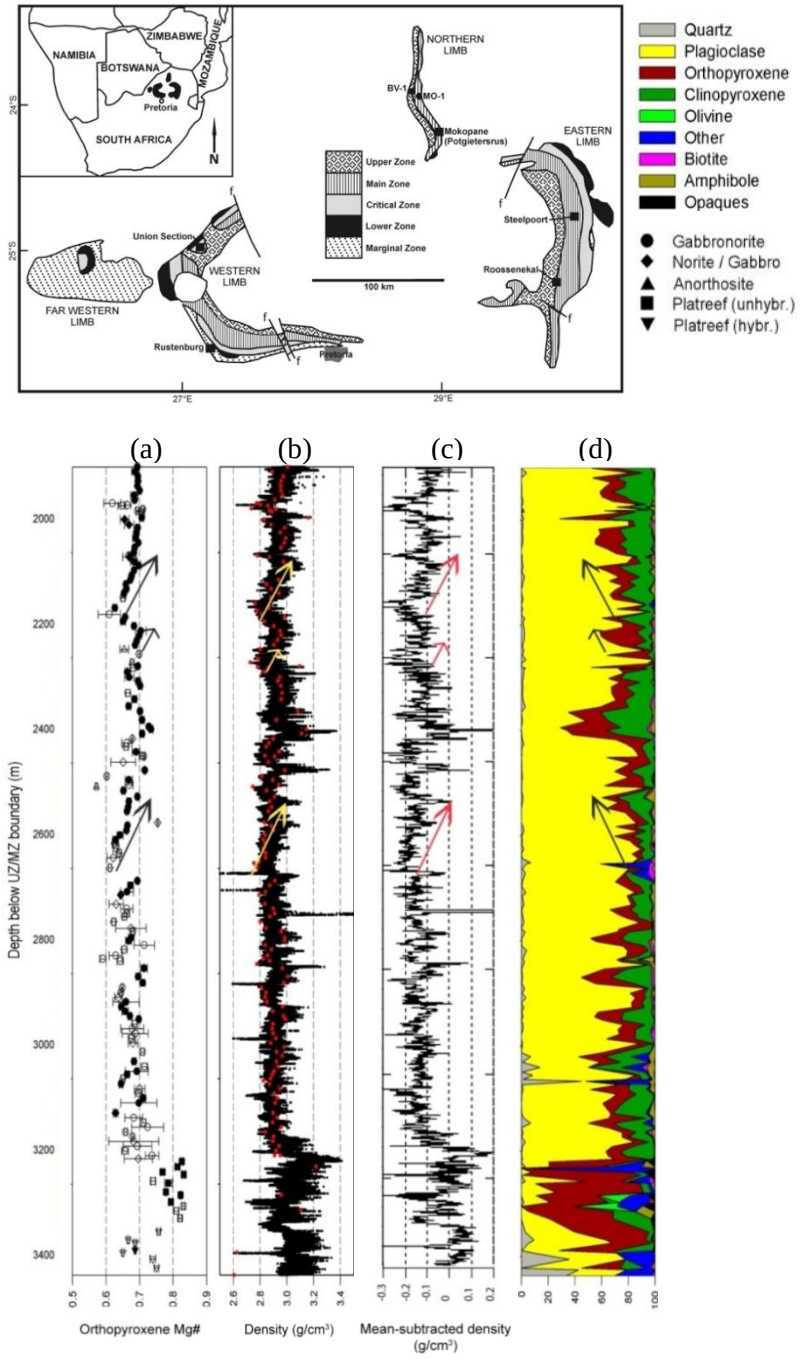

Figure 7.11 (a) Orthopyroxene Mg# for the Moordkopje MO-1 borehole in the Northern Limb. (b) Wireline density log with red dots to indicate laboratory measurements. (c) Mean-subtracted wireline density log downsampled to 100 cm. (d) Changes in modal abundance of minerals. The arrows represent changes discussed in the text (Roelofse and Ashwal, 2012).

The density log shows steady increases in their data in the same interval as the reverse in differentiation as indicated in yellow arrows in Figure 7.11b. The trends are easier to observe in the downsampled (100 cm) and mean-subtracted data in Figure 7.11c. An

increase in Mg# should lead to a decrease in density (assuming no change in modal abundance). However the density data show an increase of 0.1-0.2 g/cm^3 which correlates with an increase in the modal abundance of mafic silicates as shown in Figure 7.11d. This is evidence that modal abundance has a larger effect on density than changes in mineral composition in their study.

Reversals in mineral compositions have also been observed before in other studies, although there were no physical property logs to accompany them. An example is the study carried out by Tegner et al. (2006), which has shown cyclicity in mineral compositions in the UZ and MZ in the Western Limb (north-east of Rustenburg) (Figure 7.12).

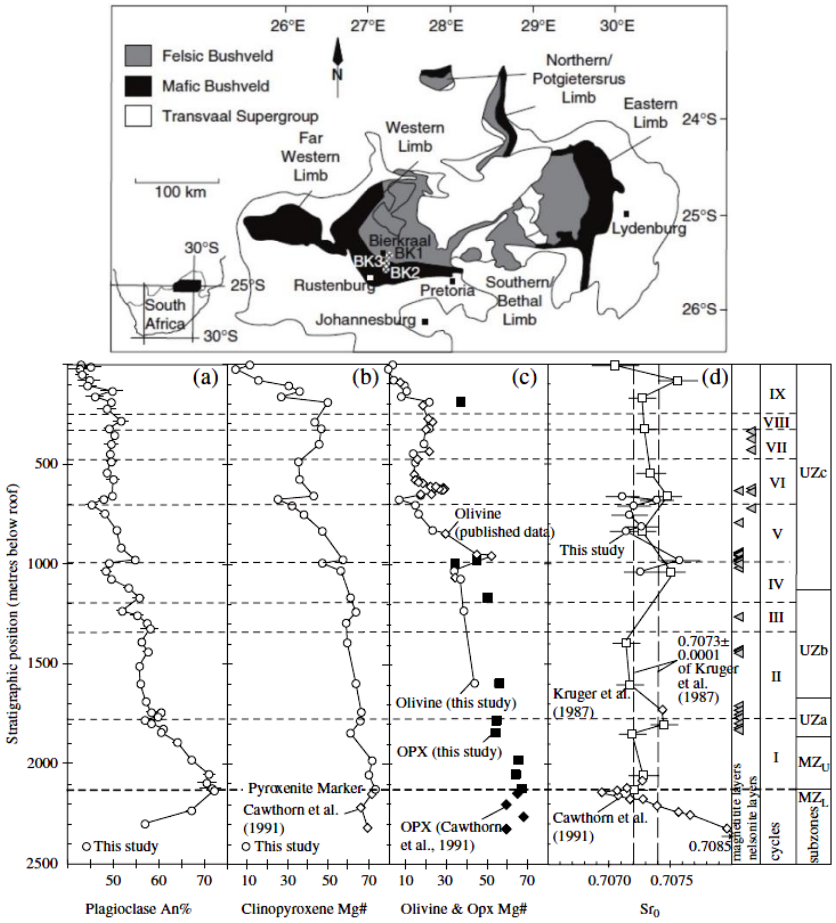

Figure 7.12 Chemical variation of (a) plagioclase (An%), (b) clinopyroxene (Mg#), (c) olivine and orthopyroxene (Mg#) and (d) initial Sr isotope with depth, in the UZ and MZ (Tegner et al., 2006). The data is a compilation of studies from Reynolds (1985), Merkle and von Gruenewaldt (1986), Kruger et al. (1987) and Cawthorn et al. (1991).

They observed approximately nine cycles in total in mineral compositions of plagioclase (%An), clinopyroxene (Mg#), olivine (Mg#), orthopyroxene (Mg#), with "near constant" Sr ($^{87}Sr/^{86}Sr$) isotopic ratio, although some variation was observed. The breaks between mineral fractionation trends have been attributed to magma mixing caused by density inversions following crystallization of magnetite, which is only applicable to the UZ where their work was mostly concentrated.

Similarly, studies in the LZ and Lower CZ by Eales et al. (1990) have also shown broad scale cyclicity in whole rock and orthopyroxene Mg# every 250-400 m in the Western Limb at Union Section (Figure 7.13). These variations are also present in the percentage of plagioclase (whose An% is almost constant), which can be seen as a proxy for rock density. Eales et al. (1990) identified approximately eight of these cycles which have been attributed to mixing of magmas.

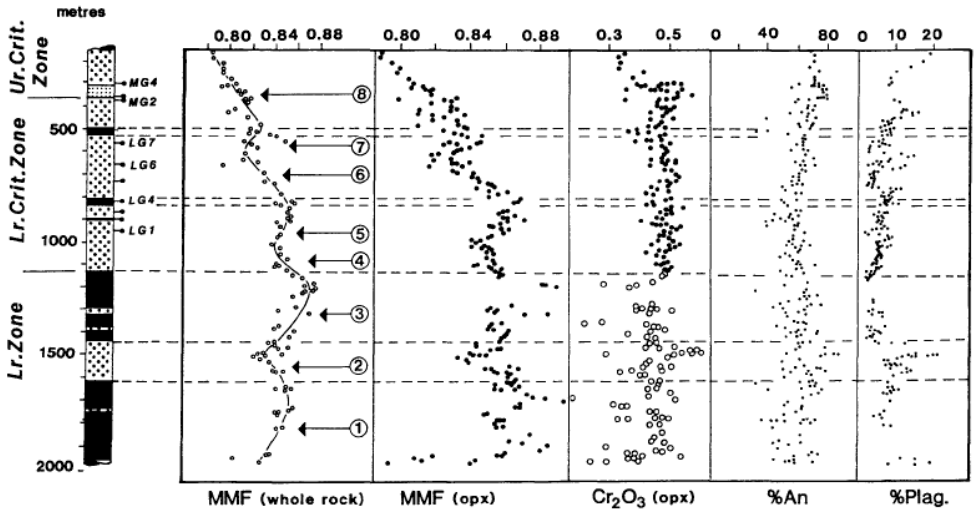

Figure 7.13 LZ and Lower CZ of at Union section. The chemical data are based on 130 whole rock analyses, and over 1000 feldspar and orthopyroxene analysis. Eight segments that show prominent reversals are shown as segments across the logs. MMF is the Mg# (Eales et al., 1990).

Cyclical changes in modal proportions in minerals are likely to have a more important role in physical property cyclicity than those in mineral compositions. The prominent density reversals discussed by Ashwal et al. (2005) were seen to reflect a change in modal colour index, which is the sum of the volume percentage of mafic silicates and Fe-Ti oxides (magnetite and ilmenite). Since Fe-Ti oxides are virtually absent in the MZ, the density can be seen as correlating with the modal abundance of pyroxenes. It is not unreasonable to extend this idea throughout the zones, since the predominant lithologies are simply composed of varying proportions of plagioclase and mafic silicate minerals.

Changes in density, therefore, represent changes in modal proportions. Ashwal (pers. comm) studied changes in lithologies, the associated density response, modal changes, and thin sections across a 200 m section in the LMZ. Their data show upward increase in density in gabbronorite which correlates with an increase in mafic silicate minerals in thin section. This makes changes in mineral proportions a key driver in cyclicity in physical properties in their study.

7.5 Emplacement Processes

Layered intrusions undergo "periodic" magma addition during their formation (Cawthorn, 2007). This is unsurprising considering that the emplacement of the BC has been estimated to have lasted for as long as 65 000 years and covers ~65 000 km^2 (Cawthorn and Webb, 2012). The data presented from various studies show clear evidence of cyclicity in whole rock and mineral chemical compositions as well as modal proportions in the BC. However the cyclicity being detected is probably due to subtle changes in mineral proportions, which drive cyclicity observed in density more than changes in chemical compositions. The modal variations may not always be easily detected in hand specimen when the scale of layering is too small or too large, but the 10 m scale of layering observed in Figure 7.4 for example should be visible in the borehole core. Thus it is the finding of this study that the cyclicity in physical property data thus far reported in all of the boreholes of the BC is controlled by changes in modal abundance. In addition to this, since layering is generally ubiquitous across layered intrusions, this cyclicity can be assumed to be present across the entire BC. The boreholes used in this study have shown that the wavelength of the cyclicity in the boreholes and the Western and Eastern Limbs respectively, correlate (Figure 6.30). This may imply that cyclicity may be produced by a chamber-wide process.

However the mechanism of layering which has produced layers in which density increases upwards is still difficult to decipher and can only be addressed with a suite of mineral composition, isotopic and thin sections data. There are at present over twenty different models for layering mechanisms (Naslund and McBirney, 1976). Magma replenishment and magma mixing (via double-diffusive convection) have been used to explain layering of some parts of the BC stratigraphy.

Wavelet analysis can be used to study magmatic processes; especially if a suite of chemical data and mineralogical data are available. This technique may become

increasingly important, if the cyclicity in physical property data correlates with reversals in fractionation trends, since Ashwal et al. (2005) have suggested that these may represent zones of magma additions. The thickness or volumes can be quantified using wavelet analysis across boreholes. This could be an important contribution since the current perspective on magma addition in the RLS is that four major additions have formed this 8 km thick suite of rocks (Eales, 2002), as opposed to smaller periodic influxes of magma.

Dramatic changes in Sr ratio are commonly attributed to magma addition and are influential in the stratigraphic subdivisions of the BC (Roelofse, 2010). The nature of the Sr variation with height for the Western Limb was compiled by Kruger (1994). These data are summarized in Figure 7.14 from Roelofse (2010). Major breaks at the Pyroxenite Marker for example, are used as evidence for magma addition.

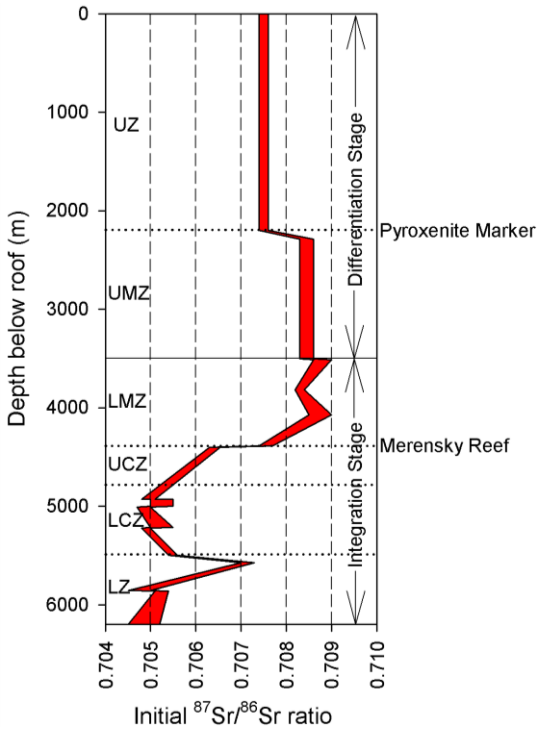

Figure 7.14 Variation in Sr isotope stratigraphy of the Western Limb of the Bushveld Complex (Roelofse, 2010).

The stratigraphic levels at which these magmas were injected are shown in Figure 7.15. The LZ is recognised as representing the first emplacement of magma. The continuous mineral evolution seen in the LZ and Lower CZ has been best described as possibly having formed by magma replenishment (Vantongeren and Mathez, 2013; Eales and Cawthorn, 1996; Eales and Reynolds, 1986).

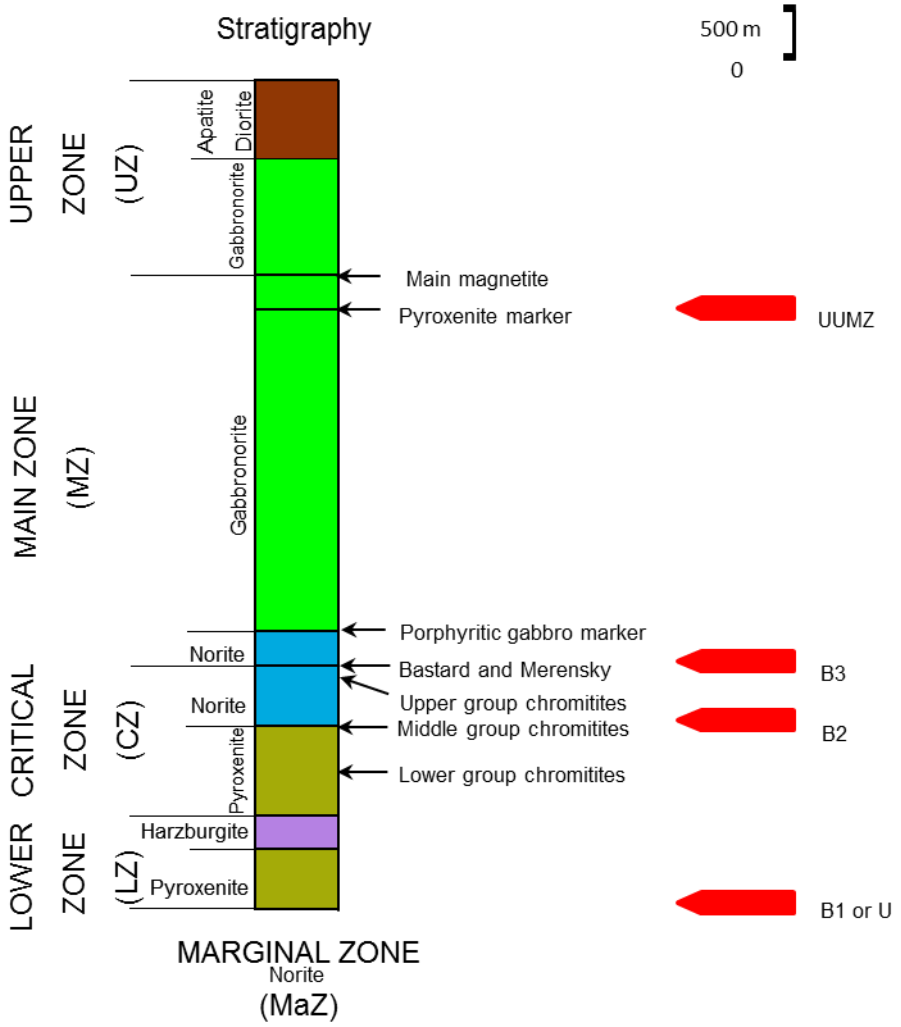

Figure 7.15 The levels of proposed magma additions to the RLS. The first magma type B1, is proposed to have formed the LZ and the Lower CZ. The overlying Upper CZ up to the Merensky Reef broadly correlate with the compositions of the B2 and B3 magmas. The final major magma addition to form the UMZ and UZ is envisioned to have occurred at the level of the Pyroxenite Marker, and is referred to as the UUMZ (Vantongeren and Mathez, 2013; Eales, 2002).

These magmas are referred to as the B1 or U-type magma and are recognised in both the Western and Eastern Limbs (Wilson, 2012). The parental magma that gave rise to the UZC and MZ are the B2 and B3 type magma (Vantongeren and Mathez, 2013). Magma mixing occurred at the level of the Merensky Reef with the intrusion of B3, which is characterised by the large Sr isotopic break evident in Figure 7.14. The signature of Sr is significantly higher than that observed in the B1 magma (Wilson, 2012). The last addition of magma is generally accepted to have been below the Pyroxenite Marker, separating the LMZ from the UMZ in both the Western and Eastern Limbs (Vantongeren and Mathez, 2013; Kruger et al., 1987). Supporting reasons for this are the reversals in cryptic trends

and the change in Sr isotope signature at this marker (Kruger et al. 1987; Cawthorn et al., 1991). This has been named the UUMZ-type (Upper and Upper Main Zone). The most recent study of this has been by Vantongeren and Mathez (2013), who determined the composition of the magma to be tholeiitic, since magma injection was first proposed 40 years earlier by von Gruenewaldt (1973) and Molyneux (1974) in the Eastern Limb. The source and nature of this magma is suggested to be similar to the B2-type magma by their study. These studies show how instrumental Sr isotopic has been in the definition of the stratigraphy of the BC as well as the level at which various magmas intruded and in some cases mixed.

However, isotopic data are not currently collected with the same continuity and density as geophysical wireline data. The compilation of data in Figure 7.14 represents approximately 100 samples in an 8 km thick suite of rock, which is ~1 sample per 80 m. For comparison, the wireline data presented in this project are sampled at every 1 cm, which is 8000 times more. It is therefore not unreasonable to suggest that if isotopic data could be sampled as densely that more magma pulses could be deciphered and various other compositions for them would then be calculated based on chemical analyses of rocks and the crystallization sequence observed. Physical property data should therefore be incorporated with the interpretation of isotopic data and whole rock and mineral compositions into the future.

7.6 Summary

Two quality control workflows have been developed for physical property and lithology logs. The physical properties can be studied by making observations on the entire wireline log and then segmenting it and studying small sections at a time, which makes the process of identifying inaccurate logging practices easier and faster. The final step should then be to study the scatter the plot of any two physical properties at hand which may reveal logging errors not obvious in the logs. It also allows for two logs to be studied simultaneously. The workflow for ensuring an accurate lithology log starts with studying histograms of the available physical property data. The modes (peaks) may be an indication of the number of different lithologies in the borehole. The next step is computing a classification scheme (e.g. *k*-means) in order to determine the classes with depth. This can be used to support lithology observations made on the actual core and should ideally match. Once the lithology and physical property logs are of the best quality possible, they can then be used in further data analysis. The second section of the chapter

has been on the wavelet analysis. The quality control has allowed for the best possible data to be used in this analysis. Cyclicity in physical properties is more likely due to changes in modal abundance than mineral compositions or phase layering. Future studies should incorporate density logs with Sr isotopic data, mineral compositions and mineral modal abundance for deciphering emplacement processes.

CHAPTER 8: CONCLUSIONS AND FURTHER WORK

This thesis has presented an extensive database of wireline geophysical logs. These data may represent the largest analysis of density and magnetic susceptibility logs for the BC and possibly of any layered intrusion. These data have been used to approximate representative averages of densities for the major constituent lithologies, while the magnetic susceptibilities show a large variation, typical of mafic intrusions. These data may be become important in future for forward modelling and or inversion for potential field data.

Simple statistical analysis has shown that anorthosites and norites are often misidentified, which confirms the already known subjective nature of geological logging. Large scattering in rock physical properties overall probably reflects rock heterogeneities as well as misidentification of lithologies. The classification has also highlighted disparities between the physical properties and the supplied geological log. The performance of the algorithm is adversely affected by clusters that overlie each other, caused by small physical contrasts between lithologies. What stands out is the ability of the analysis to easily outline the position of pyroxenite and chromitite layers which are of interest to mining companies. These analyses can be used in conjunction with the logging process for a semi-automated approach to locating the abovementioned layers of interest.

Two quality control workflows have been created for checking the quality of both physical property and lithology logs. These can be readily implemented by mining companies and the academic community. The suggested workflow for assessing the quality of physical properties is to first study small sections of log at a time. Studying the data at this scale may be able to highlight spurious data. It is also useful to study two physical simultaneously using a scatter plot as another way to visualize data. Once these steps are carried out, the data can be studied and interpreted. The second workflow developed is for incorporating physical property logs into the geological logging process. This can be carried out using histograms to infer the minimum types of lithologies present using the modes. The classification results can also give an indication of the how the physical properties change with depth, which can be used while making observations on borehole core.

The wavelet analysis shows cyclicity in physical properties most likely related to layering in the rocks. The types of layering being detected are possibly cryptic, but the cyclicity is

most likely driven by changes in modal proportions. Cyclicity may reflect magma addition as suggested by Ashwal et al. (2005). These data have shown that physical properties show cyclical variations in the Western and Eastern Limbs across the MZ and CZ. Although conventional means for studying magma additions have involved Sr isotopic data, these data are currently under sampled, and more periodic additions would probably be deciphered with improved sampling into the future. Physical property data should therefore be incorporated into studies of magmatic suites.

Further work to be carried out is to take full advantage of the large database of data to improving the classification of physical properties using supervised learning for classifying new data. This may also be useful for boreholes whose geological logs are not known but whose physical property data are available. Also, higher dimensional cluster analysis can be considered for better constraining lithology properties. The wavelet analysis should be extended to other layered mafic intrusions. There is also a need for closely sampled isotopic, mineral compositions, density logs and thin section data to definitively decipher magmatic processes.

REFERENCES

Ackermann, M.R., Blömer, J., and Sohler, C. (2010) Clustering for metric and nonmetric distance measures. *ACM Transactions on Algorithms*, **6**, 59-85.

Alsabti, K., Ranka, S., and Singh, V. (1997) An efficient k-means clustering algorithm, *Electrical Engineering & Computer Science*. http://surface.syr.edu/eecs/43[Accessed 2 May 2013].

Ashwal, L.D. (2011) Construction of the Bushveld Complex by repeated intrusion of crystal-rich magmas. Abstract of the *Geosynthesis- Integrating the Earth Sciences Conference*, Cape Town, South Africa, August 28-September 2, 2011.

Ashwal, L.D., Webb, S.J., and Knoper, M.W. (2005) Magmatic Stratigraphy in the Bushveld Northern Lobe: continuous geophysical and mineralogical data from the 2975 m Bellevue drillcore. *South African Journal of Geology*, **108**, 199-232

Barnes, S., Maier, W.D., and Ashwal L.D. (2004) Platinum-group element distribution in the Main Zone and Upper Zone of the Bushveld Complex, South Africa. *Chemical Geology*, **208**, 293-317.

Bottou, L., and Y. Bengio (1995) Convergence properties of the k-means algorithm. *Advances in Neural Information Processing Systems*, **7**, 585-592.

Cameron, E.N. (1978). The Lower Zone of the Eastern Bushveld Complex in the Olifants River trough. *Journal of Petrology*, **19**,437-462

Cameron, E.N. (1980) Evolution of the Lower Critical Zone, central sector, eastern Bushveld Complex. *Economic Geology*, **75**, 845-871.

Cameron, E.N., and Desborough, G.A. (1964) Origin of certain magnetite-bearing pegmatites in the eastern part of the Bushveld Complex, South Africa. *Economic Geology*, **59**, 197-225.

Cawthorn, R. G. (2007) Cr and Sr: Keys to parental magmas and processes in the Bushveld Complex, South Africa. *Lithos*, **95**, 381-398.

Cawthorn, R.G. and Davies, G. (1983) Experimental data at 3 Kbars pressure on parental magma to Bushveld Complex. *Contributions to Mineralogy and Petrology*, **83**, 125-135.

Cawthorn, R.G., Eales, H.V., Walraven, F., Uken, R., and Watkeys, M.K. (2006) The Bushveld Complex in: Johnson, M.R, Anhaeusser, C.R., and Thomas, R.J (editors): *The Geology of South Africa*. Geological Society of South Africa and Council for Geoscience, Pretoria, pp. 261-269.

Cawthorn, R.G., Meyer, P.S., and Kruger, F. J. (1991) Major addition of magma at the Pyroxenite Marker in the western Bushveld Complex, South Africa. *Journal of Petrology*, **32**, 739-763.

Cawthorn, R.G., and Spies, L. (2003) Plagioclase content of cyclic units in the Bushveld Complex, South Africa. *Contributions to Mineralogy and Petrology*, **145**, 47-60.

Cawthorn, R.G., and Walraven, F. (1998) Emplacement and crystallization time for the Bushveld Complex. *Journal of Petrology*, **39**, 1669-1687.

Cawthorn, R.G., and Webb, S.J. (2013) Cooling of the Bushveld Complex, South Africa: Implications for paleomagnetic reversals. *Geology*, **41**, 687-690.

Chandrasekhar, E., and Rao, E. (2012) Wavelet analysis of geophysical well-log data of Bombay offshore basin, India. *Mathematical Geosciences*, **44**, 901-928.

Chatfield, M. (2008) Wireline Logging Notes. Two-day course, CSIR, Auckland Park, Johannesburg, November 6-7 2008.

Chatfield, M., Trofimczyk, K., Harney, D., and Katchigunda, T. (2009) Downhole wireline density versus drill core density measurements in porous and vuggy rocks. Short paper of the *11th SAGA Biennial Technical Meeting and Exhibition*, Swaziland, September 16-18 2009.

Clarke, B., Uken, R., and Reinhardt, J. (2009) Structural and compositional constraints on the emplacement of the Bushveld Complex, South Africa. *Lithos*, **111**, 21-36.

Cooper, G.R.J (2009) Wavelet-based semblance filtering. *Computers and Geosciences*, **35**, 1988-1991.

Cooper, G.R.J., and Cowan, D.R (2008) Comparing time series using wavelet-based semblance analysis. *Computers and Geosciences*, **34**, 95–102.

Cormack., R.M. (1971) A review of classification. *Journal of the Royal Statistical Society*, **134**, 321-367.

Cowan, D.R, and Cooper, G.R.J (2003) Wavelet analysis of detailed drillhole magnetic susceptibility data, Brockman Iron Formation, Hamersley Basin, Western Australia. *Exploration Geophysics*, **34**, 63-68.

De Klerk, W.J. (1995) Textures exhibited by feldspars in the Giant Mottled Anorthosite (Giant Mottled Anorthosite) of the Bastard unit in the Upper CZ, Western Bushveld Complex. *Mineralogy and Petrology*, **54**, 25-34.

Eales, H. V. (2002) Caveats in defining the magmas parental to the mafic rocks of the Bushveld Complex, and the manner of their emplacement: review and commentary. *Mineralogical Magazine*, **66**, 815-832.

Eales, H.V., and Cawthorn, R.G., (1996) The Bushveld Complex in: Cawthorn R.G. (editor): *Layered Intrusions*. Amsterdam: Elsevier Science, pp. 181-229.

Eales, H.V., de Klerk, W.J., and B. Teigler (1990) Evidence for magma mixing processes within the Critical and Lower Zones of the northwestern Bushveld Complex, South Africa. *Chemical Geology*, **88**, 261-278.

Eales, H.V. and Reynolds, I.M. (1986) Cryptic variations within chromitites of the upper critical zone, northwestern Bushveld Complex. *Economic Geology*, **81**, 1056-1066.

El Agha, M. and Ashour, W.M. (2012) Efficient and fast initialization algorithm for k-means clustering. *Intelligent Systems and Applications*, **1**, 21-31.

Ellis, J.V., and Singer, J.M. (2007) *Well Logging for Earth Scientists*, 2nd Edition, Springer, pp.692.

Everitt, B. (1974) *Cluster Analysis*, 1st Edition, Heinemann Educational Books, pp. 121.

Faber, V. (1994) Clustering and the continuous k-means algorithm. *Los Alamos Science*, **22**, 138-144.

Ferré, E.C., Bordarier, C., and Marsh, J.S. (2002) Magma flow inferred from AMS fabrics in a layered mafic sill, Insizwa, South Africa. *Tectonophysics*, **35**, 1-23.

Ferré, EC., Maes, S.M. and Butak, K.C. (2009) The magnetic stratification of layered mafic intrusions: Natural examples and numerical models. *Lithos*, **111**, 83-94.

Firth, D. (1999) *Log Analysis for Mining Applications*, Reeves Wireline Services, pp. 156.

Firth D. and Elkington, P. (2000) *Reeves Mineral Services Catalogue*, Reeves Wireline Services, pp. 36.

Fullagar, P.K., Zhou, B. and Fallon, G.N (1999) Automated interpretation of geophysical borehole logs for orebody delineation and grade estimation. *Mineral Resources Engineering*, **8**, 269-284.

Gabor, D., (1946) Theory of communication. Part 1: The analysis of information. *Journal of the Institute of Electrical Engineering*, **93**, 429-457.

Grinsted, A., Moore, J.C., and Jevrejeva, S. (2004) Application of the cross wavelet coherence to geophysical time series.*Nonlinear Processes in Geophysics*, **11**, 561-566.

Gubbins, D. (2004) *Time Series Analysis and Inverse Theory for Geophysicists*, 1st Edition, Cambridge University Press, pp. 270.

Hallenburg, J.K. (1984) *Geophysical Logging for Mineral and Engineering Applications*. PennWell Books, PennWell Publishing Company, pp. 254.

Hattingh, P.J. (1983) PhD Thesis: A Palaeomagnetic Investigation of the Layered Mafic Sequence of the Bushveld Complex, University of Pretoria, Pretoria, South Africa.

Henkel, H. (1976) Studies of density and magnetic properties of rocks from northern Sweden. *Pure and Applied Geophysics*, **114**, 235-249.

Jain, A.K. (2010) Data clustering: 50 years beyond K-means. *Pattern Recognition Letters*, **31**, 651-666.

Kearey, P., Brooks, M. and Hill, I. (2002) *An Introduction to Geophysical Exploration*, 3rd Edition, Blackwell Science, London, pp. 262.

Killen, P.G (1997) Borehole geophysics: exploring the third dimension. Proceedings of *Exploration 97: Fourth Decennial International Conference on Mineral Exploration*, edited by A.G. Gubins, pp.31-42.

Kogan, J. (2007) *Introduction to Clustering Large and Higher Dimensional Data*, Cambridge University Press, 1st Edition, pp. 205.

Krane, K.S. (1988*) Introductory Nuclear Physics*, John Wiley and Sons, pp.845.

Kruger, F.J. (2005) Filling the Bushveld Complex magma chamber: lateral expansion, roof and floor interaction, magmatic unconformities, and the formation of giant chromitite, PGE and Ti-V-magnetite deposits. *Mineralium Deposita*, **40**, 451-472.

Kruger, F.J. (1994) The Sr-isotopic stratigraphy of the western Bushveld Complex. *South African Journal of Geology*, **97**, 393-398.

Kruger, F.J., Cawthorn, R.G., and Walsh, K.L. (1987) Strontium isotope evidence against magma addition in the Upper Zone of the Bushveld Complex. *Earth Planetary Science Letters*, **84**, 51-58.

Kukkonen, I.T and Peltoniemi, S. (1998) Relationships between thermal and other petrophysical properties of rocks in Finland. *Physics and Chemistry of the Earth*, **23**, 341-349.

Kumar, P., and Foufoula-Georgia, E. (1994) Wavelet analysis for geophysical applications. *Reviews of Geophysics*, **35**, 385-412.

Labat, D. (2005) Recent advances in wavelet analyses: Part 1. A review of concepts. *Journal of Hydrology*, **314**, 275-288.

Lange, T., Law, M.H., Jain, A.K., and Buhmann, J. (2005) Learning with constrained and unlabelled data. In: Proceedings of the *IEEE Conference on Computer Vision and Pattern Recognition*, **1**, 731-738.

Lee, C.A. (1996) A Review of Mineralization in the Bushveld Complex and Some Other Layered Intrusions In: R.G. Cawthorn (Editor): *Layered Intrusions*. Amsterdam: Elsevier Science, pp. 103-145.

Leeb-Du Toit, A. (1986) The Impala Platinum Mines in: Anhaeusser, C.R. and Maske, S. (editors), *Minerals Deposits of Southern Africa*, Volume II, Geological Society of South Africa, pp. 1091-1106.

Letts, A.S. (2007) PhD thesis: The Palaeomagnetic Significance of the Bushveld Complex and Related 2 Ga Magmatic Rocks in Ancient Continental Entities, University of the Witwatersrand, Johannesburg, South Africa.

Liu, C., Hu, T., Ge, Y., and Xiong, H. (2012) Which distance metric is right: An evolutionary *k*-means view. In: Proceedings of the *12th SIAM international conference on data mining*, 907-918.

Lowrie, W. (2007) *Fundamentals of Geophysics*, 2nd Edition, Cambridge, pp.381.

Maes, S.M., Ferré, E.C., Tikoff, B., Brown, P.E. and Marsh, J.S. (2008) Rock magnetic stratigraphy of a mafic layered sill: A key to the Karoo volcanics plumbing system. *Journal of Volcanology and Geothermal Research*, **172**, 75-92.

Maier, W.D., and Mitchell, A.A. (1995) Grain-size variations of cumulus plagioclase in the Main Zone of the Bushveld Complex. *European Journal of Mineralogy*, **7**, 195-204.

Mallet, S. (2009) *A Wavelet Tour of Signal Processing: The Sparse Way*, 3rd Edition, Academic Press, pp. 805.

Mcbirney, A.R. and Noyes, M. (1979) Crystallization and layering of the Skaergaard intrusion. *Journal of Petrology*, **20**, 487-554.

Merkle, R.K.W., and von Gruenewaldt, G. (1986) Compositional variation of Co-rich pentlandite: Relation to the evolution of the Upper Zone of the western Bushveld Complex, South Africa. *Canadian Mineralogist*, **24**, 529-546.

Michelle, A.A. (1990) The stratigraphy, petrography and mineralogy of the Main Zone of the northwestern Bushveld Complex. *South African Journal of Geology*, **93**, 818-831.

Middleton, R.S. (2004) Proterozoic diabase sills of Northern Ontario: magnetic properties and history, *Journal of Geophysical Research*, 109, DOI:10.1029/2003JB002581.

Milsom, J. (2003) *Field Geophysics*, 3rd Edition, Wiley, pp. 232.

Misiti, M., Misiti, Y., Oppenheim, G., and Poggi, J.M. (1997) *Wavelet Toolbox: For Use with MATLAB*, Math Works Inc., pp. 3-6.

Mitchell, A.A. (1990) The stratigraphy, petrography and mineralogy of the Main Zone of the northwestern, Bushveld Complex. *South African Journal of Geology*, **93**, 818-831.

Molyneux, T. G. (1974) A geological investigation of the Bushveld Complex in Sekhukhuneland and part of the Steelpoort Valley. *Transactions of the Geological Society of South Africa*, **77**, 329-338.

Mythili, S., and Madhiya, E. (2014) An analysis on clustering algorithms in data mining. *International Journal of Computer Science and Mobile Computing*, **3**, 334-340.

Naslund, H.R. Turner, P.A., and Keith, D.W. (1991) Crystallization and layer formation in the middle zone of the Skaergaard Intrusion. *Bulletin of the Geological Society of Denmark*, **38**, 165-171.

Naslund, H.R., and McBirney, A.R. (1996) Mechanisms of formation of igneous layering in: Cawthorn R.G. (editor): *Layered Intrusions*. Amsterdam: Elsevier Science, pp. 1-43.

Nex, P.A.M., Cawthorn, R.G. and Kinnaird, J.A. (2002) Geochemical effects of magma addition: compositional reversals and decoupling of trends in the Main Zone of the western Bushveld Complex. *Mineralogical Magazine*, **66**, 833-856.

Nex, P.A., Kinnaird, J.A., Ingle L.J., Van Der Vyver, B.A. and Cawthorn, R.G. (1998) A new stratigraphy for the MZ of the Bushveld Complex, in the Rustenburg area. *South African Journal of Geology*, **101**, 215-223.

Pan, S., Hsieh B., Lub, M., and Lin, Z. (2008) Identification of stratigraphic formation interfaces using wavelet and Fourier transforms. *Computers and Geosciences*, **34**, 77-92.

Peña, J.M., J.A. Lozano, et al. (1999) An empirical comparison of four initialization methods for the k-means algorithm. *Pattern Recognition Letters*, **20**, 1027-1049.

Prokoph, A, and Agterberg, F.P. (1999) Detection of sedimentary cyclicity and stratigraphic completeness by wavelet analysis: An application to late Albian cyclostratigraphy of the Western Canada sedimentary basin. *Journal of Sedimentary Research*, **69**, 862-875.

Prokoph, A, and Agterberg, F.P. (2000) Wavelet analysis of well-logging data from oil-source rock, Egret Member, offshore eastern Canada. *AAPG Bulletin*, **84**, 1617-1632.

Prokoph, A, and Barthalmes, F. (1996) Detection of nonstationaries in geological time series: wavelet transform of chaotic and cyclic sequences. *Computers and Geosciences*, **22**, 1097-1108.

Prokoph, A., and Bilali, H.E. (2008) Cross-wavelet analysis: A tool for detection of relationships between paleoclimate proxy records. *Mathematical Geosciences*, **40**, 575-586.

Quadling, K., and Cawthorn, R.G. (1994) The layered gabbronorite sequence, Main Zone, eastern Bushveld Complex. *South African Journal of Geology*, **97**, 442-454.

Rampino, M.R., Prokoph, A., and Adler, A. (2000) Tempo of the end-Permian event: High-resolution cyclostratigraphy at the Permian-Triassic boundary. *Geology*, **28**, 643-646.

Reynolds, I. M. (1985) Contrasted mineralogy and textural relationships in the uppermost titaniferous magnetite layers of the Bushveld Complex in the Bierkraal area north of Rustenburg. *Economic Geology*, **80**, 1027-1048.

Rider, M. (1996) *The Geological Interpretation of Well Logs*, 2nd Edition, Whittles Publishing, pp.280.

Rioul, O., and Vetterli, M. (1991) Wavelets and signal processing. *Institute of Electrical and Electronics Engineers Special Magazine*, **8**, 14-37.

Roelofse, F. (2010) PhD thesis: Constraints on the magmatic evolution of the lower Main Zone and Platreef on the Northern Limb of the Bushveld Complex as inferred from the Moordkopje drill core, University of the Witwatersrand, Johannesburg, South Africa.

Roelofse, F., and Ashwal, L.D. (2012) The lower Main Zone in the Northern Limb of the Bushveld Complex– A > 1.3 km thick sequence of intruded and variably contaminated crystal mushes. *Journal of Petrology*, **0**, 1-28.

Samworth, J.R. (1992) The dual-spaced density log- Characteristics, calibration, and compensation. *The Log Analyst*, **33**, 42-49.

Schouwstra, R.P., and Kinloch E.D. (2000) A short geological review of the Bushveld Complex. *Metals Review*, **44**, no. 1, 33-39.

Schweitzer, J.K., Hatton, C.J., and De Waal, S.A. (1997) Link between the granitic and volcanic rocks of the Bushveld Complex, South Africa. *Journal of African Earth Sciences*, **24**, 95-104.

Seabrook, C.L. (2005) PhD thesis: The Upper Critical and Lower MZs of the eastern Bushveld Complex, University of the Witwatersrand, Johannesburg, South Africa.

Seber, G. A. F. (1984) *Multivariate Observations*, John Wiley & Sons, Inc., pp.686.

Segesman, F.F. (1980) Well-logging method. *Geophysics*, **45**, 1667-84.

Serra, O. (1984) *Fundamentals of Well-Log Interpretation: The Acquisition of Logging Data*, 1st Edition, Elsevier, pp. 423.

Sharpe , M.R. (1981) The chronology of magma influxes to the eastern compartment of the Bushveld Complex as exemplified by its marginal border groups. J*ournal of the Geological Society of London*, **138**, 307-326.

Sheriff, R (2002) *Encyclopaedic Dictionary of Applied Geophysics*, 4th Edition, 13 Geophysical reference series, Society of Exploration Geophysicists, pp. 429.

Sifuzzaman, M., Islam, M.R., and Ali, M.Z. (2009) Application of wavelet transform and its advantages compared to Fourier transform. *Journal of Physical Sciences*, **13**, 121-134.

Snyder, D., and Fleming, D.B. (1985) Well-logging- A 25 year perspective. *Geophysics*, **50**, 2504-2529.

Steinhaus, H., (1956) Sur la division des corp materiels en parties. *Bulletin of the Polish Academy of Sciences*, **3**, 801-804.

Tegner, C., Cawthorn, R.G., and Kruger, F.J. (2006) Cyclicity in the Main and Upper Zones of the Bushveld Complex, South Africa: Crystallization from a zoned magma sheet. *Journal of Petrology*, **47**, 2257-2279.

Teigler, B., and Eales, H.V. (1996) The Lower and Critical Zones of the western limb of the Bushveld Complex as intersected by the Nooitgedagt boreholes. *Bulletin of the Geological Survey of South Africa*, ***111***, pp. 126.

Telford, W.M, Geldart, L.P., and Sheriff, R.E. (1990) *Applied Geophysics*, 2nd Edition, Cambridge University Press, pp. 744.

Timur, A. (1985) Downhole geophysical logging. *Annual Review of Earth and Planetary Sciences*, **13**, 315-44.

Tittman, J. and Wahl, J.S. (1965) The physical foundations of formation density logging (Gamma-Gamma). *Geophysics*, **30**, 284-294.

Verma, A.K., Mohanty, W.K., Routray, A., and Mashinha, L. (2012) Detecting stratographic discontinuities using wavelet s-transform analysis of well log data. Abstracts of the *GeoConvention 2012: Vision*, Calgary, Canada. 14-18 May 2012.

Van der Merwe, M.J. (2008) The geology and structure of the Rustenburg Layered Suite in the Potgietersrus/Mokopane area of the Bushveld Complex, South Africa. *Miner Deposita*, **43**, 405-419

Vantongeren, J.A., and Mathez, E.A. (2013) Incoming magma composition and style of recharge below the Pyroxenite Marker, eastern Bushveld Complex, South Africa. *Journal of Petrology*, **54**, 1585-1605.

Viljoen, M.J., and Scoon, R.N. (1985) The distribution and main geologic features of discordant bodies of iron-rich ultramafic pegmatite in the Bushveld Complex. *Economic Geology*, **80**, 1109-1128.

von Gruenewaldt, G. (1973) The main and upper zone of the Bushveld Complex in the Roosenekal area, eastern Transvaal. *Transactions of the Geological Society of South Africa*, **76**, 207-227.

Wager, L.R., and Brown, G.M. (1968) *Layered Igneous Rocks*, Oliver and Boyd Ltd, pp. 586.

Wagner, P.A. (1929) *The Platinum Deposits and Mines of South Africa*, C. Struik Pty. Ltd, Cape Town, South Africa.

Webb, S.J., Cooper, G.R.J., and Ashwal, L.D. (2008) Wavelet and statistical investigation of density and susceptibility data from the Bellevue drillcore and Moordkopje borehole, Bushveld Complex, South Africa. Abstract of the *2008 SEG Annual Meeting*, Las Vegas, Nevada, November 9-14 2008.

Wilson, A.H. (2012) A chill sequence to the Bushveld Complex: insight into the first stage of emplacement and implications for the parental magmas. *Journal of Petrology*, **0**, 1-46.

Zhou, B. And Esterle, J. (2008) Toward improved coal density estimation from geophysical logs. *Exploration Geophysics*, **39**, 124-132.

APPENDICES

APPENDIX A: Cluster Analysis

APPENDIX A1: Code for the *k*-Means Classification

```
function [idx,ctrs]=kmean(X,noiter,norep)

%************************************************************************
**
%Program computes the k-Means classification in R^2 space
%************************************************************************
**
%
%Program written by: Obone Sepato
%Date: July 2012
%Email: ob.sepato@gmail.com
%
%************************************************************************
**
%
%INPUT: The physical property data. These should be arranged in three
%columns with the first column as the depth of the measurements, the
second column as the density and the third column as the magnetic
%susceptibility. The import uses a text file and the extension (.txt)
%should be included in the filename when the user is prompted. The user
%is also asked for the number of iterations to be carried out
%and the number of replicates.

%OUTPUT: This will show a scatter plot of the original data, a scatter
plot of the data belonging to each of the classes, shown on the same
system of axes with different colours denoting each of the different
classes.

%************************************************************************
**

clc
clear

%Import dataset
file=input('Enter filename including .txt extension: ','s');
importdata(file);
x=importdata(file);
```

```
%Density and magnetic susceptibility data
X=x(:,2:3);

%No. of iterations
noiter=input('No of iterations: ');

%No. of replicates
norep=input('No of replicates: ');

%Scatter plot of the magnetic susceptibility vs density
figure(1);subplot(2,2,1); semilogy(X(:,1),X(:,2),'o','MarkerSize',2);
title('Magnetic Susceptibility (SI) vs Density
(g/cc)','FontSize',14);xlabel('Density (g/cc)','FontSize',14);ylabel('Log
of Magnetic Susceptibility (SI)','FontSize',14); set(gca,'FontSize',14);
axis xy; hold on;

%k-Means classification scheme- also produces scatter plots for two,
three and four classes, as well as the distribution of the classes with
depth. The code as it stands does the computation for up to four classes.

[idx,ctrs]=kmeans(X,2,'MaxIter',noiter,'display','iter','Replicates',nore
p);
cluster1 = X(idx == 1,:);
cluster2 = X(idx == 2,:);
figure(1);subplot(2,2,2);semilogy(cluster1(:,1),cluster1(:,2),'o','Marker
Size',2,'MarkerFaceColor',[0 0 .56], 'MarkerEdgeColor',[0 0 .56]);
title('Magnetic Susceptibility (SI) vs Density
(g/cc)','FontSize',14);xlabel('Density (g/cc)','FontSize',14);ylabel('Log
of Magnetic Susceptibility (SI)','FontSize',14);hold on;;
set(gca,'FontSize',14); axis xy;
semilogy(cluster2(:,1),cluster2(:,2),'o','MarkerSize',2,'MarkerFaceColor'
,[.5 0 0], 'MarkerEdgeColor',[.5 0 0]);
plot(ctrs(:,1),ctrs(:,2),'kx','MarkerSize',12,'LineWidth',2);
plot(ctrs(:,1),ctrs(:,2),'ko','MarkerSize',12,'LineWidth',2)
legend('Class 1','Class 2','Centroids','Location','SE');
figure(2);subplot(3,1,1); imagesc(x(:,1),0:0.5:0.5,idx');title(' Classes
(2) vs. Depth (m)','FontSize',14); colorbar;set (gca,'FontSize',14);


[idx,ctrs]=kmeans(X,3,'MaxIter',noiter,'display','iter','Replicates',nore
p);
cluster1 = X(idx == 1,:);
cluster2 = X(idx == 2,:);
```

```
cluster3 = X(idx == 3,:);
figure(1);subplot(2,2,3);semilogy(cluster1(:,1),cluster1(:,2),'o','Marker
Size',2,'MarkerFaceColor',[0 0 .56], 'MarkerEdgeColor',[0 0 .56]);
title('Magnetic Susceptibility (SI) vs Density
(g/cc)','FontSize',14);xlabel('Density (g/cc)','FontSize',14);ylabel('Log
of Magnetic Susceptibility (SI)','FontSize',14);hold on;
set(gca,'FontSize',14); axis xy;
semilogy(cluster2(:,1),cluster2(:,2),'o','MarkerSize',2,'MarkerFaceColor'
,[.5 1 .5], 'MarkerEdgeColor',[.5 1 .53]);
semilogy(cluster3(:,1),cluster3(:,2),'o','MarkerSize',2,'MarkerFaceColor'
,[.5 0 0], 'MarkerEdgeColor',[.5 0 0]);
plot(ctrs(:,1),ctrs(:,2),'kx','MarkerSize',12,'LineWidth',2);
plot(ctrs(:,1),ctrs(:,2),'ko','MarkerSize',12,'LineWidth',2)
legend('Class 1','Class 2','Class 3','Centroids','Location','SE');
figure(2);subplot(3,1,2); imagesc(x(:,1),0:0.5:0.5,idx');title(' Classes
(3) vs. Depth (m)','FontSize',14); colorbar; colorbar;set
(gca,'FontSize',14)

[idx,ctrs]=kmeans(X,4,'MaxIter',noiter,'display','iter','Replicates',nore
p);
cluster1 = X(idx == 1,:);
cluster2 = X(idx == 2,:);
cluster3 = X(idx == 3,:);
cluster4 = X(idx == 4,:);
figure(1);subplot(2,2,4);semilogy(cluster1(:,1),cluster1(:,2),'o','Marker
Size',2,'MarkerFaceColor',[0 0 .56], 'MarkerEdgeColor',[0 0 .56]);
title('Magnetic Susceptibility (SI) vs Density
(g/cc)','FontSize',14);xlabel('Density (g/cc)','FontSize',14);ylabel('Log
of Magnetic Susceptibility (SI)','FontSize',14);hold on;
set(gca,'FontSize',14); axis xy;
semilogy(cluster2(:,1),cluster2(:,2),'o','MarkerSize',2,'MarkerFaceColor'
,[.5 1 .53], 'MarkerEdgeColor',[.5 1 .53]);
semilogy(cluster3(:,1),cluster3(:,2),'o','MarkerSize',2,'MarkerFaceColor'
,[1 .86 0], 'MarkerEdgeColor',[1 .86 0]);
semilogy(cluster4(:,1),cluster4(:,2),'o','MarkerSize',2,'MarkerFaceColor'
,[.5 0 0], 'MarkerEdgeColor',[0.5 0 0]);
plot(ctrs(:,1),ctrs(:,2),'kx','MarkerSize',12,'LineWidth',2);hold on
plot(ctrs(:,1),ctrs(:,2),'ko','MarkerSize',12,'LineWidth',2)
legend('Class 1','Class 2','Class 3','Class
4','Centroids','Location','SE');
figure(2);subplot(3,1,3); imagesc(x(:,1),0:0.5:0.5,idx');xlabel('Depth
(m)','FontSize',14);title(' Classes (4) vs. Depth (m)','FontSize',14);
colorbar; colorbar;set (gca,'FontSize',14);
```

APPENDIX A2: Comparison of the L_1, L_2 and cosine distance metrics

The classification schemes using the L_2, L_1 and cosine distance metrics are shown in Figure A2.1. Figure A2.1a shows three easily identifiable. Figure A2.1b, c and d show the results obtained using *k*-means classification for the L_2, L_1 and cosine distance metrics respectively. The three clusters have been allocated to different classes for the L_2 and L_1 but the cosine metric is unable to distinguish them which makes it unsuitable. The same data are shown in Figure A2.2a with a smaller distance of separation in Figure A2.1a, to assess the performance of the the L_2 and L_1 metrics when the clusters are together. The results in Figure A2.2b and c show that the two metrics produce similar classifications.

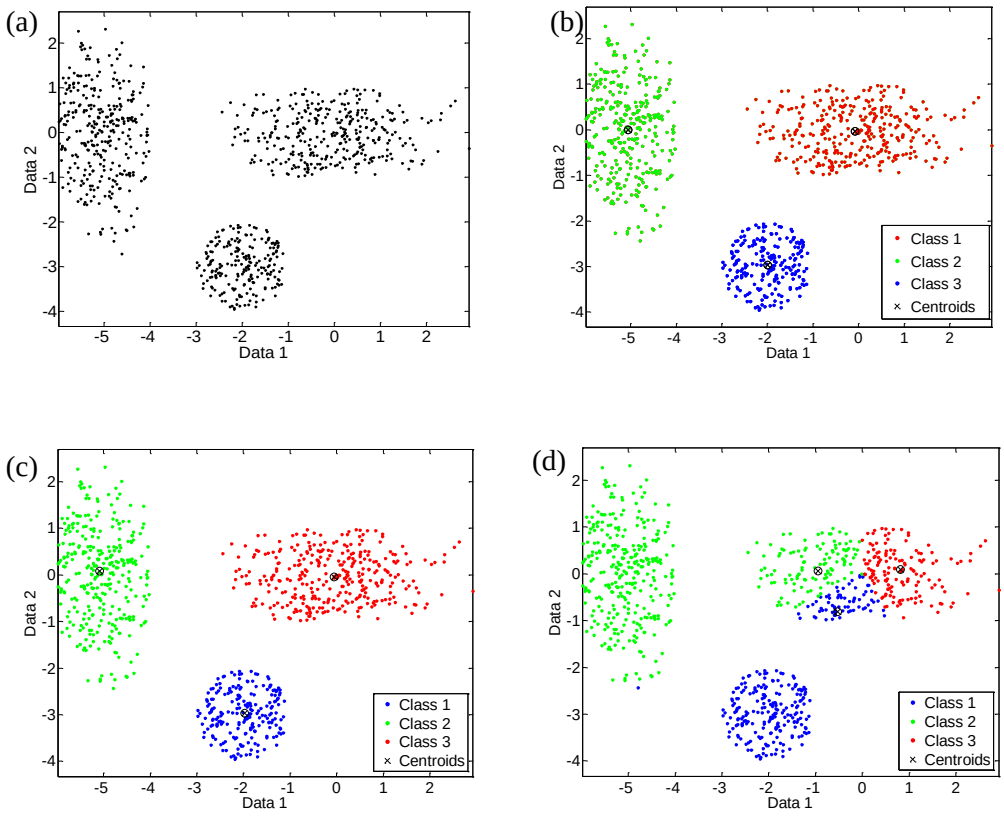

Figure A2.1 A comparison of different distance metrics. (a) Cross-plots between two arbitrary measurements, with three visible clusters. Two of the generated clusters are elliptical and the third is circular. *k*-Means classification for (b) the squared Euclidean, (c) city block and (d) cosine distances. These classifications show that the cosine is not a well-suited metric for these clusters.

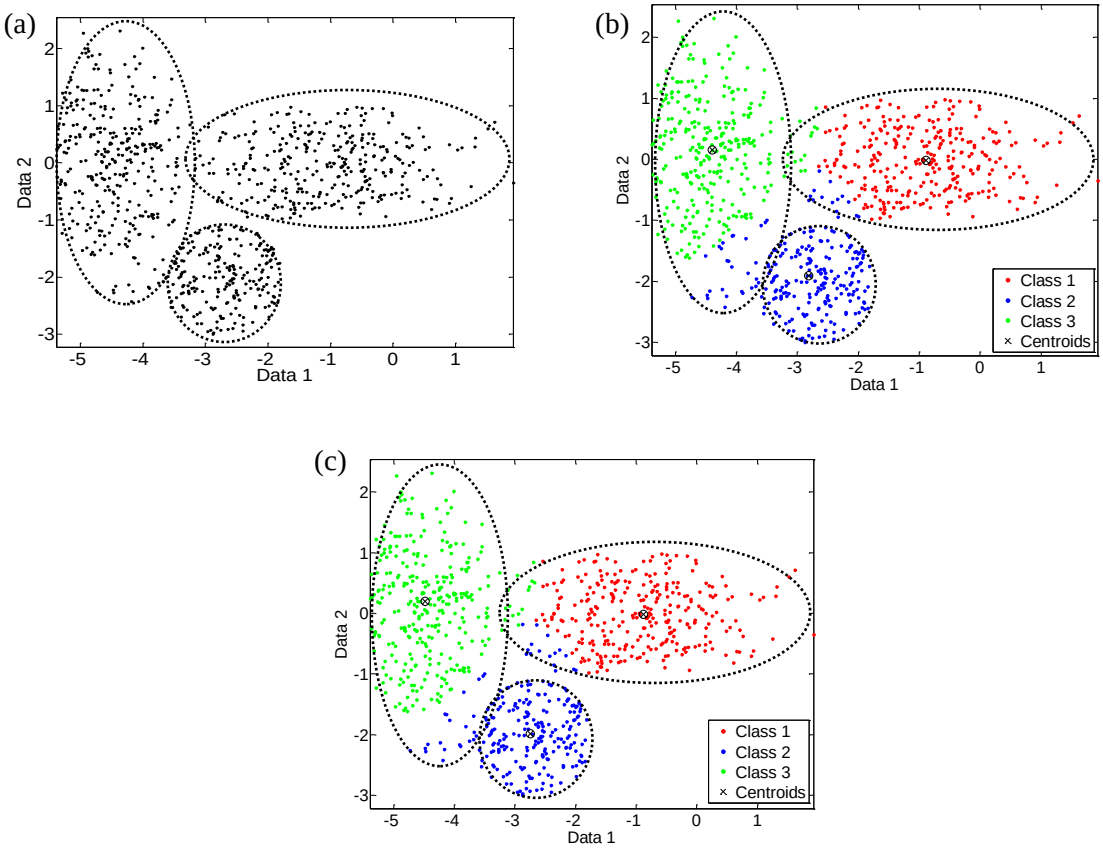

Figure A2.2 A comparison of different distance metrics. (a) Cross-plots between two arbitrary measurements, with three visible clusters with a smaller distance of separation in Figure A2.1a. *k*-Means classification for (b) the squared Euclidean and (c) city block . They show similar results.

APPENDIX B: Wavelet Analysis

APPENDIX B1: Code for calculating the power spectrum

```
function [p,w]=pwrspectrum(x)

%*************************************************************************
**
%Program computes the power spectrum
%*************************************************************************
**
%Program written by: Obone Sepato
%Date: March 2012
%Email: ob.sepato@gmail.com
%
%*************************************************************************
**
%
%INPUT: A text file is imported and the extension (.txt) should be
included
%in the filename when the user is prompted. This should consist of two
%columns. The first can be a time series or position and the second can
be
%the measured data column of data whose power spectrum is calculated

%OUTPUT: Plot of the raw data and the calculated power spectrum

%*************************************************************************
**

clc
clear

%Import dataset
file=input('Enter filename including .txt extention: ','s');
importdata(file);
x=importdata(file);

%Time or position and the measured data
d=x(:,1);
data=x(:,2);

figure(1);
subplot(2,1,1);plot(d,data);axis tight;title('Data'); xlabel('Position')
```

```
[p,w]=periodogram(data); %Computes the power spectrum

subplot(2,1,2);plot(w,p);axis tight; title('Power
Spectrum');xlabel('Frequency (radians per second)');
```

APPENDIX B2: Code for the wavelet analysis

```
function [cden,cmagsus]=cwtrans(data,ds,scale,varthresh,lb,ub)

%**************************************************************************
**
%Program computes the continuous wavelet transform (CWT)
%**************************************************************************
**
%
%Program written by: Obone Sepato
%Date: February 2012
%Email: ob.sepato@gmail.com
%
%References:
%Cooper, G.R.J. (2007) Lecture notes, Applications of  wavelets to the
%geosciences.
%
%http://www.mathworks.com/help/toolbox/wavelet/ref/cmorwavf.html
%
%Date accessed:10/08/2012
%**************************************************************************
**
%
%INPUT: The physical property data. These should be arranged in three
%columns with the first column as the depth of the measurements, the
second
%column as the density and the third column as the magnetic
%susceptibility. The import uses a text file and the extension (.txt)
%should be included in the filename when the user is prompted. The data
%are downsampled, and mean subtracted to rid the CWT of edge effects. A
%scale of the CWT is also required which should be of the format "1:xx".
%The histograms of the data can be optionally threshold.

%OUTPUT: Plot of the raw data and the CWT of the data

%**************************************************************************
**

clc
clear

%Import dataset
file=input('Enter filename including .txt extention: ','s');
```

```
importdata(file);
data=importdata(file);

%Depth, density and magnetic susceptibility data
depth=data(:,1);
den=data(:,2);
magsus=data(:,3);

%Downsample the data
ds=input('Downsample (cm): ');
den=downsample(den,ds);
magsus=downsample(magsus,ds);
depth=downsample(depth,ds);

%Subtract mean
den=detrend(den,'constant');
magsus=log(magsus);
magsus=detrend(magsus,'constant');

%CWT
scale=input('Scale of the CWT:');
cden=cwt(den,scale,'cmor1-1'); cden=real(cden);
cmagsus=cwt(magsus,scale,'cmor1-1');cmagsus=real(cmagsus);


%Adjustment of the histogram
%To threshold density data, use "cden" and to threshold magnetic
%susceptibility data use "cmagsus"
varthresh=input('Variable to threshold: ');

subplot(2,1,1);imagesc(varthresh);colorbar
subplot(2,1,2);hist(double(varthresh),50);

%The lower and upper bound values of the histogram respectively
lb=input('lb of hist: ');
ub=input('ub of hist: ');

for I=1:length(varthresh(:,1));
   for K=1:length(varthresh(1,:));
        if varthresh(I,K)<lb;
            myimt(I,K)=lb;
       elseif varthresh(I,K)>ub;
           myimt(I,K)=ub;
        else
```

```
            myimt(I,K)=varthresh(I,K);
        end
    end
end

figure(1);
if varthresh==cden;
subplot(2,1,1);imagesc(depth,scale,varthresh);axis xy;xlabel('Depth
(m)','fontsize',20);ylabel('Wavelength (m)','fontsize',20);title('CWT of
Density Data (g/cc)','fontsize',20);set (gca,'fontsize',20);colorbar
subplot(2,1,2);imagesc(depth,scale,myimt);axis xy;xlabel('Depth
(m)','fontsize',20);ylabel('Wavelength (m)','fontsize',20);title('CWT of
Density Data (g/cc)','fontsize',20);set (gca,'fontsize',20);colorbar
else
subplot(2,1,1);imagesc(depth,scale,varthresh);axis xy;xlabel('Depth
(m)','fontsize',20);ylabel('Wavelength (m)','fontsize',20);title('CWT of
Magnetic Suscpetibility Data (SI)','fontsize',20);set
(gca,'fontsize',20);colorbar
subplot(2,1,2);imagesc(depth,scale,myimt);axis xy;xlabel('Depth
(m)','fontsize',20);ylabel('Wavelength (m)','fontsize',20);title('CWT of
Magnetic Suscpetibility Data (SI)','fontsize',20);set
(gca,'fontsize',20);colorbar;
end;

figure(2);
if varthresh==cden
subplot(2,1,1);plot(depth,den);axis tight;
xlabel('Depth(m)','fontsize',20);ylabel('Density Data
(g/cc)','fontsize',20);title('Mean-subtracted Density (g/cc) vs. Depth
(m) ','fontsize',20);set (gca,'fontsize',20);
subplot(2,1,2);imagesc(depth,scale,myimt);axis xy;xlabel('Depth
(m)','fontsize',20);ylabel('Wavelength (m)','fontsize',20);title('CWT of
Density Data (g/cc)','fontsize',20);colorbar;set (gca,'fontsize',20);
else
subplot(2,1,1);plot(depth,magsus);axis tight;
xlabel('Depth(m)','fontsize',20);ylabel('Magnetic Susceptibility
(SI)','fontsize',20);title('Log of the Mean-subtracted Magnetic
Susceptibility (SI) vs. Depth (m)','fontsize',20);set
(gca,'fontsize',20);
subplot(2,1,2);imagesc(depth,scale,myimt);axis xy;xlabel('Depth
(m)','fontsize',20);ylabel('Wavelength (m)','fontsize',20);title('CWT of
Magnetic Suscpetibility Data (SI)','fontsize',20);colorbar;set
(gca,'fontsize',20);set (gca,'fontsize',20);
end;
```

```
end;
```

APPENDIX B3: Code for the semblance analysis

```
function [sembden,sembmagsus]=semb(x1,x2,ds,scale)

%************************************************************************
**
%Program computes the cross-wavelet transform (XWT) and the wavelet based
semblance analysis for the density and magnetic susceptibility for two
datasets.
%************************************************************************
%
%
%Program written by: Obone Sepato
%Date: February 2012
%Email: ob.sepato@gmail.com
%
%INPUT: The physical property data for two datasets. These should be
%arranged in three columns with the first column as the depth of the
%measurements, %the second column as the density and the third column as
%the magnetic %susceptibility. The import uses a text file and the
%extension (.txt)should be included in the filename when the user is
%prompted. The data %are downsampled, and mean subtracted to rid the CWT
of edge effects. The %user inputs the scale of the semblance analysis.
%
%OUTPUT: Plot of the semblance analysis for density and magnetic
susceptibility
%
%References:
%Cooper, G.R.J. (2007) Lecture notes, Applications of wavelets to the
%geosciences.

%************************************************************************
**

clc
clear

%Import datasets
file1=input('Enter the first filename including .txt extention: ','s');
importdata(file1);
x1=importdata(file1);
file2=input('Enter the second filename including .txt extention: ','s');
importdata(file2);
```

```
x2=importdata(file2);

%Depth, density and magnetic susceptibility data
depth1=x1(:,1); depth2=x2(:,1);
den1=x1(:,2);den2=x2(:,2);
magsus1=x1(:,3);magsus2=x2(:,3);

%Downsample the data and subtract mean
ds=input('Downsample (cm): ');
depth1=downsample(depth1,ds); depth2=downsample(depth2,ds);
den1=downsample(den1,ds); den2=downsample(den2,ds);
magsus1=downsample(magsus1,ds);magsus2=downsample(magsus2,ds);
den1=detrend(den1,'constant');den2=detrend(den2,'constant');
magsus1=log(magsus1); magsus2=log(magsus2);
magsus1=detrend(magsus1,'constant'); magsus2=detrend(magsus2,'constant');

%CWT
scale=input('CWT scale: ');
c_den1=cwt(den1,scale,'cmor1-1'); c_den2=cwt(den2,scale,'cmor1-1');
c_magsus1=cwt(magsus1,scale,'cmor1-1');
c_magsus2=cwt(magsus2,scale,'cmor1-1');

%XWT
xwt_den=c_den1.*conj(c_den2);
xwt_magsus=c_magsus1.*conj(c_magsus2);

amp_xwt_den=abs(xwt_den);
amp_xwt_magsus=abs(xwt_magsus);

%Local phase and semblance
phase_den=atan2(imag(xwt_den),real(xwt_den));
phase_magsus=atan2(imag(xwt_magsus),real(xwt_magsus));

sembden=cos(phase_den);
sembmagsus=cos(phase_magsus);

figure (1);
subplot(2,1,1);imagesc(depth1./100,scale,sembden);axis
xy;title('Semblance (n=1) of Mean-subtracted Density Data
(g/cc)');colorbar; set (gca,'fontsize',12); xlabel('Depth
(m)');ylabel('Wavelength (m)')
subplot(2,1,2);imagesc(depth1./100,scale,sembmagsus);axis
xy;title('Semblance (n=1) of the Mean-subtracted  Magnetic Susceptibility
```

```
Data (SI)');colorbar; set (gca,'fontsize',12);  xlabel('Depth
(m)');ylabel('Wavelength (m)');
```

APPENDIX B4: Code for the mean-resultant length

```
function [den_MRL,magsus_MRL]=MRL(x1,x2,x3,ds,scale)

%************************************************************************
**
%Program computes mean-resultant length (MRL) for three datasets
%************************************************************************
**
%
%Program written by: Obone Sepato
%Date: February 2012
%Email: ob.sepato@gmail.com
%
%References:
%Cooper, G.R.J. (2007) Lecture notes, Applications of wavelets to the
geosciences.
%
%Davis, J.C. (2002) Statistics and data analysis in geology,
%            3rd Edition, John Wiley & Sons, pp. 616.
%
%************************************************************************
**
%
%INPUT: The physical property data for three datasets. These should be
%arranged in three columns with the first column as the depth of the
%measurements, the second column as the density and the third column as
%the magnetic susceptibility. The import uses a text file and the
%extension (.txt)should be included in the filename when the user is
%prompted. The data are downsampled, and mean subtracted to rid the CWT
%of edge effects. The user inputs the scales to be calculated.

%OUTPUT: Plot of the MRL for density and magnetic susceptibility

%************************************************************************
**

clc
clear

%Import datasets
file1=input('1st dataset: ','s');
importdata(file1);
x1=importdata(file1);
```

```
file2=input('2nd dataset: ','s');
importdata(file2);
x2=importdata(file2);
file3=input('3rd dataset: ','s');
importdata(file3);
x3=importdata(file3);


%%Depth, density and magnetic susceptibility data
depth1=x1(:,1); depth2=x2(:,1); depth3=x3(:,1);
den1=x1(:,2);den2=x2(:,2);den3=x3(:,2);
magsus1=x1(:,3);magsus2=x2(:,3);magsus3=x3(:,3);


%Downsample the data and subtract mean
den1=detrend(den1,'constant');den2=detrend(den2,'constant');den3=detrend(
den3,'constant');%den4=detrend(den4,'constant') %detrend density
magsus1=log(magsus1); magsus2=log(magsus2);
magsus3=log(magsus3);%magsus4=log(magsus4); %log of magsus
magsus1=detrend(magsus1,'constant'); magsus2=detrend(magsus2,'constant');
magsus3=detrend(magsus3,'constant');%
magsus4=detrend(magsus4,'constant'); %detrend magsus

%CWT
scale=input('CWT scale: ');
c_den1=cwt(den1,scale,'cmor1-1'); c_den2=cwt(den2,scale,'cmor1-1');
c_den3=cwt(den3,scale,'cmor1-1'); %c_den4=cwt(den4,scale,'cmor1-1');
c_magsus1=cwt(magsus1,scale,'cmor1-1');
c_magsus2=cwt(magsus2,scale,'cmor1-1');
c_magsus3=cwt(magsus3,scale,'cmor1-
1');%c_magsus4=cwt(magsus4,scale,'cmor1-1');

%MRL of the density data
den_sum_r_cwt=(real(c_den1)+real(c_den2)+real(c_den3)).^2;
den_sum_i_cwt=(imag(c_den1)+imag(c_den2)+imag(c_den3)).^2;
den_MRL_top=sqrt(den_sum_i_cwt+den_sum_r_cwt);
den_MRL_bottom=abs(c_den1)+abs(c_den2)+abs(c_den3);
den_MRL=(den_MRL_top)./(den_MRL_bottom);


%MRL of the magnetic susceptibility data
magsus_sum_r_cwt=(real(c_magsus1)+real(c_magsus2)+real(c_magsus3)).^2;
magsus_sum_i_cwt=(imag(c_magsus1)+imag(c_magsus2)+imag(c_magsus3)).^2;
magsus_MRL_top=sqrt(magsus_sum_i_cwt+magsus_sum_r_cwt);
```

```
magsus_MRL_bottom=abs(c_magsus1)+abs(c_magsus2)+abs(c_magsus3);
magsus_MRL=(magsus_MRL_top)./(magsus_MRL_bottom);


figure (1);
subplot(2,1,1);imagesc(depth1,scale,den_MRL);axis xy;title('Mean-
resultant Length for Density Data (g/cc)');colorbar;
subplot(2,1,2);imagesc(depth1,scale,magsus_MRL);axis xy;title('Mean-
resultant Length for Magnetic Susceptibility Data (g/cc)');colorbar;
```